

University of Strathclyde, Glasgow

Department of Naval Architecture, Ocean and Marine Engineering

Effect of Added Mass and Damping on the Response of Subsea Structure Installation

By

Tarimumu Egbuson

A thesis presented in fulfilment of the requirements for the degree of

Doctor of Philosophy

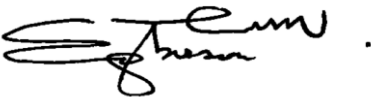
2021

Declaration

This thesis is the work of the candidate's original research and he confirms the originality of the work submitted belongs to him and that appropriate credit has been given as reference to the work of other authors.

The copyright of this thesis belongs to the author under the terms of the United Kingdom Copyright Acts as qualified by University of Strathclyde Regulation 3.51. Due acknowledgment must always be made of the use of any material contained in, or derived from, this thesis.

Tarinumu Egbuson

Signature:  .

Date: 28 November 2020

Table of Contents

List of Figures	v
List of Tables.....	ix
Nomenclature	xi
Acknowledgement.....	xvii
Abstract	xviii
1 Introduction.....	1
1.1 Background	1
1.2 Installation of Subsea Structures and Analysis Approach.....	2
1.2.1 Analysis Approach.....	6
1.3 The Installation Process and Analysis Techniques	7
1.3.1 Specific Depth Analysis.....	12
1.3.2 Staged Analysis.....	12
1.3.3 Continuous Lowering Analysis.....	12
1.4 The Importance of Installation Analysis	13
1.5 The Difficulty in Carrying Out Accurate Installation Analysis	13
1.6 Aim and Objectives	14
1.6.1 Research Aim.....	14
1.6.2 Research Objectives	14
1.7 Thesis Outline.....	15
2 Literature Review	17
2.1 Literature Review	17
2.2 Motivation for Research Study.....	23
3 Hydrodynamics of Offshore Structures: Estimation of Added Mass and Damping for Disk or Vertical Cylinder near Seabed.....	25
3.1 Introduction	25
3.2 Theoretical Formulation of Added Mass of Suction-Can	25
3.3 Basis of DNV's Method for Calculating Added Mass of Suction-Can	38
3.4 Added mass of Suction Can Very Close to the Seabed.....	39
3.5 Estimation of Damping	40

3.6	Summary of Proposed Approximate Method.....	64
4	CFD Simulation for Suction-Can	65
4.1	Introduction	65
4.2	Computational Fluid Dynamics.....	65
4.3	Numerical Determination of Vertical Added Mass and Damping of Suction-Can	66
4.3.1	Model and Simulation Domain	67
4.3.2	Mesh Generation	69
4.3.3	Mesh Sensitivity	72
4.3.4	Time Step Sensitivity	74
4.3.5	Turbulence Modelling.....	76
4.3.6	Dynamic Mesh	80
4.3.7	Solver Settings	84
4.4	Hydrodynamic Properties of Suction-Can.....	91
4.4.1	Operation Away from Surface and Seabed.....	92
4.4.2	Operations Close to Seabed	95
4.5	Chapter Summary.....	100
5	CFD Analysis of Complicated Subsea Protective Structure.....	102
5.1	Introductory Remarks	102
5.2	The Subsea Structure	102
5.3	Modelling and Meshing of the Subsea Structure	103
5.3.1	Creating the Model.....	103
5.3.2	Meshing.....	107
5.3.3	Challenges and Difficulties in the Numerical Modelling	109
5.4	Boundary Conditions and Exporting the Mesh	110
5.5	Turbulence Model Selection	112
5.6	Time Step, Courant Number and Maximum Iterations.....	112
5.7	CFD Analyses Results	113
5.8	Chapter Summary	121
6	Case Study: Installation Analysis Using the Hydrodynamic Coefficients	122
6.1	Introduction	122
6.2	Comparison between Hydrodynamic Coefficients of CFD Analysis and Approximate Method	123

6.3	Installation Analysis of Subsea Protective Structure.....	127
6.4	Modelling the Subsea Protective Structure in Orcaflex	128
6.5	Size of Lowering Line	129
6.5.1	Lowering Line Stiffness	130
6.6	Time Step Sensitivity	132
6.7	Comparison between the implicit and explicit integration scheme.....	133
6.8	Installation Acceptance Criteria	136
6.9	Static Analysis	136
6.10	Dynamic Analysis: Far from Boundaries	137
6.11	Dynamic Analysis: Close to Seabed	137
6.12	Installation analysis Results	137
6.13	Chapter Summary	141
7	Research Contribution	143
7.1	Introduction	143
7.2	Research Contribution	143
8	Conclusion and Recommendations for Further Study	145
8.1	Conclusion.....	145
8.2	Recommendations for Further Work.....	146
	References	148
	Appendix A	159
A.1	Vortex shedding from edge of disc	159
A.2	Vortex Generation around Disc for different Critical KC Values.....	161
	162
A.3	Added Mass Coefficients for Three-Dimensional Bodies	163
A.4	Subsea Structure Installation Phases	163
	Appendix B	168
B.1	Contour of Velocity Magnitude of Suction-Can Well Away from Surface and Seabed.....	168
B.2	Contours of Vorticity Magnitude of Suction-Can Well Away from Surface and Seabed.....	172
B.3	Contours of Velocity Magnitude of Suction-Can at $h/D = 0.4$	177
	APPENDIX C	181
C.1	Calculation of Added Mass and Damping of Subsea Protective Structure	181

APPENDIX D	190
D.1 Response of Subsea Protective Structure	190
D.2 Theory related to the ORCAFLEX analyses	192

List of Figures

Figure 1.1-1 World primary energy demand by fuel (International Energy Agency, 2013)	1
Figure 1.3-1 Subsea protective structure with associated hydrodynamic loads while passing through the water surface	8
Figure 1.3-2 Subsea template at target location (Braun, 2013).....	8
Figure 1.3-3 Subsea template lifted off deck of installation vessel (Braun, 2013).....	9
Figure 1.3-4 Subsea template over boarded and ready for lowering (Braun, 2013)....	9
Figure 1.3-5 Subsea template lowering through splash zone (Braun, 2013)	10
Figure 1.3-6 Subsea template lowering through splash zone (aerial view) (Braun, 2013)	10
Figure 1.3-7 Subsea template lowered through water column to near-seabed (CM Labs, 2011).....	11
Figure 1.3-8 Subsea template landed on seabed (CM Labs, 2011).....	11
Figure 2.1-1 Comparison of response of subsea deployment vessel and surface vessel (Installation Vessel) (Courtesy: Subsea Deployment Systems Ltd.)	20
Figure 3.2-1 Cylinder of water between the disc and the seabed.....	26
Figure 3.2-2 Bar with applied forces.....	27
Figure 3.2-3 Representation of added mass of ring of fluid (radius R) outside a	29
Figure 3.2-4 Comparison between Ca of approximate method (present work) and Caref of Garrido-Mendoza et al. (2015) for different h/R	32
Figure 3.2-6 Comparison of added mass coefficient at different heights above seabed using approximate method	36
Figure 3.2-7 Comparison of added mass coefficient at different heights above seabed, with Ca for smaller h/R included, using approximate method	36
Figure 3.4-1 Added mass coefficient of suction-can at different h/D ratios.....	40
Figure 3.5-1 Graph showing original inflow data (black – ξ_p vs hDP) and fitted equation (red – ξ_{fit} vs h/D)	47

Figure 3.5-2 Graph showing comparison between damping ratios of Garrido-Mendoza et al. (2015) (black – ξ_0 vs Dh_0) and approximate method (red – ξ_{fit} vs D/h).....	48
Figure 3.5-3 Graph showing comparison between damping ratios of Garrido-Mendoza et al. (2015) (black – ξ_0 vs Dh_0^{-1}) and approximate method (red – ξ_{fit} vs h/D)	49
Figure 3.5-4 Drag coefficient at low Keulegan-Carpenter numbers. +, Flat plate (Singh, 1979); \diamond , square cylinder (Singh, 1979); O, circular cylinder (Sarpkaya, 1975; Singh, 1979) (Courtesy: Graham, 1980).....	50
Figure 3.5-8 C_p for different h/R (internal flow losses included)	58
Figure 3.5-9 C_p for different h/R (internal flow losses included)	58
Figure 3.5-13 Comparison between C_t (above) and C_{t1} (below)	63
Figure 4.3-1 Simulation domain	68
Figure 4.3-2 Total force for 40D (domain1), 60D (domain2) and 80D (domain3) domain sizes	68
Figure 4.3-3 Cell size transition away from wall boundary of suction-can on horizontal plane (XY plane).....	70
Figure 4.3-4 Cell size transition away from wall boundary of suction-can at $h/D = 0.2$ on vertical plane (ZX plane)	70
Figure 4.3-5 Force report of oscillating suction-can far from boundaries	75
Figure 4.3-6 Force time history for k-epsilon, k-omega SST and SST Transition turbulence models	79
Figure 4.3-7 Contours of velocity magnitude of suction-can well away from surface and seabed for one oscillation	84
Figure 4.3-8 Solution set-up in Fluent	87
Figure 4.3-9 Pressure contour of suction-can well away from surface and seabed ...	88
Figure 4.3-10 Pressure contour of suction-can at $h/D = 1.2$	89
Figure 4.3-11 Pressure contour of suction-can at $h/D = 0.6$	89
Figure 4.3-12 Pressure contour of suction-can at $h/D = 0.2$	90
Figure 4.4-1 Added mass coefficients of suction-can away from surface and seabed	94

Figure 4.4-2 Equivalent damping ratio of suction-can away from surface and seabed	94
Figure 4.4-3 Suction-can at $h/D = 0.4$ (figure above) and $h/D = 0.2$ (figure below) above seabed	95
Figure 4.4-4 Residuals for 20 inner iterations at $KC = 0.1$ ($h/D = 0.4$)	97
Figure 4.4-5 Hydrodynamic force of suction-can at $h/D = 0.4$	97
Figure 4.4-6 Added mass coefficient of suction-can at $h/D = 0.40$ from seabed.....	98
Figure 4.4-7 Equivalent damping of suction-can at $h/D = 0.40$ from seabed	98
Figure 4.4-8 Added mass coefficient of suction-can at $h/D = 0.20$ from seabed.....	99
Figure 4.4-9 Equivalent damping of suction-can at $h/D = 0.20$ from seabed	99
Figure 5.3-3 Mesh of subsea protective structure far from boundaries	109
Figure 5.7-1 Pressure contour of subsea protective structure far from boundaries at $KC 0.02$	115
Figure 5.7-2 Pressure contour of subsea protective structure far from boundaries at $KC 0.21$	117
Figure 5.7-3 Pressure contour of subsea protective structure at $h/D = 0.4$, $KC 0.02$	118
Figure 5.7-4 Pressure contour of subsea protective structure at $h/D = 0.2$, $KC 0.02$	118
Figure 5.7-5 Added mass coefficient of subsea protective structure far from boundaries and close to seabed	119
Figure 5.7-6 Equivalent linearized damping of subsea protective structure far from boundaries and close to seabed	120
Figure 6.2-1(a – c) Added mass coefficient of subsea protective structure at different heights above seabed.....	125
Figure 6.2-2 Damping ratio of subsea protective structure at different heights above seabed.....	126
Figure 6.4-1 Subsea protective structure.....	128
Figure 6.4-2 OrcaFlex model of subsea protective structure	129
Figure 6.5-1 Comparison between DAF (T_{max}/WT) of steel and fibre rope.....	132
Figure 6.12-1 Response ratio of subsea protective structure far from boundaries...	138
Figure 6.12-2 Response ratio of subsea protective structure at $h/D = 0.2$	138

Figure 6.12-3 Non-dimensional line tension far from boundaries.....	139
Figure 6.12-4 Non-dimensional line tension at $h/D = 0.2$	139
Figure 6.12-5 Line tension DAF of subsea protective structure far from boundaries	140
Figure 6.12-6 Line tension DAF of subsea protective structure at $h/D = 0.2$	141
Figure A.1- 1 Vortex shedding from edges of disc for one cycle of oscillation (Tao et al. 2003).....	161
Figure A.2- 1 Vortex generation around disc at different KC to critical KC ratios Garrido-Mendoza et al. (2015).....	162
Figure A.3- 1 Analytical added mass coefficient for three-dimensional bodies far from boundaries	163
Figure B.1- 1 Contours of velocity magnitude of suction-can well away from surface and seabed for KC 0.1 - 0.9.....	172
Figure B.2- 1 Contours of vorticity magnitude of suction-can well away from surface and seabed for KC 0.1 - 0.9.....	176
Figure B.3- 1 Contours of velocity magnitude of suction-can for KC = 0.1 – 0.8 at $h/D = 0.4$	180
Figure D.2- 1 Numerical line model (Source: Orcina)	192
Figure D.2- 1 Showing a single mid-line node and the segments either side of it, and various spring-dampers	193
Figure D.2- 2 Regular travelling wave properties (Source: DNV-RP-H103).....	196

List of Tables

Table 3.2-1 Added mass coefficient at various h/R , $KC = 0$	31
Table 3.2-2 Comparison between added mass coefficients of suction-cans at gap ratios 0.2, 0.4 and 1.2, $KC = 0.1$	37
Table 3.3-1 Comparison between added mass coefficient of proposed approximate method and DNV of suction-can far from boundaries.....	39
Table 3.5-1 Damping ratio for smallest bellmouth radius (I.E. Idel'chick, 1966)	45
Table 3.5-2 Damping ratio for outflow data (I.E. Idel'chick, 1966)	47
Table 4.3-1 Main characteristics of suction-can	69
Table 4.3-2 Size function parameters.....	69
Table 4.3-3 EquiAngle Skew, θEAS vs. Mesh Quality (Sharenet, 2009)	71
Table 4.3-4 Number of cells for mesh sensitivity study	72
Table 4.3-5 Added mass coefficients for various levels of the computational grid... ..	73
Table 4.3-6 Added mass coefficients and equivalent damping ratios for time step sensitivity study for the suction-can away from surface and seabed with 161,692 cells, and percentage change of parameters relative to shortest time step at $KC = 0.1$	75
Table 4.3-7 Added mass coefficient and equivalent damping ratio for various turbulence models at time step 0.01 secs ($KC = 0.1$).....	79
Table 4.3-8 Under-Relaxation Factors	85
Table 4.4-1 Equivalent damping results of CFD analysis and of model test by Roe et al. of the suction-can away from surface and seabed.....	93
Table 4.4-2 Added mass coefficient results for various time step and fluid domain sizes of suction-can at $h/D = 0.40$ from seabed	96
Table 5.3-1 Main characteristics of Subsea Protective Structure	104
Table 5.7-1 Equivalent linearized damping ratio of subsea protective structure.....	121
Table 6.5-1 Input parameters for numerical analysis.....	130
Table 6.5-2 Fibre rope properties.....	131

Table 6.6-1 Maximum effective tension in lowering line, crane tip and subsea structure motion at various time steps.....	133
Table 6.7-1 Comparison between the implicit and explicit integration scheme	134
Table 6.7-2 Input parameters for explicit integration scheme	134
Table 6.7-3 Influence of lowering line segmentation on dynamic effective tension and motion in lowering line and on subsea structure respectively for various time steps.....	135
Table C.1- 1 Added mass and damping of outer bucket	182
Table C.1- 2 Added mass and damping of central bucket	183
Table C.1- 3 Damping of H-Beam at various KC numbers.....	184
Table C.1- 4 Drag coefficient and damping of Horizontal beam at various KC numbers	185
Table C.1- 5 Drag coefficient and damping of Hatch beam at various KC numbers	185
Table C.1- 6 Drag coefficient and damping of inclined beam at various KC numbers	186
Table C.1- 7 Added mass and damping of subsea protective structure	187
Table C.1- 8 Added mass and damping contribution from each member of the subsea protective structure, initial KC for each member.....	188
Table C.1- 9 Comparison between added mass and damping coefficient of approximate method and CFD analysis of the subsea protective structure	188
Table D.1- 1 Response of subsea protective structure far from boundaries	190
Table D.1- 2 Response of subsea protective structure at $h/D = 0.2$	190
Table D.1- 3 Line tension far from boundaries.....	191
Table D.1- 4 Line tension at $h/D = 0.2$	191
Table D.2- 1 Definition of wave parameters with formulas	195

Nomenclature

a	Uniform acceleration of object	m/s^2
A_p	Horizontal projected area of suction-can	m^2
A_r	Reference area	m^2
A_s	Slamming area	m^2
Be	Equivalent damping ratio	Dimensionless
c	Damping coefficient	Dimensionless
c_{33}	Heave damping	Ns/m (kg/s)
Ca	Added mass coefficient	Dimensionless
C_{a33}	Added mass coefficient	Dimensionless
C_d	Drag coefficient	Dimensionless
C_m	Inertia coefficient	Dimensionless
C_s	Slamming coefficient	Dimensionless
D	Diameter of suction-can	m
Dw	Vertical weight distribution	N
E	Young's modulus of elasticity	KN/m^2
F_w	Winch drive force	N
F	Applied force	N
F_μ	Frictional force	N
f_0	Excitation amplitude	N
F_h	Measured force	N
F_s	Safety factor	Dimensionless
F_c	Damping force	N
F_{ext}	External force	N
F_k	Spring force	N
f_e	Amplitude of external force	N
f_d	Drag force	N
f_i	Inertia force	N

F_m	Measured force	N
f	Frequency of oscillation	Hz
F_{hydro}	Hydrodynamic force	N
F_D	Hydrodynamic drag force	N
F_{slam}	Slamming force	N
F_p	Varying buoyancy force	N
g	Acceleration due to gravity	m/s^2
h/D	Water depth ratio	Dimensionless
h	Grid spacing	m
H	Height of cylinder	m
k	Amplification factor	Dimensionless
K	Wire stiffness	N/m
k_{COG}	Centre of gravity factor	Dimensionless
L	Length of cylinder	m
l	Total length of wire	m
l_0	Unstretched length of paid out wire	m
M	Mass of object	kg
Ma	Added mass of object	kg
m_{a33}	Heave added mass away from surface and seabed	kg
MBL_{sling}	Minimum breaking load of sling	N
MBL	Minimum breaking load	N
m	Mass of structure	kg
Ma_{330}	Added mass of flat plate	kg/m
N	Number of sample points	Dimensionless
\vec{n}	Outward normal vector on surface	Dimensionless
$Pr_{h=0}$	Richardson extrapolation	Dimensionless
p_{GCI}	Order of convergence	Dimensionless
P	Pressure at the surface of the fluid on a point	N/m^2
r	Grid refinement ratio	Dimensionless
Re	Reynolds number	Dimensionless

$S(\omega_k)$	Wave spectrum	m^2s/rad
t	Time	$secs$
T	Period of oscillation	$secs$
T_{static}	Static tension	N
T_{max}	Maximum component of dynamic tension	N
T_w	Tension in wire	N
T_d	Damped natural period	$secs$
u	Component of velocity in the x direction	m/s
U_r	Relative velocity of water to structure	m/s
\dot{U}_r	Relative acceleration of water to structure	m/s
\dot{U}_w	Acceleration of water	m/s^2
\dot{U}_s	Acceleration of structure	m/s^2
$U_c(z)$	Total current velocity at a given location (x,y) with respect to water depth	m/s
$\dot{U}(t)$	Flow acceleration with respect to time	m/s^2
$U(t)$	Flow velocity with respect to time	m/s
$U_{33}(t)$	Oscillatory velocity of body in the heave direction	m/s
\vec{U}	Velocity field	m/s
v_s	Slamming impact velocity	m/s
v_c	Lowering velocity of hook	m/s
v_{ct}	Amplitude of velocity at the crane tip	m
v_w	Vertical water particle velocity	m/s
\vec{v}	Body surface velocity	m/s
V	Volume of structure	m^3
V_b	Volume of body	m^3
v	Component of velocity in the y direction	m/s
w	Component of velocity in the z direction	m/s
W	Weight of object	N
X_p	Distance of water particles to the body surface in harmonic motion	m

$x(t)$	Total response	m
x_0	Initial displacement	m
\dot{x}_0	Initial velocity	m/s
z_{33}	Oscillatory motion in heave	m
\dot{z}	Oscillatory velocity in heave	m/s
\ddot{z}	Oscillatory acceleration in heave	m/s^2
z_{wdr}	Distance of suction can from seabed	m
z	Water depth	m
z_{ct}	Crane tip motion	m
z_w	Wave induced response	m
Z_{static}	Static displacement of structure from its equilibrium position	m
Z_{max}	Maximum component of dynamic motion	m
Z_{ct}	Corresponding maximum displacement of crane tip (top end of lowering line)	m

Greek Symbols

ρ	Density of seawater	kg/m^3
ρ_s	Density of structure	kg/m^3
θ_{EAS}	EquiAngle Skew	Dimensionless
θ_{ESS}	EquiSize Skew	Dimensionless
θ_{MAS}	MidAngle Skew	Dimensionless
ω_e	Angular frequency of external disturbance	rad/sec
ω_d	Frequency of damped oscillation	Hz
ω_n	Natural frequency	Hz
ω	Angular frequency of oscillation	rad/sec
ω	Vorticity	Hz
φ_k	Parameter for uniform distribution of random phases between 0 and 2π	rad
φ	Phase shift	rad
\emptyset	Phase angle between oscillatory motion of structure and force	rad

η	Amplitude	m
η_w	Wave elevation	m
η_{33}	Amplitude of vertical motion	m
η_{ct}	Amplitude of response at crane tip	m
η_p	Amplitude of response for particular solution	m
ξ_{33}	Heave damping ratio	Dimensionless
ξ	Damping ratio	Dimensionless
ϵ	Sling angle factor (SAF)	Dimensionless
ε	Minimum error (Least Squares Method)	N
ϵ	Wire strain	Dimensionless
τ	Viscous stress	N/m^2
δ	Logarithmic decrement	Dimensionless
∇	Del operator	m^{-1}
Δ_{body}	Displacement of submerged structure	kg

Abbreviations

2D	Two-dimensional
3D	Three-dimensional
AHTS	Anchor handling tug supply
CFD	Computational Fluid Dynamics
DNV	Det Norske Veritas
DoF	Degrees of freedom
DAF	Dynamic amplification factor
<i>ELM</i>	Equation of a line
EPCI	Engineering, Procurement, Construction and Installation
GCI	Grid convergence indices
IEEE	Institute of Electrical and Electronic Engineers
KC	Keulegan Carpenter number
kW	Kilowatts
mph	Miles per hour
mT	Metric tonne

PISO	Pressure-Implicit with Splitting of Operators
RAOs	Response amplitude operators
ROVs	Remotely operated vehicles
SDV	Subsea deployment vessel
SSCVs	Semi-submersible crane vessels
SST	Shear-Stress Transport
Te	Tonne
UDF	User defined function
UKCS	United Kingdom Continental Shelf
WD	Water depth

Acknowledgement

I would like to thank Professor Nigel Barltrop for his outstanding supervision and academic advice. Not only was he helpful over the years in supervising my research, but through his years of experience in my field of study, he was able to shape my thinking and improve my thesis writing skills. I would say I have learned a lot during this period and I am grateful for his patience, support and assistance.

I would like to express my gratitude to Professor Shan Huang, who was my first supervisor before he moved to BP. With his help, I was able to define my research area, and gain the motivation required to carry out this research.

I am grateful to the faculty and staff of the department. I appreciate the support received from the department especially from Thelma Will before she retired, who was always willing to help with a smile on her face. I would like to use this opportunity to thank other PhD students who offered their assistance during my research.

I also would like to thank Dr Richard Martin and Dr Karina Kubiak-Ossowska of the High Performance Computing Support Team at the Department of Physics for their assistance and support during this research. The CFD results of this thesis were obtained using the ARCHIE-WeSt High Performance Computer (www.archie-west.ac.uk) based at the University of Strathclyde.

I would like to thank my partner for her patience, love and continuous support throughout my study and her encouragement most especially during my writing up stage.

Finally, I would like to express my profound gratitude to my parents and family for their support and continuous encouragement throughout my years of study and throughout my research.

Abstract

Remotely located deepwater fields with challenging environmental conditions are now being explored and developed because of their good energy resource. This means technology advancement in marine operations is required to influence the field development cost. This is hindered by the difficulty in estimating the added mass and damping parameters which are important influencing factors in the installation process of subsea structures required for the field development.

These issues are addressed by developing an analytical calculation and Fluent simulation method to estimate the hydrodynamic coefficients of complicated subsea structures far from boundaries and in close proximity to the seabed at different KC numbers. The analytical method is developed from standard hydrodynamic theory, and the CFD analysis is based on estimating the hydrodynamic force on the structure and then splitting the force into its added mass component, while the equivalent linearized damping is derived from the sinusoidal varying force over a time record by fitting a line that touches the peak of these forces. The results from the analytical method and CFD analysis were found to be satisfactory after validating with existing literature and through numerical flow visualisation.

The added mass and damping of the structure show KC dependency. As KC increases, the flow field around the vertically oscillating structure and the vortex shedding pattern changes. The increase in KC leads to an independent and interactive vortex shedding regime for the different heights above seabed.

The installation analysis performed, showed increasing response of the subsea protective structure at different KC as it progresses to the seabed, which is useful in understanding the influence of submergence on the added mass and damping of subsea structures oscillating in heave direction at various KC number.

1 Introduction

1.1 Background

The increasing demand for energy over the years has led to companies increase investment in the energy sector. Over the years, companies have moved into deeper waters due to the depleted onshore and shallow water reserves. One of the challenges faced by the industry is the security of supply which has led to an increase in exploration activities in much deeper waters but after June 2014, the International Energy Agency reported oil and gas supply was greater than its demand leading to a continuous price drop which still did not affect demand as shown in Figure 1.1-1 with a long-term forecast predicting global energy demand to increase by one-third in 2035.

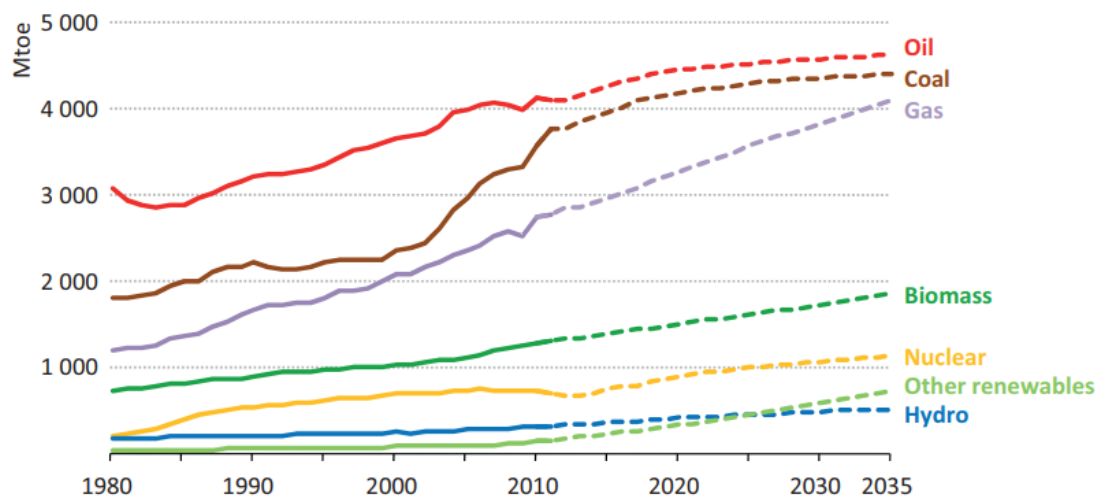


Figure 1.1-1 World primary energy demand by fuel (International Energy Agency, 2013)

As a result of this, there has been a cut down in exploration activities and oil field developments, hence the need for cost effective solutions to harness this form of energy.

The energy industry comprises of several activities carried out offshore which could be in either shallow water or deepwater environments and it is made up of different

sectors such as: the oil and gas sector, the wind energy sector, tidal and wave energy sector which are involved in subsea installation operations in these environments.

There are peculiar operational methods associated with each sector but these sectors all rely on an effective marine operation for their successful operation and the basic principles in marine hydrodynamics underpin the analysis of these operations.

1.2 Installation of Subsea Structures and Analysis Approach

A typical conventional installation method uses a drilling riser through a moon-pool or an A-frame vessel where the structure is over boarded at the stern of the vessel. When lowered below the waterline, the fully immersed subsea structure undergoes acceleration due to the motion at the crane tip. These top end excitations impact on the subsea structure and produce a net hydrodynamic force on the structure that is associated with the energy possessed by the structure due to its motion in water. The structure moves water in its path thereby experiencing a dissipation of its energy as a result of viscosity in the boundary of the fluid and structure and the pressure drag. The mass of the accelerated fluid is called the added mass while the effect of the dissipative process, loss of energy due to oscillatory motion of the structure that leads to decay of amplitudes, is known as the damping. The added mass and damping loads are steady-state hydrodynamic forces and moments due to forced harmonic rigid body motions which results in oscillating fluid pressures on the surface of the structure (Faltinsen, 1990).

Installation covers a wide range of methods used in placing offshore structures such as oil and gas structures, renewable energy structures and other structures. These structures are used for harnessing energy or other operations conducted in the offshore environment. In this thesis, installation deals with the lowering of subsea oil and gas structures used for drilling and production purposes while retrieval of these structures after their service life or during operation and maintenance activities is the reversal of the lowering process. The objectives of this thesis is not only limited to oil and gas structures and can be extended to other offshore sectors.

The challenges faced during such operations can be categorised into challenges from environmental conditions and from system properties. From the two categories, the structure's properties which lies within the system properties influence, to an extent, what installation or retrieval technique should be applied. Offshore structures could range from several linear structures to wide complex shaped geometrical structures, which explain why not one installation technique fits all.

These challenges pose a risk to the installed structure and could lead to technical failures such as loss of the subsea structure during lowering, damage to the subsea structure, and injuries to on-board personnel. Zhou, et al. (2015) presented similar consequences for a subsea jumper with high risk failure modes such as fatigue or wear of rigging or ropes, installation vessel's collision with jumper and sudden change of sea state. The project delivery time can be affected as a result of such failures or by simply underestimating or not taking accurate account of environmental factors such as the influence of sea waves or inaccuracy of weather forecast as reported by Zhou, et al. (2005), etc and hardware properties.

A brief description of the challenges from both environmental conditions and system properties associated with subsea installation is outlined below. These conditions take into account all water depths with emphasis on deepwater. There is no clear distinction between shallow, deepwater and ultra-deepwater depths. Deepwater is defined as depths greater than or equal to 500m and ultra-deepwater depths are those water depths greater than or equal to 1500m (Howes et al., 2008). With advancing technologies in this area and the industry goes deeper, this definition is bound to change.

Water Depth

The influence of water depth on deepwater offshore installation activities is significant when looking at the cost drivers during field development. The transition from shallow water to deepwater results in an increase in the number of technical challenges where conventional operational methods and equipment might not work (Rowe, et al., 2001) or be more expensive if applied, thereby increasing the operational risks associated with such operations, setting limitations for the vessel, the lowering line and the

installation technique. Increased water depth would result to longer exposure time of the structure to the dynamic excitation from the installation vessel, which would increase installation fatigue.

Strong current

The shape of the lifting line can be forced into a lateral catenary shape as a result of strong currents experienced in deepwater regions (Rowe, et al., 2001). Not only does this affect the lifting line, Rowe et al. (2001) further explained how relatively small currents introduces large offsets between the surface vessel and the subsea structure. Due to horizontal current variations the submerged structure's control and positioning becomes an issue in this case as it needs to be landed on the seabed safely taking into consideration the tight tolerance limit influenced by the field architecture and the water depth. As a result of the horizontal current loading on the structure, the structure tends to have a greater response compared to the deployment line because of its large surface area and both systems could move in same direction or in completely different directions due to the influence of multidirectional current. If this is the case, then the stresses at hook, the attachment point between the line and structure will be increased as the line tries to bring the structure back to its original position.

Wave Intensity

The response of the floating unit is partly due to the wave loading. Offshore waves are characterised by their period and height which have a significant influence on the subsea structure as a result of the motion transferred to it by the surface vessel. During lowering to the seabed, the subsea structure could experience resonance and snap loading for certain combinations of wave heights and periods. The wave properties are critical for a preliminary design through to detailed design of offshore structures. They are required in deriving the controlling parameters to have an idea on the limiting sea states. According to Bunnik and Buchner (2004) offshore structures experience excessive loading in the splash zone and this is the highest loading a structure will experience during the installation phases or when retrieved to deck and they also pointed out the difficulty in estimating the hydrodynamic loads in this zone. At this stage the lifting line undergoes excessive vibrations due to its stiffness and coupled response of the entire system.

Seabed Characteristics

After going through the water column, the structure has to be landed safely on the seabed at a tight tolerance limit. The challenges involved in such an operation are landing equipment with a large footprint area on uneven seabed topography (Example: The slide area of the Ormen Lange gas field and its uneven seabed topography) and a low bearing soil capacity. These challenges affect the structure's in situ stability and fluid flow within it.

System Properties

Offshore installation systems are equipment used during an installation campaign. They are the on-board equipment, the subsea module, the rigging, crane, tuggers and lowering line. The subjects of interest are the properties of the lowering line and the subsea module which are susceptible to environmental forces. In deepwater, the submerged weight of the line is important. According to Caley (2019), "At 3,000 meters the weight of a 5" wire rope is about the same as its 170t payload at a depth of about 6,000 meters the safe working load (SWL) of the steel wire rope is entirely used up by its self-weight, leaving zero payload capacity." This is not the case for synthetic ropes which have been developed to tackle this challenge. Substituting steel with synthetic ropes, which are wholly or partly buoyant when submerged in deepwater, can be of great advantage by carrying higher loads and still retaining their deepwater installation capacity, and freeing up useful deck space (DSM Dyneema Press Releases, 2010).

Deep water subsea modules are made large to reduce subsurface tieback. Safety is paramount when carrying out a marine operation. Large structures could pose a threat to personnel safety and on board equipment when lifted off a deck as a result of its response to environmental excitations (IMCA, 2007). The forces associated with lifting in-air, splash zone and submerged phases should be well accounted for during design. Another challenge is the time it takes to flood a submerged module to mitigate implosion. Water entry time increases with an increased module size and this needs to be taken into account.

Another challenge is the issue of resonance and snap loading caused by the dynamic excitations of the offshore construction vessel due to the wave loads. This should be well accounted for during the design stage and can be avoided by changing the system's parameters at particular depths.

1.2.1 Analysis Approach

There are several approaches that are adopted in carrying out installation analysis. Each approach is described in this section and they all depend on cost, time and quality.

Numerical Approach

A detailed analysis of the installation process is carried out during the final design stage in order to capture the nonlinearities which arise during the lowering operation. Several software packages are available for this purpose however the most widely used software is OrcaFlex which is a time domain software programme developed by Orcina Limited in Cumbria, UK. The dynamic behaviour of the structure and the lowering line that is attached to the winch is represented in OrcaFlex with the imposed vessel motions at the crane tip.

Analytical Approach

The analytical approach to the installation of subsea structures can easily be achieved by representing the system as a linearised single degree of freedom system. This method was adopted by Niedzwecki and Thampi (1991). Niedzwecki and Thampi used this simplified analytical method to investigate the possibility of snap loading occurring during the lowering process of the subsea structure. The simplified method was also useful in identifying the controlling parameters and how to reduce the effects of snap loading. Snap loading is one of the deepwater installation challenges and it is one of the design conditions that more attention should be paid to if or when it occurs. The regular wave design model was applied in this case and the assumption of a massless lowering line/cable with stiffness was applied. The continuous lowering method, explained in Section 1.4.3, is not possible with the analytical approach because the winch payout cannot be incorporated which means the installation analysis is carried out at key stages through the water column.

Experimental Approach

This is a more reliable approach although time consuming and expensive. Model tests are important when there is no available literature on previous work carried out on that particular model. With the experimental approach, the specific depth, staged and continuous lowering installation analysis techniques can be carried out. This approach will still be dependent on either the analytical or numerical analysis in order to validate the results obtained.

1.3 The Installation Process and Analysis Techniques

The subsea installation process may be categorised as a process for line structures and equipment with robust geometry. Line structures are installed using a lay vessel while large equipment is installed with an installation vessel, crane barge or a drill rig.

A typical installation process after the subsea equipment has been transported to the target location and properly rigged would involve lifting the equipment off the deck of the installation vessel which could be fitted with a crane of sufficient capacity. At this stage, the uncontrolled motion of the structure can be prevented by on board personnel. The structure is then lowered through the splash zone, also known as the air-sea interface, where it is susceptible to wave forces. Figure 1.3-1 adopted from DNV-RP-H103 (2011) shows the associated hydrodynamic loads on the subsea structure while passing through the water surface. After this phase, the structure is lowered through the water column until it is between 3 – 10 m above the seabed and lowering is stopped to prepare for final set down. Heave compensation is applied at this stage to reduce the vertical motions of the structure as it approaches the seabed with reduced lowering speed as compared to the speed when lowered through the water column. The seabed landing phase is the last phase of the installation process and care must be taken to avoid seabed impact which could damage the structure. Remotely Operated Vehicles are used to monitor the subsea equipment as it progresses to the seabed. See Appendix A.4 for more details on the various phases of the installation process and Figures 1.3-2 – 1.3-8 show the description of the installation process (Snapshots from animated videos of a subsea template by Tjeerd Braun and CM Labs).

After the equipment has been safely landed on the seabed, the lowering line is the retrieved. Retrieval is also a delicate operation because at this stage the equipment which produces a constant tension is no longer attached to the line thereby leaving the line to flex freely underwater. This could pose a threat to the installed equipment or already existing infrastructure in the event of a collision.

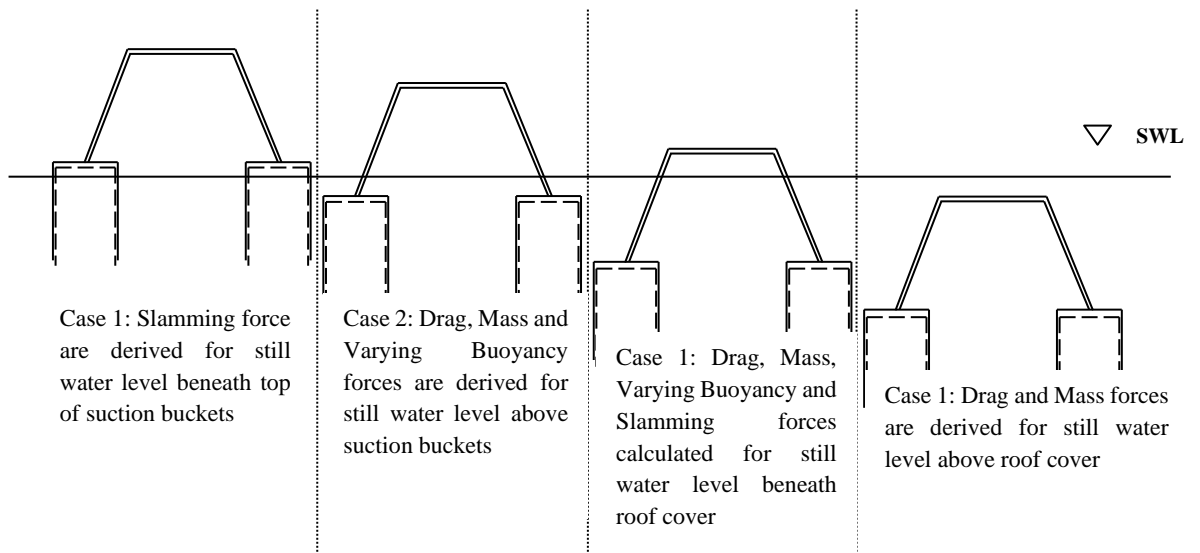


Figure 1.3-1 Subsea protective structure with associated hydrodynamic loads while passing through the water surface



Figure 1.3-2 Subsea template at target location (Braun, 2013)

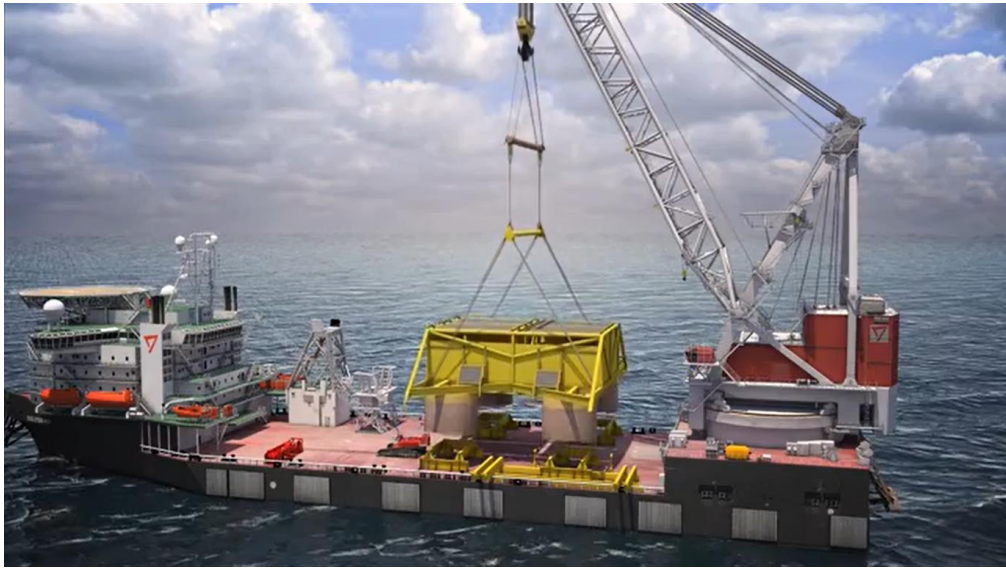


Figure 1.3-3 Subsea template lifted off deck of installation vessel (Braun, 2013)



Figure 1.3-4 Subsea template over boarded and ready for lowering (Braun, 2013)



Figure 1.3-5 Subsea template lowering through splash zone (Braun, 2013)



Figure 1.3-6 Subsea template lowering through splash zone (aerial view) (Braun, 2013)



Figure 1.3-7 Subsea template lowered through water column to near-seabed (CM Labs, 2011)

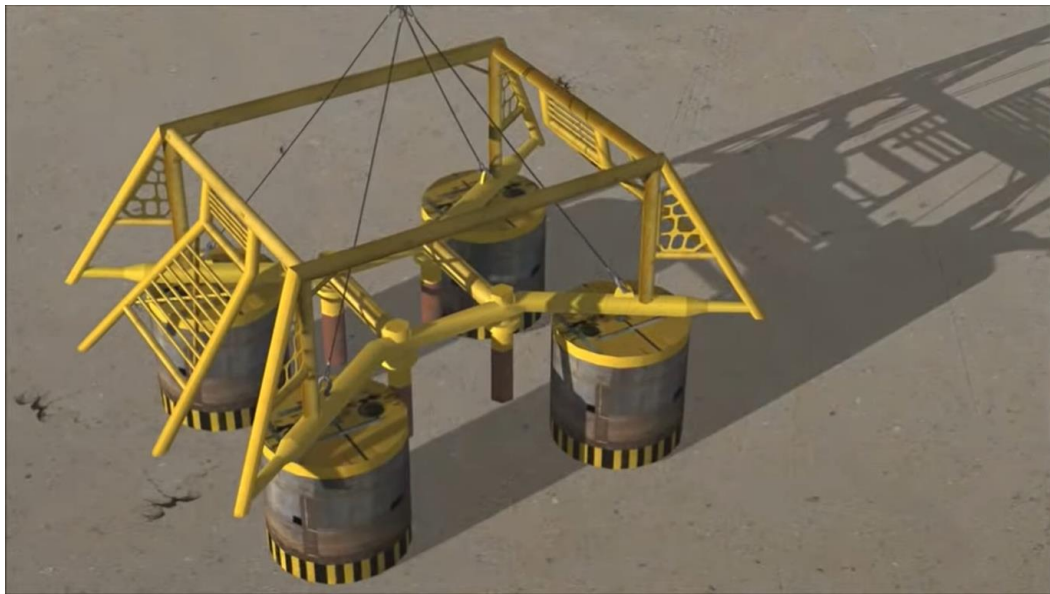


Figure 1.3-8 Subsea template landed on seabed (CM Labs, 2011)

Installation analysis is either done analytically or numerically depending on work scope requirements. Sections 1.3-1 – 1.3.3 covers the analysis techniques used for the installation or retrieval of subsea structures in deepwater. At the beginning of any simulation, analytical or numerical, the length of the lowering line has to be fixed

making it impossible to increase the line length during the course of the simulation. To make line length addition possible, the numerical software, Orcaflex, is equipped with the winch payout option which pays out additional finite line elements and assumes the paid out line increases the line length thereby changing the line's axial stiffness and damping. The paid out line is represented as a spring and damper system rather than by the finite line element method because the associated mass, hydrodynamic mass and normal drag forces are ignored.

1.3.1 Specific Depth Analysis

The specific depth analysis takes into consideration key stages in the lowering process. There is lowering line payout and the structure is suspended at a specific depth through the entire duration of analysis. This method has the advantage of focusing on the critical phases of the installation process but the drawback is that the line payout effects is ignored and unexpected events at certain depths may be missed since it is onerous to consider the entire water depth so only the key stages are considered.

1.3.2 Staged Analysis

This is only applicable to numerical analysis where lowering is done in stages. In this method, the lowering operation is stopped at intervals to allow for the replacement of paid-out line by dynamic line elements then the lowering simulation is restarted. The approach is most likely to provide more realistic results compared to the specific depth analysis since continuous lowering is achieved but in stages and the model is close to a real-life scenario. The only disadvantage here is that the modelling process is cumbersome and it will take a very long time to simulate the entire lowering process if the entire process is to be simulated as a requirement.

1.3.3 Continuous Lowering Analysis

The analysis method is the most realistic. It represents the real-life scenario of the lowering process by making use of the winch payout option to pay out line at a specific speed. The drawback in this numerical method is that there is no update on the mass of the lowering line as the length increases, the added mass and drag, and is only valid for light weight lines and when the system dynamics are determined by those of the subsea structure rather than those of the lowering line.

1.4 The Importance of Installation Analysis

It is paramount to have knowledge on the subsea structure's behaviour and the entire system's response beforehand. This is because limiting conditions and operable weather windows would have been defined to eliminate or mitigate the technical risks associated with the execution phase and ensure a smooth project delivery. In some cases the visual performance of the structure would be relevant to engineers to see the actual effect of the top end excitation on the subsea structure to justify the final results.

Looking at the importance of installation analysis, not from the project delivery point of view, but from the research perspective, installation analysis could actually be useful during the design of oil and gas structures. Design optimization to improve the response of the structure which would involve making it more hydrodynamic. Hence the need for accuracy in the derivation of added mass and damping of the subsea structure.

It helps in selecting suitable cost effective materials and equipment required to carry out the installation. These materials or equipment are the lowering line or rigging, the crane or winch system, and the vessel.

To conclude, the importance of good understanding of installation is that it helps engineers respond, adapt and accept new challenges that arise in the course of the analysis, which in turn will push them in developing new installation methods.

1.5 The Difficulty in Carrying Out Accurate Installation Analysis

Due to the need for accuracy, installation engineers continually strive to overcome the difficulties faced while carrying out installation analysis. Some of the difficulties associated with the process are:

1. The difficulty in deriving accurate dynamic loads for all stages of the installation process.
2. Difficulty in deriving accurate hydrodynamic coefficients of the structure for all stages of the installation process.

3. The governing equation for the structure's response is comprised of many parameters that influence the calculated response.
4. The installation analysis requirements are quite challenging due to the need for accuracy. The installation analysis should be carried out over a range of wave heights, wave periods and directions, and accuracy must be maintained, with analysis run times that are still acceptable, by the selection of a suitable time step size.

1.6 Aim and Objectives

The aim and objectives of this research are presented in this chapter to give a clear purpose of study and an understanding on why this research was conducted. The objectives cover the industry needs in the area of subsea installation analysis.

1.6.1 Research Aim

This research is aimed at providing the industry with knowledge and solutions to the problems involving the hydrodynamics of offshore structures with a focus on subsea structures, and installation of these structures away from the surface and the seabed and in close proximity to the seabed.

1.6.2 Research Objectives

Based on the intent of this research, the following objectives listed below have been developed to look into the existing problems.

1. To better understand the flow field around vertically oscillating complex subsea structures well away from surface and seabed and close to seabed using Computational Fluid Dynamics.
2. To understand the influence of submergence on the added mass and damping of subsea structures oscillating in heave direction at various Keulegan Carpenter number.
3. Develop an analytical method to estimate the added mass and damping of subsea structures far from boundaries and in close proximity to the seabed.
4. Carry out a case of study to validate the numerical method and analytical method proposed in point 1 and 3.

1.7 Thesis Outline

The thesis is made up of eight chapters. The first two chapters look at the background of the research and present the existing problems faced by the offshore industry, outline a list of objectives of this study and present a review on offshore installation techniques, challenges and hydrodynamics of subsea structures. The solutions to these challenges faced by the industry as highlighted in the list of objectives are spread through three chapters, chapters three to five with chapter six presenting the installation analysis of the subsea protective structure using the derived hydrodynamic coefficients of the Fluent simulation and approximate methods. The last chapters, chapters seven and eight present the contributions to industry, conclusion and recommendations for further research work. A brief summary of these chapters is given below.

Chapter 1: This is the introductory chapter that gives an overview of the background of the research with a focus on subsea structures installation and analysis approach, and the installation process and analysis techniques. The difficulties in carrying out installation analysis and concludes with the aim and objectives of the research.

Chapter 2: This chapter presents the literature review by considering other works related to this research. The research gap is discussed in this chapter, which is the motive for carrying out this research.

Chapter 3: This chapter looks at one of the main objectives of the research. It presents the development of an analytical calculation method for the vertical added mass and damping coefficients away from surface and seabed and in close proximity to the seabed.

Chapter 4: This chapter presents a Fluent simulation method using a user defined function, to determine vertical added mass and damping of a suction-can away from surface and seabed and in close proximity to the seabed and validates the results with previous publications.

Chapter 5: Chapter five presents the application of the Fluent simulation method to calculating the hydrodynamic coefficients of the subsea protective structure well away from surface and seabed, and in close proximity to seabed.

Chapter 6: This chapter presents the installation analysis of the subsea protective structure using the hydrodynamic coefficients obtained from the approximate method and CFD analysis.

Chapter 7: Chapter 8 discusses the research contribution.

Chapter 8: The research conclusions are drawn in this chapter and recommendations for further works are outlined.

Appendices: The appendices are made up of four sections, Appendix A, B, C and D.

Appendix A presents the vortex shedding from the edge of a disc forced to oscillate vertically and the vortex generation around a disc for different critical KC values.

Appendix B shows contours of velocity magnitude of the suction-can well away from surface and seabed, and in close proximity to seabed. The figures of the numerical flow visualisation were from the CFD analysis of the suction-can.

Appendix C presents the analytical calculation of added mass and damping of the subsea protective structure, and motion calculation of the subsea protective structure using Mathcad.

Appendix D presents the response of the subsea protective structure far from boundaries and close to the seabed using results of added mass and damping from the approximate and Fluent simulation method.

2 Literature Review

2.1 Literature Review

The hydrodynamic added mass and damping are important parameters in the design of offshore structures. This has made these parameters a subject of interest over the years in offshore engineering. Many offshore structures are designed from tubular members because they exhibit a high structural strength and low fluid loading compared to other members. Complex structures are often fabricated from the combination of these members. This is why an extensive study on the hydrodynamics around circular cylinders has been carried out over the years.

One of objectives of this thesis is the study of the hydrodynamic properties of a subsea intergrated structure. The structure is made up of suction-cans and circular cylinders and there exists a vast amount of literature on the hydrodynamics of circular cylinders compared to suction-cans. Potential flow theory is an analytic method applied to calculating the added mass and damping of bodies based on the incompressibility, irrotational and inviscid conditions of the fluid. It serves as an approximation of the solution to the problem. Several authors such as Lamb (1945), Birkhoff (1960) and Yih (1969) have contributed to the study of the added mass by developing a theoretical approach to estimation of the added mass coefficients of simple geometries while for complicated geometries, it is quite difficult to estimate these properties and it is important to note that the motion of the body in a certain direction could result in the deveopment of added mass forces in another direction.

The boundary value problem was solved by Ursell (1949). Ursell formulated the problem for a partially immersed heaving circular cylinder for the linearised free surface model by representing the potential function as a sum of an infinite set of multipoles, each multipole satisfying the free surface condition and each being

multiplied by a coefficient that is determined by requiring the series to satisfy the kinematic boundary condition at a number of points located on the cylinder.

The approach adopted by Ursell was further applied by Grim (1953), Tasai (1959) and Porter (1960). Grim solved the problem by conformal mapping the two parameter Lewis form cylinders onto a circle by variation of the Ursell method. Tasai (1959) and Porter (1960) derived the added mass and damping for oscillating contours mappable onto a circle by the more general Theodorsen transformation (Frank, 2007).

As at 1779, Du Buat (Du Buat, 1779) was the first to come up with the theory of added mass. He conducted a series of experiments on spheres oscillating in water and his conclusion was the basis of the definition of added mass. He established that the inertia force was proportional to the acceleration of the structure. For an object of mass, M with uniform acceleration, a , another mass, M_a will be introduced and added to account for the forces expressed as,

$$F = (M + M_a)a \quad \text{Equation 2.1-1}$$

Since then, experiments conducted to determine the added mass have reported inconsistent and varying results of larger values for the added mass when measured. Results of tests carried out in 1949 on circular disks were reported by Luneau (1949) which showed values of the added mass in a range of three to nine times the theoretical values. This was as a result of the wake induced mass not being accounted for during the test. This mass is dependent on the shape of the accelerating body and the wake volume together with the rates of change. The added mass does not relate to the displacement of a body wholly or partially immersed in a fluid but it is dependent on the motion time history which was concluded later on by Iverson and Balent (1951) that added mass is not a constant as shown by previous studies of potential flow and it is a variable dependent on the state of motion.

Sarpkaya and Isaacson (1981) showed that the added mass could be expressed in many ways by examining the various forms for two and three dimensional bodies. In an infinite fluid domain with irrotational flow, the hydrodynamic coefficients are derived from the forces and moments acting on the body through the use of a potential function.

Marintek (Marintek, 2003), in a review on deepwater marine operations looked at the transition of oil and gas activities beyond water depths of 1000 metres and they identified the requirement of installation contractors to perform subsea installations in a safe and efficient manner which was the ability to estimate and regulate the dynamic motions necessary for the close to seabed condition. A model similar to the one used in this research showed an increase in the hydrodynamic mass and a sharp increase in the hydrodynamic damping of the bucket foundation of the subsea protective structure as it approached the seabed. One of their objectives was to develop a cost-effective method of installing subsea structures in deep and ultra-deepwater without employing costly heavy crane vessels.

The TTA group (TTA Group, 2008) discussed cost effective installation methods in deepwater, alongside the need for a reliable weather forecast for such operations. They concluded that more work needed to be done on the design of subsea structures and equipment such as a lightweight deployment system which was already successfully applied in a water depth of 1000 metres. Operable weather windows could be determined from these forecasts if the system's dynamic response is accurately determined, hence the need for a quick and accurate method to derive the hydrodynamic parameters of the subsea structure.

In terms of cost saving and reduction in the dynamic response of subsea structures in deepwater, a Subsea Deployment System (SDS), a method of installing large subsea structures without a heavy lift vessel (HLV) was developed by Subsea Deployment Systems Limited in the United Kingdom (Subsea Deployment Systems Ltd, 2013). The dynamic response of the Subsea Deployment Vessel (SDV) and the subsea structure (SDV houses the subsea structure) which make up the payload will be lower than the response of the installation vessel (see Figure 2.1-1) during the landing phase. The vertical motions of the installation vessel would cause minimal dynamic response of the SDV because the control chains suspended from the installation vessel and responsible for final set-down are not directly connected to the SDV and only rests within the chain tower, which means the installation vessel and SDV can move independently (Subsea Deployment Systems Ltd., 2013).

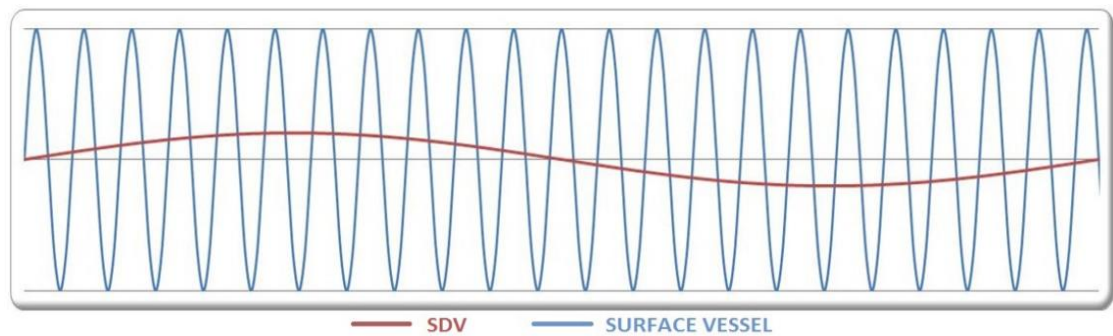


Figure 2.1-1 Comparison of response of subsea deployment vessel and surface vessel (Installation Vessel) (Courtesy: Subsea Deployment Systems Ltd.)

The installation analysis for the SDS method is dependent on accurate estimation of the added mass and damping of the entire structure which is composed of the SDV and the subsea structure. With this method, the structure is susceptible to environmental loading thereby reducing its fatigue life as a result of longer periods of exposure to these loads during transportation to target location.

The importance of the hydrodynamic properties does not only relate to the heave motion of the subsea structure but to other translational and rotational motions such as the horizontal motions in the x and y direction. Chen et al. (2017) concluded in this regard that the horizontal offsets of the subsea structure were highest in the x direction, higher than the offset in the vertical direction (heave). They also highlighted the importance and difficulty in obtaining the added mass and damping, and they suggested that extensive tests and analysis must be carried out to determine these coefficients. These coefficients affect the complicated installation process and the response, as a result these coefficients would be of great value in engineering design (Yunxia, et al., 2016).

With the added mass and damping parameters identified as important influencing factors in the installation process of subsea structures, several experiments and analyses have been conducted to accurately determine these parameters and show their influence on the dynamic response of subsea structures during installation. Gu et al. (2018) noted that understanding the hydrodynamic properties and response of a subsea structure, in this case a Mid Water Arch (MWA), to environmental conditions is relied

upon in the design of the structure. The hydrodynamic properties were investigated by Gu et. al (2018) through numerical simulations using CFD and experimental model scale testing, and results for the drag in the x and y direction and a 6 by 6 added mass matrix were obtained for each wave frequency. Garrido-Mendoza, Thiagarajan, Souto-Iglesias, Colagrossi and Bouscasse (2015) also carried out a numerical study to look at the flow characteristics around a heave plate oscillating close to the seabed. The results showed that the added mass and damping parameters increased continuously as the structure moved closer to the seafloor. The parameters showed linear variation with the KC number which is the ratio of the amplitude of oscillation of the structure, η to its diameter, D given as: $2\pi\eta/D$, and this trend was broken when a certain critical KC value was reached.

These show the need for accurate estimation of the hydrodynamic parameters of subsea structures in all phases of the installation process since the parameters vary for the different stages. The gap effect results of the added mass and damping by Garrido-Mendoza et al. (2015) were similar to the results of Wadhwa, Krishnamoorthy and Thiagarajan, (2010) who conducted forced oscillation experiments on a solid disc at various elevations of the seabed. Their numerical study concluded that the hydrodynamic parameters increase monotonically and as the disc gets closer to the seabed, the slope of the added mass curve plotted against the KC number decreases.

Morrison and Cermelli (2003) identified the hydrodynamic parameters of the subsea structure and the wire rope damping as the contributing factors to the gentle response of the structure. They pointed out that, the internal damping in a very long offshore wire rope is a source of significant damping in the system and it helps reduce resonance effects. They determined the hydrodynamic added mass and damping by applying a sinusoidal fit to the displacement and force signals at each time step for a duration of ten consecutive periods. The extrapolation method by Nam, Kim and Hong (2017) was used to determine the added mass of a subsea manifold. This method was based on the structure's perforation value, while the drag coefficient of the manifold was calculated using CFD. They reported the difficulty in estimating the added mass and damping coefficients and also stated their significance in the dynamic response of the lifted structure.

Numerical and experimental studies on the added mass and damping of subsea structures, like horizontally submerged and perforated rectangular plates, were conducted by An and Faltinsen (2013). Perforated subsea structures are used offshore as protective covers against dropped objects. According to An et al. (2013), when the structure is fully submerged, the numerically and experimentally predicted and measured hydrodynamic parameters respectively, show strong dependence on the Keulegan Carpenter number rather than on the frequency.

In relation to suction-cans, Ireland, Macfarlane and Drobyshevski (2007), Roe, Macfarlane and Drobyshevski (2008), and Zoontjes, Siegersma and Ottens (2009) have carried out studies to address the issue of an accurate estimate of the hydrodynamic coefficients.

Ireland et al. (2007) conducted model tests in order to determine the added mass and damping of a suction can more accurately when well away from the surface and the seabed. It was observed that small changes in the geometry of the subsea structure may significantly affect the structure's hydrodynamic properties. They recommended that these changes should be thoroughly examined and taken into consideration if accurate results of the subsea installation analysis are desired.

Roe et al. (2008) conducted model tests to quantify the effect of the seabed on the added mass and damping of a suction can. The tests showed that the hydrodynamic parameters increased as the gap between the structure and the seabed reduced. They reported that the added mass increase in this region (close to seabed) was 20% of its deepwater value. Both coefficients increased gradually as the bottom clearance reduces. This incremental trend was also observed as the KC numbers increased.

Zoontjes et al. (2009) used CFD to determine the added mass and damping of a subsea structure far from boundaries and at various heights above seabed. They applied the oscillating flow and dynamic fluid body interaction method to derive the parameters and concluded that the oscillating flow method produced very good results well away from the surface and seabed. The oscillating flow method could not be applied to the seabed proximity condition because of insufficient space between the base of the

suction can and the seabed, which made the dynamic fluid body interaction method used in simulating a decay test the only suitable option in this case.

2.2 Motivation for Research Study

Accurate prediction of added mass and damping is very important in analysing the motion response of subsea structures. The parameters if predicted accurately would help the installation process. Subsequent chapters presented in this research are concerned with estimating the added mass and damping of subsea structures well away from surface and seabed and in close proximity to seabed in deepwater.

From the literature, there is a need to accurately estimate the added mass and damping of complicated subsea structures rather than simplifying the complicated geometry to standard shapes and underestimating or overestimating the response of the complicated structure. The change in added mass and damping of simple geometries like a disc from deepwater to close-to-seabed has been predicted rather than for complicated geometries. It would be beneficial to the installation process if this change is also estimated for complicated geometries since the landing phase is critical during the installation process.

Subsea structures can be fabricated from various standard members with their added mass and drag coefficients readily available in Det Norske Veritas (DNV-RP-H103). For quick estimation of the hydrodynamic coefficients of subsea structures, Det Norske Veritas has proposed formulas and values of added mass and drag coefficients of standard structural members and also proposed an analytical method to estimate the added mass of a suction-can well away from the surface and seabed. There is a gap that exists in the need for an approximate analytical method that can be applied in estimating the hydrodynamic coefficients for various Keulegan Carpenter number at various heights above the seabed for complex geometries. In the case of the subsea protective structure considered in this research, which is made up of various members including a suction-can where standard hydrodynamic theory can be applied in estimating the suction-can's added mass and damping.

Model tests are preferred to analytical and numerical methods in estimating the hydrodynamic coefficients of subsea structures, but they require large amount of resources such as time and cost when compared to analytical and numerical methods. Conducting model tests for several subsea structures of different geometries is not economically feasible for installation operations during subsea field development. Hence analytical and numerical calculations would be beneficial for installation analysis, where the actual hydrodynamic force experienced by the complicated subsea structure can be quantified by the latter method.

3 Hydrodynamics of Offshore Structures: Estimation of Added Mass and Damping for Disk or Vertical Cylinder near Seabed

3.1 Introduction

The hydrodynamic coefficient estimation is difficult because there is limited data, the steady flow behaviour is complicated and the oscillating structure considerably complicates and increases the heave added mass and drag coefficients. An attempt is made here to build up the coefficients from their component parts and, whilst this provides some useful insights, particularly for the effects of oscillation and friction, the final equations can only be regarded as empirical. Fitting equations that have some physical basis have the advantage that they are likely to work better outside the range for which they have been checked. In this case the complexity of the flow is such that for any real installation, detailed CFD and model tests should still be undertaken to demonstrate the proposed installation methodology. Nevertheless, a starting point is needed for design and the approach used here does provide a relatively simple way of assessing the likely behaviour of a structure with suction cans as they approach the seabed. The method is also useful for assessing the likely effect of frictional damping, which, owing to Reynolds number effects, may be much greater in a model test than at full scale.

3.2 Theoretical Formulation of Added Mass of Suction-Can

The calculation method presented is an approximate first principles calculation of the heave added mass for a thin cylinder that is used with linear interpolation to the case where the seabed has little influence.

The analysis calculates the radial flow velocity, $U(r)$ and then estimates the added mass taking into account that: The added mass is proportional to the mass of water moving times its movement squared. For sinusoidal motion the calculation can be based on

displacement, velocity or acceleration as displacement and velocity are proportional to acceleration, here velocity is used.

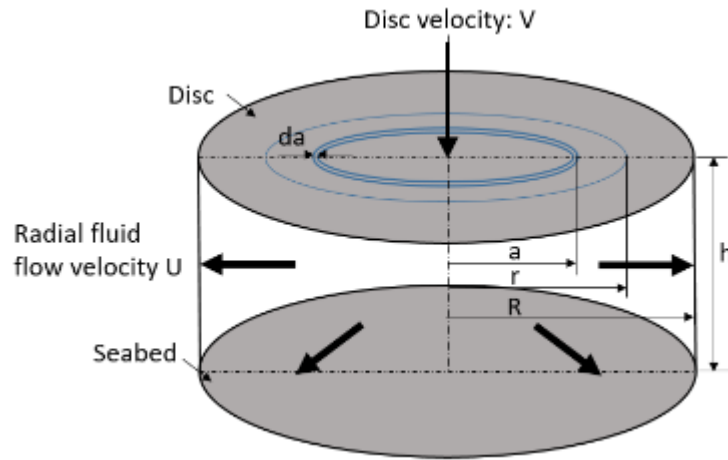


Figure 3.2-1 Cylinder of water between the disc and the seabed

1) Calculation of radial flow velocity at radius 'r' from annulus 'a'

$$2 \cdot \pi \cdot a \cdot V \cdot da = 2 \cdot \pi \cdot r \cdot h \cdot dU$$

Therefore

$$dU = \frac{V}{r \cdot h} \cdot a \cdot da$$

Equation 3.2-1

2) Integrate over all annuli inside 'r'

$$U(r) = \frac{V}{rh} \cdot \int_0^r a da = \frac{V}{rh} \cdot \frac{r^2}{2} = \frac{Vr}{2h}$$

Equation 3.2-2

3) Contribution of fluid mass to added mass proportional to velocity squared

This is demonstrated by a bar (Figure 3.2-2) with a mass at one end and forces applied at the other end. The top, where the force is applied and the acceleration is measured and represents the disc, and F/a is the 'apparent' mass that the force appears to be accelerating.

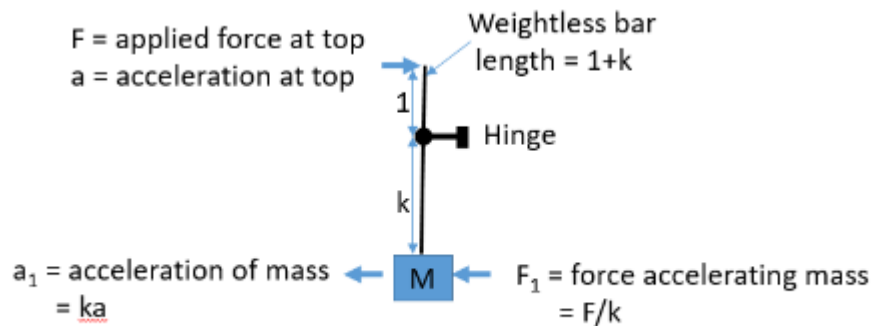


Figure 3.2-2 Bar with applied forces

Considering a lever system, when balanced, $F_1 k = F$, and this implies that $F_1 = F/k$.

The velocity ratio of the lever system is

$$\frac{a_1}{a} = \frac{k\ddot{\theta}}{\ddot{\theta}}$$

Therefore,

$$a_1 = ak$$

From Figure 3.2-2,

$$F_1 = Ma_1$$

This implies

$$F = (Mk^2)a$$

Therefore

$$M_{\text{apparent}} = Mk^2 \quad \text{Equation 3.2-3}$$

That is, for an element volume of the fluid between the disc and the seabed, its contribution to the added mass or virtual mass, also termed apparent mass in Equation 3.2-3 will be its

$$\text{Actual mass} \times (\text{Fluid velocity} / \text{Disc velocity})^2 \quad \text{Equation 3.2-4}$$

Mass is a second order tensor quantity and transforms differently because it is a ratio of two vectors (Force and acceleration). The force required to accelerate the position of the force application is proportional to the square of the lever arms (whereas simple forces would be proportional to the lever arm itself). This idea is often important when analysing structural and mechanical systems. E.g. the moment of inertia of an item (or its damping) attached to the output of a gearbox appears to have (gearbox ratio squared) times the inertia (or damping) when measured on the input shaft.

4) Calculation of vertical added mass

The added mass of a vertically oscillating disc is expressed as the sum of

Ma: added mass of water in the cylinder between disc and seabed,

Mb: added mass of ring of fluid (radius R) outside a,

Mc: added mass from vertical movement of fluid between plate and seabed, and

Md: added mass of fluid above the disc.

4a) Ma: added mass of water in the cylinder between disc and seabed.

Integrate

$$\rho U^2 d\text{volume} \quad (\text{between disc and seabed})$$

$$\begin{aligned}
Ma \cdot V^2 &= \rho \cdot \int_0^R U(r)^2 \cdot 2 \cdot \pi \cdot r \cdot h dr = \rho \cdot \int_0^R 2 \cdot \pi \cdot r \cdot h \cdot \frac{V^2 \cdot r^2}{4 \cdot h^2} dr \\
&= \rho \cdot \frac{\pi}{2} \cdot \frac{V^2}{h} \cdot \int_0^R r^3 dr
\end{aligned}$$

Therefore

$$Ma = \frac{\pi}{8} \cdot \rho \cdot V^2 \cdot \frac{R^4}{h}$$

Equation 3.2-5

4b) Mb: added mass of ring of fluid (radius R) outside 'a'.

Figure 3.2-3 was developed in order to derive an expression for the added mass around the disc. Ring cross section assumed to be a quarter circle of radius h. This assumption is reasonable for a $h \gg R$ because it is correct for the fluid on one side of a long narrow plate when the seabed is treated as a plane of symmetry.



Figure 3.2-3 Representation of added mass of ring of fluid (radius R) outside a

$$\begin{aligned}
U(R) &= \frac{V \cdot R}{2 \cdot h} & Mb &= \rho \cdot U(R)^2 \cdot 2 \cdot \pi \cdot R \cdot \frac{\pi \cdot h^2}{4} \\
Mb \cdot V^2 &= \rho \cdot \left(\frac{V^2 \cdot R^2}{4 \cdot h^2} \right) \cdot 2 \cdot \pi \cdot R \cdot \left(\frac{\pi \cdot h^2}{4} \right)
\end{aligned}$$

Therefore,

$$Mb = \frac{\pi^2}{8} \cdot \rho \cdot V^2 \cdot R^3$$

Equation 3.2-6

4c) M_c : added mass from vertical movement of fluid between plate and seabed.

Assuming the velocity varies linearly from V to zero over height 'h'.

$$V(z) = V \cdot \frac{z}{h}$$

$$M_c \cdot V^2 = \int_0^h V(z)^2 \cdot \rho \cdot \pi \cdot R^2 dz = V^2 \cdot \frac{h^3}{3 \cdot h^2} \cdot \rho \cdot \pi \cdot R^2$$

Therefore

$$M_c = \frac{\pi}{3} \cdot \rho \cdot V^2 \cdot h \cdot R^2$$

Equation 3.2-7

4d) M_d : added mass of fluid above the disc.

This is assumed to be half M_o : the added mass for a disc in an unbounded fluid.

$$M_o = \rho \cdot \left(\frac{2}{\pi} \cdot \frac{4}{3} \cdot \pi \cdot R^3 \right) = \rho \cdot \frac{8}{3} \cdot R^3$$

$$M_d \cdot V^2 = \frac{1}{2} \cdot M_o$$

Therefore

$$M_d = \frac{4}{3} \cdot \rho \cdot V^2 \cdot R^3$$

Equation 3.2-8

Hence, the added mass is the ratio of the added mass near seabed, M_{nsb} to added mass in unbounded fluid, M_o

$$= \frac{\left(\frac{\pi}{8} \cdot \rho \cdot \frac{R^4}{h} \right) + \left(\frac{\pi^2}{8} \cdot \rho \cdot R^3 \right) + \left(\frac{\pi}{3} \cdot \rho \cdot h \cdot R^2 \right) + \left(\frac{4}{3} \cdot \rho \cdot R^3 \right)}{\frac{8}{3} \cdot \rho \cdot R^3}$$

Equation 3.2-9

$$Ca = \frac{Mnsb}{Mo} = \left(\frac{3 \cdot \pi \cdot R}{64 \cdot h} \right) + \left(\frac{3 \cdot \pi^2}{64} \right) + \left(\frac{\pi \cdot h}{8 \cdot R} \right) + \frac{1}{2}$$

Equation 3.2-10

5) Data from Garrido-Mendoza et al. (2015) paper for Stationary Disc.

Results of the added mass coefficient were compared with data from Garrido-Mendoza's paper, where numerical simulations were performed using the finite volume open-source solver OpenFOAM. Mendoza looked at the hydrodynamic coefficients around heave plates by conducting simulations on a solid circular disc of diameter 200 mm and 2 mm thickness, oscillating vertically in water at various elevations (20 – 200 mm) above seabed for KC 0.03 – 1.5.

The Approximate values of the heave added mass coefficients, Caref at various h/R for the disc at KC = 0 are presented in Table 3.2-1.

Table 3.2-1 Added mass coefficient at various h/R, KC = 0

h/R	0.01	0.05	0.1	0.2	0.3	0.4	0.5	1	1.5
Caref	12	3.8	2.3	1.8	1.5	1.3	1.2	1.2	1.2
Ca	15.543	3.768	2.303	1.579	1.344	1.228	1.16	1	1

As h increases to R then the Ca tends to the unbound value of 1.0. A linear interpolation formula of

$$pr = 1 - \frac{h}{R}$$

is used to achieve this.

$$pr_{ih} = \text{if}(pr_{ih} < 0, 0, pr_{ih})$$

$$ih = 1 \dots 9$$

where, *ih* is the number of h/R ratios considered. Therefore, the added mass coefficient

$$Ca = \left(\frac{3 \cdot \pi \cdot R}{64 \cdot h} + \frac{3 \cdot \pi^2}{64} + \frac{1}{8} \cdot \frac{h}{R} + 0.5 \right) \cdot pr + 1 \cdot (1 - pr)$$

Equation 3.2-11

Note:

$$\text{if} \left(\frac{h}{R} > 1 \right) \quad Ca = 1$$

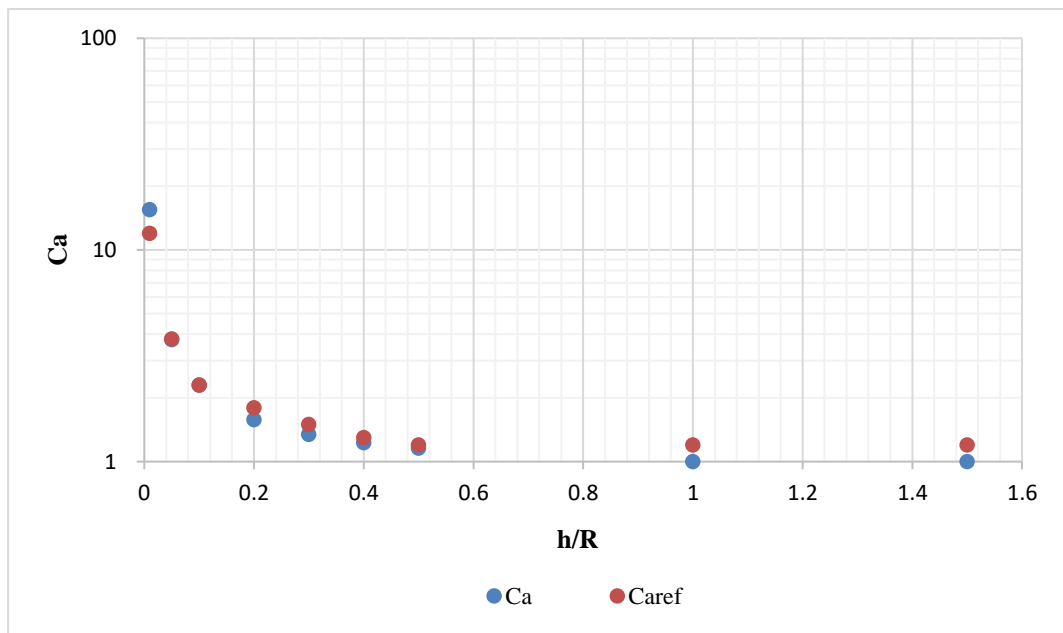


Figure 3.2-4 Comparison between Ca of approximate method (present work) and Caref of Garrido-Mendoza et al. (2015) for different h/R

This calculation is reasonable for small KC. $KC = \pi \cdot uz/R$, where the vertical motion amplitude, $uz \ll h$.

From Garrido-Mendoza et al. (2015), as KC increases the Ca increases until KC is approximately h/D, when Ca drops considerably. The increased KC leads to some kind of vortices generated from the two edges of the plate with one vortex pair formed below or above the plate per oscillation cycle as shown in Figure 3.2-5. Evident in Graham (1980), who talked about the pattern of vortex shedding from a single isolated edge which consists of one vortex pair shed per cycle, and Tao and Thiagarajan (2003)

showed the positive and negative vortices shed from the edges of a disc, as seen in Appendix A.1.

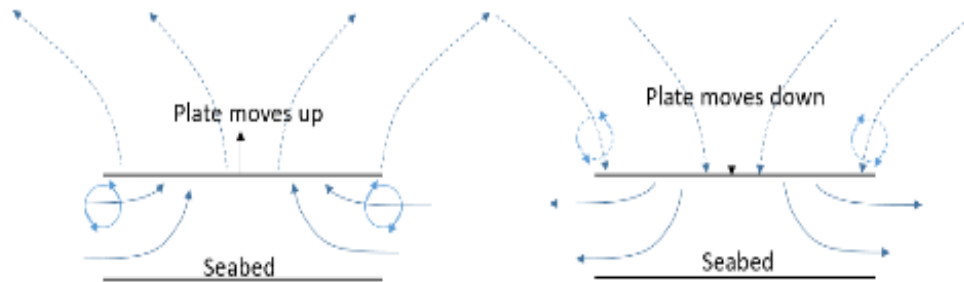


Figure 3.2-5 Vortices above plate, and between plate and seabed

Velocities and vortices are less strong above plate than in gap between plate and seabed. The vortices synchronized with plate acceleration increase added mass as KC increases – for half cycle, as the plate accelerate upwards, vortices will be generated simultaneously at the bottom of the plate, and the strength of these vortices generated at the plate bottom increase as KC increases. The drop in added mass could be as a result of the breakdown of vortex between plate and seabed when it is sufficiently large. It will breakdown into several vortices that are no longer synchronized with the acceleration. Same happens to vortices above plate but at much larger plate movement. The damping is also increased by vortices that are synchronized with the motion.

The sufficiently large vortex is formed at KC number just over the critical KC when the plate oscillates at this critical KC value. This causes the vortices from previous cycles to be trapped between the plate bottom and seabed, and it influences the shedding pattern (vortex breakdown), thereby altering the added mass on the disc. Figure A.2-1 of Appendix A by Garrido-Mendoza et al. (2015) explains this phenomenon.

6) Empirical fit to Garrido-Mendoza et al. (2015) Figure 4: Ca curves for KC from 0 to 2

Empirical formula for added mass, Ca curves: The added mass, Caa1 defines the curves from KC = 0 for different h/R, Ca includes the vertical cut offs.

$$Caa1_{ia,ih} = Ca_{ih} + \left[\left(\frac{\left(\frac{R}{h_{ih}} - 0.5 \right)}{3} + 0.5 \right) \cdot 7.3 \right] \cdot a_{D_{ia}}$$

Equation 3.2-12

$$Ca_{ia,ih} := \begin{cases} \text{“Limit increase in Ca to } 1.1h/R\text{”} \\ \text{if } KC_{ia} < 1.1 \cdot \frac{h_{ih}}{R} \\ \quad \left\| \begin{array}{l} Caa_{ia,ih} \leftarrow Caa1_{ia,ih} \\ \text{“For peak drop back towards Caa for } h/R = 1 \text{ with empirical slope of } -10R/h\text{”} \\ \text{“}R/h \text{ multiplier needed to steepen slope for very small } h/R \text{ values”} \end{array} \right. \\ \text{if } KC_{ia} \geq 1.1 \cdot \frac{h_{ih}}{R} \\ \quad \left\| \begin{array}{l} Caa_{ia,ih} \leftarrow Caa1_{ia,ih} - 10 \cdot \frac{R}{(h_{ih})} \cdot \left(KC_{ia} - 1.1 \cdot \frac{h_{ih}}{R} \right) \\ \text{“When curve meets Caa for } h/R = 1, \text{ it follows that curve”} \end{array} \right. \\ Caa_{ia,ih} \leftarrow \max(Caa_{ia,ih}, Caa1_{ia,9}) \\ Caa_{ia,ih} \end{cases}$$

Na , is the number of oscillation amplitudes to consider. In this case, $Na = 64$, while $ia = 1 \dots Na$

To define KC,

$$a_{D_{ia}} = 0.005 \cdot (ia - 1) \quad a_{D_1} = 0.001 \quad a_{ia} = a_{D_{ia}} \cdot D \quad KC = 2 \cdot \pi \cdot a_D$$

Where, ‘a’ is the amplitude of oscillation. Writing the equation for Caa as a function of a and h by incorporating the previous equations (except the downward slope) into one equation:

$$\text{Caf}(a, h) = \text{if} \left[\frac{2\pi a}{D} < 1.1 \cdot \frac{h}{R}, \left(\left(\frac{3\pi}{64} \cdot \frac{R}{h} + \frac{3\pi^2}{64} + \frac{1}{8} \cdot \frac{h}{R} + 0.5 \right) \cdot \text{if} \left(1 - \frac{h}{R} < 0, 0, 1 - \frac{h}{R} \right) + 1 \cdot \left(1 - \text{if} \left(1 - \frac{h}{R} < 0, 0, 1 - \frac{h}{R} \right) \right) + \left(\left(\frac{R-h}{3} + 0.5 \right) \cdot 7.3 \right) \cdot \frac{a}{D} \right), 1 + \left(\left(\frac{1}{1.5} - 0.5 \right) + 0.5 \right) \cdot 7.3 \right] \cdot \frac{a}{D}$$

Equation 3.2-13

Therefore, the added mass, A33 of the disc in terms of amplitude, ‘a’ and height above seabed, ‘h’ is

$$A33(a, h) = \text{Caf}(a, h) \cdot \frac{8}{3} \cdot \rho \cdot R^3$$

Equation 3.2-14

Equation 3.2-13 was developed by defining the added mass curves of Figure 4 of Garrido-Mendoza et al. (2015) for KC 0 to 2 through an empirical fit to develop Equation 3.2-12 and then limiting the increase in the added mass coefficient to $1.1h/R$. Equation 3.2-13 is expressed in terms of amplitude of oscillation of the disc and the ratio of height above seabed to radius of disc, h/R .

7) Plot of C_a against KC : approximation to Garrido-Mendoza et al. (2015)
Figure 4

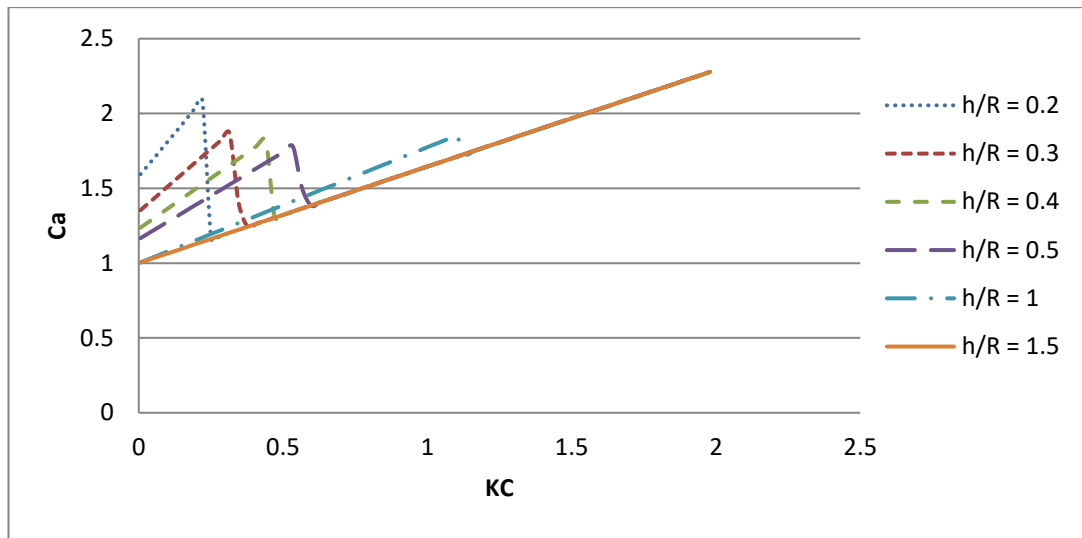


Figure 3.2-6 Comparison of added mass coefficient at different heights above seabed using approximate method

8) Plot of C_a against KC Approximation to Garrido-Mendoza et al. (2015)
Figure 4 with C_a for smaller h/R included

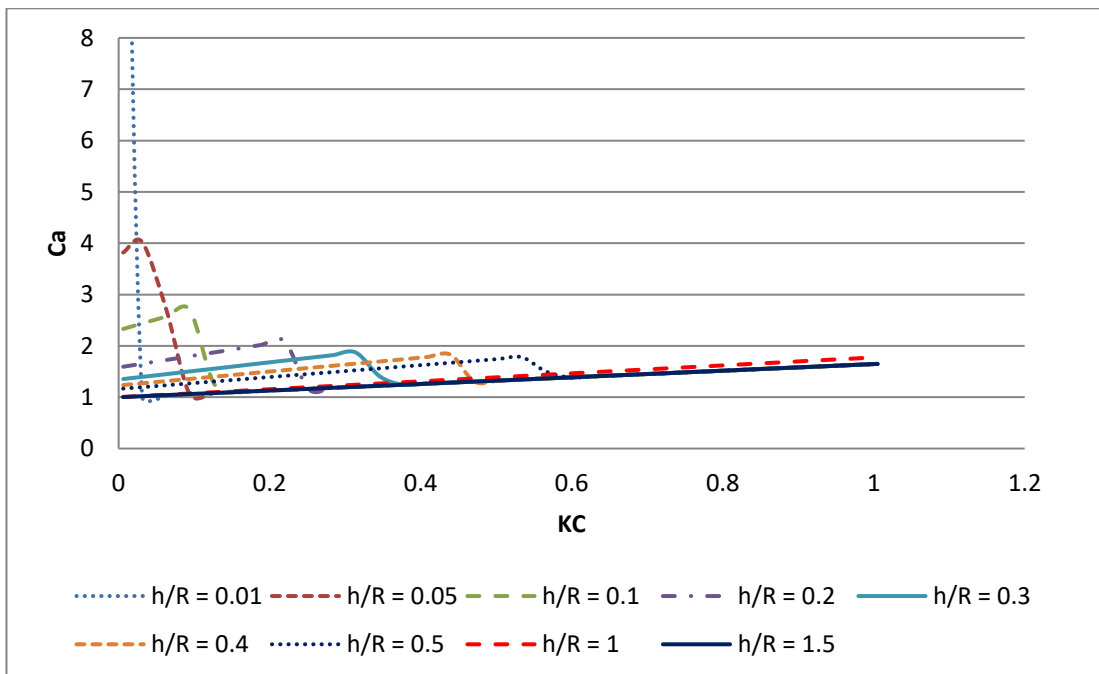


Figure 3.2-7 Comparison of added mass coefficient at different heights above seabed, with C_a for smaller h/R included, using approximate method

The approximate method (present work) and the simplified method of DNV (Det Norske Veritas, 2011) used in calculating the heave added mass in Section 3.3 of a suction-can moving vertically in infinite water depth at a high frequency of oscillation, would produce the same results, except for suction-cans with radiuses, R greater than gap to seabed, h ($h/R < 1$), because both methods are based on the derivation of added mass of a flat circular plate.

To derive the heave added mass of a suction-can, the added mass of the disc derived from the approximate method can be multiplied by 1.57 plus the mass of the water volume inside the suction-can, m_{int} only if the diameter and height of the suction-can are equal (Det Norske Veritas, 2011). Alternatively, the disc's added mass could be multiplied by the expression for height variation of Equation 3.3-1.

Results of the approximate method are in good agreement with CFD analysis and model test results by Zoontjes et al. (2009) and Roe et al. (2008). Zoontjes et al. (2009) presented CFD analysis results for 0.2 and 0.4 water depth ratios while Roe et al. (2008) conducted model tests for the three water depth ratios of 0.2, 0.4 and 1.2. The approximate formula developed considered the heave added mass for gap ratios equal or greater than 1.0, and gap ratios less than 1.0, where the previous represents the case of a suction-can well away from the boundaries, and the latter represents the case where the suction-can was close to the seabed. This is evident in Table 3.2-1, where the added mass coefficient obtained from model test results at a gap ratio of 1.2 is equal to or approximately the added mass coefficient of the suction-can far from the boundaries.

Table 3.2-2 Comparison between added mass coefficients of suction-cans at gap ratios 0.2, 0.4 and 1.2, $KC = 0.1$

Diameter / Height (m)	Added Mass Coefficient, C_a	
	Approximate method	CFD Analysis/Model Test (Zoontjes, et al., 2009)

	$\frac{h}{D} = 0.2$	$\frac{h}{D} = 0.4$	$\frac{h}{D} = 1.2$	$\frac{h}{D} = 0.2$	$\frac{h}{D} = 0.4$	$\frac{h}{D} = 1.2$
6 / 6	1.799	1.68	1.648	1.92 (Decay)	1.72 (Decay)	1.65
				1.70 (Diffraction)	1.61 (Diffraction)	
				1.75 (Model test)	1.65 (Model test)	

3.3 Basis of DNV's Method for Calculating Added Mass of Suction-Can

DNV can be used to estimate the heave added mass of a suction-can and it based its derivation of added mass of a suction-can far from boundaries on a flat plate's added mass with a shape equal to the horizontal projected area of the object in Kilogrammes (Det Norske Veritas, 2011). According to DNV, the added mass in heave for a body with vertical sides is

$$A_{33} \approx \left[1 + \sqrt{\frac{1 - \lambda^2}{2(1 + \lambda^2)}} \right] \cdot A_{330}$$

Equation 3.3-1

Expression for variation of height of suction can

where, A_{330} is the added mass for a flat plate (see Figure A.3-1 of Appendix A) with a shape equal to the horizontal projected area of the object, mathematically expressed in DNV-RP-H103 as

$$A_{330} = \rho \cdot \left(\frac{2}{\pi}\right) \cdot \left(\frac{4}{3}\right) \cdot \pi \cdot R^3$$

Equation 3.3-2

and λ is equal to

$$\frac{\sqrt{A_p}}{h + \sqrt{A_p}}$$

Equation 3.3-3

Where, A_p is the projected area of the flat plate and h is the height of the suction-can. This means if the height of the suction-can is zero, then, $A_{33} = A_{33o}$.

Comparison between the added mass coefficient of the approximate method and that of DNV for the suction-can far from boundaries showed the approximate method was in good agreement with the DNV method. Table 3.4-1 presents the heave added mass coefficient of both methods.

Table 3.3-1 Comparison between added mass coefficient of proposed approximate method and DNV of suction-can far from boundaries

Ca	
Approximate Method	DNV's Method
1.65	1.65

3.4 Added mass of Suction Can Very Close to the Seabed

It was stated earlier that the heave added mass increases when the suction-can approaches the seabed. This statement was further investigated and presented in Figure 3.5-1 which shows the added mass coefficient of a suction-can of height, 6 meters and diameter, 6 meters. As h/D , the ratio of height above seabed to diameter of suction-can increases, Ca reduces until it reaches the value for Ca of the suction-can well away from the surface and seabed.

As the vertical distance of the structure from the seabed reduces during the lowering of the structure, this distance approaches and eventually becomes smaller than the uncontrolled amplitude of motion of the oscillating structure until it gets to zero, when the structure rests on the seabed. Without some sort of motion control of the subsea

structure, in reality it will hit the seabed when this distance is less than the motion amplitude.

It should be noted that the rate of change of added mass with distance to seabed is also important because the hydrodynamic force related to added mass can be considered as:

$$F = d/dt(mv) = mdv/dt + vdm/dt \quad \text{Equation 3.4-1}$$

The mdv/dt term is the ordinary added mass loading term that applies when the added mass is constant. The vdm/dt term also applies when the added mass is changing and this might have an effect on landing on the seabed.

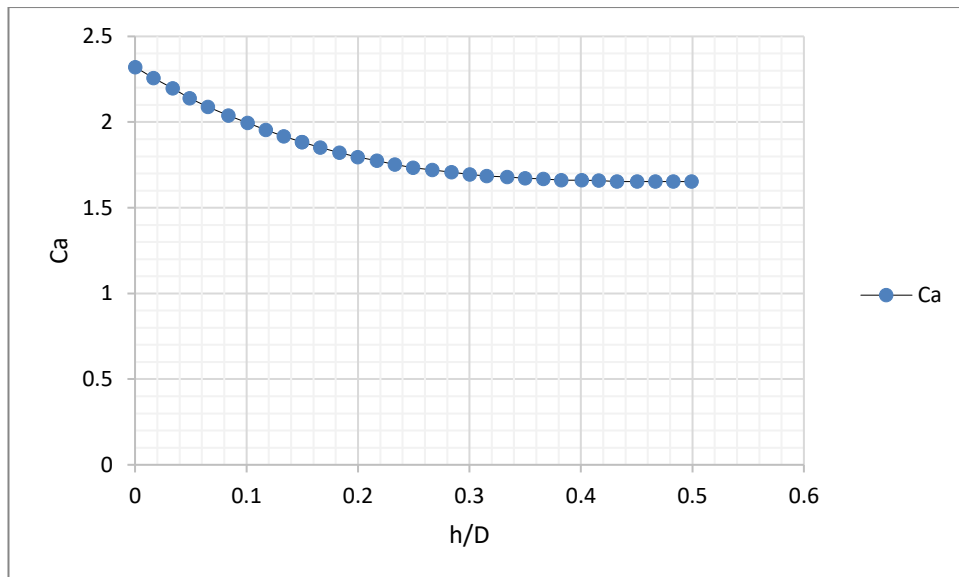


Figure 3.4-1 Added mass coefficient of suction-can at different h/D ratios

3.5 Estimation of Damping

This section presents the development of an analytical method to estimate the damping of a suction-can for various h/R ratios by taking into consideration the following components: **a)** friction on side of suction-can, **b)** frictional drag from flow between suction-can bottom and seabed, and **c)** pressure losses. The disc damping is added to account primarily for the form drag and frictional resistance. The orifice and plate

normal-to-flow drag is largely caused by flow separation while the flow parallel to a surface is largely frictional.

Data from I.E. Idel'chick, 1966, Handbook of hydraulic resistance was used to account for the directional change of the flow which will result in a drag force, and the case of an exhaust vent also from I.E. Idel'chick, 1966 was used to check the equivalent quadratic drag coefficient to represent the orifice effect on the disc, C_o and the pressure lost to rotate the flow from vertical motion of disc to horizontal flow through the orifice which will result in a drag force, C_{ro} .

a) Frictional drag on side of suction-can

For water temperature at 4 degree Celsius, kinematic viscosity, $\nu = 1.432 \cdot 10^{-6}$

Velocities for the calculation are: $iv = 1 \dots 6$ $V_{iv} = 2^{iv-4}$

Reynolds number, $Rn = V \cdot D / \nu$ Equation 3.5-1

ITTC Frictional coefficient (ITTC, 2002)

$$C_f = \frac{0.075}{(\log(Rn) - 2)^2}$$

Equation 3.5-2

Area of cylinder, $A_c = 2 \cdot \pi \cdot R \cdot L$

Area of end, $A_e = \pi \cdot R^2$

where, R is the radius of the cylinder and L is the height of the cylinder.

Therefore, the frictional quadratic drag coefficient for the cylinder side is

$$C_{fs_{iv}} = C_{f_{iv}} \cdot \frac{A_c}{A_e}$$

Equation 3.5-3

b) Frictional drag from flow between suction-can bottom and seabed

As r/h becomes small then velocity over bottom of structure and seabed will become higher and lead to a pumping frictional force from radial velocity in gap of:

$$U(r) = \frac{V}{r \cdot h} \cdot \int_0^r a \, da = \frac{V}{r \cdot h} \cdot \frac{r^2}{2} = \frac{V \cdot r}{2 \cdot h} \quad (\text{from above})$$

Equation 3.5-4

The frictional power loss is calculated and used to determine the contribution to the vertical C_d .

$$\begin{aligned} P &= \int_{r=0}^R \int_{\theta=0}^{2\pi} \left(\frac{1}{2} \cdot C_f \cdot \rho \cdot U^2 \cdot r \right) \cdot U \, d\theta \, dr = \frac{1}{2} \cdot C_f \cdot \rho \cdot \left(\frac{V}{2h} \right)^3 \int_{r=0}^R \int_{\theta=0}^{2\pi} r^4 \, d\theta \, dr \\ &= \frac{1}{2} \cdot C_f \cdot \rho \cdot \left(\frac{V}{2h} \right)^3 2\pi \int_{r=0}^R r^4 \, dr = \frac{1}{2} \cdot C_f \cdot \rho \cdot \left(\frac{V}{2h} \right)^3 2\pi \cdot \frac{r^5}{5} \\ &= \frac{1}{2} \cdot C_f \cdot \rho \cdot \left(\frac{V}{h} \right)^3 \cdot \left(\frac{\pi}{20} \right) \cdot R^5 \end{aligned}$$

Equation 3.5-5

Equate with power lost to drag force from moving cylinder with drag coefficient C_{fb}

$$\frac{1}{2} \cdot C_{fb} \cdot \rho \cdot \pi \cdot R^2 \cdot V^3 = \frac{1}{2} \cdot C_f \cdot \rho \cdot \left(\frac{V}{h} \right)^3 \cdot \left(\frac{\pi}{20} \right) \cdot R^5$$

Therefore,

$$C_{fb} = \frac{1}{20} \cdot C_f \cdot \left(\frac{R}{h} \right)^3$$

Equation 3.5-6

C_{fb} is the bottom friction drag coefficient, to be used with the vertical velocity and can cross sectional area, per horizontal surface (seabed and, if applicable, can bottom) Account could be taken here of seabed roughness which would increase C_f for the seabed and hence C_{fb} .

Cfb is now calculated for each vertical velocity and gap to seabed.

The velocity U for frictional calculation across bottom of the can in terms of the vertical velocity of the can for each gap (h) and velocity is

$$U_{f_{iv, ih}} = \frac{V_{iv} \cdot \frac{R}{2}}{2 \cdot h_{iv}}$$

Equation 3.5-7

The Reynolds number is given as

$$Rne_{iv, ih} = \frac{U_{f_{iv, ih}} \cdot \frac{D}{2}}{\nu}$$

Equation 3.5-8

The local drag coefficient,

$$Cfbl_{iv, ih} = \frac{0.075}{(\log(Rne_{iv, ih}) - 2)^2}$$

Equation 3.5-9

Effective contribution to drag coefficient on the can

$$Cfb_{iv, ih} = \frac{1}{20} \cdot Cfbl_{iv, ih} \cdot \left(\frac{R}{h_{ih}}\right)^3$$

Equation 3.5-10

c) Orifice drag coefficient

As the disc drops to the seabed water is pushed out from underneath it through the water cylinder of radius R and height h (from seabed to disc). The cylinder is treated as an orifice. The orifice drag coefficient is largely caused by flow separation.

Area of orifice

$$A_{o_{ih}} = \pi \cdot R \cdot h_{ih}$$

Equation 3.5-11

Flow velocity

$$U_{iv, ih} = \frac{V_{iv} \cdot \pi \cdot R^2}{2 \cdot \pi \cdot R \cdot h_{ih}} = \frac{V_{iv} \cdot R}{2 \cdot h_{ih}}$$

Orifice head loss, H (Webber, 1965)

$$U = 0.61 \cdot \sqrt{2 \cdot g \cdot H} \quad H = \frac{1}{0.61^2} \cdot \frac{1}{2g} \cdot U^2 = \frac{1}{2} \cdot \frac{8}{3} \cdot \frac{1}{g} \cdot U^2$$

Equation 3.5-12

Pressure drop

$$\Delta p = \rho g H = \frac{1}{2} \cdot \frac{8}{3} \cdot \rho \cdot U^2$$

Equation 3.5-13

Power loss (Force multiplied by velocity)

$$P = \frac{1}{2} \cdot \frac{8}{3} \cdot \rho \cdot U^2 \cdot A_o \cdot U$$

Equation 3.5-14

Power loss for equivalent cylinder drag coefficient, C_o

$$P = 1/2 \cdot \rho \cdot C_o \cdot A_e \cdot V^3 \quad \text{Equation 3.5-15}$$

$$C_o = \frac{8}{3} \cdot \frac{A_o}{A_e} \cdot \left(\frac{U}{V}\right)^3$$

Equation 3.5-16

But $A_o/A_e = V/U$, therefore, equivalent quadratic drag coefficient to represent the orifice effect on the disc is

$$C_o = \frac{8}{3} \cdot \left(\frac{A_o}{A_e}\right)^2 \quad \text{or} \quad C_{o_{ih}} = \frac{8}{3} \cdot \left(\frac{R}{2 \cdot h_{ih}}\right)^2$$

Equation 3.5-17

d) Pressure loss to rotate the flow from vertical motion of disc to horizontal flow through the orifice

$$p = 1/2 \cdot \xi \cdot \rho \cdot V^2 \quad \text{Equation 3.5-18}$$

The flow from under the suction-can is horizontal-radial but the suction-can is moving vertically. This requires the flow to change direction which will result in a drag force. To estimate the effect, data from Diagrams 3-4 and 11-6 of Sections III and XI respectively of I.E. Idel'chick, 1966, Handbook of hydraulic resistance, translated from Russian, USAES/NSF/IPST is used.

Diagram 3-4 of Section III shows the damping ratios for flow into a smooth converging bellmouth made by an arc of a circle, with flat end wall and with a screen while Diagram 11-6 of Section XI shows the damping ratio for discharge from a straight stretch with rounded edges against a baffle.

Note that the flow in the opposite direction (Diagram 11-6, Section XI) has very different drag coefficients from into a pipe (Diagram 3-4, Section III), however the vortices formed in the reverse flow case (flow into pipe) are in the pipe, which is not likely in the case of the lowered can (flow out of pipe), so the outflow case, where the vortices are primarily in the gap between the can and the seabed is assumed the best estimate for both directions of motion.

The data for the smallest bellmouth radius (0.2D - which is still substantial and likely to lead to lower drag) is taken (see Table 3.5-1).

Table 3.5-1 Damping ratio for smallest bellmouth radius (I.E. Idel'chick, 1966)

ξp	0.8	0.45	0.19	0.12	0.09	0.07	0.06	0.05	0.045
h_{DP}	0.125	0.15	0.2	0.25	0.3	0.4	0.5	0.6	0.8

A fifth order polynomial is now fitted to the bellmouth data. Note that the coefficients are forced to be positive because otherwise the polynomial fits the data better in the range of the data but gives a physically implausible fit outside the range of the data.

Powers to be used: $pf := 6$ $pe := 5$ $pd := 4$ $pc := 3$ $pb := 2$ $pa := 1$

And the function to be fitted

$$F(x, a, b, c, d, e, f) := |f|x^{pf} + |e|x^{pe} + |d|x^{pd} + |c|x^{pc} + |b|x^{pb} + |a|$$

Guessed starting values of a to f for 'genfit' fitting function are 0.01. Curve fit is to D/h rather than h/D .

$$D_h = \frac{1}{h_{DP}}$$

$$Rfit = \text{genfit} \left(D_h, \xi p, \begin{array}{|c|} \hline 0.01 \\ 0.01 \\ 0.01 \\ 0.01 \\ 0.01 \\ 0.01 \\ \hline \end{array}, F \right)$$

$$Rfit = \begin{array}{|c|} \hline -0.033 \\ 0.01 \\ 5.225 \cdot 10^{-4} \\ 7.139 \cdot 10^{-7} \\ 1.609 \cdot 10^{-4} \\ -3.742 \cdot 10^{-13} \\ \hline \end{array}$$

Results used to define a to f

$$af := |Rfit_1| \quad b := |Rfit_2| \quad c := |Rfit_3| \quad d := |Rfit_4| \quad e := |Rfit_5| \quad f := |Rfit_6|$$

$$\xi fit = f \cdot \left(\frac{D}{h}\right)^{pf} + e \cdot \left(\frac{D}{h}\right)^{pe} + d \cdot \left(\frac{D}{h}\right)^{pd} + c \cdot \left(\frac{D}{h}\right)^{pc} + b \cdot \left(\frac{D}{h}\right)^{pb} + af$$

Note: af rather than a is used as a is the amplitude of oscillation.

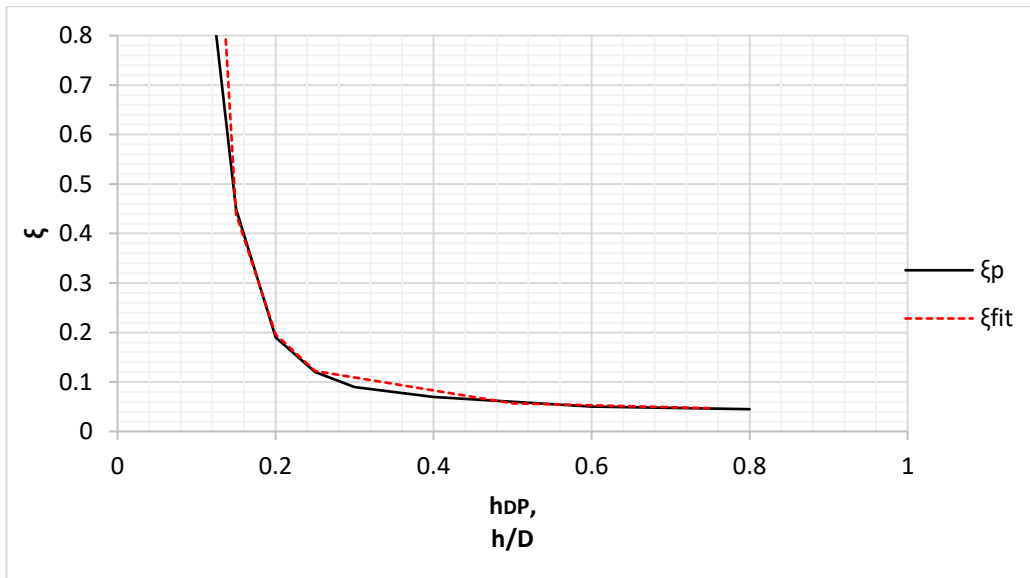


Figure 3.5-1 Graph showing original inflow data (black – ξ_p vs h_{DP}) and fitted equation (red – ξ_{fit} vs h/D)

Therefore

$$C_r = \xi_{fit}$$

Equation 3.5-19

Now fitting outflow data, since this seems more sensitive to the r/D this is (roughly) extrapolated by assuming the difference between $r/D = 0.5$ and $r/D = 0.2$ is the same as from $r/D = 0.2$ to $r/D = 0$.

Table 3.5-2 Damping ratio for outflow data (I.E. Idel'chick, 1966)

h_{do}	0.07	0.1	0.15	0.2	0.25	0.3	0.35	0.4	0.5	0.6	1.0
ξ_2	2.3	0.9	0.52	0.51	0.62	0.75	0.82	0.85	0.86	0.85	0.85
ξ_5	1.3	0.63	0.44	0.41	0.49	0.58	0.65	0.71	0.76	0.87	0.78
$\xi_0 = \xi_2 + (\xi_2 - \xi_5)$											
ξ_0	3.3	1.17	0.6	0.61	0.75	0.92	0.99	0.99	0.96	0.83	0.92

$$D_{ho} = \frac{1}{h_{do}}$$

$$F_0(x, a, b, c, d, e, f) := fx^{pf} + ex^{pe} + dx^{pd} + cx^{pc} + bx^{pb} + a$$

$$Rfito = \text{genfit} \left(D_{ho}, \xi_0, \begin{pmatrix} 1.00 \\ -0.11 \\ 0.01 \\ 0.01 \\ 0.01 \\ 0.01 \end{pmatrix}, F_0 \right)$$

$$Rfito = \begin{pmatrix} 0.523 \\ 0.51 \\ -0.184 \\ 0.022 \\ -8.982 \cdot 10^{-4} \\ 1.176 \cdot 10^{-5} \end{pmatrix}$$

$$af := Rfito_1 \quad b := Rfito_2 \quad c := Rfito_3 \quad d := Rfito_4 \quad e := Rfito_5 \quad f := Rfito_6$$

Note that for a slightly better fit, by eye, coefficient d was increased by 0.5%.

$$\xi_{fito} = f \cdot \left(\frac{D}{h}\right)^{pf} + e \cdot \left(\frac{D}{h}\right)^{pe} + d \cdot \left(\frac{D}{h}\right)^{pd} + c \cdot \left(\frac{D}{h}\right)^{pc} + b \cdot \left(\frac{D}{h}\right)^{pb} + af$$

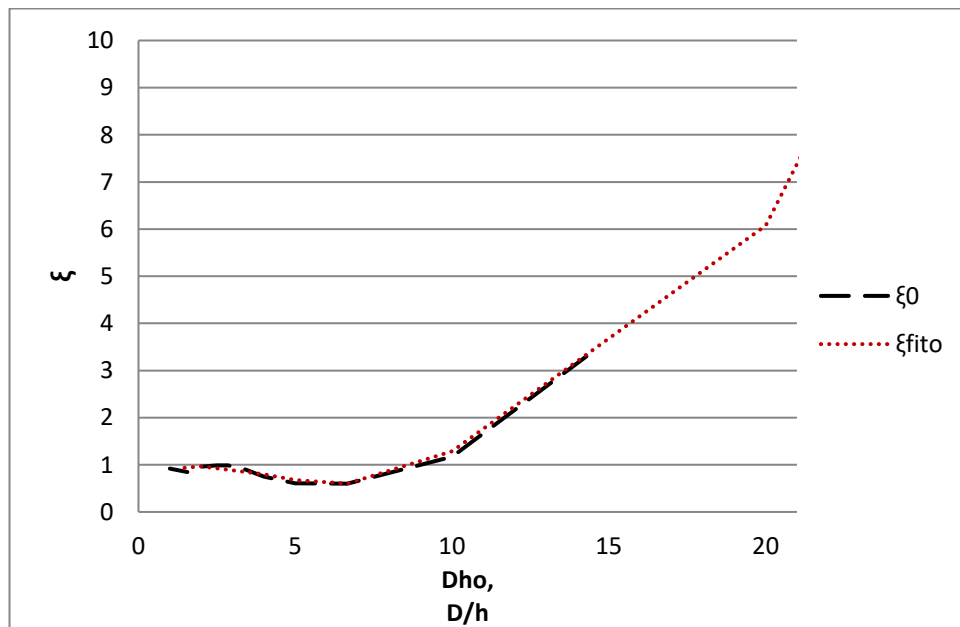


Figure 3.5-2 Graph showing comparison between damping ratios of Garrido-Mendoza et al. (2015) (black – ξ_0 vs D_{ho}) and approximate method (red – ξ_{fito} vs D/h)

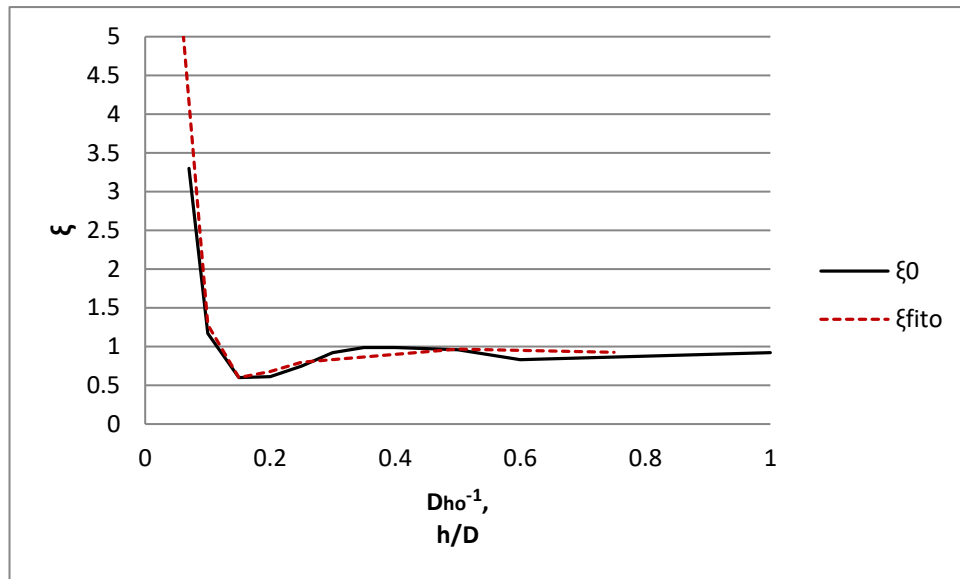


Figure 3.5-3 Graph showing comparison between damping ratios of Garrido-Mendoza et al. (2015) (black – ξ_0 vs Dho^{-1}) and approximate method (red – ξ_{fito} vs h/D)

Therefore

$$C_{ro} = \xi_{fito}$$

Equation 3.5-20

To cross-check the C_o and C_{ro} results, the case for an exhaust vent (Diagram 11-14, Section XI) from I.E. Idel'chick, 1966, was also considered. Diagram 11-14 showed the resistance coefficient of straight rectangular exhaust vents for various openings. Note that the \bar{f} column (flow area through outlets / duct area) appears to be incorrect and the first 4 values should read 0.36, 0.72, 1.08 and 1.44.

The four opening, 4th case has a resistance coefficient of 2.2. The equivalent h/D , for the same ratio of outlet area to duct area = 0.25 and assuming the duct combines the orifice and flow turning effects ($C_o + C_{ro}$) the coefficient would be $0.61 + 0.8 = 1.41$ which is significantly lower than the 2.2 for the four opening exhaust vent. However, the 4-opening vent does have 4 substantial support columns, which will introduce additional drag so the results may be compatible.

Effect of oscillating motion

So far only steady flow cases have been considered. However, Graham (1980) reported (see below) experiments and calculated the effect of oscillatory flow on a sharp-edged plate and showed that the vortices generated substantially changed the drag coefficient and that for a flat plate that C_D was theoretically proportional to $KC^{-1/3}$ providing the Reynolds number was sufficiently high that inviscid analysis was satisfactory.

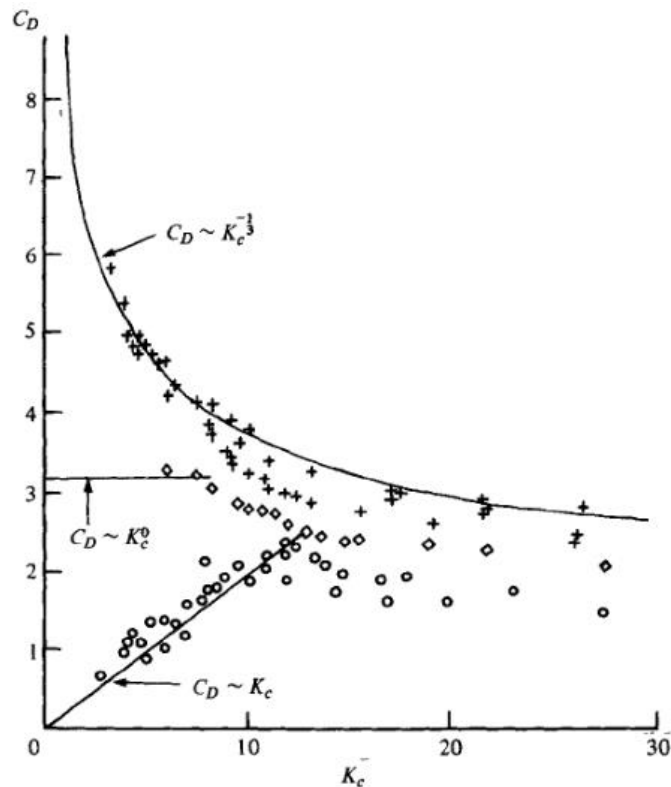


Figure 3.5-4 Drag coefficient at low Keulegan-Carpenter numbers. +, Flat plate (Singh, 1979); ◇, square cylinder (Singh, 1979); O, circular cylinder (Sarpkaya, 1975; Singh, 1979) (Courtesy: Graham, 1980)

The general form of $C_D = \text{const} \times KC^{-1/3}$ is assumed valid, as a further multiplier on the drag coefficient for the can. The constant is the drag coefficient at $KC = 1$. This, to be consistent with the C_b results presented by Garrido-Mendoza et al. (2015), is set at

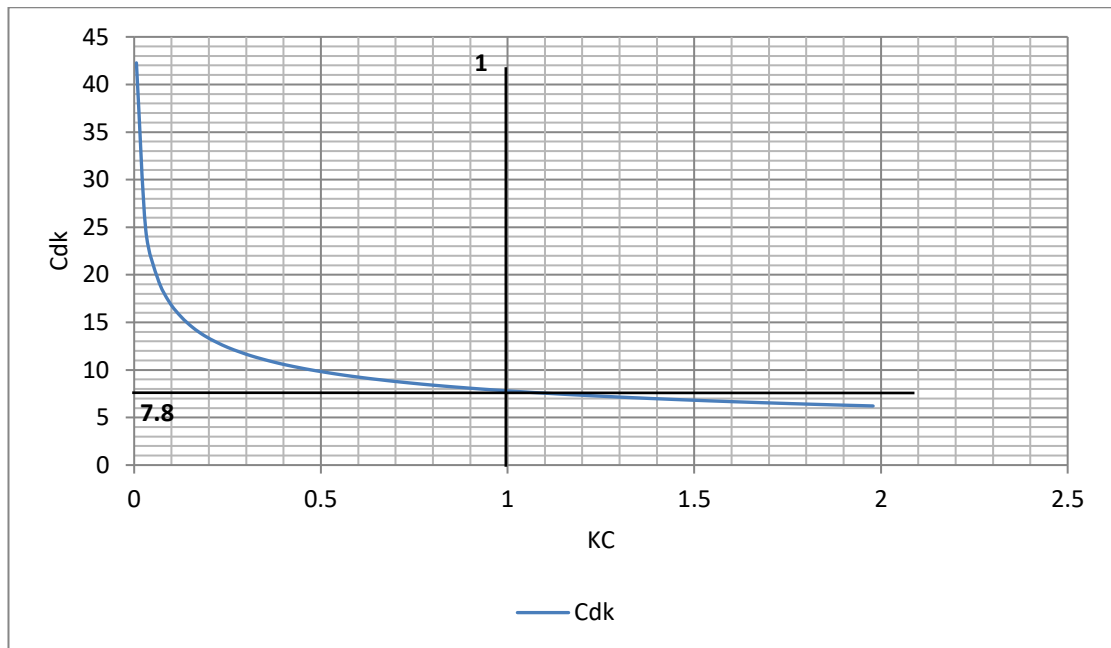
$$DCd.kc1 = 7.8$$

The steady flow drag coefficient is: $SCd = 1.14$

Note that their own paper (figs C5 and C6) suggests the C_d for $KC = 1$ should be 7. It is not clear what causes the inconsistency.

$$C_{dk_{ia}} = DC_d \cdot kc_1 \cdot KC_{ia}^{-\frac{1}{3}}$$

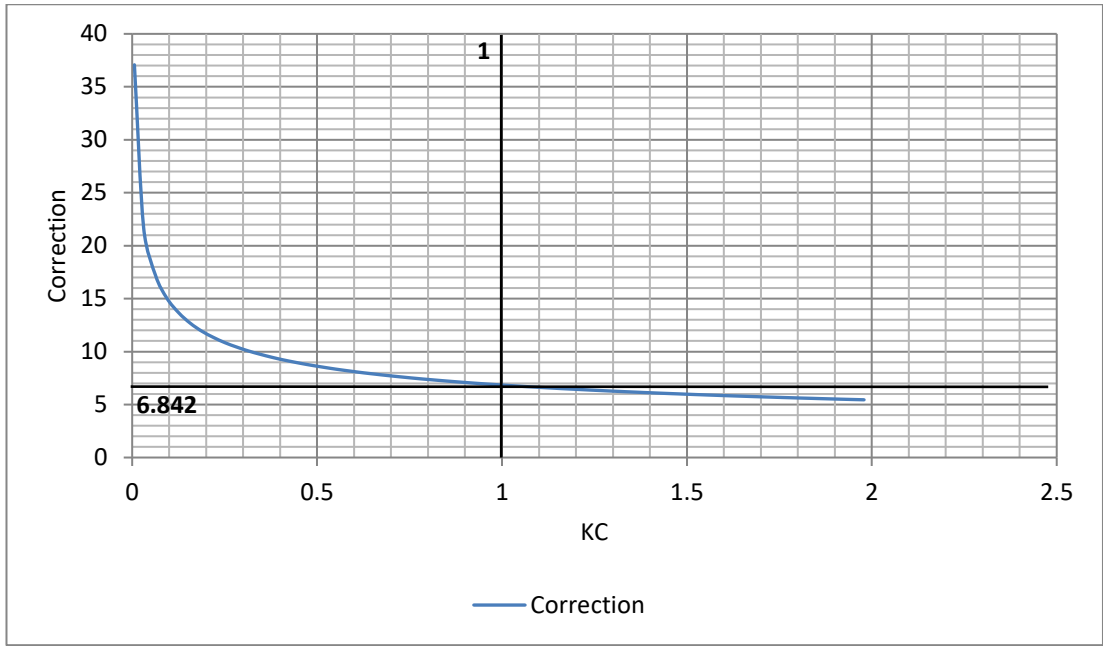
Equation 3.5-21



A KC correction to the steady flow drag coefficient SC_d can now be estimated.

$$\text{Correction}_{ia} = \frac{DC_d \cdot kc_1 \cdot KC_{ia}^{-\frac{1}{3}}}{SC_d}$$

Equation 3.5-22



In this case, $iv1 = 1$, and $p = 1$.

By interpolation and application of limiting KC value,

$$pra_{ia,ih} = if \left(KC_{ia} < 1.3 \cdot \frac{h_{ih}}{R}, pr_{ih}, 0 \right)$$

Equation 3.5-23

$iv1 = 5$ and $Ns = 1$.

Quadratic Ct

(Half steady flow circular plate Cd interpolated with h/D to Steady flow circular plate Cd) x KC correction + Orifice Cd + Corner Cd + Friction Cd

$$\begin{aligned} Ctfp1_{ia,ih} = & \left(\frac{SCd}{2} \cdot pra_{ia,ih}^p + SCd \cdot (1 - pra_{ia,ih}^p) \right)^{-1} \cdot \left(\frac{DCd \cdot kc1 \cdot KC_{ia}^{-\frac{1}{3}}}{SCd} \right) \\ & + \left((Co_{ih} + Cr_{ih}) \cdot pra_{ia,ih}^p \right) + (Cfs_{iv1} + Cfb_{iv1,ih} \cdot Ns) \cdot 1 \end{aligned}$$

Equation 3.5-24

$$C_{tfp1o_{ia,ih}} = \left(\frac{SCd}{2} \cdot pra_{ia,ih}^p + SCd \cdot (1 - pra_{ia,ih}^p) \right)^{-1} \cdot \left(\frac{DCd \cdot kc1 \cdot KC_{ia}^{-\frac{1}{3}}}{SCd} \right) + \left((Co_{ih} + Cro_{ih}) \cdot pra_{ia,ih}^p \right) + (Cfs_{iv1} + Cfb_{iv1,ih} \cdot Ns) \cdot 1$$

Equation 3.5-25

Conversion from quadratic drag coefficient to linear damping coefficient:

Quadratic damping power dissipation

$$Pq = \frac{1}{2} \cdot Cd \cdot \rho \cdot A \cdot |v| \cdot v \cdot v \quad \text{Equation 3.5-26}$$

Linear damping power dissipation

$$Pl = B \cdot v \cdot v \quad \text{Equation 3.5-27}$$

where, $v = V \cdot \sin(\theta)$

For the $Pq = Pl$ over a complete cycle

$$B = \int_0^{2\pi} \frac{1}{2} \cdot Cd \cdot \rho \cdot A \cdot |V| \cdot V \cdot V d\theta \bigg/ \int_0^{2\pi} V \cdot V d\theta$$

$$= \frac{1}{2} \cdot Cd \cdot \rho \cdot A \cdot V \cdot \left(\int_0^{2\pi} |\sin(\theta)| \cdot \sin(\theta)^2 d\theta \bigg/ \int_0^{2\pi} \sin(\theta)^2 d\theta \right)$$

Equation 3.5-28

Since

$$\int_0^{2\pi} |\sin(\theta)| \cdot \sin(\theta)^2 d\theta \bigg/ \int_0^{2\pi} \sin(\theta)^2 d\theta = 0.848826$$

and

$$\frac{8}{3 \cdot \pi} = 0.848826$$

Then

$$B = \frac{8}{3 \cdot \pi} \cdot \frac{1}{2} \cdot C_d \cdot \rho \cdot A \cdot V$$

Equation 3.5-29

And C_b as defined by Garrido-Mendoza et al. (2015):

$$C_b = B / M_o \cdot \omega$$

Equation 3.5-30

where

$$M_o = 1/3 \cdot \rho \cdot D^3$$

Equation 3.5-31

and

$$\omega = V/a$$

Equation 3.5-32

$$C_p = \frac{\frac{8}{3 \cdot \pi} \cdot \frac{1}{2} \cdot C_d \cdot \rho \cdot \left(\frac{\pi \cdot D^2}{4}\right) \cdot V}{\frac{1}{3} \cdot \rho \cdot D^3 \cdot \frac{V}{a}} = C_d \cdot \frac{a}{D}$$

Equation 3.5-33

Results using coefficients for flow into a pipe:

$$C_{p_{ia,ih}} = C_{tfp1_{ia,ih}} \cdot \frac{a_{ia}}{D}$$

Equation 3.5-34

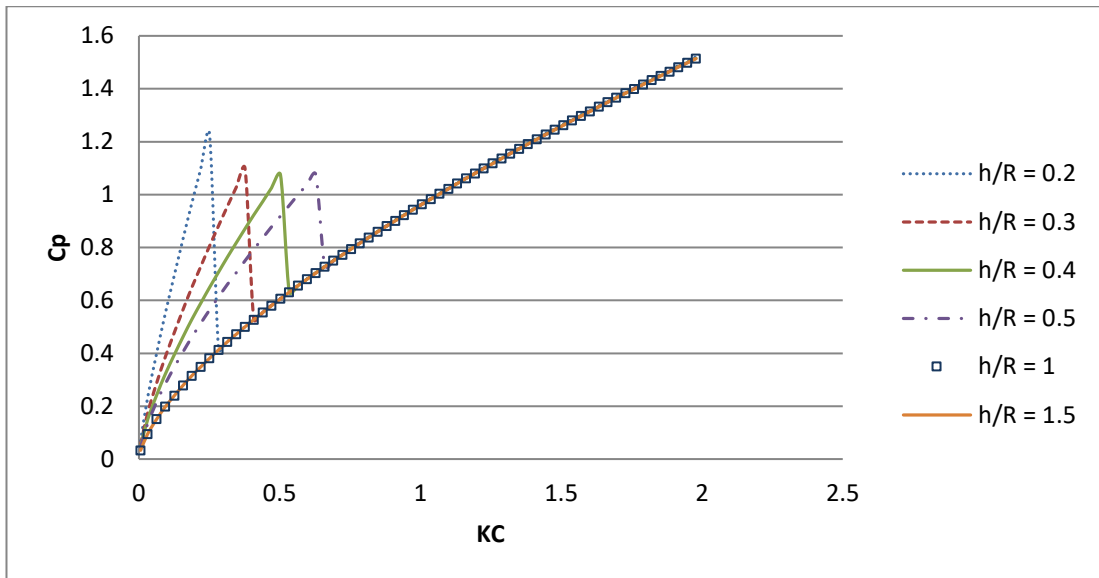


Figure 3.5-5 Cp for different h/R for flow into a pipe

This calculation leads to coefficients that are not too far from those shown by Mendoza et al. (2015) but the trend with increasing h/R is slightly downwards instead of slightly upwards from Mendoza et al. (2015).

Results using coefficients for flow from a pipe:

$$C_{p_{ia,ih}} = C_{t_{fp1}} o_{ia,ih} \cdot \frac{a_{ia}}{D}$$

Equation 3.5-35

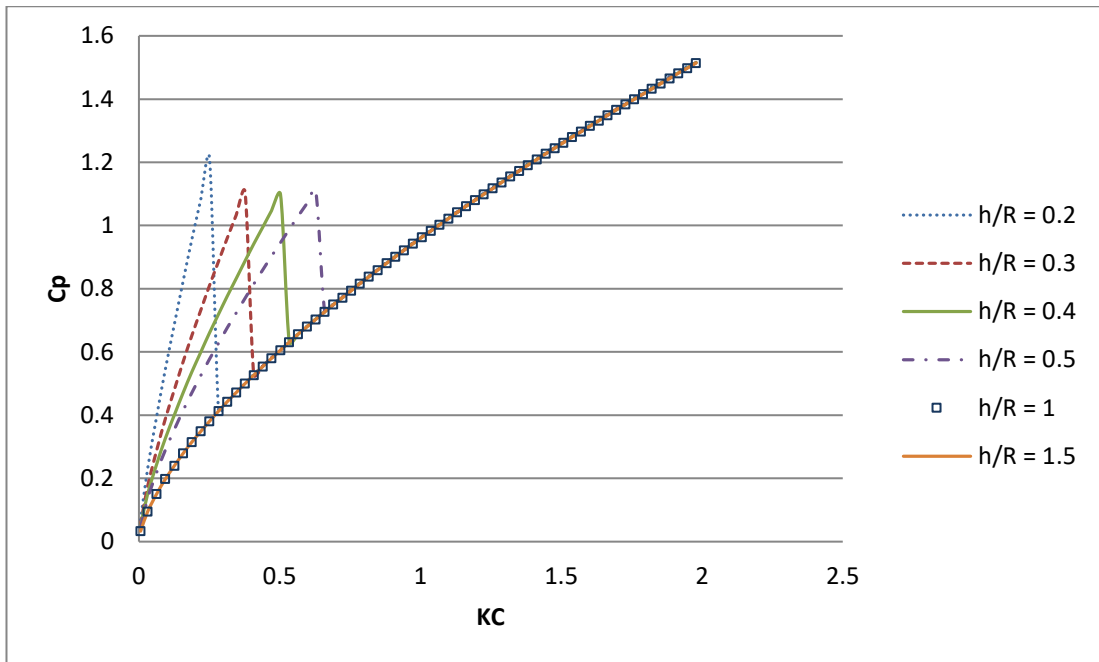


Figure 3.5-6 Cp for different h/R for flow from a pipe

These results are not too different to those obtained using the inflow coefficients, the trend is still down, when it should be up, with increasing h/R.

Alternatively, the quadratic Ct can be expressed as

(Half steady flow circular plate Cd + Orifice Cd + Corner Cd interpolated with h/D to Steady flow circular plate Cd) x KC correction + Friction Cd

$$C_{t_{ia,ih}} = \left(\left(\left(\frac{SCd}{2} \right) + (C_{o_{ih}} + C_{r_{ih}}) \right) \cdot pra_{ia,ih}^p + SCd \cdot (1 - pra_{ia,ih}^p) \right) \cdot \left(\frac{DCd \cdot kc1 \cdot KC_{ia}^{-\frac{1}{3}}}{SCd} \right) + (C_{fs_{iv1}} + C_{fb_{iv1,ih}} \cdot Ns) \cdot 1$$

Equation 3.5-36

$$C_{p_{ia,ih}} = C_{t_{ia,ih}} \cdot a_{D_{ia}}$$

Equation 3.5-37

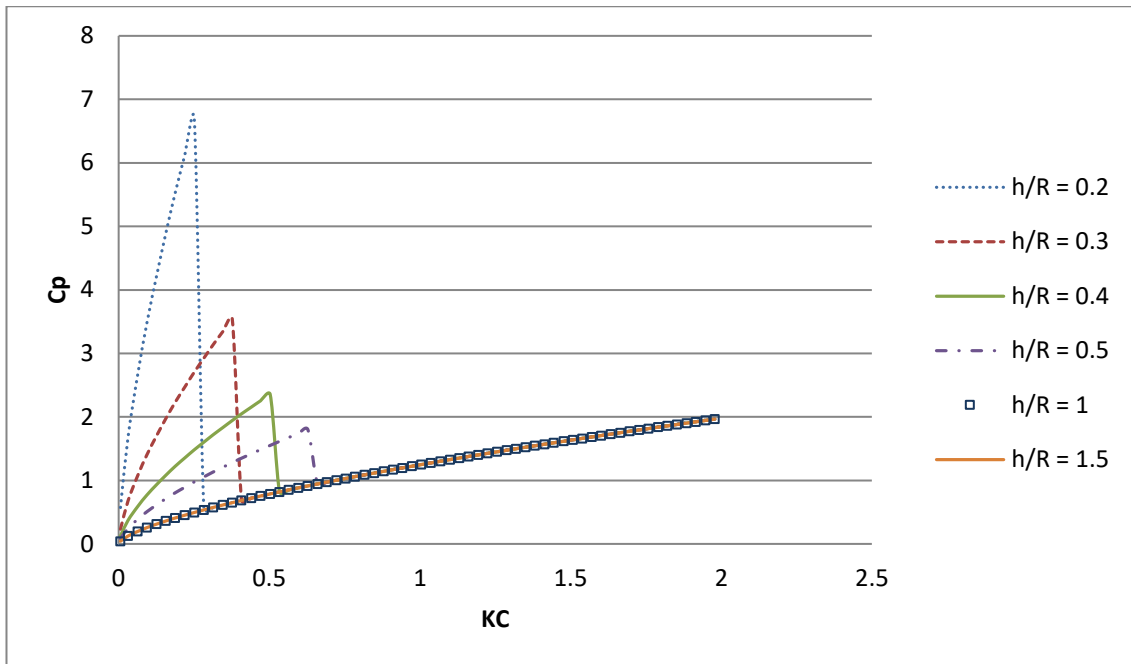


Figure 3.5-7 Cp for different h/R for flow from a pipe

Multiplying the internal flow losses by the dynamic correction factor makes the agreement worse.

Or,

(Half steady flow circular plate Cd + empirical allowance for internal flow interpolated with h/D to Steady flow circular plate Cd) x KC correction + Friction Cd

$$\begin{aligned}
 C_{t_{ia,ih}} = & \left(\left(\left(\frac{SCd}{2} \right) + \left(0.9 \cdot \left(\frac{Ae}{Ao_{ih}} \right)^{0.7} + 1 \right) \right) \cdot pra_{ia,ih}^p + SCd \right. \\
 & \left. \cdot (1 - pra_{ia,ih}^p) \right) \cdot \left(\frac{DCd \cdot kc1 \cdot KC_{ia}^{-\frac{1}{3}}}{SCd} \right) \\
 & + (Cf_{s_{iv1}} + Cf_{b_{iv1,ih}} \cdot Ns) \cdot 1
 \end{aligned}$$

Equation 3.5-38

$$Cp_{ia,ih} = C_{t_{ia,ih}} \cdot \frac{a_{ia}}{D}$$

Equation 3.5-39

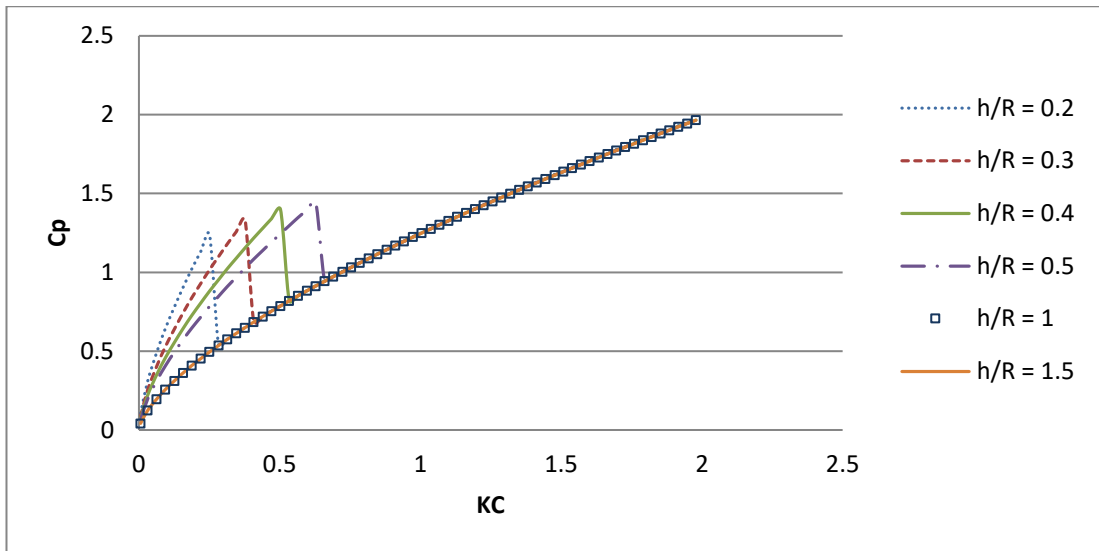


Figure 3.5-8 Cp for different h/R (internal flow losses included)

The empirical allowance for the internal flow is determined to give the correct trend

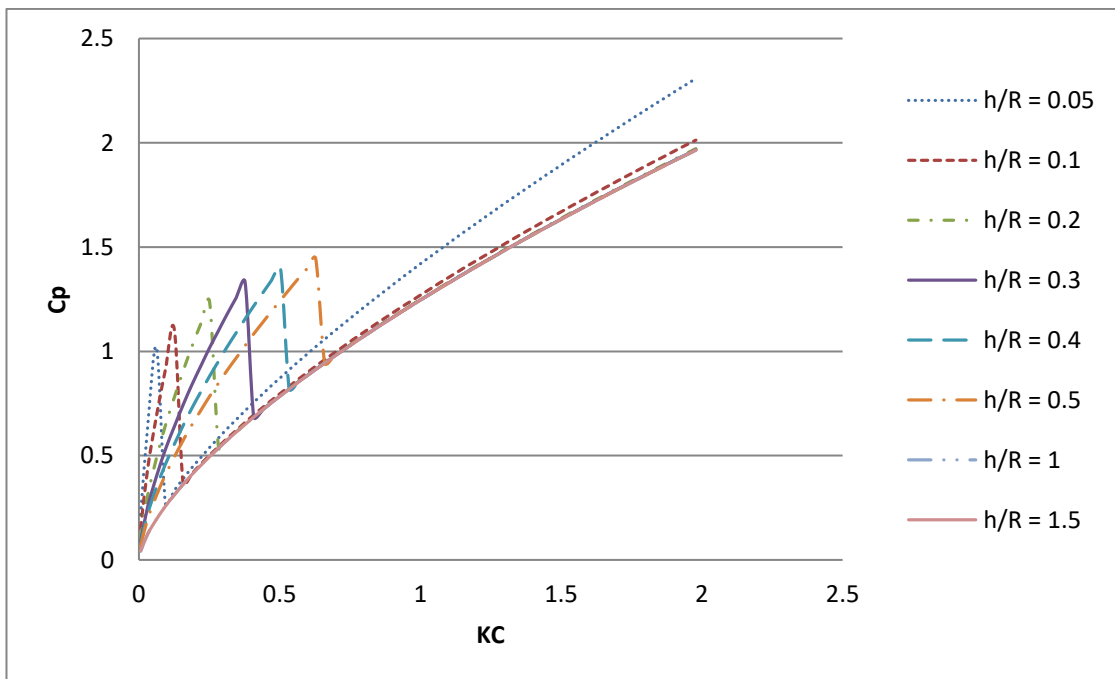


Figure 3.5-9 Cp for different h/R (internal flow losses included)

To make any time history analysis more stable, the curves are now slightly adjusted to put a specified gradient on the curve as it drops back to the curve for $h/R = 1.5$.

$$C_{p_{ia,ih}} := \begin{cases} \text{“Limit increase in } C_p \text{ to } 1.3h/R\text{”} \\ \text{if } KC_{ia} < 1.3 \cdot \frac{h_{ih}}{R} \\ C_{pp_{ia,ih}} \leftarrow C_{pp1_{ia,ih}} \\ \text{“For peak drop back towards } C_{pp} \text{ for } h/R = 1 \text{ with empirical slope of } -10R/h\text{”} \\ \text{“}R/h \text{ multiplier needed to steepen slope for very small } h/R \text{ values”} \\ \text{if } KC_{ia} \geq 1.3 \cdot \frac{h_{ih}}{R} \\ C_{pp_{ia,ih}} \leftarrow C_{pp1_{ia,ih}} - 10 \cdot \frac{R}{(h_{ih})} \cdot \left(KC_{ia} - 1.3 \cdot \frac{h_{ih}}{R} \right) \\ \text{“When curve meets } C_{pp} \text{ for } h/R = 1, \text{ it follows that curve”} \\ C_{pp_{ia,ih}} \leftarrow \max(C_{pp_{ia,ih}}, C_{pp1_{ia,9}}) \\ C_{pp_{ia,ih}} \end{cases}$$

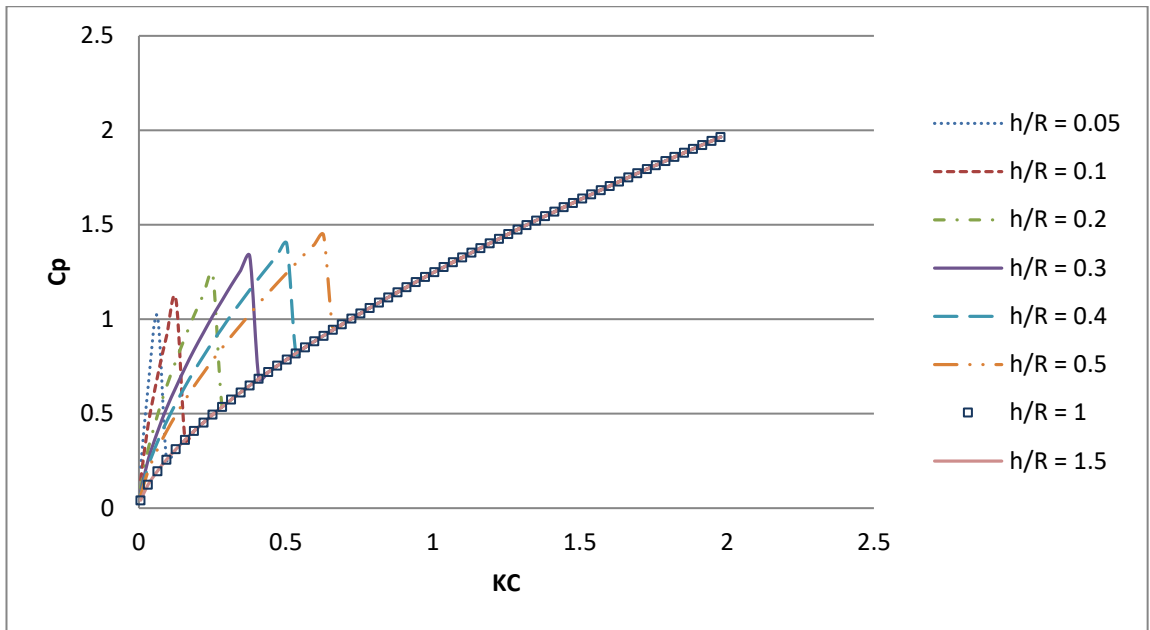


Figure 3.5-10 Cp for different h/R

$$Ct_{ia,ih} = \frac{Cp_{ia,ih}}{a_{Dia}}$$

Equation 3.5-40

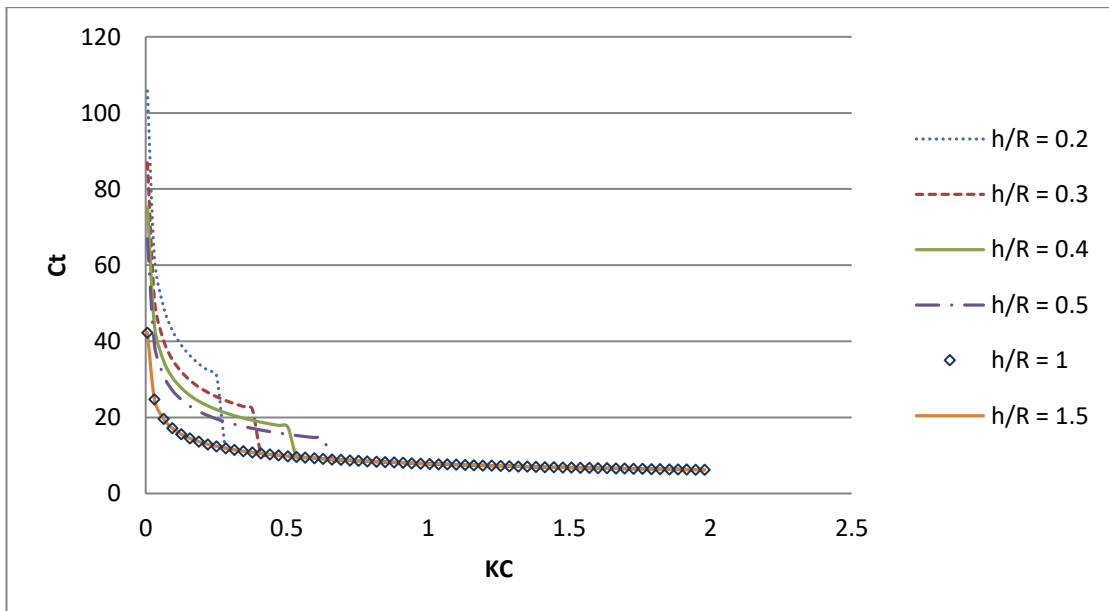


Figure 3.5-11 Ct for different h/R

The influence of friction can be seen.

$$Scale \equiv \frac{1}{1}$$

$$Cdf_{iv,ih} = \left(C_{fiv} \cdot \frac{Ac}{Ae} + C_{fb_{iv,ih}} \cdot Ns \right) \cdot 1$$

Equation 3.5-41

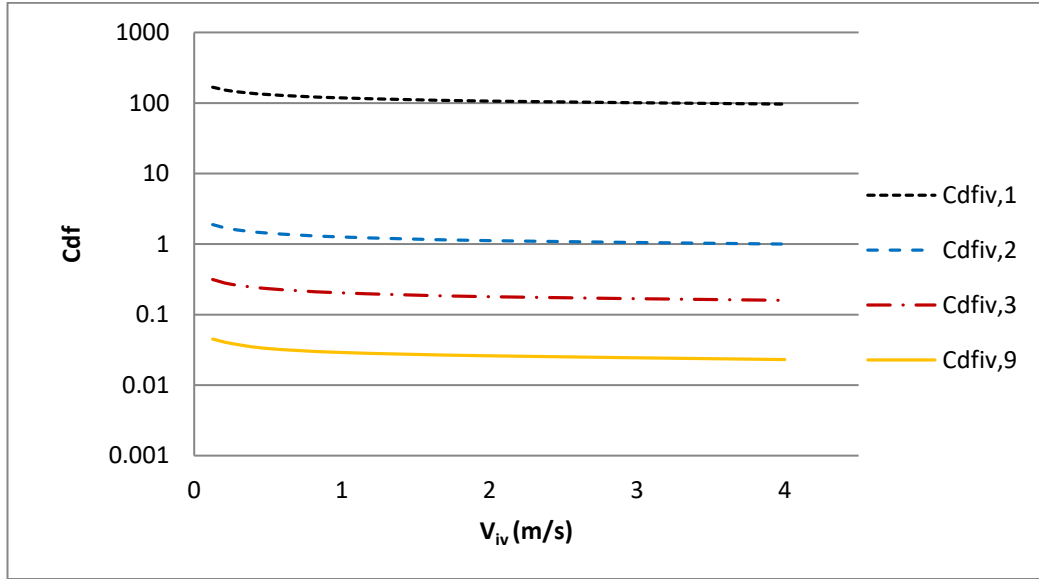


Figure 3.5-12 Influence of friction on damping

For 20 sec waves and an oscillation amplitude of 2m, It appears that frictional effects only become important at h/D about 0.025 (for $D = 5m$, 125mm from the seabed), so friction will not affect the oscillation before touch down or impact with the seabed.

Since C_t is

$$C_{t_{ia,ih}} = \left(\left(\left(\frac{SCd}{2} \right) + \left(0.9 \cdot \left(\frac{Ae}{Ao_{ih}} \right)^{0.7} + 1 \right) \right) \cdot pra_{ia,ih}^p + SCd \right. \\ \left. \cdot (1 - pra_{ia,ih}^p) \right) \cdot \left(\frac{DCd \cdot kc1 \cdot KC_{ia}^{-\frac{1}{3}}}{SCd} \right) \\ + (C_{fs_{iv1}} + C_{fb_{iv1,ih}} \cdot Ns) \cdot 1$$

Substituting into the above expression the previous equations so that Ct becomes a function of variables a and h only.

$$\begin{aligned}
 Ct1(a, h) = & \left(\left(\left(\frac{SCd}{2} \right) + \left(0.9 \cdot \left(\frac{D}{4 \cdot h} \right)^{0.7} + 1 \right) \right) \right. \\
 & \cdot \text{if} \left(\frac{2 \cdot \pi \cdot a}{D} < 1.3 \cdot \frac{h}{R}, \text{if} \left(1 - \frac{h}{R} < 0, 0, 1 - \frac{h}{R} \right), 0 \right) + SCd \\
 & \cdot \left(1 - \text{if} \left(\frac{2 \cdot \pi \cdot a}{D} < 1.3 \cdot \frac{h}{R}, \text{if} \left(1 - \frac{h}{R} < 0, 0, 1 - \frac{h}{R} \right), 0 \right) \right) \left. \right) \\
 & \cdot \left(\frac{DCd \cdot kc1 \cdot \left(\frac{2 \cdot \pi \cdot a}{D} \right)^{-\frac{1}{3}}}{SCd} \right) \\
 & + \left(\frac{0.075}{\left(\log \left(\frac{(\omega \cdot a \cdot D)}{v} \right) - 2 \right)^2} \cdot \frac{\pi \cdot D \cdot L}{\pi \cdot \frac{D^2}{4}} + \frac{1}{20} \right. \\
 & \left. \cdot \frac{0.075}{\left(\log \left(\frac{(\omega \cdot a \cdot \frac{D}{4}) \cdot \frac{D}{2}}{v} \right) - 2 \right)^2} \cdot \left(\frac{R}{h} \right)^3 \cdot Ns \right) \cdot 1
 \end{aligned}$$

Equation 3.5-42

Comparison of C_t and C_{t1} :

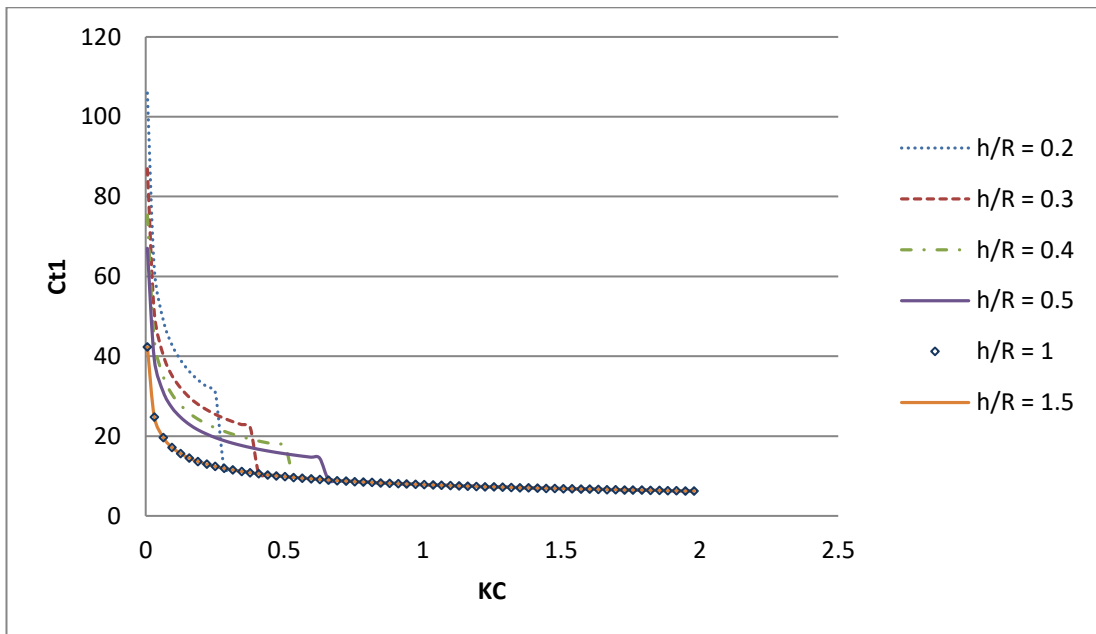
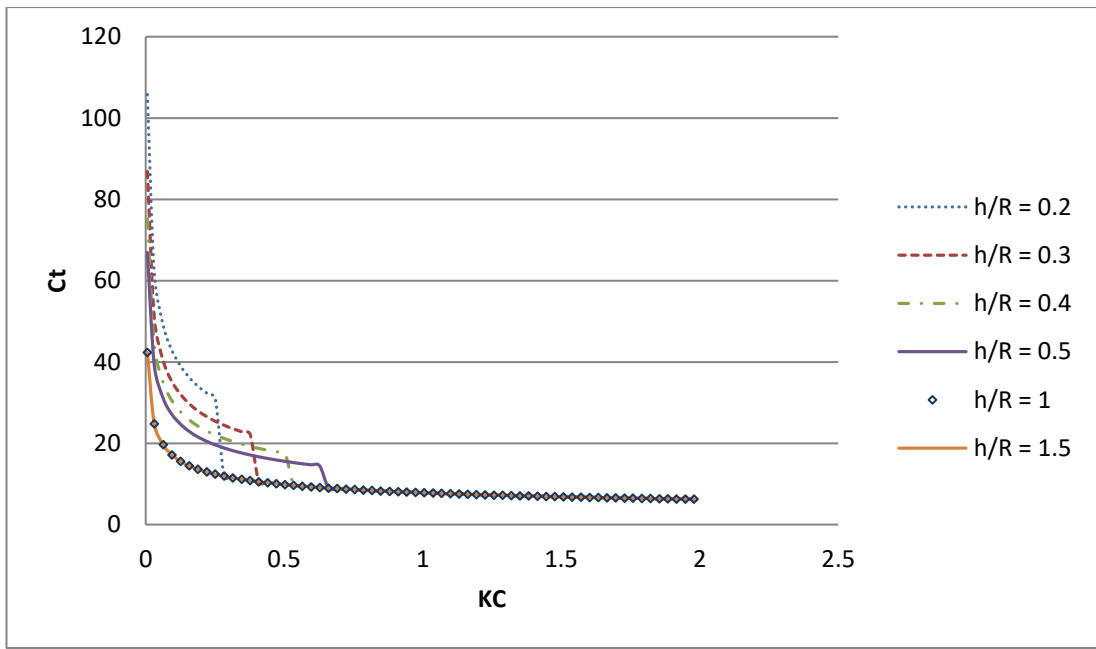


Figure 3.5-13 Comparison between C_t (above) and C_{t1} (below)

3.6 Summary of Proposed Approximate Method

The hydrodynamic coefficients of a disc or cylinder well away from the surface and seabed and in close proximity to the seabed was presented in this chapter. The location of the structure in water is important, because it determines the approach to be adopted. Straight forward analytical formulas can be applied to structures located at depths far away from or unaffected by the free surface or seabed. This formula becomes more complicated when these structures are located very close to the seabed.

The vertical added mass of a structure located mid water can be derived on the basis of the surrounding fluid, not rigidly connected to the body, but formed as the structure oscillates in the fluid. The surrounding fluid formed in most cases is in the form of common shapes with known added mass derivations.

To calculate the vertical added mass of a subsea structure, in this case a cylinder, firstly, determine if seabed influence exist. For complex structures, this can be done for each component member, by checking if each member's radius, projected on the horizontal plane is less than, equal to, or greater than the gap to seabed, h . Equation 3.2-14 can then be applied. This equation estimates the heave added mass for various suction-can sizes and seabed gaps. For complicated subsea structures with component members other than suction-cans, their hydrodynamic added mass can be obtained from known formulas.

The damping can be calculated if the drag coefficient of the structure is known. There exists literature with known drag coefficients of simple shapes. The damping is estimated from the quadratic drag of Equation 3.5-42. The quadratic drag should be derived first by identifying the various components of damping. In this case the components of damping considered were: friction on side of suction-can, frictional drag from flow between suction-can bottom and seabed, and pressure losses, which included the orifice drag coefficient and pressure loss to rotate the flow from vertical motion of disc to horizontal flow through the orifice.

4 CFD Simulation for Suction-Can

4.1 Introduction

Suction-can structures are widely used by the offshore industry for underwater foundations. They were introduced to the industry in 1980 in the Gorm field but then the experience gained with the installation for a loading buoy by a Heavy Lift Vessel (HLV) did not merit its usage until it was considered again after 10 years (Tjelta 2001). Their dynamics while submerged during installation is greatly affected by the added mass and damping. The added mass of the can with a closed top is amplified (many times the weight of the can in air) as a result of entrapped water within the suction-can (Bai and Bai, 2012). This chapter deals with the CFD analysis of a suction-can with the aim of deriving its hydrodynamic properties. The suction-can in this case was chosen based on previous studies that have been conducted numerically and backed by experimental results. The analysis was conducted for two cases – when the suction-can was well away from surface and seabed, and at varying proximities to the seabed (close to seabed). The model took into account a situation where the lowering or lifting was stopped mid water, and close to the seabed in order to activate active heave compensation or constant tension to reduce the risk of impact with the seafloor. This was achieved using the CFD software Fluent and the computational mesh was produced using Gambit.

4.2 Computational Fluid Dynamics

Computational fluid dynamics is a branch of fluid mechanics that provides an often time consuming way of simulating marine operations numerically by simulating the actual velocity fields. The CFD method solves the Navier Stokes equation and includes essential parameters such as turbulence, free surface, submerged bodies and bodies with a prescribed motion. Computational fluid dynamics is aimed at providing solutions to fluid flow problems making use of inputs such as the model enclosed in

the fluid domain in the case of external flows and the fluid properties with predefined values. The equations associated with the fluid flow problem which form a set of partial differential equations are the continuity and Navier-Stokes equations which represent the conservation of momentum.

CFD is a useful tool in simulating marine operations, where its application in marine operations would be to compute and study both hydrodynamic and aerodynamic coefficients care must be taken when choosing the methodology so that it fits in with the project schedule.

4.3 Numerical Determination of Vertical Added Mass and Damping of Suction-Can

The numerical determination of heave added mass and damping in this section involved simulating the developed 3D model of the suction can in the commercial software Fluent to determine the hydrodynamic forces acting on the body as it oscillates in the fluid domain by applying the dynamic fluid body interaction method.

The aim of this section is to estimate the added mass and damping of a suction-can which is a part of a subsea protective structure using CFD and comparing results with already existing experimental results.

This section begins with a description of the geometry and the simulation domain in Fluent followed by the material model and a mesh sensitivity study of the suction can in an unsteady flow. A discussion of the user defined external function is presented and a detailed explanation of the numerical algorithm applied in the unsteady flow problem to determine fluid force. Numerical results of the fluid forces obtained are presented for the structure away from surface and seabed, and in close proximity to seabed scenarios and finally the total forces are separated into the inertial and drag components.

Finally, results are presented alongside model test results of Roe et al. (2008) and Ireland et al. (2007), backed up with calculations using the developed analytical calculation method. The heave added mass and damping by Zoontjes et al. (2009) in

mid water and in close proximity to seabed were derived using the oscillatory flow and dynamic fluid body interaction methods. Both methods gave good results for a suction can well away from the surface and seabed with all the hatches closed. The dynamic fluid body interaction method was applied while simulating a decay test to quantify the floor effects instead of moving the fluid while the body is stationary and this same method was applied in this research but eliminating the use of a fixed mesh as adopted by Zoontjes et al. (2009), where the solid floor was modelled as a very dense and viscous fluid because the motion of the body may generate waves on the interface between the two phases, therefore the density and viscosity of the “floor fluid” have to be as high as possible to limit this effect. A well-defined mesh between the interface of the body and the floor with a wall boundary condition was sufficient in this case.

4.3.1 Model and Simulation Domain

The suction can was modelled using a pre-processing tool, Gambit. Gambit, a geometry and mesh building tool was developed by ANSYS Fluent. Gambit is widely used in creating simple geometries. It can also be used in creating more complex geometries but this is time consuming so other standard CAD software may be used. The geometry was created using the “Bottom-up” approach where points or vertices were created and these vertices were connected to form edges. These edges or lines were then connected to create the required faces and final volume created by joining the faces. The suction can geometry was created and enclosed within a 10D by 10D by 40D bounded box (see Figure 4.3-1) where D represented the diameter of the suction can in meters. The Can was then subtracted from this box to create the fluid domain and the structure with boundary condition type set as “wall”. The wall boundary type is usually useful in most rigid body fluid structure interaction problems for turbulent flows where the wall boundary requires special treatment.

Selection of a suitable domain was based on results obtained after running a domain size sensitivity study based on a basic setup of the problem to obtain the total force report for each domain size. It was observed that there was a difference in the force values presented in Figure 4.3-2 for the three different domains as the height of the initial domain was changed from 60D to 40D and 80D, where D is the diameter of the Can in meters.

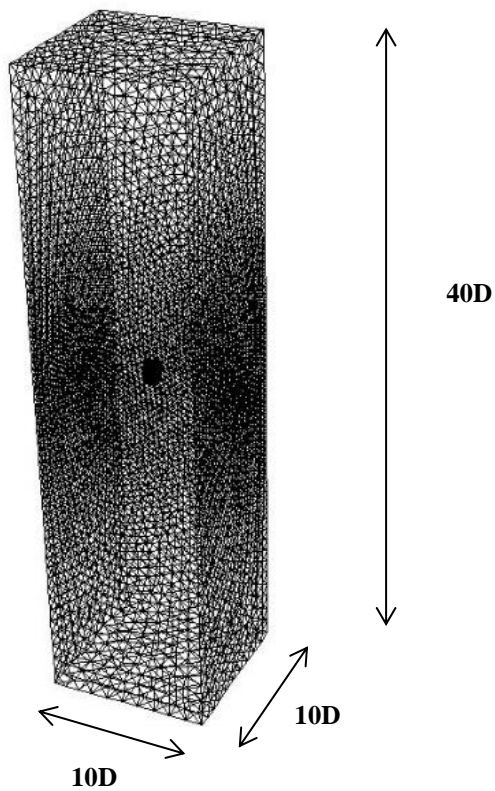


Figure 4.3-1 Simulation domain

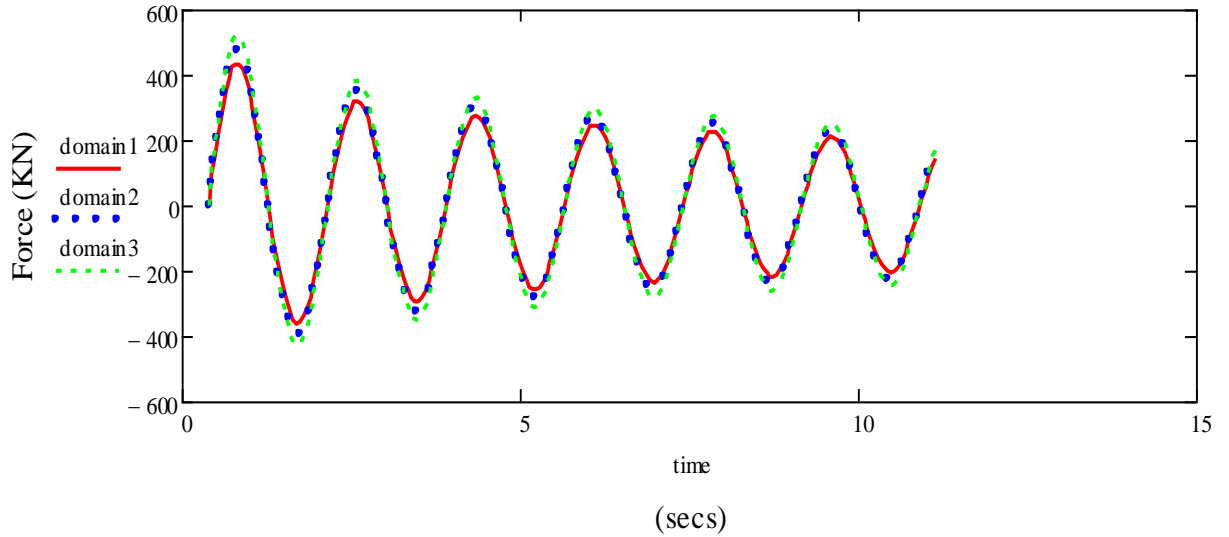


Figure 4.3-2 Total force for 40D (domain1), 60D (domain2) and 80D (domain3) domain sizes

The wall and symmetry boundary conditions were later assigned to the developed model. The wall boundary condition was assigned to the structure and the symmetry

boundary condition was assigned to all external faces, with large enough spacing from the structure, required to model an infinite fluid. This depicted the structure in deepwater far away from free surface effects and seabed interactions.

The simulated fluid was specified as “water-liquid” which was selected from the Fluent database with a density of 1025 kg/m³. In this case, seawater was specified as the material model because the dimensionless heave added mass coefficient was dependent on this value, while other parameters remained constant (ANSYS, 2009).

Table 4.3-1 Main characteristics of suction-can

Description	Units	Value
Height	m	6.000
Diameter	m	6.000
Thickness	m	0.020

4.3.2 Mesh Generation

The three-dimensional computational grid was developed with unstructured tetrahedral meshes. The cell sizes very close to the wall boundary were reduced using the Gambit size function and to control the growth rate until it blended into the neighbouring volume mesh. The size function details are presented in *Table 4.3-2* below which shows values for the minimum and maximum cell sizes and the growth rate used in creating the final volume mesh.

Table 4.3-2 Size function parameters

Description	Values
Minimum size	0.001m
Maximum size	10m
Growth rate	1.05
Type	Curvature
Source	Faces
Attachment	Faces
Angle	10

Figures 4.3-3 and 4.3-4 show cell size transition away from the wall boundary (suction-can).

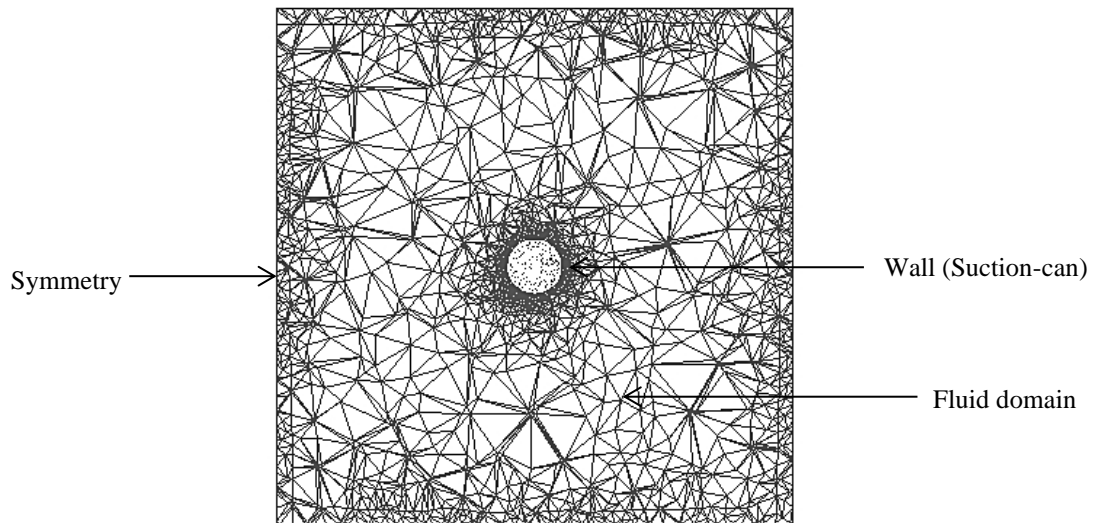


Figure 4.3-3 Cell size transition away from wall boundary of suction-can on horizontal plane (XY plane)

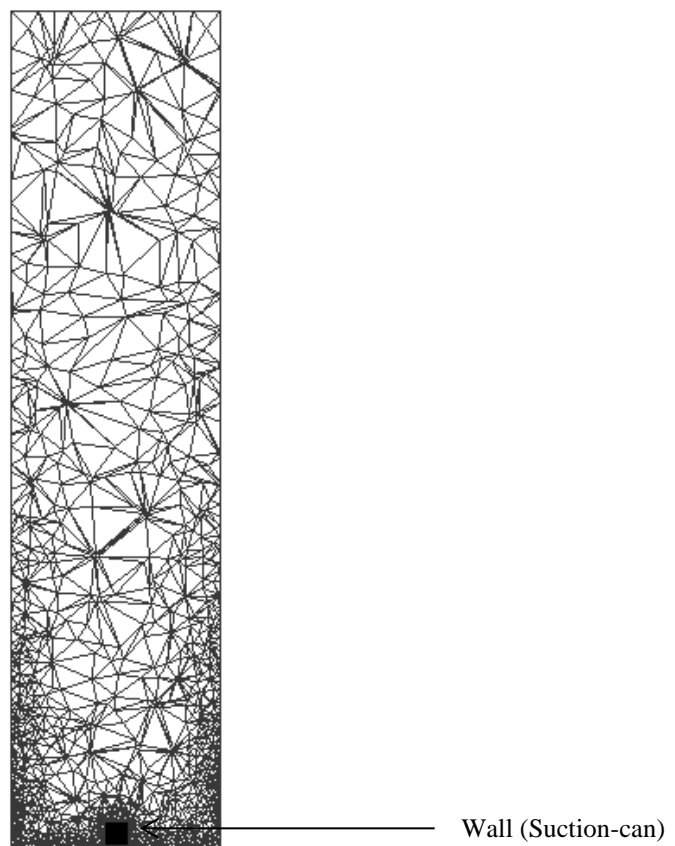


Figure 4.3-4 Cell size transition away from wall boundary of suction-can at $h/D = 0.2$ on vertical plane (ZX plane)

The size function was introduced to control the size of mesh intervals for the volume. The final result greatly depends on the mesh quality therefore before the mesh was exported to Fluent, it was examined to determine if it fell within the acceptable range documented by (ANSYS 17.0, 2016). The computational grid had 161,692 cells. Comparing this value with the number of cells of Zoontjes et al. (2009), this was much higher because the full structure was taken into consideration. The density of the mesh adjacent to the wall was high and fine to capture the significant flow features and resolve the flow around the wall boundary, the examined mesh skewness value was below 0.90 which is a requirement for a good quality mesh.

Skewness is a measure of symmetry, or more precisely, the lack of symmetry (National Institute of Standards and Technology, 2003). This measurement can be carried out by applying the EquiAngle Skew, θ_{EAS} , the EquiSize Skew, θ_{ESS} and the MidAngle Skew, θ_{MAS} method presented in the Gambit 2.4 Documentation (Sharcnet, 2009).

The EquiAngle Skew, θ_{EAS} method was applied in this research to report the quality of the volume mesh. The quality of these volume meshes fell within the region of 0.75 and 0.9. This region as shown in Table 4.3-3 is categorised as “Poor” but there was a trade-off that arose during the modelling of the structure. The idea of a more realistic model with low quality or a less realistic model with high quality bearing in mind that three-dimensional volume meshes’ quality is lower than two dimensional meshes.

Table 4.3-3 EquiAngle Skew, θ_{EAS} vs. Mesh Quality (Sharcnet, 2009)

EquiAngle Skew, θ_{EAS}	Quality
$\theta_{EAS} = 0$	Equilateral (Perfect)
$0 < \theta_{EAS} \leq 0.25$	Excellent
$0.25 < \theta_{EAS} \leq 0.5$	Good
$0.5 < \theta_{EAS} \leq 0.75$	Fair
$0.75 < \theta_{EAS} \leq 0.9$	Poor
$0.9 < \theta_{EAS} \leq 1$	Very poor
$\theta_{EAS} = 1$	Degenerated

4.3.3 Mesh Sensitivity

A total of three meshes were selected for the sensitivity study on the suction can. The three cases were expected to be in good agreement with model tests carried out by Roe et al. (2008) on a suction-can with same parameters. The number of cells for each mesh is shown in Table 4.3-4. The initial mesh, Mesh 3, was constructed with an unstructured tetrahedral mesh having 153,102 cells as indicated in Table 4.3-4. There was no set guideline during this process to follow but the aim was to produce a volume mesh of adequate density to capture all significant flow features and of good quality with a skewness value less than 0.90. With Mesh 3 as base, subsequent meshes with different minimum cell sizes and cell numbers were constructed. The volume mesh for Mesh 1 and 5 could not be constructed from the face meshes as a result of a too coarse and a too dense grid respectively.

Table 4.3-4 Number of cells for mesh sensitivity study

Mesh Number	1	2	3	4	5
Number of cells	-	143,232	153,102	161,692	-
Minimum Size (m)	0.10	0.01	0.005	0.001	0.0001
Skewness	-	0.90	0.87	0.85	-

The hydrodynamic coefficients obtained from the force reports of Mesh Number 3 and 4 were similar compared to the result obtained from Mesh Number 2 due to good quality grid (skewness less than 0.90). The heave added mass and equivalent damping results obtained from Mesh number 4 with 161,692 cells were in good agreement with past experiments and numerical simulations, therefore, 161,692 cells was selected for use in further studies.

Check for Asymptotic Range of Convergence

The accuracy is determined using the GCI method outlined in Roache (1998), to fulfil the asymptotic condition. In this case, the GCI is calculated using three grid levels with

heave added mass coefficients of approximately 1.569, 1.565 and 1.550 at a time step of 0.05 seconds.

Calculation:

Table 4.3-5 Added mass coefficients for various levels of the computational grid

No.	Number of cells	Added Mass Coefficient, Ca
1	161,692	1.569
2	153,102	1.565
3	143,232	1.550

The theoretical order of convergence is

$$p_{GCI} = \ln[(1.55 - 1.565)/(1.565 - 1.569)] / \ln(2) = 1.91$$

Applying Richardson extrapolation using the finest two grids, would result to

$$Pr_{h=0} = 1.569 + (1.569 - 1.565)/(2^{1.91} - 1) = 1.57$$

The grid convergence index for the fine grid solution will be computed with a factor of safety, $F_s = 1.25$ since three grid levels were used to estimate $Pr_{h=0}$.

The GCI for grids 1 and 2 is

$$GCI_{12} = [1.25 |(1.569 - 1.565)/1.569| / (2^{1.91} - 1)] 100\% = 0.116\%$$

The GCI for grids 2 and 3 is

$$GCI_{23} = [1.25 |(1.565 - 1.55)/1.565| / (2^{1.91} - 1)] 100\% = 0.434\%$$

Check for asymptotic range of convergence,

$$0.434 / (2^{1.91} \times 0.116) = 0.996$$

This shows that the solutions are within the asymptotic range of convergence.

The result shows that the heave added mass coefficient for the suction-can is estimated to be $Ca = 1.570$ with an error band of 0.116% or 0.00116.

4.3.4 Time Step Sensitivity

Simulations were performed for the sensitivity of the time step on the suction-can using the kw-sst turbulence model (Refer to Section 4.3.5: Selection of turbulence model) and the selected mesh number from Section 4.3.3. Results of the heave added mass coefficients for various time step sizes are shown in Table 4.3-5 for KC number 0.10 and were estimated following the procedure (see Equations 4.3-1 and 4.3-2) of Zoontjes et al. (2009) which was based on the application of Fourier analysis to the force time history.

$$c_a = \frac{m_a}{\rho V}$$

Equation 4.3-1

where, ρ is the fluid density, V is the volume of the suction-can and

$$m_a = -\frac{1}{\pi\eta\omega} \int_0^{2\pi} F(t) \sin(\omega t) dt - \Delta_{sc}$$

Equation 4.3-2

where, F is the hydrodynamic force, ω is the frequency, η is the amplitude of motion of the suction-can and Δ_{sc} is the suction-can displacement.

The equivalent damping ratio is derived from the sinusoidal varying force over a time record by fitting a line that touches the peak of these forces (see Figure 4.3-5). This line is formed by calculating the force magnitude expressed as

$$mag F = F_{33}e^{-B_e\omega t} + A$$

Equation 4.3-3

where, F_{33} is the amplitude of force in the heave direction, B_e is the equivalent damping ratio, ω is the frequency of oscillation and A is a constant.

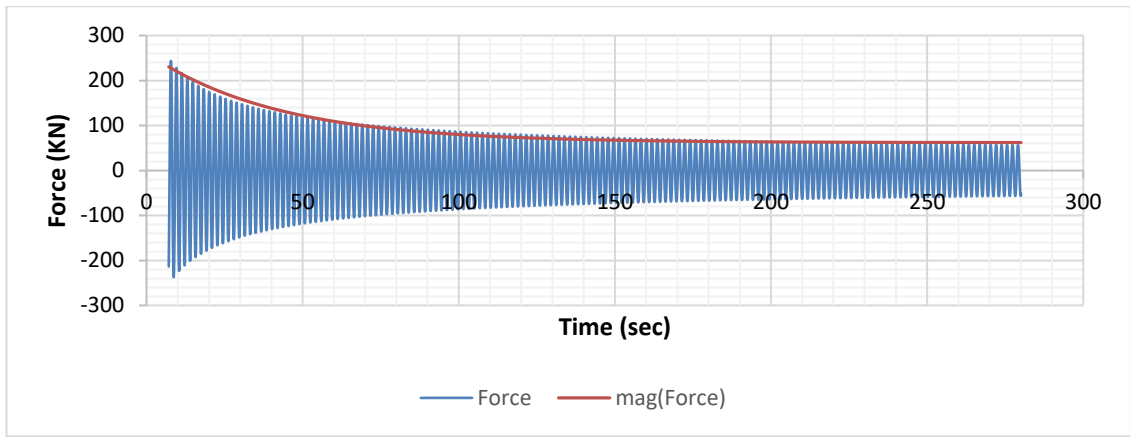


Figure 4.3-5 Force report of oscillating suction-can far from boundaries

Table 4.3-6 Added mass coefficients and equivalent damping ratios for time step sensitivity study for the suction-can away from surface and seabed with 161,692 cells, and percentage change of parameters relative to shortest time step at $KC = 0.1$

Time step size (seconds)	0.001	0.002	0.01	0.04975	0.05
Added Mass Coefficient	1.550	1.551	1.558	1.566	1.569
Equivalent Damping Ratios	0.018	0.018	0.020	0.021	0.021
Change Relative to Shortest Time Step for Added Mass Coefficient (%)	-	0.065	0.516	1.032	1.226
Change Relative to Shortest Time Step for Equivalent Damping (%)	-	-	10.00	14.286	14.286
Equivalent Damping Ratio – Error (%): CFD/Roe et al. (2008)	0.00	0.00	11.11	16.67	16.67

The k-omega SST model was applied. The results show an increase in the heave added mass coefficient as the time step size increases. There was no significant difference in the numerical error between a time step size of 0.05 and 0.04975 seconds. The decision to use a time step size of 0.04975 seconds was to check if the very small change from 0.05 sec would have caused a significant difference in the results – which might have indicated an instability in the numerical solution – but it did not. The calculated difference was less than 1% (0.192%). Between time step size of 0.05 and 0.001 seconds there was a difference of 1.226%. This was adequate for the calculation of heave added mass. The damping results were not as good at the longer time steps, the damping ratio increased by 14% with an increase from 0.001 to 0.05 seconds time step. Although 0.002 sec would have given a converged damping ratio, the extra computational effort was difficult to justify for the 14% damping accuracy benefit, corresponding to a maximum error of $1-11.14^{0.5} = 7\%$ in random sea conditions; therefore, the time step size of 0.05 seconds was adopted for the study.

The equivalent damping ratio, Be at KC number 0.1 obtained with a time step size of 0.001 seconds (See Table 4.3-6) was compared to an approximate model test result of Roe et al. (2008) ($Be = 0.018$) with an estimated error of 0.00%. A 16.67% error would be obtained with a time step size of 0.05 seconds when the equivalent damping ratio, Be at KC number 0.1 is compared to model test result of Roe et al. (2008).

The estimated errors between equivalent damping ratios of Roe et al. and the CFD analysis were 0.00 and 16.67% for time step sizes of 0.001 and 0.05 seconds respectively, where the equivalent damping ratio of the CFD analysis was equal and slightly higher than that of Roe's damping as time step size increased. Roe's low damping might be due to the accuracy of the measurements, possibly the overestimation of support equipment damping.

4.3.5 Turbulence Modelling

According to ANSYS FLUENT 12.0 User's Guide (2009), there is no single universally accepted turbulence model being superior for all classes of problems. Turbulence modelling has been one of the difficult aspects in fluid dynamics. It still remains a complicated phenomenon in today's engineering applications due to the violent nature of fluid flow covering a wide range of scales in space and time. Various

turbulence models have been developed for different flow problems. This study is concerned with three-dimensional flow and the idea is to solve the governing equations by averaging these equations over either a time or space scale so that the resulting equations would describe the sinusoidal varying motion of the structure (Garrido-Mendoza, 2015)

The Reynolds-averaged Navier-Stokes turbulence model selected for this study was the k-omega SST (Shear-Stress Transport) turbulence model. This was selected after a turbulence model selection process was carried out on several models. The other turbulence models applied were the SST Transition and k-e model. Numerical analyses for all three models were carried out on the suction-can. The most suitable model was the k-omega SST model (justified in Table 4.3-7). The k-omega SST model was appropriate because its results agreed with available data of Ireland et al. (2007). Figure 4.3-6 shows the hydrodynamic force obtained from various turbulence models.

The k-omega SST model is a two-equation model developed to combine the k-omega model and the k-epsilon model, and used to compute the turbulent eddy viscosity, μ_t required to close the momentum equations in the Reynolds-averaged Navier-Stokes model (see Equation 4.3-4) as expressed in ANSYS Fluent 12.0 User's Guide.

$$\frac{\partial}{\partial t}(\rho u_i) + \frac{\partial}{\partial x_j}(\rho u_i u_j) = -\frac{\partial p}{\partial x_i} + \frac{\partial}{\partial x_j} \left[\mu \left(\frac{\partial u_i}{\partial x_j} + \frac{\partial u_j}{\partial x_i} - \frac{2}{3} \delta_{ij} \frac{\partial u_l}{\partial x_l} \right) \right] + \frac{\partial}{\partial x_j} (-\rho \overline{u_i' u_j'})$$

Equation 4.3-4

where, u_i' is the mean fluctuating velocity component ($i = 1,2,3$), and $-\rho \overline{u_i' u_j'}$ are the Reynolds stresses which must be modelled in order to close Equation 4.3-4 according to ANSYS Fluent 12.0 User's Guide.

Developed to take into account the near wall viscous region, the k-omega turbulence model was able to predict from the onset, separation of the fluid flow from the surface of the structure and the amount of separation of the fluid flow later on, as the suction-can experiences vertical oscillations as a result of the external force exerted.

The k-omega SST model was developed due to the free-stream dependence on the k-omega model. Since the k-epsilon model is not susceptible to the free-stream values

of turbulence it is applied far away from the wall in free-stream where there is no influence of small changes in k-omega, while the k-omega model is applied very close to the wall because it gives a very good prediction of the skin friction. The boundary between these two models is called the blending region. The idea of using a blending between the two models is the basis of the k-omega SST model. The two-equation model according to Langley Research Center (NASA, 2021) is expressed as:

$$\frac{\partial}{\partial t}(\rho k) + \frac{\partial}{\partial x_j}(\rho u_j k) = P - \beta^* \rho \omega k + \frac{\partial}{\partial x_j} \left[(\mu + \sigma_k \mu_t) \frac{\partial k}{\partial x_j} \right]$$

Equation 4.3-5

$$\begin{aligned} \frac{\partial(\rho \omega)}{\partial t} + \frac{\partial(\rho u_j \omega)}{\partial x_j} \\ = \frac{\gamma}{v_t} P - \beta \rho \omega^2 + \frac{\partial}{\partial x_j} \left[(\mu + \sigma_\omega \mu_t) \frac{\partial \omega}{\partial x_j} \right] + 2(1 - F_1) \frac{\rho \sigma_{\omega 2}}{\omega} \frac{\partial k}{\partial x_j} \frac{\partial \omega}{\partial x_j} \end{aligned}$$

Equation 4.3-6

where, Equations 4.3-5 and 4.3-6 represent the turbulent kinetic energy and specific turbulence dissipation rate respectively, and the blending function F_1 is equal to one in the near-wall region and zero far from the wall, ρ is the density, v_t is the turbulent kinematic viscosity expressed as μ_t/ρ , μ is the molecular dynamic viscosity, $P = \frac{\partial u_i}{\partial x_j} (\tau_{ij})$ and the turbulent eddy viscosity

$$\mu_t = \frac{\rho a_1 k}{\max(a_1 \omega, \Omega F_2)}$$

Equation 4.3-7

where, Ω is the vorticity magnitude, F_2 is the blending function, and γ , β , β^* , a_1 and σ_ω are constants (expressions for these terms are presented in the turbulence modelling resource of NASA (NASA, 2021)).

Equations 4.3-5 and 4.3-6 were derived by multiplying both the standard k-omega model and the transformed k-epsilon model (Menter, 1994). by the blending function,

F_1 and both models were added together. The blending function is required to switch between the k-omega and k-epsilon models.

When $F_1 = 0$, the k-epsilon model is activated and when $F_1 = 1$, the k-omega model is activated.

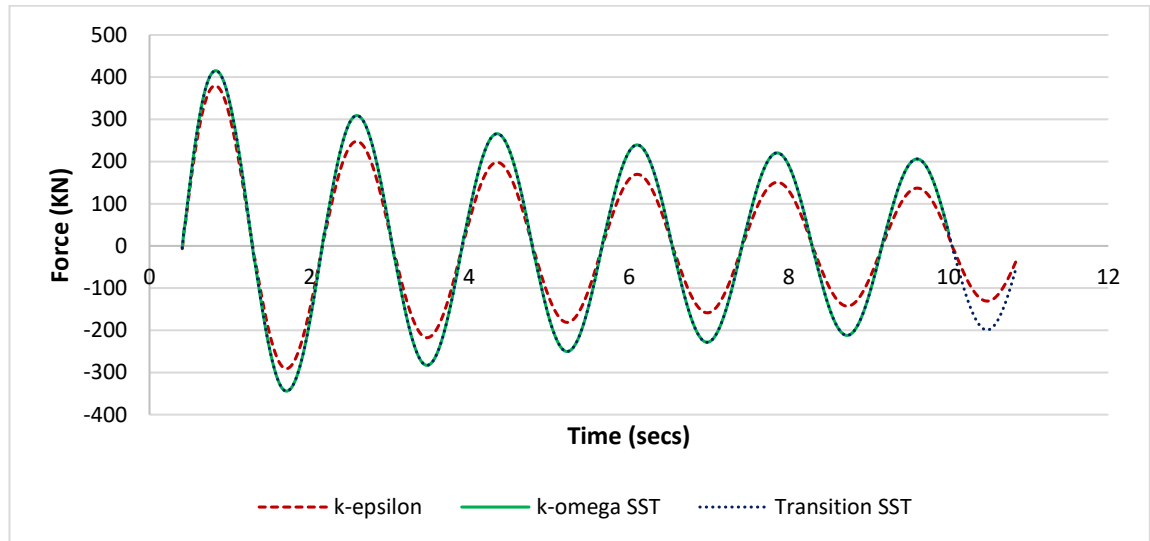


Figure 4.3-6 Force time history for k-epsilon, k-omega SST and SST Transition turbulence models

The calculated heave added mass coefficient and equivalent damping ratio from the total force of the heaving suction-can for the different turbulence models at a time step size of 0.01 seconds are shown in Table 4.3-7.

Table 4.3-7 Added mass coefficient and equivalent damping ratio for various turbulence models at time step 0.01 secs (KC = 0.1)

Turbulence Model	k-epsilon	k-omega SST	SST Transition
Added Mass Coefficient	1.489	1.558	1.558
Equivalent Damping Ratio	0.03	0.021	0.021

It was observed that the results obtained from the k-epsilon model varied from both the k-omega SST and SST Transition model. The SST Transition and k-omega SST models gave the same results because the SST Transition model being a four equation

turbulence model is built on the coupling of the transport equations of the k-omega SST with two other transport equations where one equation is for the near transition to turbulence and the other for the fully developed turbulence. The SST Transition is computationally expensive for industrial applications, analyses require more computational time and hence the k-omega SST model was adopted.

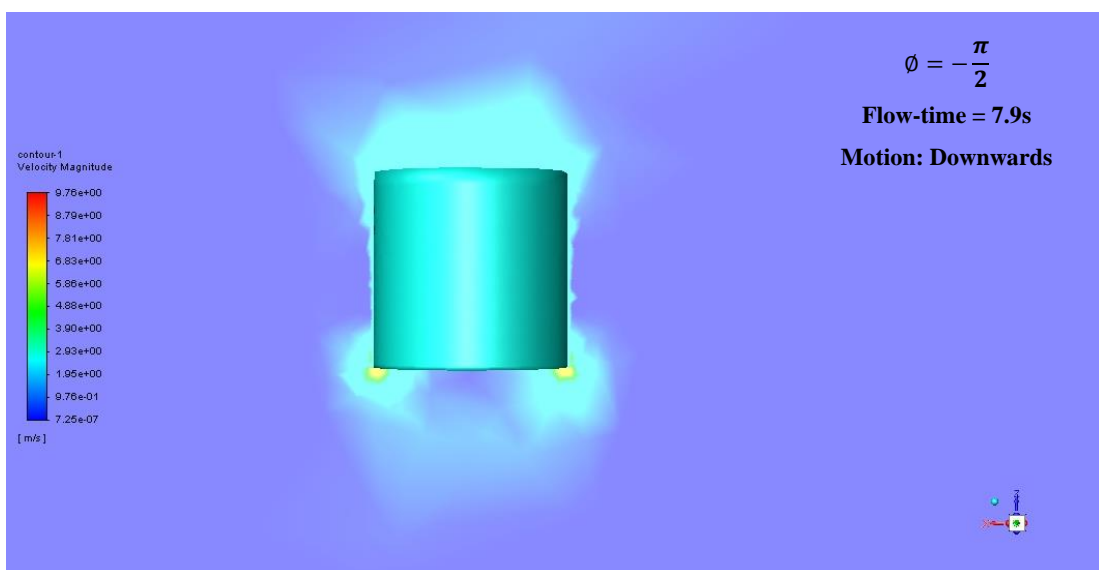
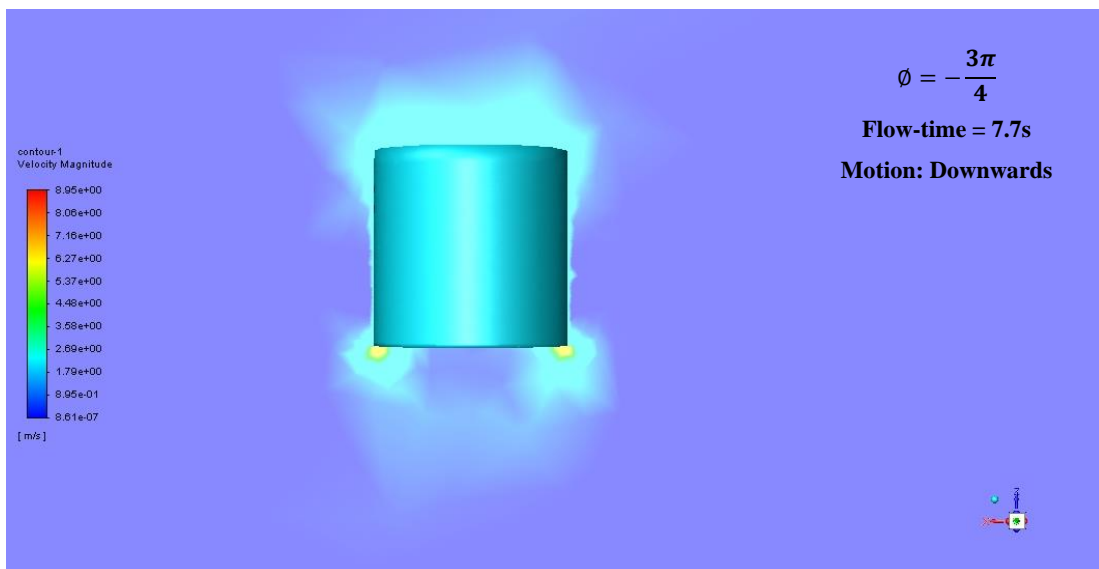
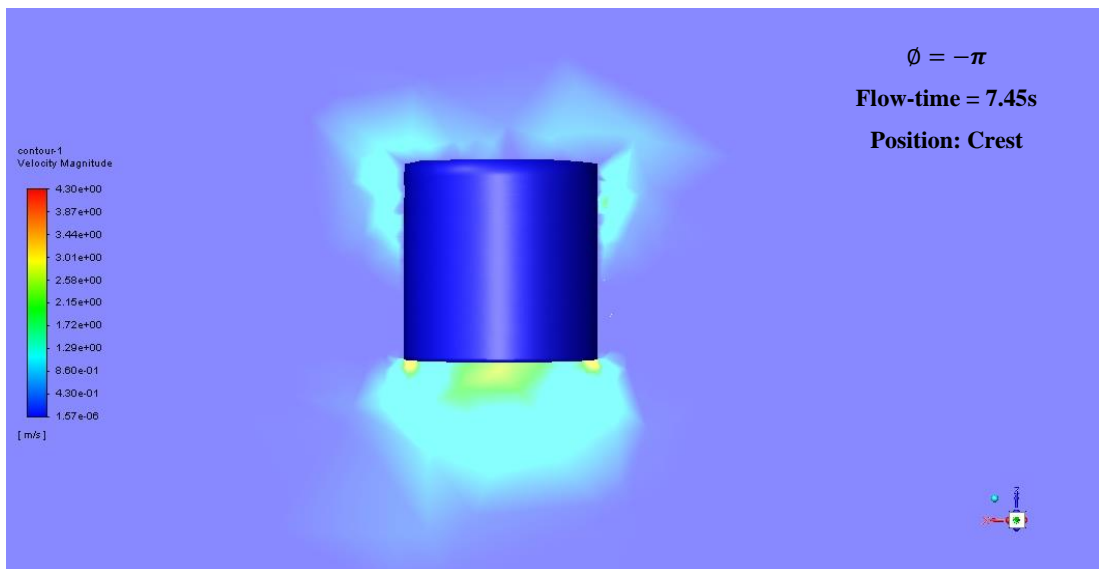
Both the k-epsilon and the SST Transition models encompass the enhanced wall treatment function used for comparison along with the k-omega SST model. This allowed for the wall function to be used for the near wall region which takes into consideration the viscous sub-layer, buffer layer and the fully turbulent region.

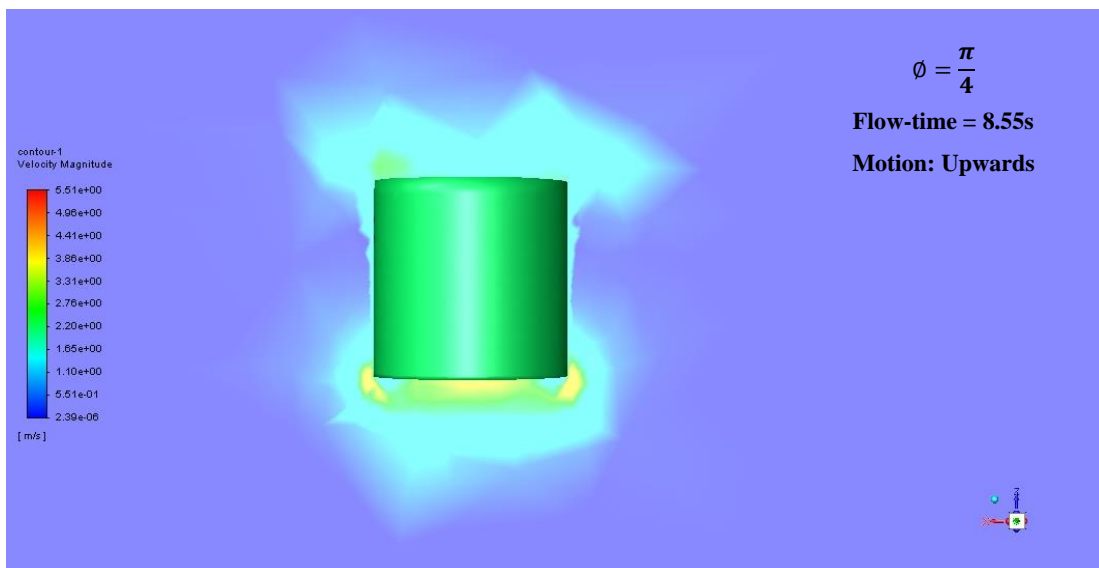
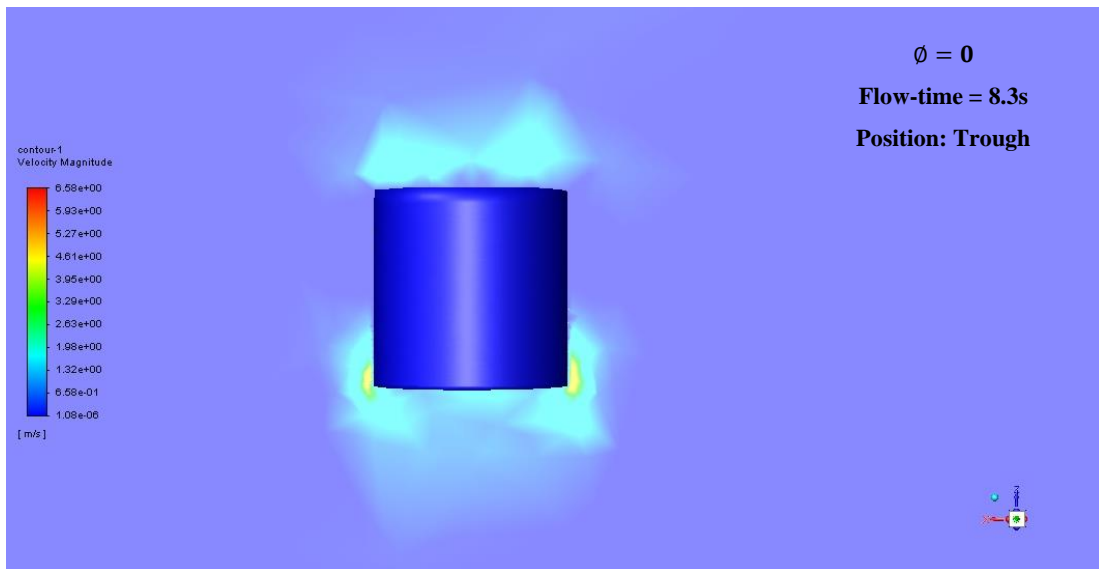
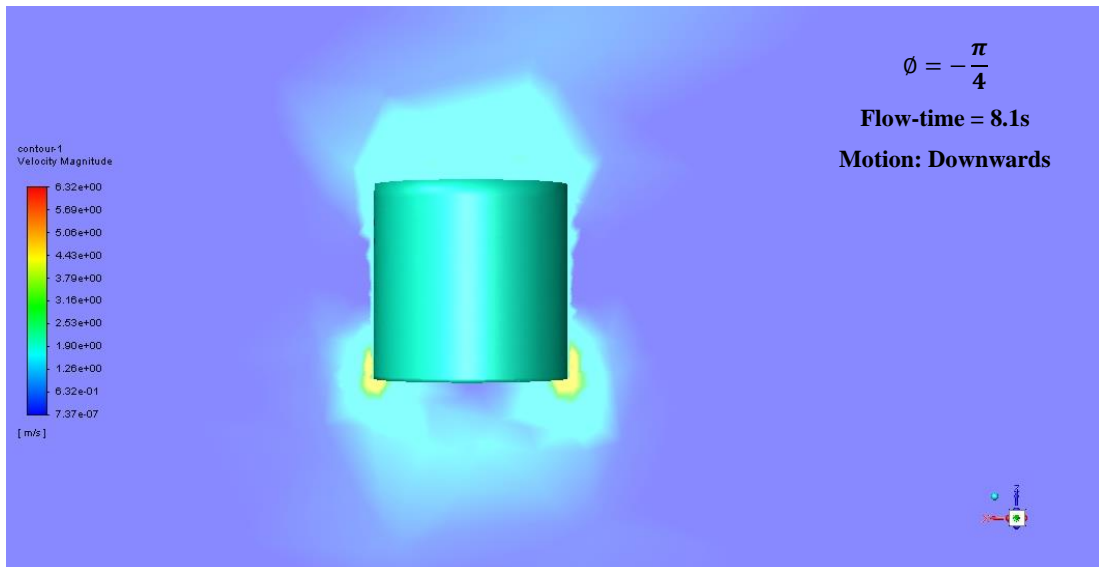
4.3.6 Dynamic Mesh

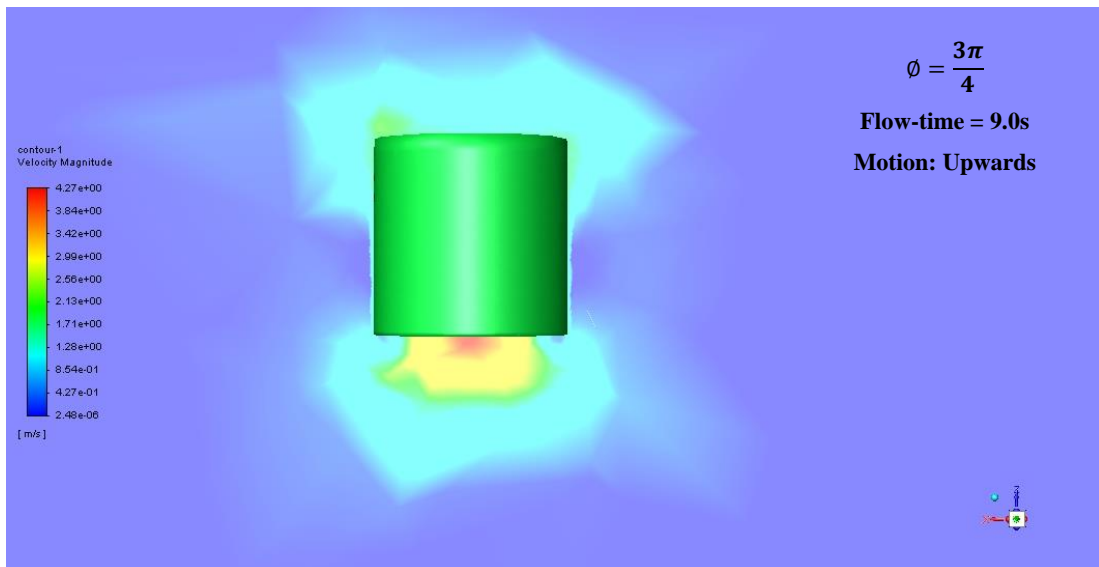
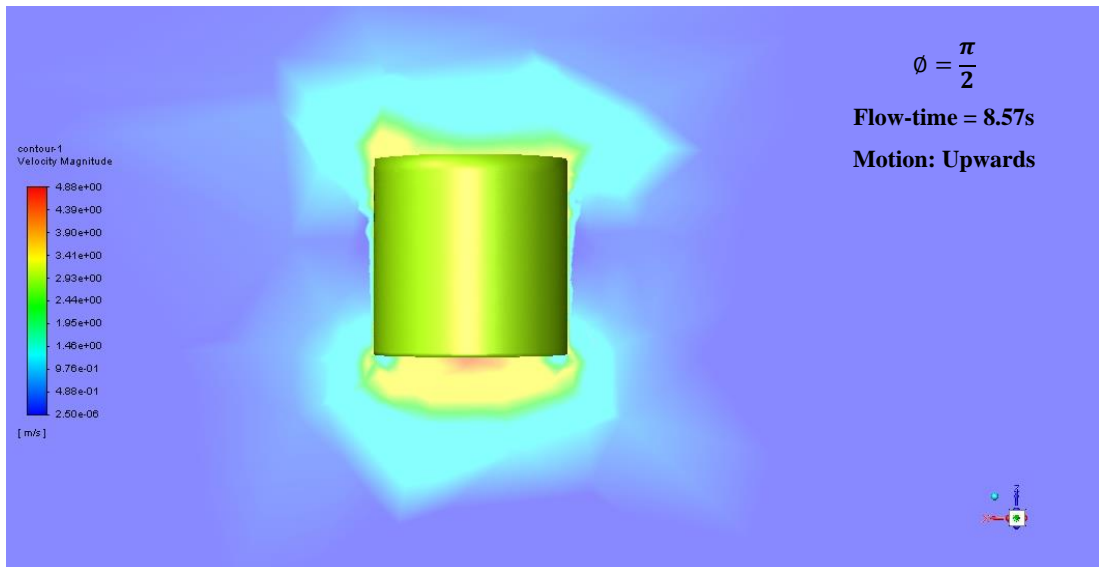
The dynamic mesh model was activated to model the unsteady flow as the fluid domain changes with respect to time as a result of the motion of the vertical oscillation of the suction-can. The volume mesh was updated automatically at each time step by ANSYS Fluent by taking into consideration the new positions of the structure's boundary after the vertical velocity was prescribed about the centre of gravity of the structure using a User-Defined Function (UDF).

The motion of the structure was specified on the wall boundary in the dynamic mesh zones during the solution set up and this zone was considered as a rigid body where the motion UDF was then dynamically linked to the motion attributes in Fluent. The UDF was developed in a C-programming language and compiled in Fluent using the following procedure highlighted below.

- i. After setting up the solution and writing the Case and Date file in Fluent, go to "Define" select "User-Defined", then select "Functions" and Compiled.
- ii. Add the Developed UDF source code to the working directory.
- iii. Create the UDF by clicking the build tab and
- iv. Load the library.
- v. UDFs are external functions required as inputs due, in this case, to the limitation of the Fluent solver not being able to move the solid boundary.







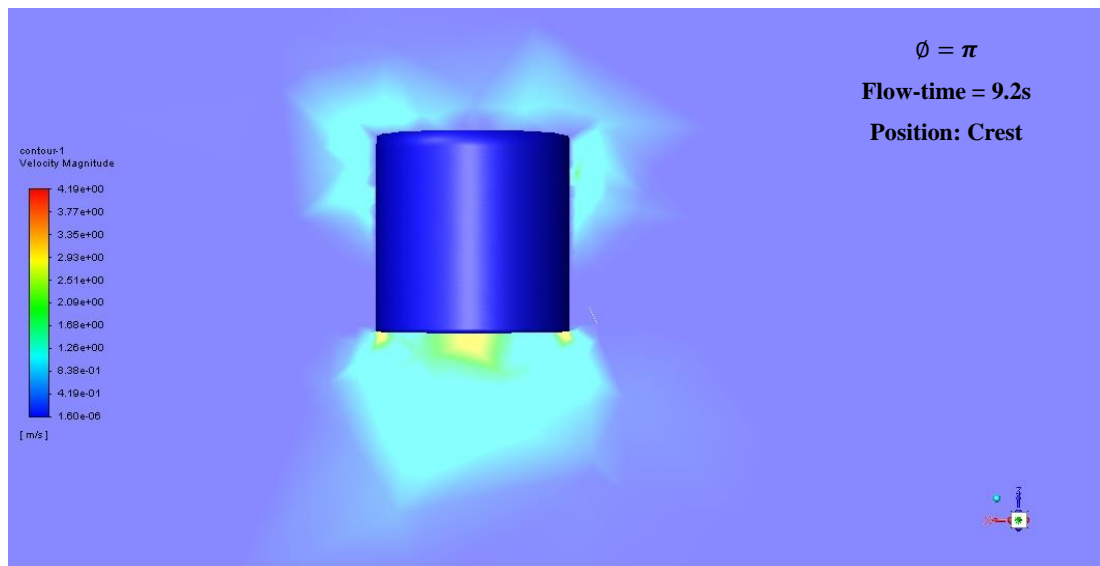


Figure 4.3-7 Contours of velocity magnitude of suction-can well away from surface and seabed for one oscillation

Figure 4.3-7 shows the velocity contours of the suction-can at various phase angles, ϕ . The downward motion of the suction-can from the crest ($\phi = -\pi$) results in the formation of vortices at the bottom of the can due to the pressure exerted on the fluid within the suction-can. This stream discharge continues with increasing vortex formations until the suction-can approaches the trough position ($\phi = 0$) and then followed by an upward movement. Here, the increasing velocity until the structure approaches the crest ($\phi = \pi$) was as a result of the fluid discharge within the suction-can due to the suction-can's upward motion and no downward pressure exerted on the fluid by the suction-can.

The downstroke and upstroke do not produce the same effects on the flow because of the closed top of the suction-can. This causes different flow circulation values to be produced in both downstroke and upstroke. A net lift force is thus obtained over each cycle as a result of this.

4.3.7 Solver Settings

A further set up of the CFD simulation required setting up the solvers which entailed specifying the solution methods. Since this analysis was a transient simulation, the PISO (Pressure-Implicit with Splitting of Operators) scheme, an algorithm by Issa

(Issa, 1985) was selected for the pressure-velocity coupling. This algorithm with neighbour correction is a highly recommended algorithm for all transient flow analysis (ANSYS, 2009) because: it takes less computational time and gives more stable results than the SIMPLE and SIMPLEC schemes; it is fitted with the ability to perform the skewness and neighbour correction to improve on the limitation of the SIMPLE and SIMPLEC schemes where after the pressure-correction equation is computed, the accompanying fluxes do not meet the requirement of the momentum balance; and it accommodates the use of large time steps for problems which normally require small time step sizes.

Under Relaxation Factors, URF

The under-relaxation factors applied in the numerical simulation were significant because they were used to reduce the change in the variables (pressure, density, body forces and momentum) produced during each iteration. Each variable represents an equation the solver, Fluent is trying to solve with the result (approximate solution) of the next iteration getting closer to the real solution thereby reducing the discretization error (convergence).

The under-relaxation factors shown in Table 4.3-8 were set to 1.0 for density and body forces, 0.80 for turbulence kinetic energy, and 0.3 and 0.7 to sum to 1.0 for both pressure and momentum respectively because only the PISO skewness correction was applied since the meshes were highly distorted.

Table 4.3-8 Under-Relaxation Factors

Parameters	Under-Relaxation Factors
Pressure	0.3
Density	1.0
Body Forces	1.0
Momentum	0.7
Turbulent Kinetic Energy	0.8

For this case, the value of the new pressure variable, P_n within the cell from the iteration depends on the value of the old pressure variable, P_{n-1} within the previous cell. Under-relaxation of this pressure variable is mathematically represented as

$$P_n = P_{n-1} + 0.3(P_n - P_{n-1})$$

Equation 4.3-8

where, $(P_n - P_{n-1})$ is the change in pressure variable.

The under-relaxation factors were selected based on the User Guide of ANSYS Fluent 6.3 Documentation (ANSYS, 2006). The under-relaxation values of Table 4.3-8 are default values set by Fluent, and they were suitable for the numerical analysis since there was no increase in the residuals after the first 5 iterations.

The second order solver was assigned to the momentum, turbulent kinetic energy and the specific dissipation rate equations since this scheme (Second-Order Upwind scheme) produced more accurate results because it is an improvement on the spatial accuracy of the First-Order Upwind scheme and it makes use of 3 data points for computation instead of 2 data points. The justification for applying the Second-Order Upwind scheme was because it provided stability and accuracy for poor quality meshes, and it accommodates the use of large time steps.

The First-Order Implicit scheme was selected for the transient formulation. This was the only option available because the dynamic mesh option was activated earlier during the solution set-up in Fluent for the numerical analysis. Its advantages are: it is easy to converge, it is less accurate but stable when compared to a higher order scheme, and it is sufficient for most problems (ANSYS, 2011)

The body-force weighted scheme was also used during the solution setup since the problem involved large body forces (ANSYS, 2006).

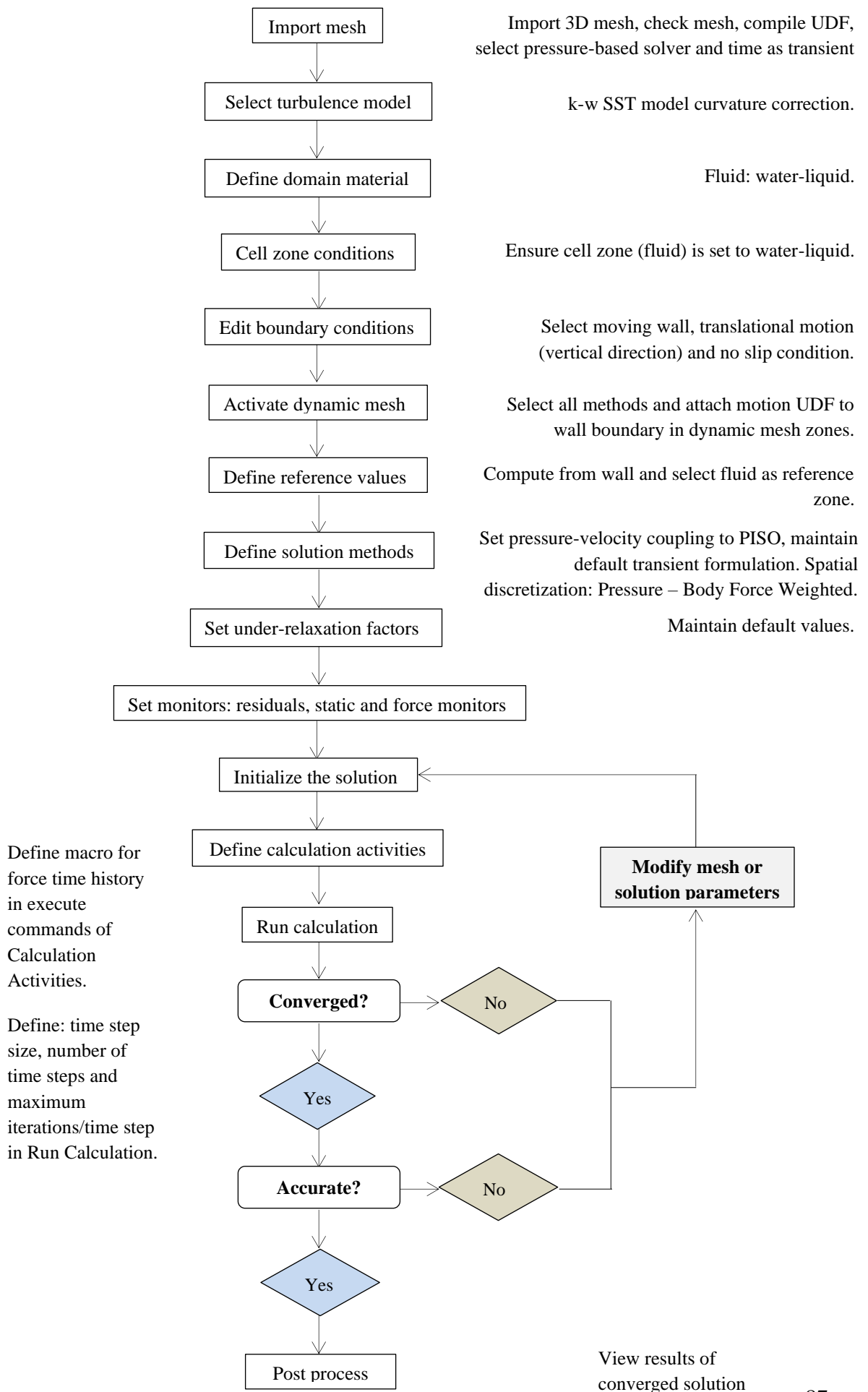


Figure 4.3-8 Solution set-up in Fluent

Figure 4.3-8 describes the solution set-up used for the CFD analysis, and Figures 4.3-9 to 4.3-12 show results of the pressure contour of the suction-can at KC number 0.9 for different h/D ratios, where h is the height above seabed and D is the diameter of the suction-can.

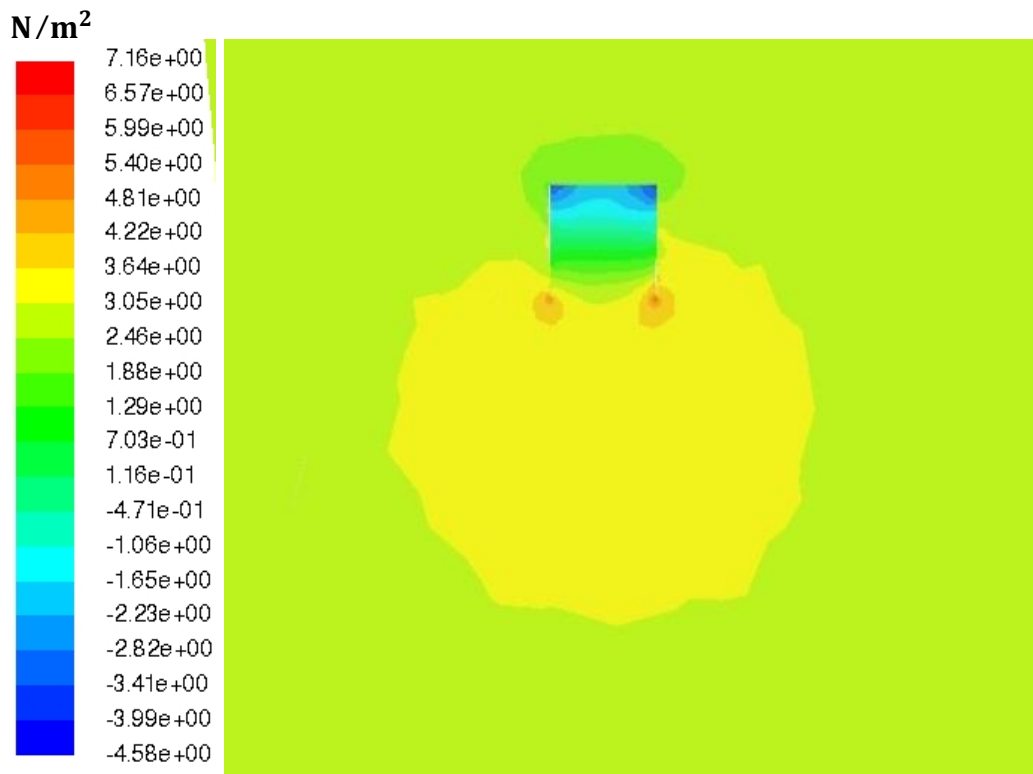


Figure 4.3-9 Pressure contour of suction-can well away from surface and seabed

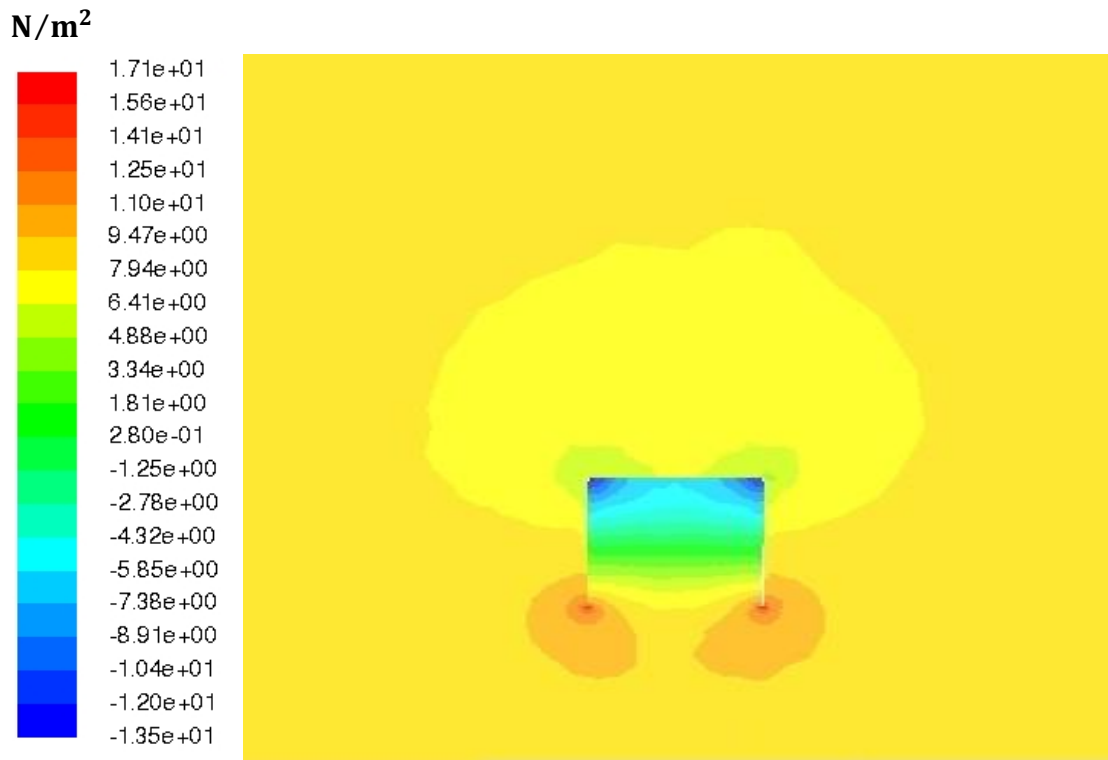


Figure 4.3-10 Pressure contour of suction-can at $h/D = 1.2$

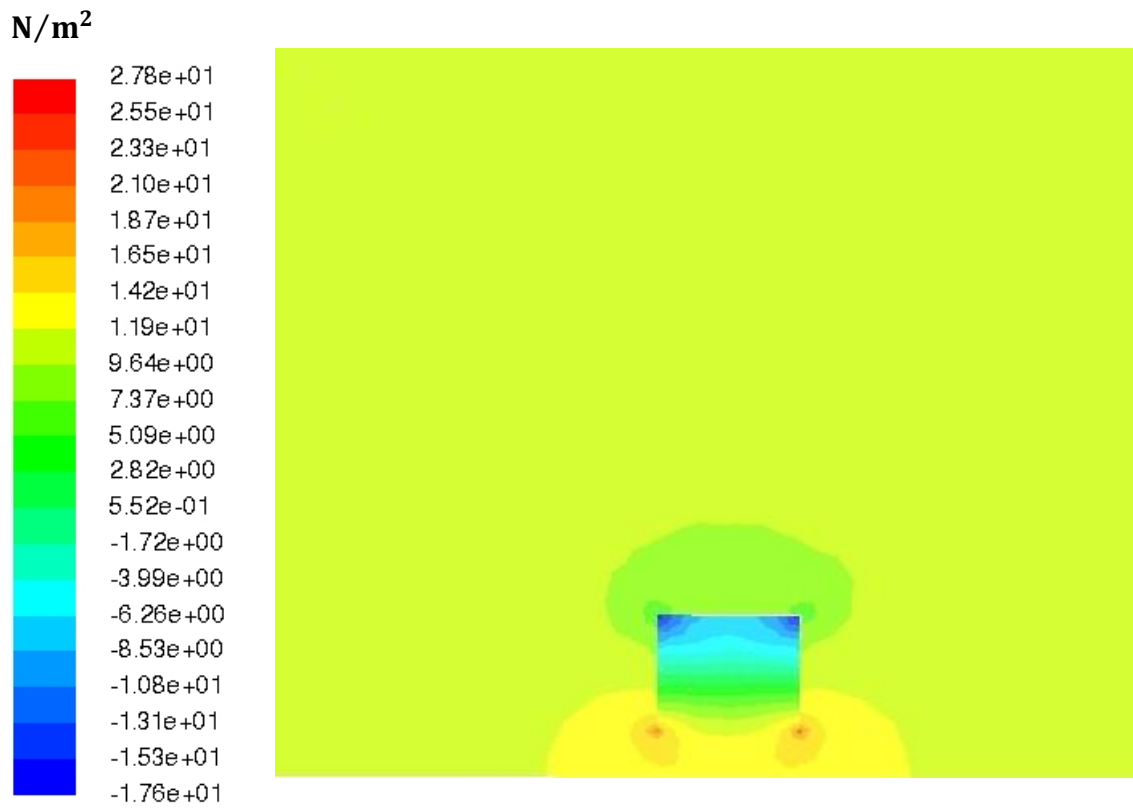


Figure 4.3-11 Pressure contour of suction-can at $h/D = 0.6$

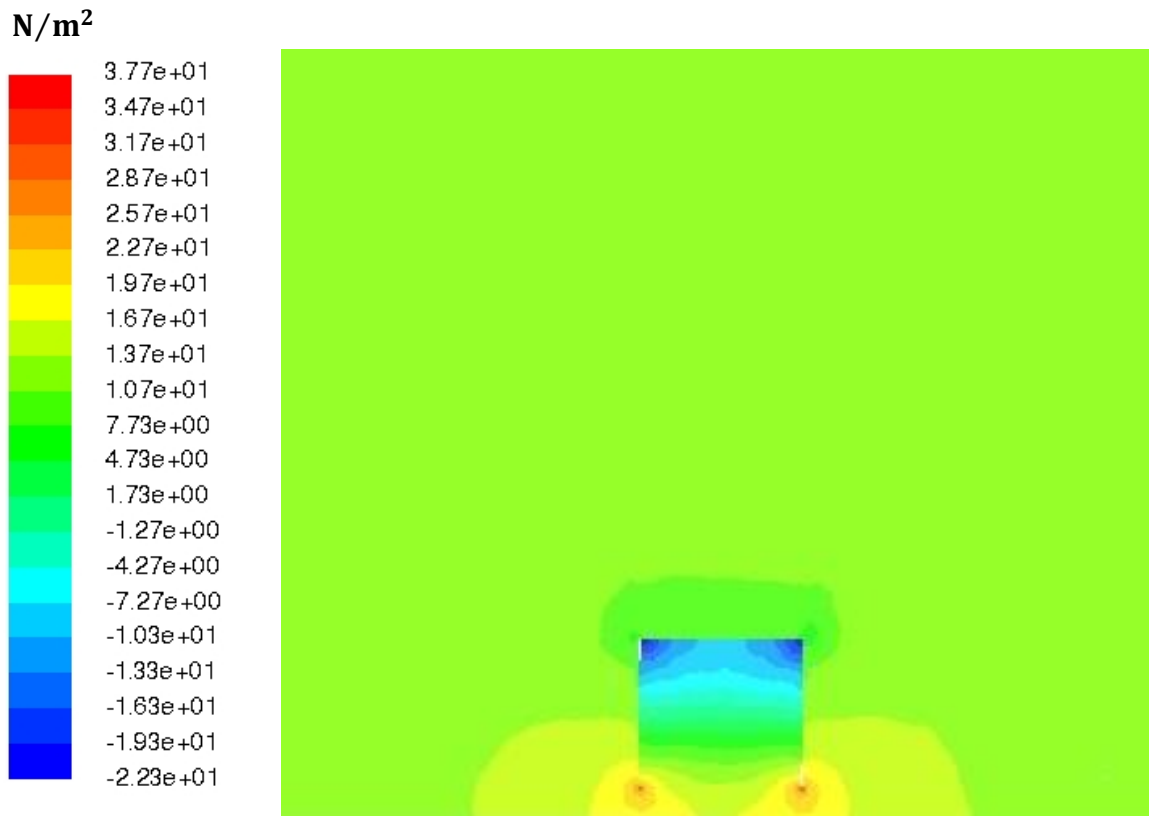


Figure 4.3-12 Pressure contour of suction-can at $h/D = 0.2$

Figures 4.3-9 to 4.3-12 show the pressure distribution around the suction-can. The pressure force increases due to the suction-can's closeness to seabed. The pressure acting at the bottom of the suction-can represents the downward motion of the structure in the stationary fluid. The net pressure in the upward direction is the drag force pushing the suction-can upwards. This contribution to the drag force due to the pressure is the form drag because of the low pressure region at the top of the suction-can due to the separation. The friction or the viscous shear at the wall which acts in the tangential direction also contributes to the drag and makes up the total force reported by Fluent.

The oscillating suction-can exhibits varying pressure at each point due to varying velocity and the increase in the velocity of the structure means there would be an

increase in displacement of the fluid particles, therefore increasing the added mass of the suction-can in the heave direction. The increase in pressure would increase the net hydrodynamic force on the structure thereby leading to an increase in the drag force. The formation of vortices at the bottom of the suction-can contributes to the damping of the structure. It can be seen from the figures that the formation increases as the suction-can approaches the seabed.

4.4 Hydrodynamic Properties of Suction-Can

Results of the heave added mass and damping of the suction-can are presented in this section. Current offshore engineering practices may simplify the geometry of the suction-can to a standard shape with known hydrodynamic coefficients making such results conservative for installation analysis. Model tests and CFD analyses are the preferred analyses techniques, where the latter was employed in this thesis. The numerical analysis was carried out with an oscillation period of 1.75 seconds for all cases. 1.75 seconds was chosen for analyses because it was in line with reference (Zoontjes, et al., 2009) used for calculation. A typical range of period for installing subsea structures would depend on the installation analyses results, where this range is determined based on operable sea states.

The results showed the dependency of the added mass and damping on the Keulegan-Carpenter number – Ratio of amplitude of oscillation, η to diameter of structure, D given as: $2\pi\eta/D$. Two scenarios were considered to represent the installation of a subsea work package. The first was the far from boundaries condition which represented the subsea module in a stationary position and the second was the close to seabed condition with two water depth ratios (h/D) of 0.40 and 0.20 from the seabed. This fell within the range of the close-to-seabed installation process where either active heave compensation or a constant tension approach is adopted for the final set down of the subsea module from a distance of 3 meters above the seabed.

The KC and frequency dependent hydrodynamic force from CFD analyses consisted of pressure and viscous forces with the viscous force less dominant when velocity was minimum (crest and trough position of Figure 4.3-7), and more dominant at maximum

velocity ($\phi = -\pi/2$ of Figure 4.3-7) as a result of the shear stresses developed between boundary layer of the oscillating body and fluid known as skin friction. The pressure or form drag was associated with the pressure force which also resulted in the formation of vortices at the bottom edge of the suction-can.

There was noticeable reduction in the amplitude of force over time until it got to a stage where there was no significant change in the reduction of successive amplitudes. At this stage, the numerical analysis was stable and was stopped in order to reduce computational time.

The estimated hydrodynamic coefficients of the suction-can were lower when the structure was well way from the surface and seabed compared to when it was close to the seabed. This was as a result of the structure placed far away from the free surface and seabed which led to no interaction effect due to increase in the fluid particle motion, shear stresses between particles and between particles and structure. Figure 4.3-12 shows the contours of pressure of the suction-can far from the seabed and at various heights above the seabed. This shows an increase in the pressure due to the dynamic excitations of the fluid particles beneath the structure as a result of its closeness to the seabed.

4.4.1 Operation Away from Surface and Seabed

The results shown in this section are based upon the methodology outlined in the previous sections. The analysis was carried out over a range of KC numbers to show the dependency of the hydrodynamic coefficients. The results of the CFD analyses were reported alongside results of model tests by Roe et al. (2008) as a means of validation of the Fluent simulation method.

The increase in heave added mass coefficient as KC number increased from 0.1 to 0.5 was not pronounced which signifies these coefficients do not overly depend on the increase in amplitude of motion of the structure in this range. For each increase in the motion amplitude of the heaving body, there is an incremental mass of fluid added to the previous mass derived from the preceding amplitude which is nonlinear and can

only be determined from experiments, numerical analysis and analytically in the case of simple geometries. The results showed good agreement with model test results.

The equivalent damping ratios were also reported alongside results of model tests by Roe et al. (2008). By fitting the data points of the equivalent damping ratios at each KC number, a line of best fit would be achieved and this can be used in deriving the linear and quadratic damping ratios. The recommended practice (DNV-RP-H103) stated that the nonlinear quadratic term should be applied during design for more accurate results (Det Norske Veritas, 2011). Figure 4.4-2 shows a comparison between the equivalent damping ratios from the CFD analysis and Roe et al. (2008). Table 4.4-1 shows a tabular comparison.

Table 4.4-1 Equivalent damping results of CFD analysis and of model test by Roe et al. of the suction-can away from surface and seabed

KC number	Equivalent Damping Ratio, B_e			
	CFD	Roe et al. (2008)	Difference: CFD/Roe et al. (2008)	Error (%): CFD/Roe et al. (2008)
0.1	0.018	0.018	0.00048	2.611
0.2	0.027	0.026	0.00057	2.212
0.3	0.035	0.033	0.00221	6.779
0.4	0.043	0.039	0.00410	10.434
0.5	0.052	0.046	0.00574	12.477
0.6	0.060	0.053	0.00763	14.480
0.7	0.069	0.059	0.00953	16.032
0.8	0.078	0.067	0.01058	15.803
0.9	0.086	0.074	0.01222	16.592

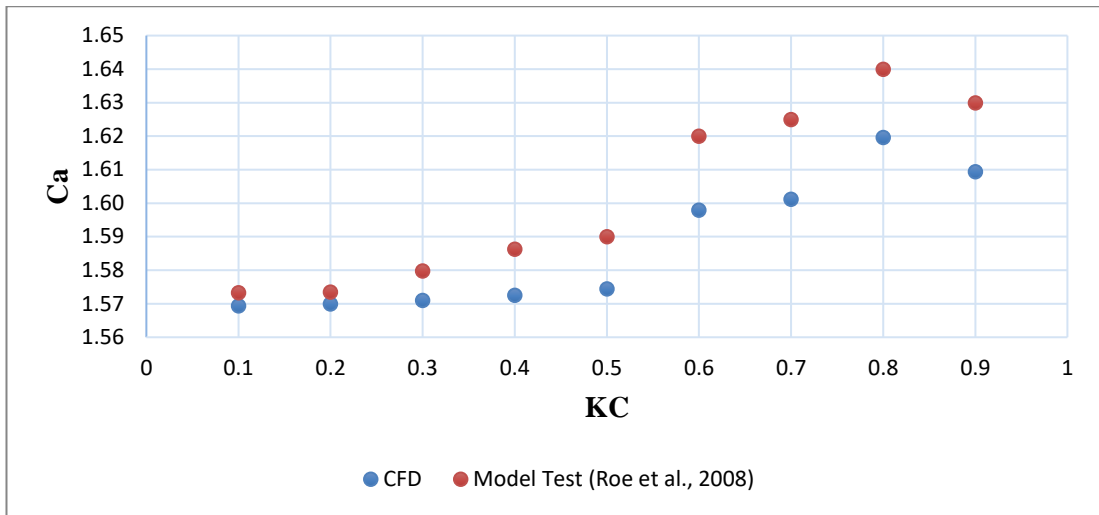


Figure 4.4-1 Added mass coefficients of suction-can away from surface and seabed

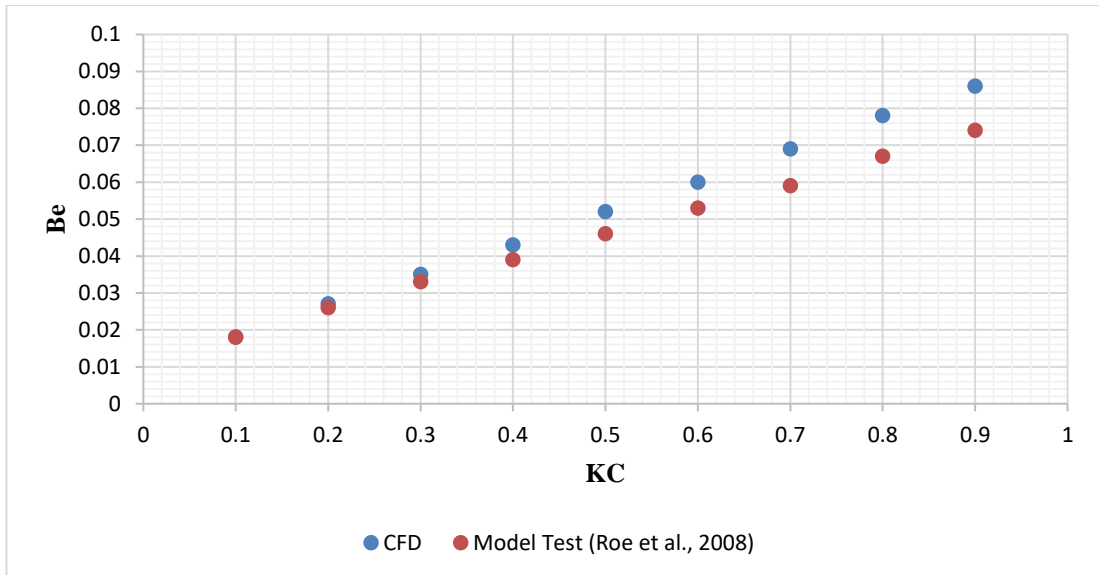


Figure 4.4-2 Equivalent damping ratio of suction-can away from surface and seabed

Figures 4.4-1 and 4.4-2 show results of the suction-can well away from the surface and the seabed, free from the influence of the free surface and seabed. It was observed from the results of Figures 4.4-1 and 4.4-2 that the hydrodynamic coefficients increased with an increase in KC number. From $KC = 0.4$, the added mass and damping coefficients become less accurate due to the transition of the flow from laminar to turbulent. This can be observed in Appendix A, Figure A.1-1, which shows increase

in the magnitude of velocity from KC 0.1 – 0.9 of the suction-can at maximum velocity as it moves downwards.

The numerical flow visualization demonstrates in detail the mechanism of vortex shedding at the bottom edge of the suction-can at various amplitudes of oscillation. For $KC = 0.1$, the vortices move through a very short distance before being diffused away. The distance moved by the vortices increase as the amplitude of oscillation of the suction-can increases. This is noticeable between KC 0.1 and 0.5 (See Appendix A.1-1 and A.2-1). There is no interaction between the vortices shed from the bottom edge (the circumference) of the suction-can observed.

At higher KC , from $KC = 0.6$, the vortices move over a longer distance and diffuse away slowly. There is noticeable interaction between the vortices shed from the bottom edge of the structure observed. There is no noticeable movement of flow away from the suction-can in the horizontal direction due the movement of vortices around the bottom edge of the suction-can and particles of the flow above the suction-can as a result of increase in amplitude of oscillation structure.

4.4.2 Operations Close to Seabed

An adjustment to the boundary conditions was made for the proximity to seabed condition and was maintained for all h/D ratios. The suction-can was placed above the seabed at a gap ratio (h/D) of 0.40 and 0.20 (See Figure 4.4-3). A wall boundary was then assigned to the seafloor due to its closeness to the structure and the mesh density of the volume mesh was much higher at the interface between the seafloor and structure.

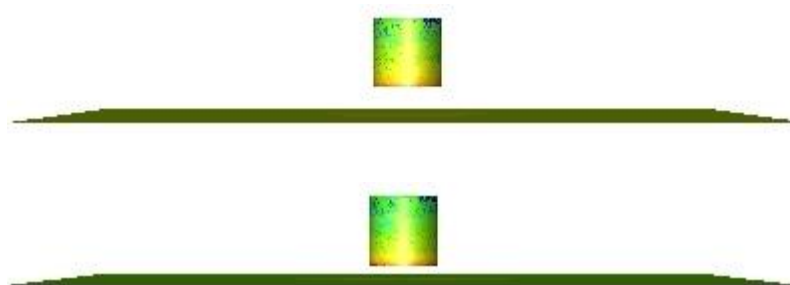


Figure 4.4-3 Suction-can at $h/D = 0.4$ (figure above) and $h/D = 0.2$ (figure below) above seabed

A parametric study had to be conducted on the time step size to ensure the initial time step size selected when the suction can was away from surface and seabed was still relevant. Since the fluid region of concern is close to, and shares a boundary with the sea bottom, a reduction in the height of the computational grid above the top of the suction can would reduce the number of cells needed for the numerical analysis and hence save computational time. A final domain size height of 30D was selected while other dimensions remained the same.

Table 4.4-2 Added mass coefficient results for various time step and fluid domain sizes of suction-can at $h/D = 0.40$ from seabed

Time Step Size (seconds)	0.001	0.002	0.01	0.04975	0.05
Ca	1.657	1.658	1.665	1.673	1.676
Domain Size (m)	25D	30D	35D	40D	-
Ca	1.71	1.699	1.699	1.699	-

The numerical simulations were run at a time step size of 0.04975 seconds for the domain size sensitivity study. The results presented in Figures 4.4-7 to 4.4-10 show the heave added mass coefficients and equivalent damping ratios of the Fluent simulation method compared with model tests by Roe et al. (2008) for both gap ratios of 0.40 and 0.20 respectively.

Iterations were performed within each time step. Figure 4.4-4 shows a consistent trend in the decreasing residuals. The sawtooth pattern of the residuals indicates the unsteady flow and each spike in the residual plot represents a new time step of the simulation. The successive peaks of most residuals were of the same height. The continuity residual did not drop as much compared to other residuals but this was sufficient for the simulation based on comparison with model test result of Roe et al. and the consistency in the hydrodynamic force report of the CFD analysis as shown in Figure 4.4-5. These were used in judging convergence and also flow patterns presented in Section 4.3.6 which showed practical sensibility of the simulation.

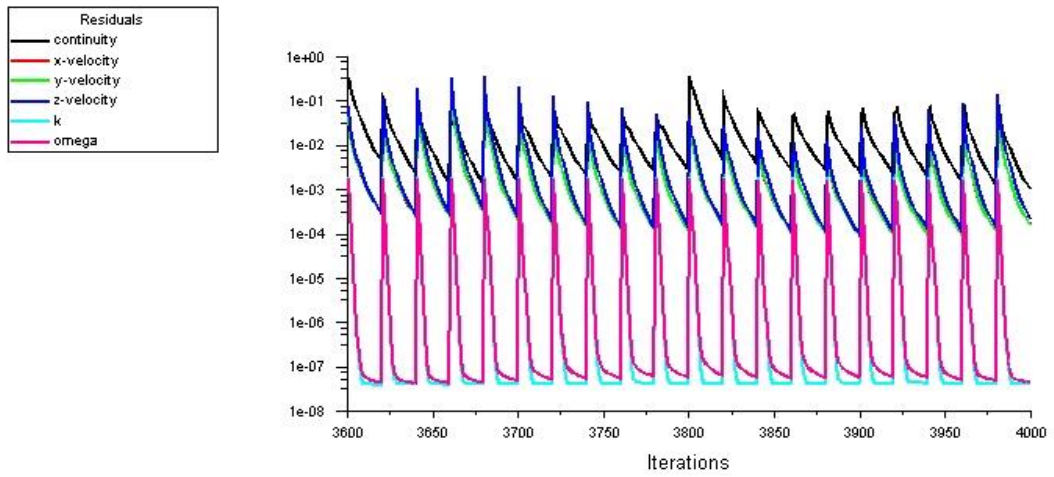


Figure 4.4-4 Residuals for 20 inner iterations at $KC = 0.1$ ($h/D = 0.4$)

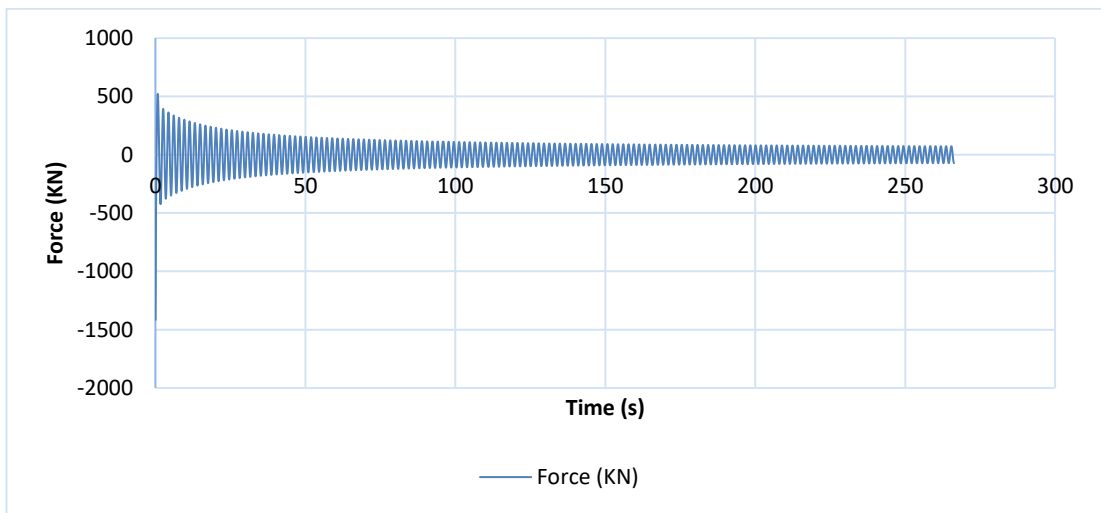


Figure 4.4-5 Hydrodynamic force of suction-can at $h/D = 0.4$

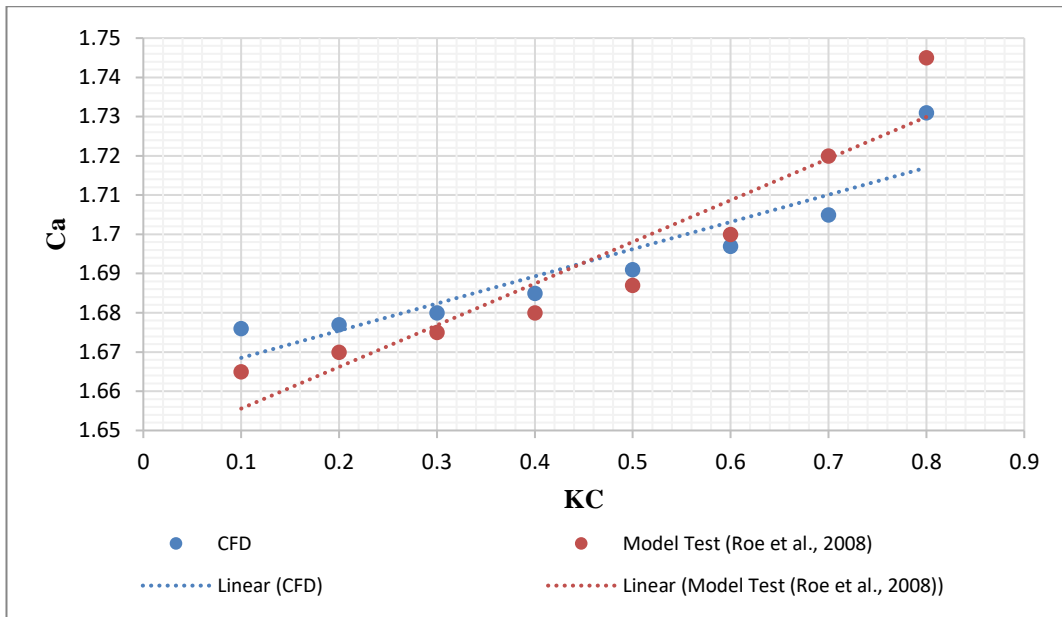


Figure 4.4-6 Added mass coefficient of suction-can at $h/D = 0.40$ from seabed

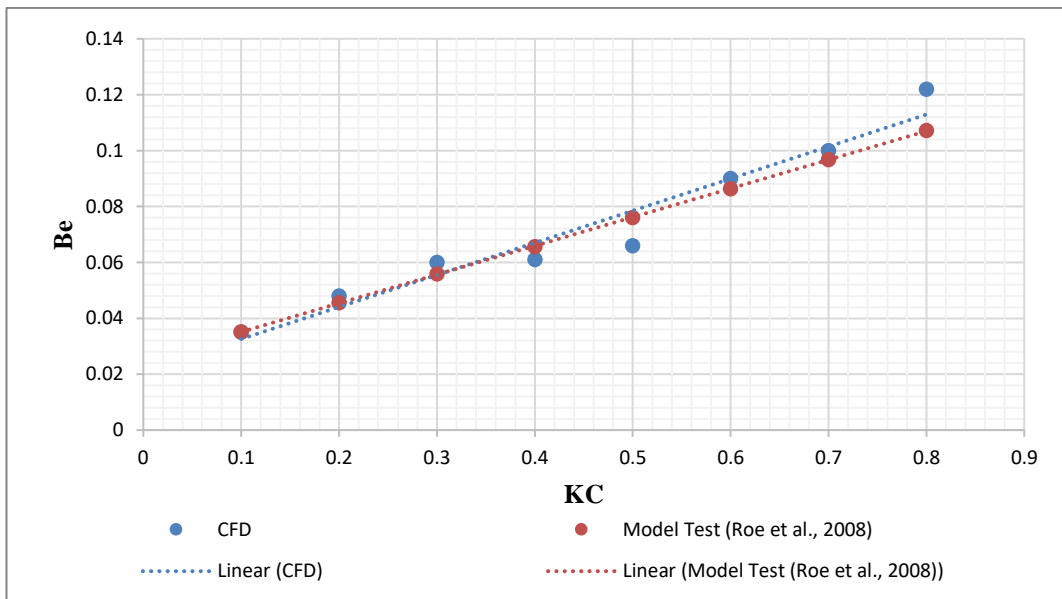


Figure 4.4-7 Equivalent damping of suction-can at $h/D = 0.40$ from seabed

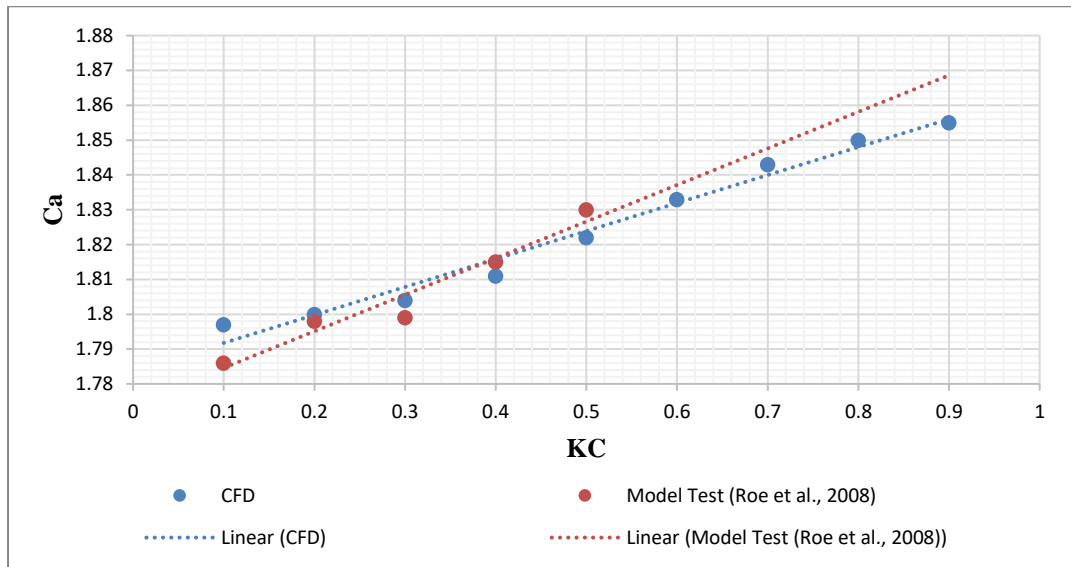


Figure 4.4-8 Added mass coefficient of suction-can at $h/D = 0.20$ from seabed

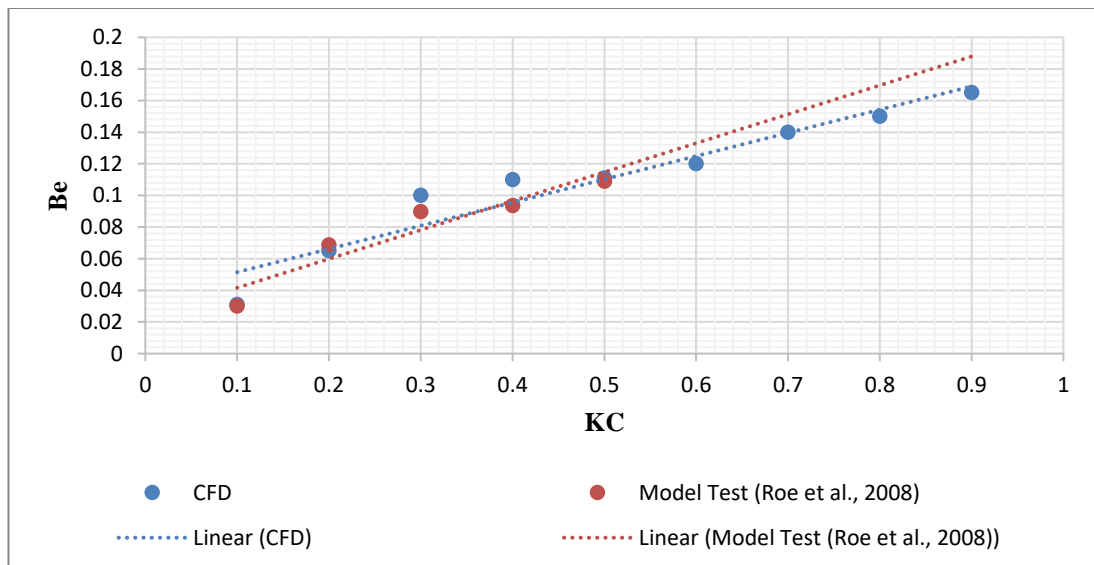


Figure 4.4-9 Equivalent damping of suction-can at $h/D = 0.20$ from seabed

The results show a consistent increase in the hydrodynamic coefficients of both gap ratios. The model test results of Roe et al. presented in Figures 4.4-9 and 4.4-10 were for a Keulegan Carpenter number range of 0.10 – 0.50 and could not be extended to the highest KC value of 0.9 due to unavailable data from Roe et al. (2008). Although an extension of these data to $KC = 0.9$ was achieved by adding a linear trendline drawn

as a best fit through the data points, which denotes the average in the case of the added mass coefficients and the equivalent damping ratios.

The curve fitting method was applied to estimate the equivalent damping ratios as explained in Section 4.3.4. The results of the curve fitting method are influenced by the accuracy in fitting the curve on the data points (amplitude of force).

As KC increases, the strength of the vortices at the bottom edge of the suction-can increase (See Appendix B.3). At KC 0.1, the vortices convect slowly but are not being diffused away fully at maximum velocity – downward motion of structure. This results in the particles of the flow touching the seabed. This seabed interaction of the particles of flow increases as KC increases.

4.5 Chapter Summary

The Fluent simulation method applied to calculate the heave added mass and damping of the suction-can, involved the introduction of a user defined function, and eliminated the adjustment of the density and viscosity of the fluid (Zootjes, et al., 2009), by concentrating more cells in the region between the bottom of the suction-can and the seabed (seabed gap), for the cases where the suction-can was close to the seabed. The results were validated using model test results by Roe et al. (2008) and Ireland et al. (2007). The objective was to provide a Fluent simulation method that could be applied in estimating the hydrodynamic coefficients of complicated subsea structures well away from the surface and seabed and close to the seabed.

Flow visualization showed that vortices formed beneath the suction-can contributed to the added mass and damping of the structure, and the vortices shed only occurred during decent of the structure. The hydrodynamic force was dependent on KC and the interaction of the suction-can's edge with the fluid, and its size.

The review in Chapter 2 showed there were other methods used in estimating the hydrodynamic coefficients, but these methods were applied to subsea structures with geometry different from the one used in this research. Some of the methods were applied simplified geometries to represent the subsea structure, like in the case of the subsea manifold which was reduced to a cuboid to simplify the hydrodynamic

calculation (Chen, et al., 2017). The Fluent simulation method in this chapter was applied to a suction-can and a slightly simplified subsea protective structure (Chapter 5) which meant the results of the hydrodynamic coefficients were not under or overestimated as a result of geometry simplification.

5 CFD Analysis of Complicated Subsea Protective Structure

5.1 Introductory Remarks

The aim of this chapter is to apply the Fluent simulation method to complicated subsea structures far from boundaries and in close proximity to seabed. The subsea structure (see Figure 5.3-1) chosen for this study is mainly used for subsea oil and gas operations in areas with increased risk of dropped objects. The foundations are used to support the upper part of the structure (structure resting on foundation) when impacted by vertical and horizontal loads (Det Norske Veritas, 2015).

It is a complex shaped structure which makes modelling quite different from the suction-can which is termed a simple geometry, presented in the Chapter 4. The procedure in developing the computational mesh will be discussed together with the selection of suitable boundary types because the model was divided into four parts due to symmetry in order to reduce computational time.

Finally, the results derived from the CFD analyses are presented.

5.2 The Subsea Structure

The subsea structure is an integrated structure used in the offshore industry especially in oil and gas production. It rests on the seabed encompassing either a subsea manifold or tree and anchored to the seabed by embedding its suction-cans with its top hatch used to protect the housed unit. Figure 5.3-1 shows a model of the structure with its dimensions reported in Table 5.3-1. The suction-can has an open hatch to allow the passage of water as its bottom end penetrates the seabed. Due to the small size of the vent, it was assumed in the proposed approximate method in Chapter 3 that the fluid flow through the vent is negligible and would not affect the structure's added mass. This assumption was taken from the recommended standard of DNV, DNV-RP-H013.

A study of the dynamics of this structure to accurately predict its response during installation is of importance to installation engineers as an installation failure would pose a great risk to personnel safety and impact negatively on the overall field development cost.

5.3 Modelling and Meshing of the Subsea Structure

5.3.1 Creating the Model

This was the first and important step required to run the CFD analysis because the simulation time and results were dependent on the model. The subsea protective structure is symmetrical in shape therefore one quarter of the model was modelled. The modelling strategy depended on the degree of complexity of the subsea protective structure. The strategy adopted was the bottom-top approach for the subsea protective structure, where either lines or faces were created for each component member before its volume. This was achieved through the use of Boolean operations to create faces from lines or to sweep faces to form volumes. Other models may require either a bottom-up approach or a top-down construction method, or a combination of both methods. The top-down construction method starts with the creation of volumes which may be cylindrical structures or bricks, depending on the geometry, and would entail the application of either the intersect option or the subtract, unite options to these volumes in order to obtain the final geometry.

The model was produced with the 3D CAD software Gambit. The first element was created and located on the primary x, y, z axis (0, 0, 0) with subsequent members further translated to target location and rotated as required. Table 5.3-1 shows the main characteristics and dimensions of each structural member of the subsea protective structure.

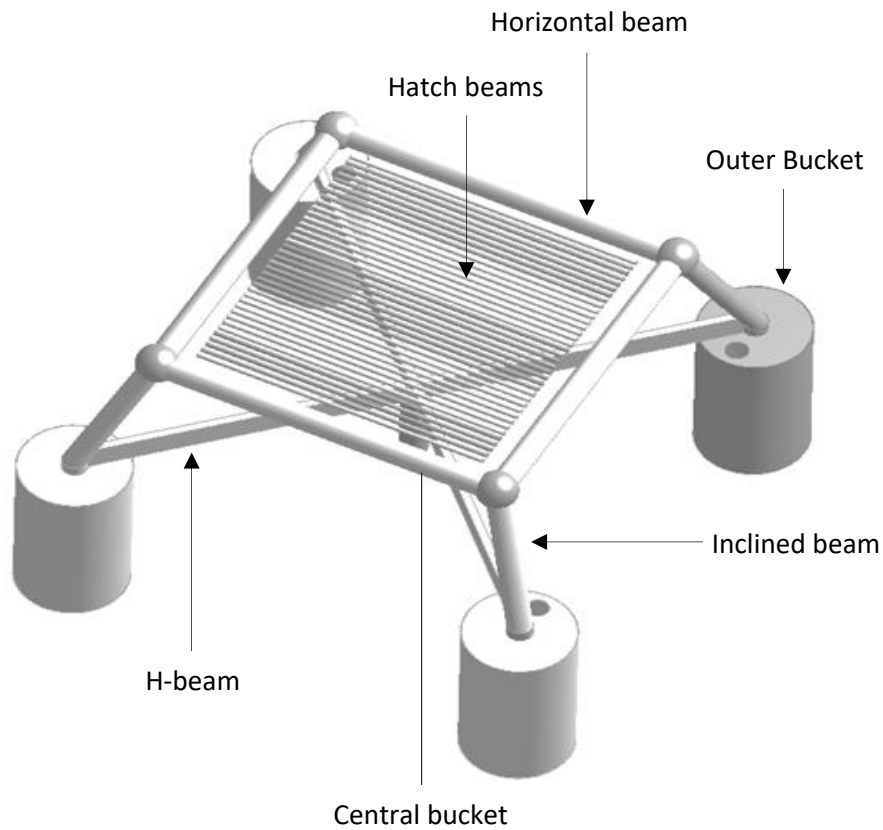


Figure 5.3-1 Subsea Protective Structure

The complexity of the subsea protective structure arises from the number of component members such as: hatch beams close to one another, H-beams located below hatch beams and resting on central and outer buckets. The interaction of each component member with the fluid results to a complex flow pattern that is dependent on KC.

Table 5.3-1 Main characteristics of Subsea Protective Structure

Parameters	Units	Values
Volume of structure	m ³	20.237
Displacement of structure	N	20743
Outer Buckets		
Diameter	m	4.000
Thickness	m	0.025
Height	m	6.500
Perforation diameter	m	0.8

Number of outer buckets		4
Central Bucket		
Internal mass	kg	77993
Diameter	m	1.000
Thickness	m	0.025
Height	m	3.000
H-Beams (Placed centre-to-centre on Outer Buckets)		
Length	m	24.000
Breadth	m	0.300
Height	m	0.900
Number of H-Beams		2
Horizontal Beams		
Diameter	m	0.914
Length	m	13.042
Number of horizontal beams		4
Hatch Beams		
Diameter	m	0.170
Length	m	10.900
Number of hatch beams		35
Inclined Beams		
Diameter	m	0.914
Length of inclined beams	m	5.600
Inclination of inclined beams	deg	60
Number of inclined beams		4

Estimating the hydrodynamic coefficients of subsea protective structures using CFD is an external flow problem, therefore, after creating the final volume (the geometry), it was subtracted from an enclosed domain. After subtraction, the final volume (domain) had a hollow space which takes the shape of the subsea structure (the geometry). Before creating the volume mesh, the domain should be decomposed into smaller volumes, but this might not be necessary for a simple subsea structure.

Splitting the domain into subdomains will allow for a better control of the meshing process and will control the cell transition in the domain.

The model was further discretized into smaller volumes as shown in Figure 5.3-2 due to the difficulty in producing the final volume mesh as a result of Gambit's inability to handle a huge number of cells. This was also advantageous because the meshing procedure was controlled manually since each volume had to be meshed separately by following a hierarchical manner which starts from meshing the edges, then the faces produced from the edges and then advance to the volume. This process ensured the mesh quality was maintained below the recommended value for all stages where a quality with a skewness of less than 0.50 was acceptable for a face mesh and a skewness of less than 0.90 was acceptable for a volume mesh (Refer to Section 4.3.2). The size function parameters (Refer to Section 4.3.2) selected for the suction-can in Chapter 4 were applied in this case with a total number of 6746481 tetrahedral cells.

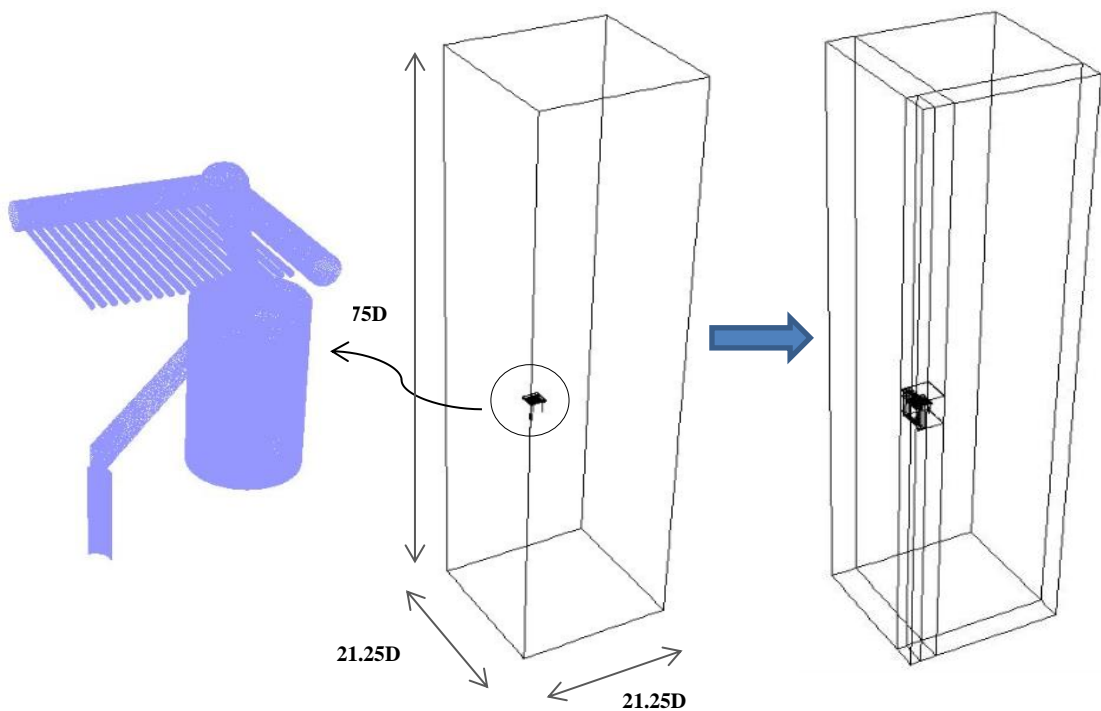
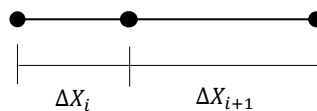


Figure 5.3-2 Showing quarter model of subsea protective structure, simulation domain and discretized domain

5.3.2 Meshing

The meshing process was the next step after creating the model, and decomposing the domain, if necessary. The mesh method in this case was dependent on the model complexity and the nature of the problem, for example, moving boundaries were required to simulate the heave motion of the structure, therefore, an unstructured mesh with tetrahedral cells was applied. Choosing an appropriate mesh type would depend on the nature of the problem and the geometry. Estimating the hydrodynamic coefficients for a stationary structure in a fluid might require a hexahedral mesh (structured mesh) for both simple and complex geometries, but on the other hand, tetrahedral meshes (unstructured mesh) are much better compared to hexahedral meshes because they fit better in complex geometries. The meshing process in this thesis can be applied to other simple and complicated geometries. The process involved the creation of the final volume mesh made up of tetrahedral cells. Since the domain was split into subdomains, creating the mesh for the subdomains farther away from the structure was quite straightforward (direct meshing of the volumes). This was not the case for the subdomains that had parts of the geometry within them because the mesh had to be controlled in this case, a fine grid had to be created and the cell sizes had to change gradually which was defined by a growth rate. It is recommended that the maximum change in the grid spacing between two neighbouring cells should be less than 20% (ANSYS 17.0, 2016).

That is



$$\frac{\Delta X_{i+1}}{\Delta X_i} \leq 1.2$$

Equation 5.3-1

The growth rate in this case was kept at 1.05 because a higher rate would have compromised the quality of the final volume mesh which resulted in a skewness of over 0.85.

After achieving the final mesh, its quality should be checked. If the quality is below the acceptable value as explained in Section 4.3.2, mesh refinement should be carried out. Refinement is carried out in order to obtain an acceptable mesh quality and to investigate the dependence of the solution or results on the mesh size.

There are two refinement options available in CFD, manual and automatic. In the latter, there is an option to locally refine the mesh by selecting nodes, lines, or elements, or the option of globally refining the mesh by selecting all elements.

Simple geometries can benefit from global refinement, like the case of the suction-can which is not the case for complicated geometries such as the subsea protective structure. Local mesh refinement by manually adjusting the mesh in regions of poor quality was conducted because global refinement was not adequate since the mesh needed to be refined in areas of interest or areas that were considered would improve the overall mesh quality.

Normally, mesh refinement is conducted after producing the first domain mesh which would be coarse. Refinement should be carried out until there is no significant difference between the results of the current mesh and the previous mesh or previous meshes.

As stated in the mesh sensitivity study (Section 4.3.3), there may be instances where it is impossible to create the volume mesh due to either a too coarse or too dense grid. This means there is an extent to which mesh refinement will no longer be acceptable in the refinement process.

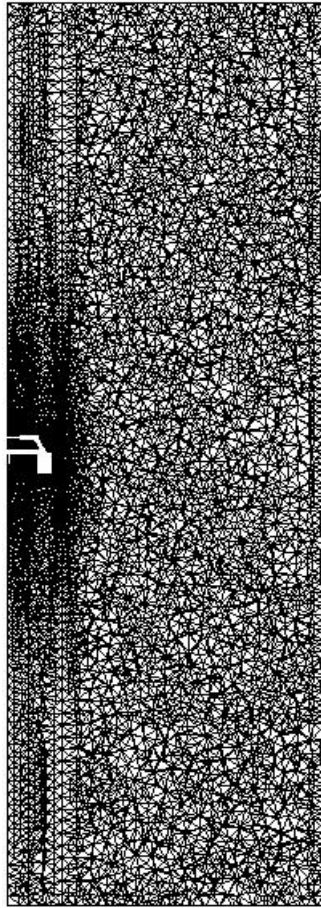


Figure 5.3-3 Mesh of subsea protective structure far from boundaries

5.3.3 Challenges and Difficulties in the Numerical Modelling

The numerical modelling consisted of the modelling and the numerical method. The physical representation of the model considered if it was appropriate to estimate the hydrodynamic coefficients of each component member or the whole geometry. The latter was considered to be more appropriate because of interaction effect from structural members. Therefore, in order to reduce the computational time of the CFD simulation, symmetry was applied and a challenge faced but not related to the modelling software, although it had a significant impact on the calculated properties of the structure, was the simplification of the original geometry. Although it is advantageous in cutting down on simulation time due to the ease of the Fluent programme in calculating the nonlinear equations, on the other hand over-simplification could lead to inaccurate estimation of the properties of the structure, and

will result in the inaccurate response of the structure in the installation analysis. In this case, insignificant parts or members of the structure were eliminated, especially parts or members that were shielded by other members.

It was observed in the end, after producing the volume mesh that the difficulties encountered favoured the meshing process because: based on the knowledge of the software, a proper plan on how to create the geometry and the mesh was set out before the start of the model development; the software granted full control of the meshing process, which meant the mesh quality was improved manually through the bottom-to-top approach, by meshing the lines, then the faces and then the volume, which makes it possible to concentrate more cells at corner points or wall boundaries, and it was fully compatible with Fluent because there were no issues when the mesh was exported and imported to and from Fluent.

A difficulty was the discretization of the domain to fit the meshing strategy. The fluid domain was continually discretized into smaller volumes until the final volume mesh was achieved, and as a result of a very low t/D ratio, thickness to diameter of outer bucket (0.0063), the recommended volume mesh quality was difficult to achieve.

The dynamic mesh setup which is different from a steady flow problem with predefined velocity could lead to divergence of the solution due to a moving boundary.

The calculation times for running the model was too long even with the application of symmetry and simplifying the geometry.

5.4 Boundary Conditions and Exporting the Mesh

Appropriate boundary conditions should be assigned to the domain after meshing. The flow characteristics determine what boundary condition is needed for each face while for external flows, the wall boundary condition is most times assigned to the geometry.

The boundary selection was carried out after the mesh process. Due to the discretization of the volume, an interior boundary was assigned to the internal faces produced. This selection was made based on the interior faces located in the fluid area and not having any function or effect on the fluid particle motion. Other boundaries,

such as the wall and symmetry boundaries were selected based on the selection of Chapter 4. This was done for both conditions (structure far from boundaries and close to seabed). The number of cells produced in both conditions is reported in Table 5.4-1.

Table 5.4-1 Number of cells produced away from surface and seabed, and close to seabed condition

Condition	Number of tetrahedral cells
Away From Surface and Seabed	6746481
Close to Seabed (h/D = 0.40)	6947764
Close to Seabed (h/D = 0.20)	7006107

The number of cells of the volume mesh for both cases of the seabed proximity condition was higher than that of the far from boundaries condition because more cells were needed in the region between the base of the structure and the seabed in order to obtain an overall good quality volume mesh. The number of cells required increased with a reduction in the water depth ratio. Figure 5.4-1 is an illustration of the seabed proximity condition.

The next step would be to define the zones. For the fully submerged subsea structure in this case, oscillating in a fluid, a single zone was applied which was defined as “fluid”, known to be “water-liquid”. Other external flow problems might require the definition of two or more zones depending on the model.

The 3D mesh is now ready to be exported to Fluent from Gambit after creation. For other CFD software and new versions of Ansys Fluent, modelling, meshing, solution setup, etc are all done in the same graphical user interface, GUI.

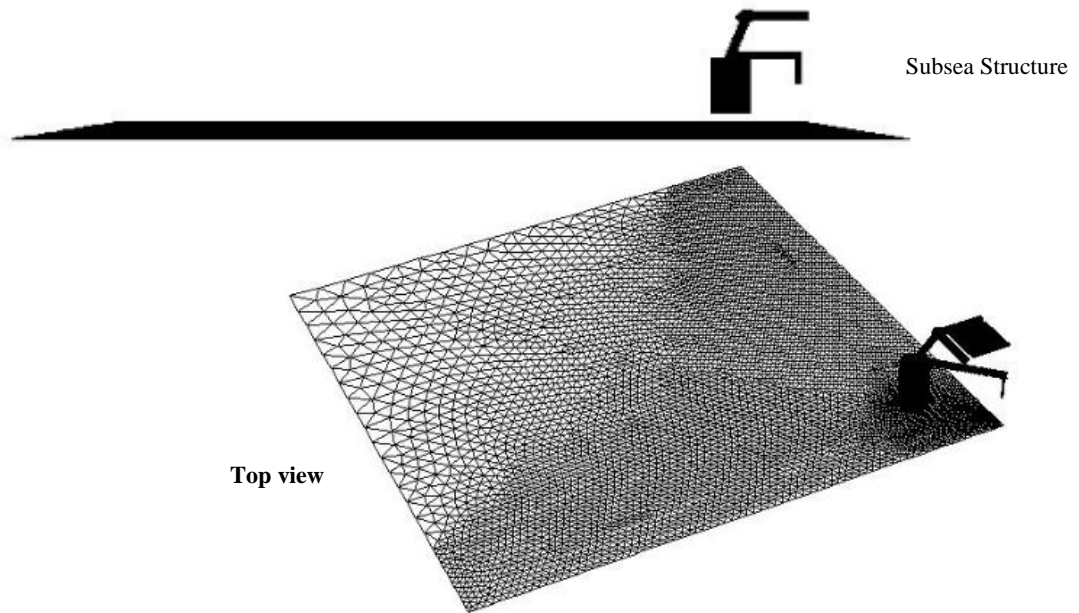


Figure 5.4-1 Views of subsea structure and seabed for seabed proximity condition

5.5 Turbulence Model Selection

Selecting an appropriate turbulence model for CFD analysis is quite difficult because each case might differ, therefore it depends on the need to reduce cost and computational time. As applied in this thesis, choosing the right turbulence model for the external flow problem was dependent on, an understanding of the fluid interaction with the structure, and running a turbulence model sensitivity study to verify that the result or results are in line with experimental data.

If the turbulence model results match with experimental data related to the specific case, the same model can then be applied to other geometries.

For cases related to a suction can and subsea protective structure, the k- ω SST turbulence model can be applied.

5.6 Time Step, Courant Number and Maximum Iterations

The influence of time step size on the hydrodynamic coefficients should be investigated. An initial selection should be based on engineering judgement or on previously conducted numerical analysis. A selection should be based on comparison

of results of several time step sizes with experimental data. An appropriate time step size can also be obtained from the Courant number. This is not always the case because there is no restriction on the time step ($CFL < 1$) if the implicit time discretization is applied instead of the explicit scheme which puts a restriction on the time step size. Equation 5.6-1 is an expression for the Courant number (Courant, et al., 1928).

The pressure-based solver, which is an implicit solver, should be applied to problems that require the estimation of hydrodynamic coefficients of subsea structures because of no CFL restrictions which allows for results comparison with experimental data from a time step sensitivity study.

Pressure based solvers are for incompressible flows while density-based solvers are recommended for compressible flows.

$$CFL = U \frac{dt}{dx} < 1$$

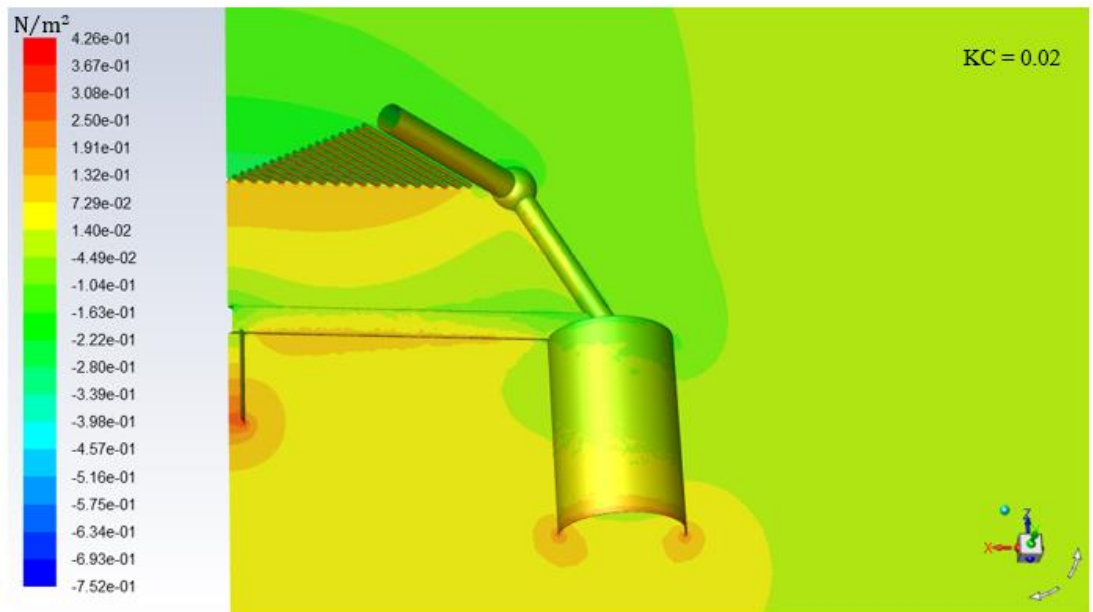
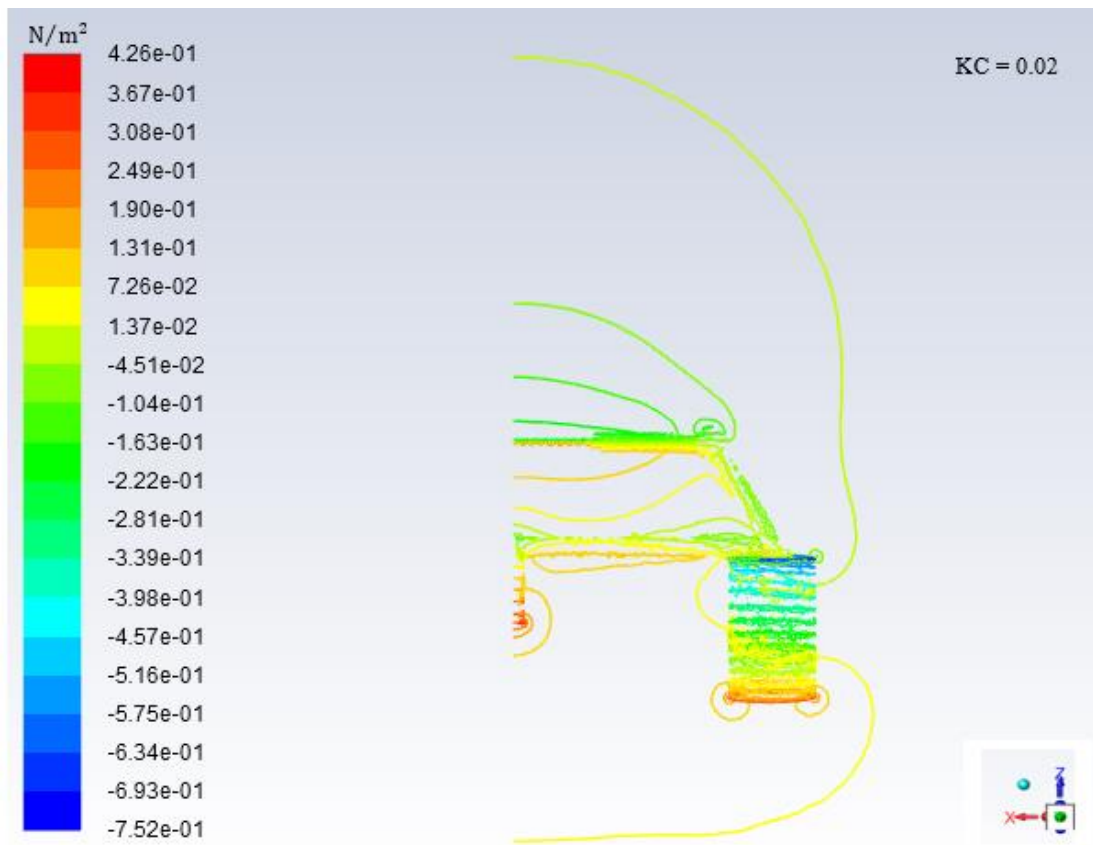
Equation 5.6-1

where, U is the magnitude of velocity, dt is the time step and dx is the length between two neighbouring mesh elements.

For maximum iteration, a sensitivity study would be ideal in order to see its effect on the results.

5.7 CFD Analyses Results

The added mass and damping coefficients of the subsea protective structure are presented in this section. The equivalent diameter of the structure used in calculating KC was 13 m, which is the distance from the outer edge of the outer bucket to the centre of the central bucket. The KC number is dependent on the amplitude of motion of the structure and defines the value of the hydrodynamic coefficients.



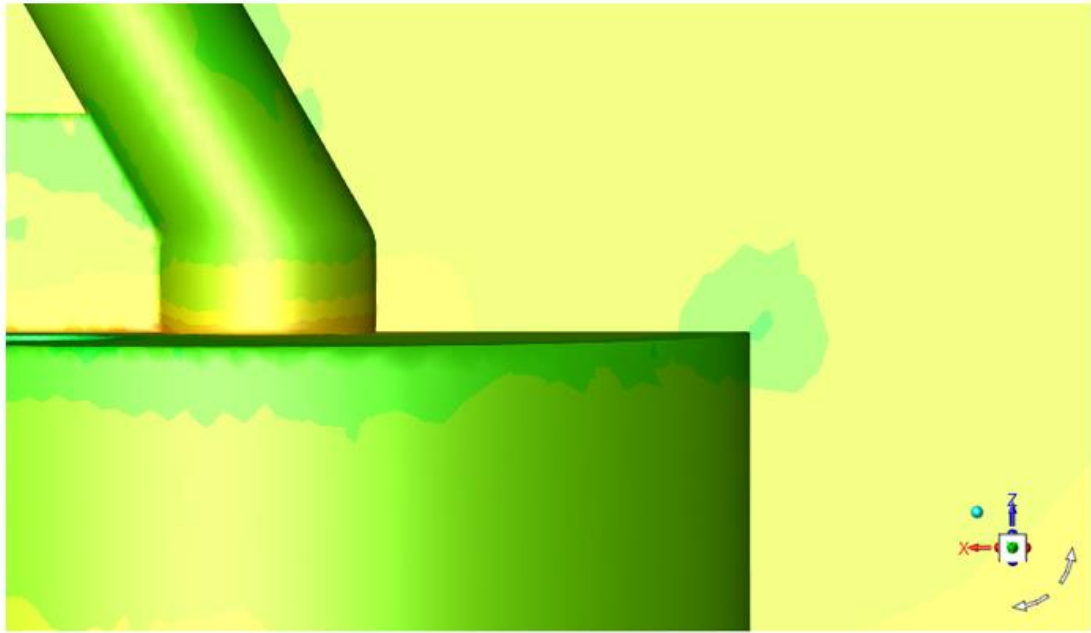
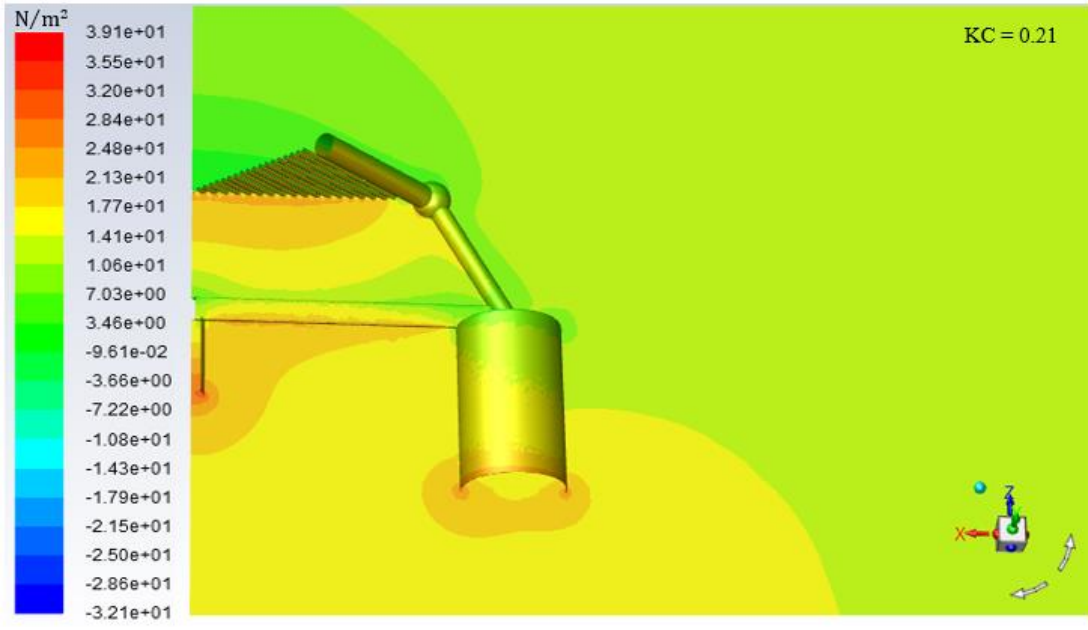
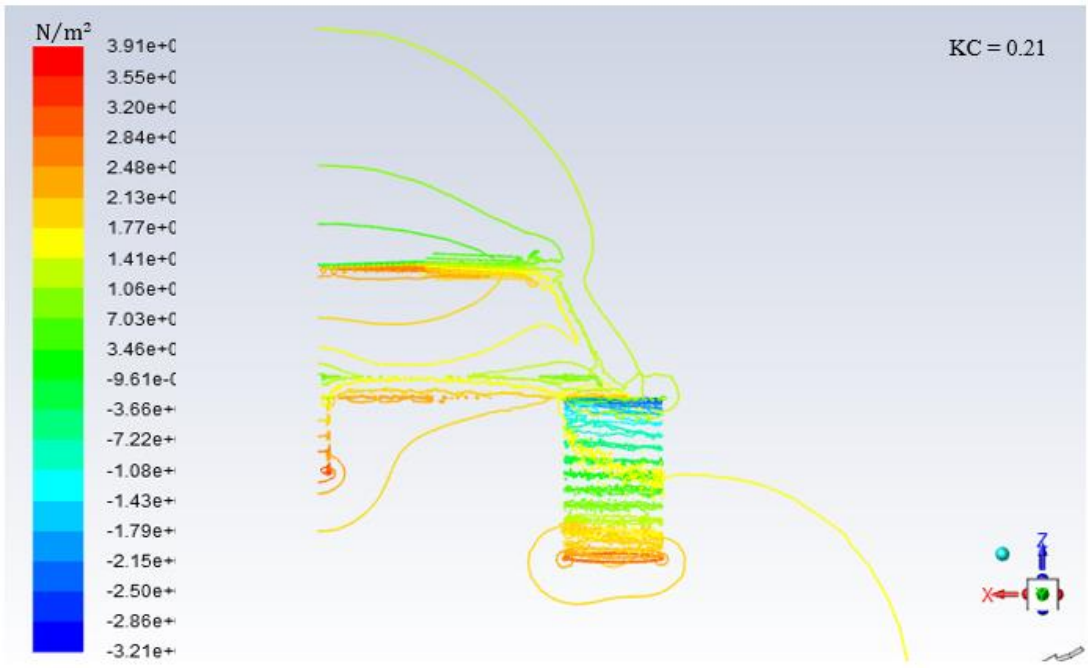


Figure 5.7-1 Pressure contour of subsea protective structure far from boundaries at KC 0.02

The vortices shed at the bottom edge of the outer bucket as shown in Figure 5.7-1 are detached. There is no interaction between vortices at KC 0.02. At KC 0.02 the vortices convect through a short distance and gradually diffuse away. Same condition applies to vortices shed at the bottom edge of the central bucket. There was no interaction with closest structural member, the H-beam. Due to the descent of the structure, there is a small vortex generated at the top edge of the outer bucket, as a result of low KC.



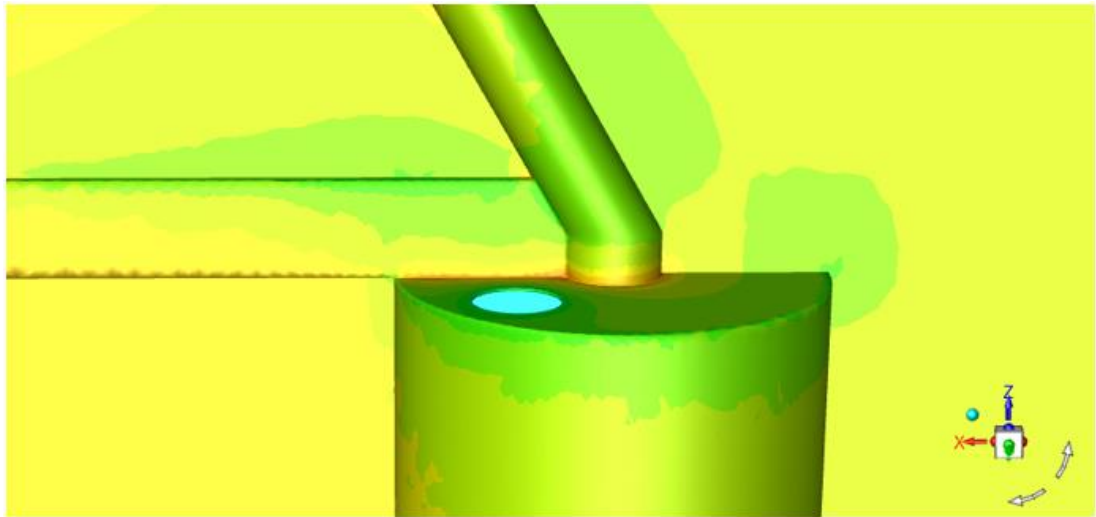


Figure 5.7-2 Pressure contour of subsea protective structure far from boundaries at KC 0.21

As KC increases, the velocity of the structure increases, with increasing curled fluid motion at the bottom edge of the outer bucket which increases the dynamic pressure at the edge of the bucket. Figure 5.7-2 shows the subsea protective structure at KC 0.21. The hydrodynamic force in this case is increased compared to the force at KC 0.02. Before the vortices shed at the bottom edge of the outer bucket diffuse away, they convect through a greater distance as compared to the case of KC 0.02. At KC 0.21, the vortices shed eventually interact, and the vortex formed at the top edge of the bucket is seen to have an increased formation when compared to KC 0.02.

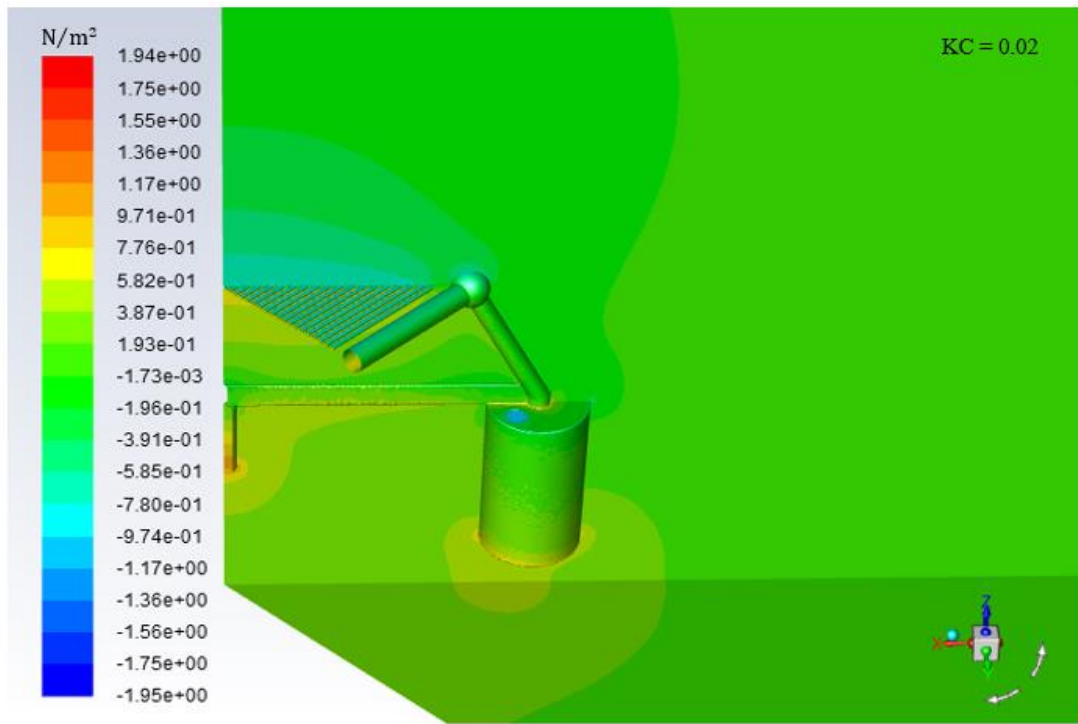


Figure 5.7-3 Pressure contour of subsea protective structure at $h/D = 0.4$, $KC = 0.02$

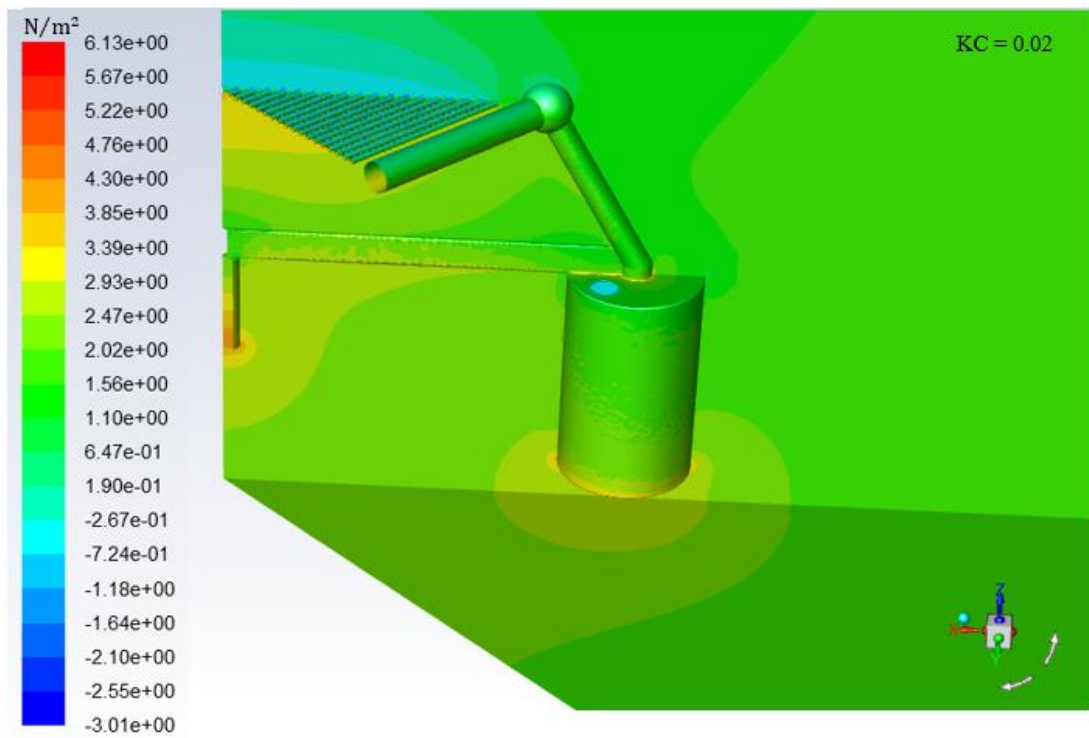


Figure 5.7-4 Pressure contour of subsea protective structure at $h/D = 0.2$, $KC = 0.02$

At low KC, KC 0.02, for both $h/D = 0.4$ and 0.2 , the vortices formed at the bottom edge of the outer bucket interact. This is as a result of the bottom edge's closeness to the seabed. The particles of the flow from the structure move a short distance before touching the seabed.

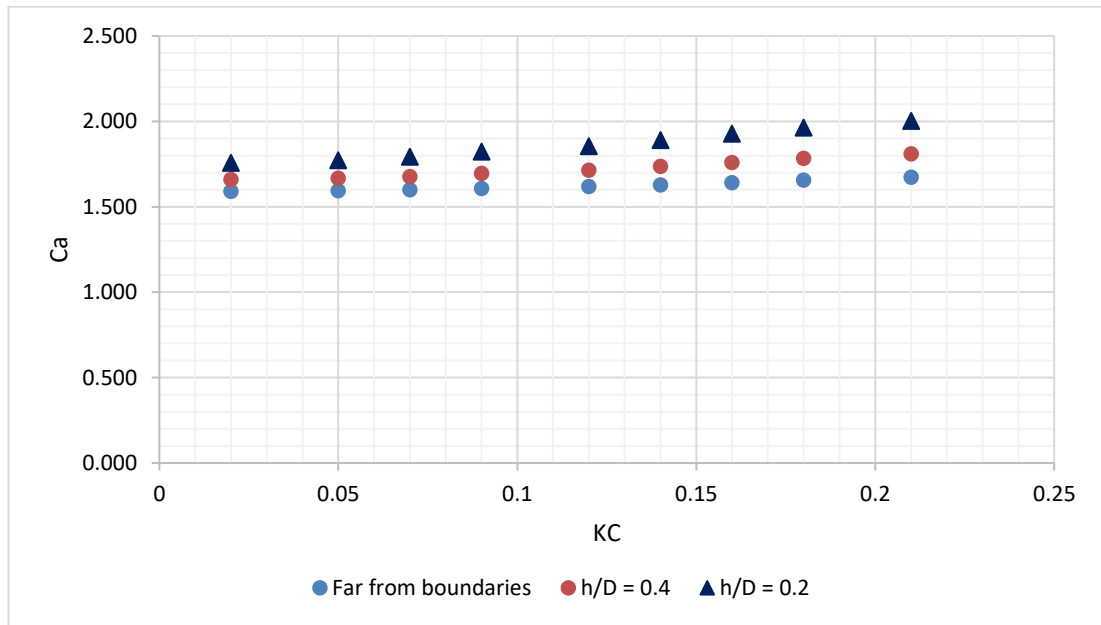


Figure 5.7-5 Added mass coefficient of subsea protective structure far from boundaries and close to seabed

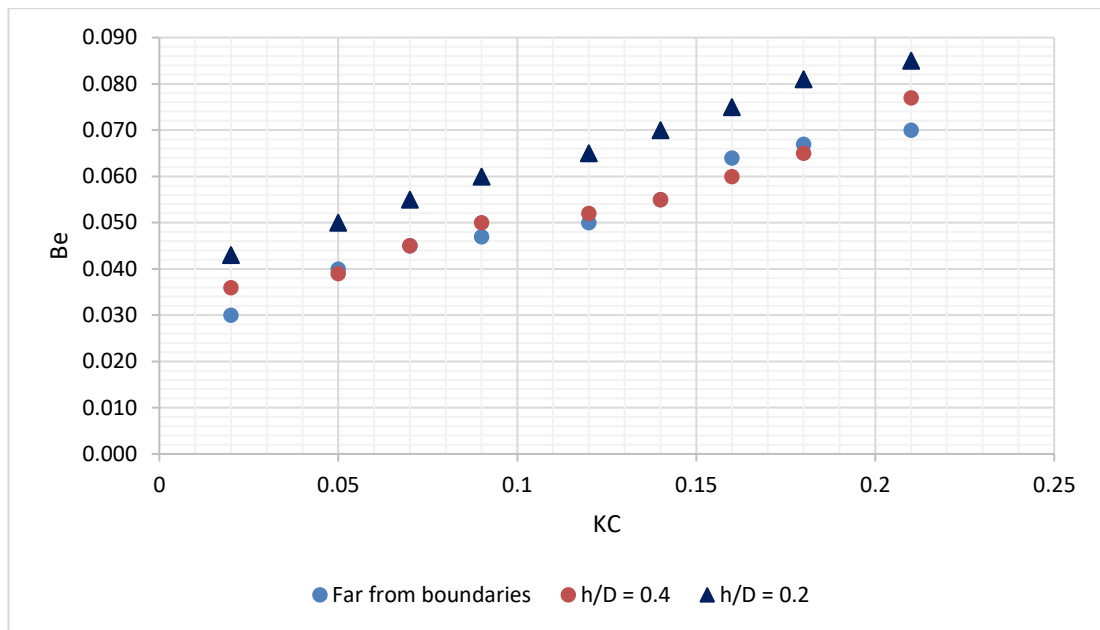


Figure 5.7-6 Equivalent linearized damping of subsea protective structure far from boundaries and close to seabed

Figures 5.7-5 and 5.7-6 show the influence of KC on the heave added mass coefficient and the equivalent linearized damping ratio respectively of the subsea structure far from boundaries and at various heights above the seabed. There was a gradual increase in the added mass coefficients for all water depth ratios as the Keulegan Carpenter number increased as a result of increase in the motion amplitude. The trace of the added mass coefficients for the far-from-boundaries condition showed a slightly linear trend between KC 0.02 and 0.21 (Figure 5.7-5), while this linear trend was not that pronounced in the other two conditions, $h/D = 0.4$ and 0.2 . The equivalent linearized damping also increased with an increase in the Keulegan Carpenter number for all conditions. The equivalent linearized damping values of the structure well away from surface and seabed, when compared with those of water depth ratio 0.4 were almost indistinguishable from each other. This was attributed to reduced influence of the seafloor's presence on the motion of the fluid particles in the region between the structure and the seabed. This influence increases with a reduction in the water depth ratio. See Figure 5.7-6, which shows the equivalent linearized damping of the structure at $h/D = 0.2$ increasing with an increase in KC.

In the case of the suction-can and subsea protective structure, the KC number was used to estimate the damping ratio, although it is not the only relevant parameter that could be applied to do so, since there are other parameters such as the drag coefficients, which can be applied in the formula $\xi_{33} = \frac{2}{3\pi} \frac{\rho D^2}{(m_s + m_{a33})} \frac{\eta_{33}}{D} C_d$ (Kaneko, et al., 2014) and also the Borgman drag linearization. The drag coefficient is estimated from the Reynolds number which is dependent on the diameter of the structure.

Table 5.7-1 Equivalent linearized damping ratio of subsea protective structure

KC	Equivalent Linearized Damping Ratio, Be		
	Far from boundaries	h/D = 0.4	h/D = 0.2
0.02	0.03	0.036	0.043
0.05	0.04	0.039	0.05
0.07	0.045	0.045	0.055
0.09	0.047	0.05	0.06
0.12	0.05	0.052	0.065
0.14	0.055	0.055	0.07
0.16	0.064	0.06	0.075
0.18	0.067	0.065	0.081
0.21	0.07	0.077	0.085

5.8 Chapter Summary

This chapter presented the application of the Fluent simulation method in calculating the hydrodynamic coefficients of the subsea protective structure, and it was observed from results that the vertical added mass and damping ratios far from boundaries and in close proximity to seabed increased as KC increased. The Ca results for all h/D ratios considered were quite close (see Figure 5.7-4), because the seabed influence affected only the outer-bucket due to its closeness to the seabed.

From numerical flow visualization of the subsea protective structure, it can be seen that at high KC, the particles of flow of each component member of the structure interact with neighbouring members. This justifies the importance of visualizing the flow which can also serve as a means of validation of the CFD analysis.

6 Case Study: Installation Analysis Using the Hydrodynamic Coefficients

6.1 Introduction

This chapter discusses the installation analysis of the subsea protective structure using the hydrodynamic coefficients obtained from the approximate method and CFD analysis. The heave response of the subsea protective structure and line tension are derived using Orcaflex. The objective is to show the effect of the added mass and damping derived from both methods on the heave response and line tension using steel wire rope as the lowering line. The analysis method requires the top end excitation (amplitude of motion) at the crane tip of the installation vessel, the vessel motions in the form of RAOs at the crane tip, and the environmental conditions such as the design wave height and period which are specified with a selected vessel heading. These parameters can be obtained from a particular seastate. For the Orcaflex analysis, other parameters listed below would be determined, and are useful for determining the dynamic amplification factor (DAF). The dynamic amplification factor expression of Equation 6.1-1 from DNV-RP-H103 is used in determining the occurrence of snap loading.

$$DAF = \frac{T_{static} + T_{max}}{T_{static}} \quad \text{line tension DAF}$$

Equation 6.1-1

where, T_{static} is the static tension which represents the structure's weight in water and is given by $T_{static} = (M_s - \rho \nabla)g$, M_s is the structure's mass in air, ρ is the density of water, ∇ is the structure's displaced volume and g is the acceleration due to gravity. T_{max} is maximum component of the dynamic tension and $T_{static} + T_{max}$ is the maximum total line tension.

$$DAF = \frac{Z_{static} + Z_{max}}{Z_{ct}} \quad \text{motion DAF}$$

where, $Z_{static} + Z_{max}$ is the maximum total vertical motion, Z_{static} is the static displacement of the structure from its equilibrium position, Z_{max} is the maximum component of the dynamic motion and Z_{ct} is the corresponding maximum displacement of the crane tip which is the top end of the lowering line.

The dynamic amplification factor for either the line tension or the structure's motion should be less than 2.0 if snap loading is to be avoided.

6.2 Comparison between Hydrodynamic Coefficients of CFD Analysis and Approximate Method

The comparison between the CFD analysis and the approximate method for calculating the vertical added mass and damping of the subsea protective structure is presented. The approximate method will only consider the suction-can in the case of the subsea protective structure, while other known formulas from existing literature will be applied to calculate the coefficients for the other members of the complicated structure.

The subsea protective structure is made up of six types of members: Outer Bucket, Central Bucket, H-Beam, Horizontal Beam, Hatch Beam and an Inclined Beam. Due to shielding of the Inclined Beam by the Outer Bucket, calculating the added mass for the Inclined Beam was ignored.

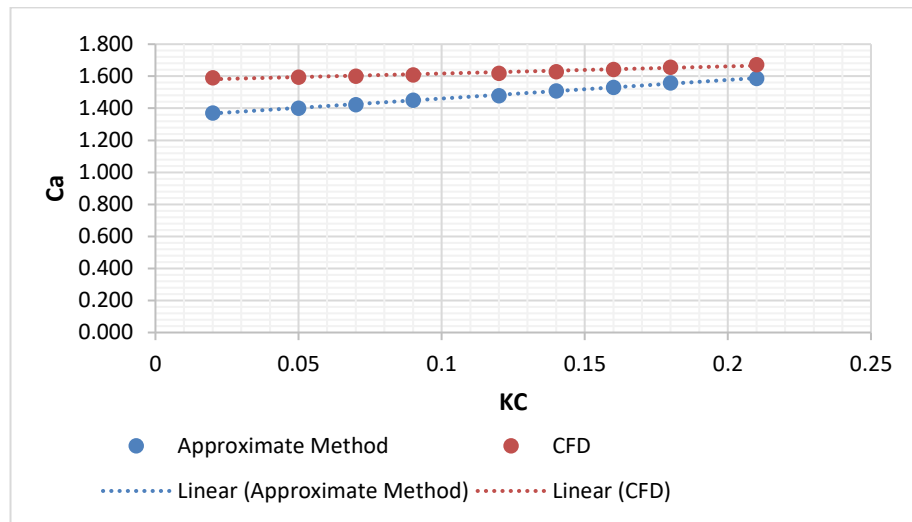
When the structure is well away from the surface and the seabed, the approximate method will be applied to both the Outer Bucket and Central Bucket. For the other three members (H-Beam, Horizontal Beam and Hatch Beam), their added mass coefficients would be 1.0 due to the fact that their L/r ratio was infinite (stated in DNV-RP-H103), where, L is the length of the horizontal cylinder and r is its radius.

For $h/D = 0.4$, the added mass coefficients for all members would be 1.0 since the distance of the closest member's (Outer Bucket) bottom to the seabed was greater than the radius of the outer bucket.

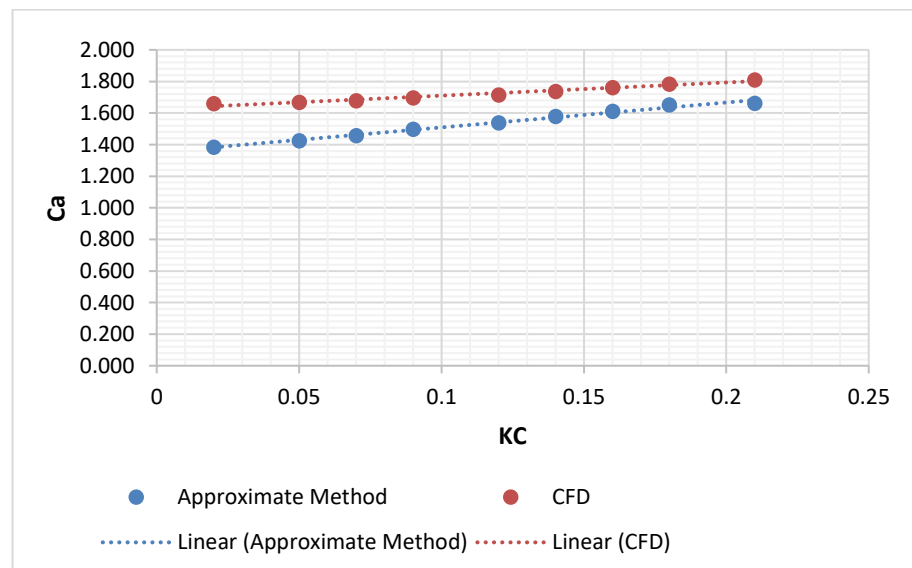
For $h/D = 0.2$, the added mass coefficients were 1.0 for all members except for the Outer Bucket since the seabed clearance was less than the radius Bucket.

Figures 6.2-1(a – c) and 6.2-2 (a – c) show the comparison between the added mass and damping coefficients of the approximate method and CFD analysis of the subsea protective structure respectively for KC 0.02 – 0.21.

a) Far from boundaries



b) $h/D = 0.4$



c) $h/D = 0.2$

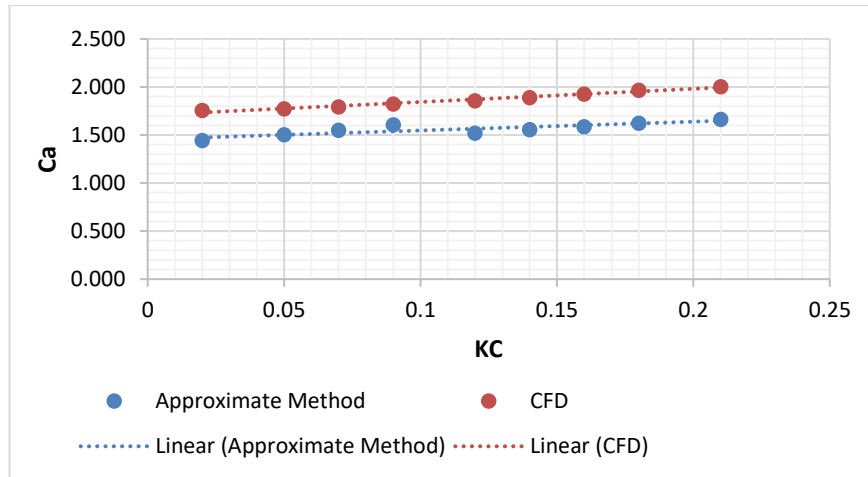
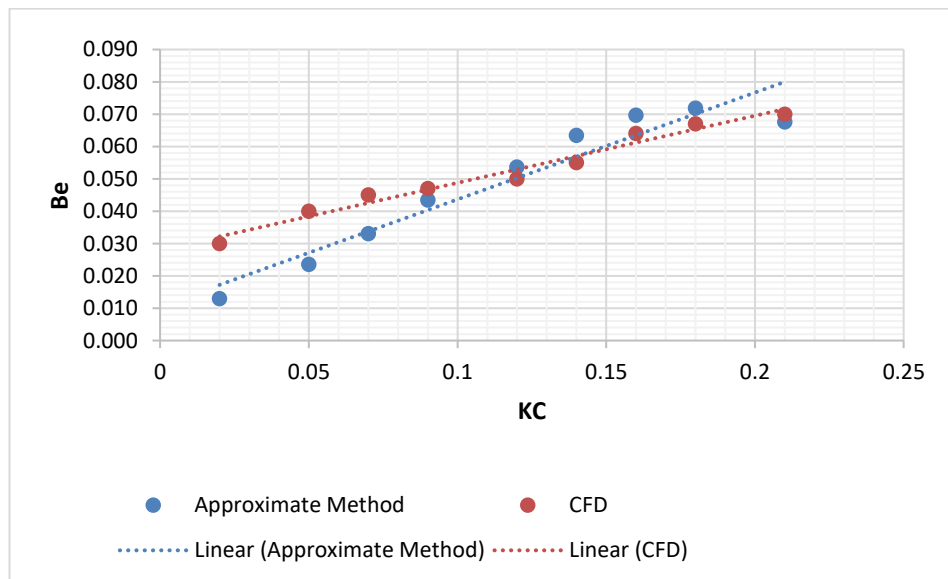
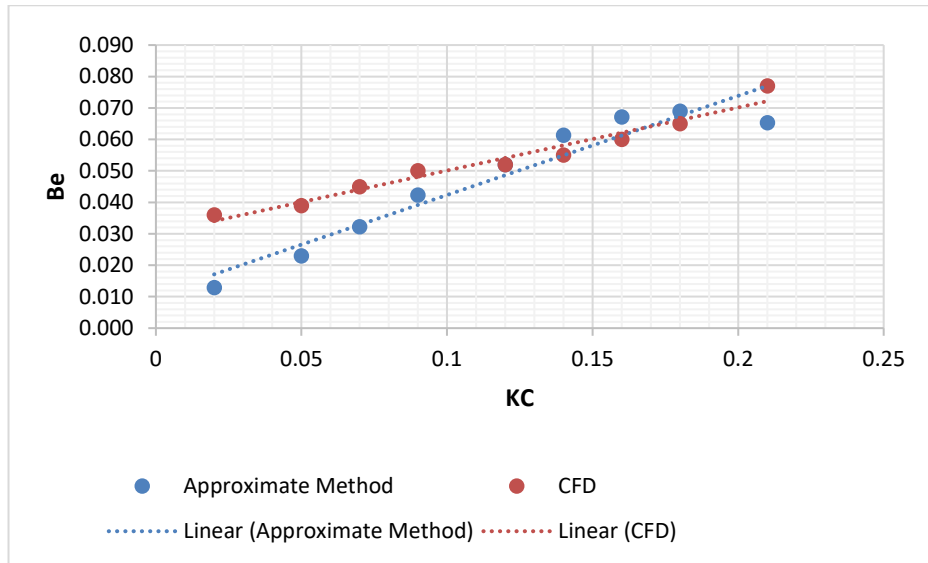


Figure 6.2-1(a – c) Added mass coefficient of subsea protective structure at different heights above seabed

a) Far from boundaries



b) $h/D = 0.4$



c) $h/D = 0.2$

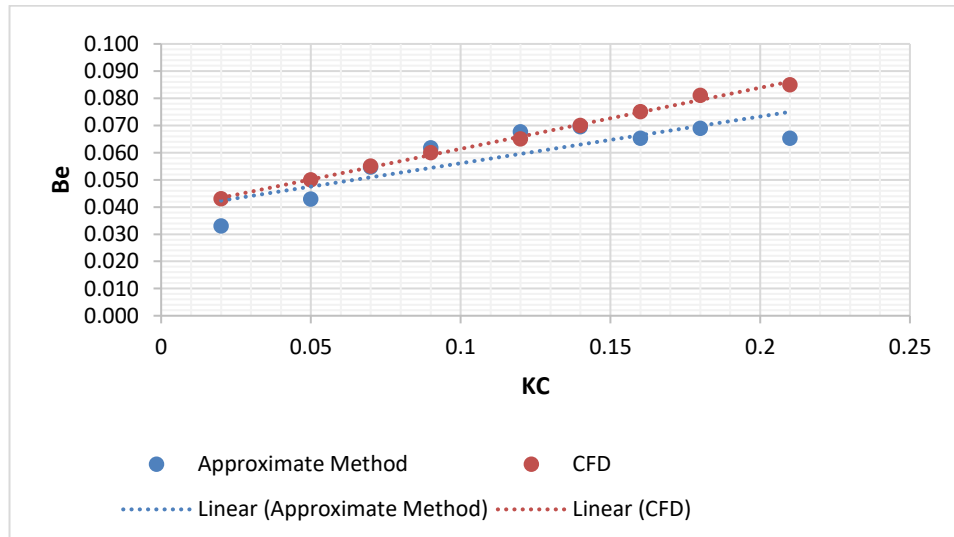


Figure 6.2-2 Damping ratio of subsea protective structure at different heights above seabed

The results show increasing added mass and damping as KC increases for all h/D ratios. The estimated added mass coefficients of the CFD analyses were higher than results obtained using the approximate method because of interaction of particles of the flow with structural members. The CFD analysis took into consideration the opening at the top of the outer-bucket while the approximate method considered the top as fully closed. Results of added mass coefficient obtained using CFD for the

different h/D ratios considered were still higher than results obtained from the approximate method regardless of the opening at the top of the outer-bucket, which was meant to reduce the added mass due to the open hatch but in this case it did not because of the presence of other structural members. Roe et al. (2008) reported the reduction in added mass due to opening at the top of the suction-can (outer-bucket).

From the figures (Figure 6.2-1) representing the added mass coefficient, it was observed that the added mass coefficient in all cases showed less dependency on KC while the damping ratios for the different h/D and KC considered (Figure 6.2-2), showed a higher dependency on KC . Figures 6.2-2(a), (b) and (c) show a point of intersection between the data of the approximate method and CFD analysis, which occurs between KC 0.1 and 0.15 for (a) and (b), and between KC 0.5 and 0.15 for (c). There is a gradual increase of the damping ratios of the CFD results from these points of intersection which might have resulted from the increase in particle interaction with the seabed as a result of increased velocity of the oscillating subsea protective structure. Particles of the flow from the structural members with bottoms very close to the seabed such as the central and outer buckets, where the entrapped fluid within them is pushed out through the bottom of the buckets during descent.

6.3 Installation Analysis of Subsea Protective Structure

Installation analysis of the subsea protective structure using the hydrodynamic coefficients derived from CFD analysis and the approximate method will be carried out with the finite element programme, Orcaflex which allows for static and dynamic analysis. Carrying out installation analysis using Orcaflex involves knowing beforehand the hydrodynamic properties of the subsea protective structure, the vessel characteristics, the properties of the lowering line such as its size, material type, etc, and the environment where the structure would be installed.

6.4 Modelling the Subsea Protective Structure in Orcaflex

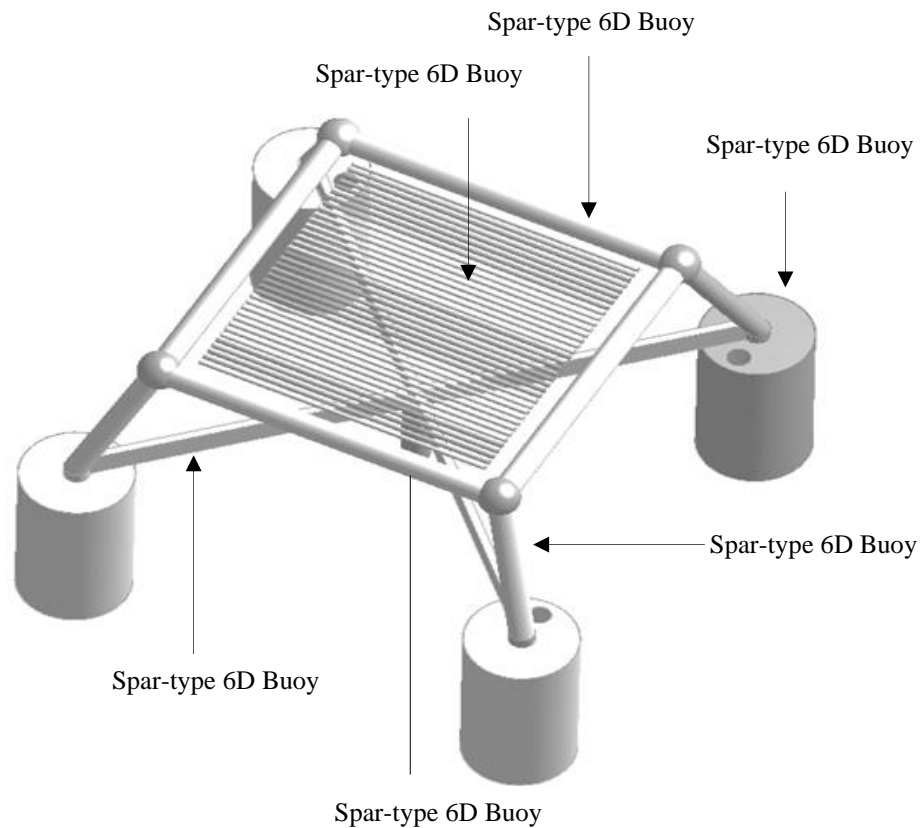


Figure 6.4-1 Subsea protective structure

The decision to model each component member of the subsea protective structure was made over representing the entire structure as a single buoy since accuracy was of the essence. A fast approach would be to represent the entire structure as a buoy since the structure was fully submerged in water (Orcina, 2019). In this case, each component member was modelled with a *spar-type 6D buoy* because it was suitable for modelling cylindrical structures, and structural members with little or no influence on the hydrodynamic performance of the structure were modelled as *new shapes*.

A master object, *master buoy* with dimensions: 16.97m by 16.97m by 11.93m was used to enclose the structure. Component members of the structure were connected to the *master buoy* and some results such as static deflection and dynamic motion of the

structure were read from the *master buoy* since it served as a reference object. The actual OrcaFlex model of the structure is shown in Figure 6.4-2.

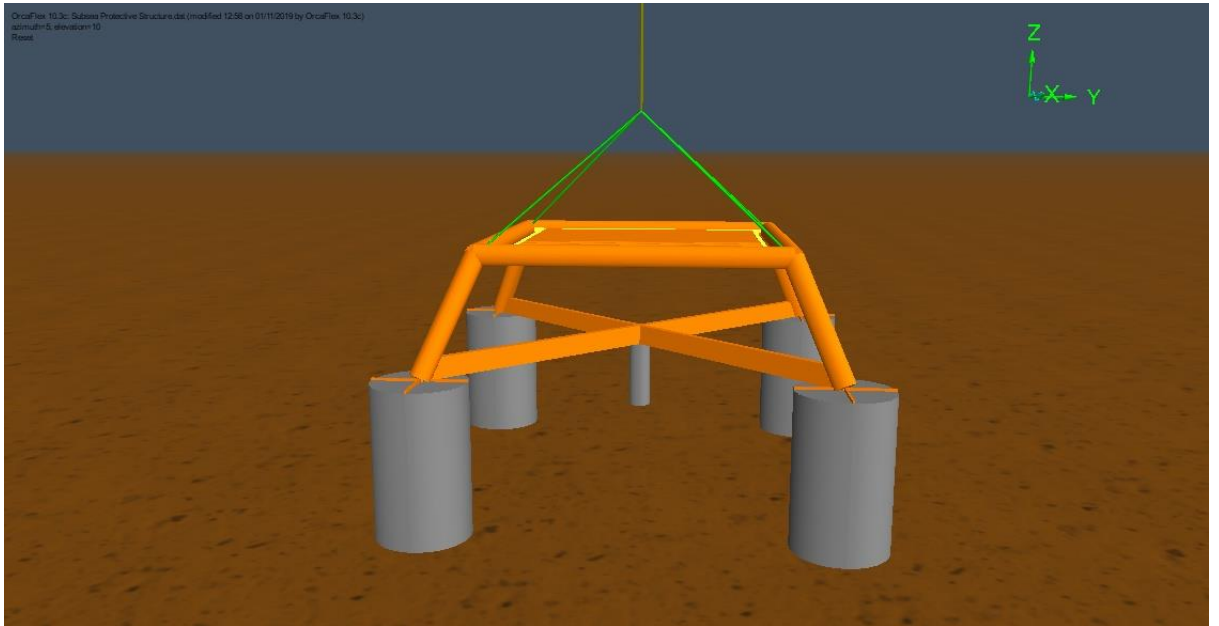


Figure 6.4-2 OrcaFlex model of subsea protective structure

6.5 Size of Lowering Line

The size of the lowering line was determined based on safe working load which was initially chosen by multiplying the weight of the subsea structure, W_s by a safety factor of 3.5. The rope size selection based on this method could be a useful starting point, but in practice the rope selection will probably need to be updated on the basis of the analysis results. The weight of the subsea structure in this case was the minimum breaking load of the lowering line. The line diameter which corresponds to the derived safe working load can be selected using a rope catalogue. In this case the OrcaFlex line wizard was used to select the line size by gradually adjusting the rope diameter until the minimum breaking load ($MBL = W_s \times SF$) was attained. SF is the factor of safety and W_s , is the weight of the subsea structure. The rope size (diameter) varies for the same MBS of each rope manufacturer. An increase in the factor of safety would lower the response of the subsea structure because it increases the required rope size

at a specific water depth. The required parameters for the installation analysis are shown in Table 6.5-1.

Table 6.5-1 Input parameters for numerical analysis

Model	Value
Lowering Line	
Type	6 by 19 wire with wire core
Modulus of elasticity (N/m ²)	0.85E11
Diameter (m)	0.18 (nominal)
Cross sectional area (m ²)	0.016
Weight in air (te/m)	0.129
Weight in water (te/m)	0.113
Minimum Breaking Load (te)	2092.540 (20.521E3kN)
Subsea Protective Structure	
Density of water (kg/m ³)	1,025
Density of steel (kg/m ³)	7,850
Mass in air (kg)	629,294
Mass displacement (kg)	82,169.011
Submerged mass of structure (kg)	547,124.989
Volume (m ³)	80.164
Projected area (z) (m ²)	171.52
Installation vessel	
Length (m)	103
Mass (te)	9017.95

6.5.1 Lowering Line Stiffness

The line stiffness can affect the calculated response of the structure. This can be beneficial to installation engineers if other low-weight line materials such as fibre ropes are selected for installation. Fibre ropes have a lower stiffness than steel ropes.

The sizes of both lines can be fixed for comparison. Based on the rope catalogues for the two types of line, the rope sizes associated with the same minimum breaking strength were different. Refer to the wire rope hand book of Usha Martin (Usha Martin, 2014) for steel rope and the product catalogue of Hendrik Veder Group (Hendrik Veder, 2013) for fibre rope.

It would be unrealistic to fix the sizes of both line types because a 0.18 m diameter fibre rope would have a minimum breaking load, MBL of 5523.12KN (536.20te), which is close to the submerged weight of the protective structure (5367.29KN) and less than the safe working load, SWL of 18.77E3KN using a factor of safety of 3.5. Therefore, the size of the line (fibre rope) was increased and its properties are presented in Table 6.5-2.

Table 6.5-2 Fibre rope properties

Parameter	Value
Rope type	Polyester (8-strand Multiplait)
Rope nominal diameter (m)	0.34
Minimum Breaking Load (KN)	19.71E3 (2009.45te)
Axial stiffness (KN)	126E3
Weight in air (te/m)	0.09223 (0.90442KN/m)
Displacement (te/m)	0.06883 (0.67498KN/m)
Weight in water (te/m)	0.0234 (0.22945KN/m)

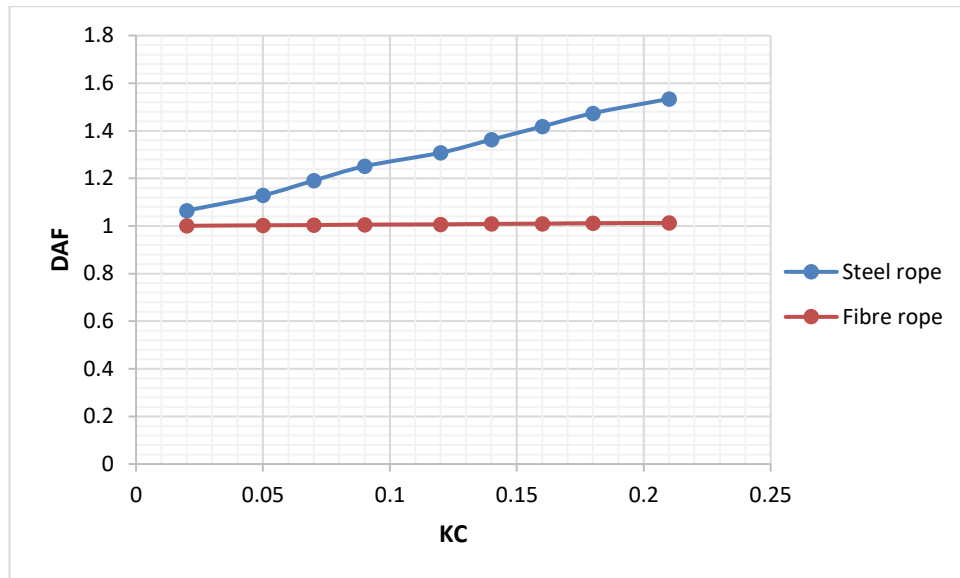


Figure 6.5-1 Comparison between DAF (Tmax/WT) of steel and fibre rope

For the same minimum breaking strength of steel and fibre rope when compared in the rope catalogue, the rope diameter for steel was lesser than that of fibre rope. This is because steel ropes have higher modulus but weigh more than fibre rope in water. Figure 6.5-1 compares the performance of steel and fibre ropes when subjected to the same conditions.

Since the KC considered (0.02 – 0.21) contributed to the increase in the calculated response of the subsea protective structure as it responded to the motion at the crane tip. Further studies beyond this range of values should be considered to see if there would be a change in the trend.

6.6 Time Step Sensitivity

A time step sensitivity study was carried out in order to observe if there were significant changes in the results. The numerical analysis was run at several time step sizes in order to observe the effect on the results. A time step size of 0.1 seconds was selected for further analysis. The selection was based on the convergence of the results of the dynamic tension and the slight difference in the results of the crane tip motions at the various time step sizes (See Table 6.6-1).

Table 6.6-1 Maximum effective tension in lowering line, crane tip and subsea structure motion at various time steps

Wave direction (deg) = 0.00 $H_s = 4\text{m}$ $T_z = 6\text{s}$ Pierson-Moskowitz Spectrum Static $T_{eff} = 5365.8667\text{KN}$						
Time step size (secs)	0.001	0.005	0.01	0.05	0.1	0.2
Crane tip motion (m)	5.3831	5.7276	5.7275	5.7274	5.7273	5.7219
Dynamic motion of subsea structure, Z_{dyn} (m)	7.2665	7.0245	7.0242	7.0162	6.9989	6.9595
Maximum effective tension, $T_{eff(max)}$ (KN)	10073.8574	10373.5556	10374.1525	10375.8661	10376.141	10359.9758

The response reported in Table 6.6-1 for each time step size was large for installation and not necessarily a realistic installation condition. The time step sensitivity study was carried out for testing purposes.

6.7 Comparison between the implicit and explicit integration scheme

The result of the dynamic tension and motion of the subsea structure obtained from the implicit integration scheme was compared with result obtained from the explicit scheme in order to be certain that there was no significant difference between results from the former and those from latter.

Table 6.7-1 Comparison between the implicit and explicit integration scheme

Integration scheme	Maximum effective tension (KN)	Dynamic motion of subsea structure, Z_{dyn} (m)
Implicit	10376.7014	6.9958
Explicit	10366.0339	7.0817

The explicit integration scheme implemented by Orcaflex is the semi-implicit Euler with a constant time step, which at the start of the dynamic analysis the static analysis results such as initial positions and orientations of all objects in the model, including all nodes in all lines, are known. OrcaFlex uses the generalised- α integration scheme for the implicit integration as described by (Chung & Hulbert, 1993). The forces, moments, damping, mass etc. are calculated in the same way as for the explicit scheme. Then the system equation of motion is solved at the end of the time step (Orcina, 2018).

Table 6.7-2 Input parameters for explicit integration scheme

Parameter	Value	Condition
Inner time step (sec)	0.00196	Inner time step should not be greater than $1/10th$ to $1/20th$ of the shortest natural period of motion for any degree of freedom in the model (Orcina, 2019).
Outer time step (sec)	0.0588	Time step should not be more than 30 times the inner time step, and in addition should not be more than $1/40th$ of the wave period (Orcina, 2019).
<p><i>Wave period (s) = 6</i></p> <p><i>Shortest natural period (s) = 0.0196</i></p> <p><i>Inner time step (s) = 0.0196 × 0.1 = 0.00196</i></p> <p><i>Outer time step (s) = 30 × 0.00196 = 0.0588</i></p>		

Table 6.7-3 Influence of lowering line segmentation on dynamic effective tension and motion in lowering line and on subsea structure respectively for various time steps

Wave direction (deg) = 0.00 $H_s = 4$ $T_z = 6$ Pierson-Moskowitz Spectrum Static $T_{eff} = 5365.8667KN$				
Time step (sec)	Target segment length (m)	Number of segments	Maximum effective Tension (KN)	Dynamic motion of Subsea Structure, Z_{dyn} (m)
0.01	50	30	10373.5277	7.0143
	20	75	10374.2983	7.0285
	15	100	10373.7613	7.0166
	10	150	10374.1525	7.0242
	5	300	10377.3487	7.0278
	2	751	10431.8622	7.0605
0.05	50	30	10375.3021	7.0106
	20	75	10376.0725	7.02
	15	100	10375.6283	7.0097
	10	150	10375.8661	7.0162
	5	300	10385.534	7.0209
	2	751	10451.735	7.051
0.1	50	30	10376.6191	7.0049
	20	75	10376.2958	6.9995
	15	100	10376.7014	6.9958
	10	150	10376.141	6.9989
	5	300	10373.1163	7.0085
	2	751	10386.0786	7.0359

Reducing the target segment length or increasing the number of segments of the lowering line resulted in increased simulation time. The sensitivity study was conducted to ensure there was no significant influence on the results at various time steps.

6.8 Installation Acceptance Criteria

DNV-RP-H103 outlines two installation criteria to be considered. These criteria are:

1. The amplitude of the dynamic tension should not exceed the static tension. Slack cable will occur if this happens.
2. The absolute difference between the motion of the subsea structure and the crane tip motion should not be greater than the static stretch of the cable, otherwise slack cable will occur.

6.9 Static Analysis

Static analysis is carried out before dynamic analysis in order to determine the initial equilibrium position of the entire system.

The static stretch of the lowering line was determined from the static analysis. Other results such as the static displacement of the structure, effective tension, etc can also be determined from static analysis. The lowering line was stretched from its original length of 1501m to a new length of 1507.8328m, known as the stretched length of the line. The difference, 6.8328m is known as the static stretch of the line. The end of the line, End B, connected to the shackle, modelled in Orcaflex, was located 1482.5m below surface, before static analysis, and later located at 1488.8328m below surface level, after static analysis.

Analytical derivation of the static stretch from DNV-RP-H103 is shown in Equation 6.12-1.

$$\eta_{st} = L_s - L = \left[(W_{ssu}L) + \left(\frac{1}{2} w_{line} L^2 \right) \right] / EA \quad \text{Equation 6.9-1}$$

where, L_s is the stretch length of lowering line, W_{ssu} is the submerged weight of the subsea protective structure, w_{line} is the subsea weight of the lowering line per meter length of line, E is the modulus of elasticity of the line and A is the cross-sectional area of the line. The static stretch obtained from the analytical method was 6.716m.

6.10 Dynamic Analysis: Far from Boundaries

The dynamic response of the structure and the varying tension in the line in deep water arise due to environmental loading experienced by the installation vessel, and it is analysed with respect to time. These time dependent parameters are also influenced by the properties of the system such as line stiffness, added mass and damping of the subsea structure. Far from boundaries is one of the phases of the installation process whereby the structure may experience resonance at some point in the lowering process. 1500 m below the sea surface was considered as far-from-boundaries in this case to study the performance of the structure by comparing the response and line tension results obtained using input data (added mass and damping) from approximate method and CFD analysis.

6.11 Dynamic Analysis: Close to Seabed

In this phase, the properties of the subsea structure and line length influence the dynamic response of the subsea structure resulting to limited operable sea states. Clearly the motions calculated above will be too large as the structure approaches the seabed.

The motion of the subsea structure close to the seabed should not exceed the seabed gap. In the event of exceedance, the risk of damage to the structure as a result of impact on the seabed could impact negatively on the field development project hence such unfavourable motions should be mitigated.

6.12 Installation analysis Results

The results presented in this section are installation analysis results of the subsea protective when installed with steel rope far from boundaries and close to the seabed. The analysis was carried out at 135 degrees wave heading, 6 seconds wave period and at various wave heights.

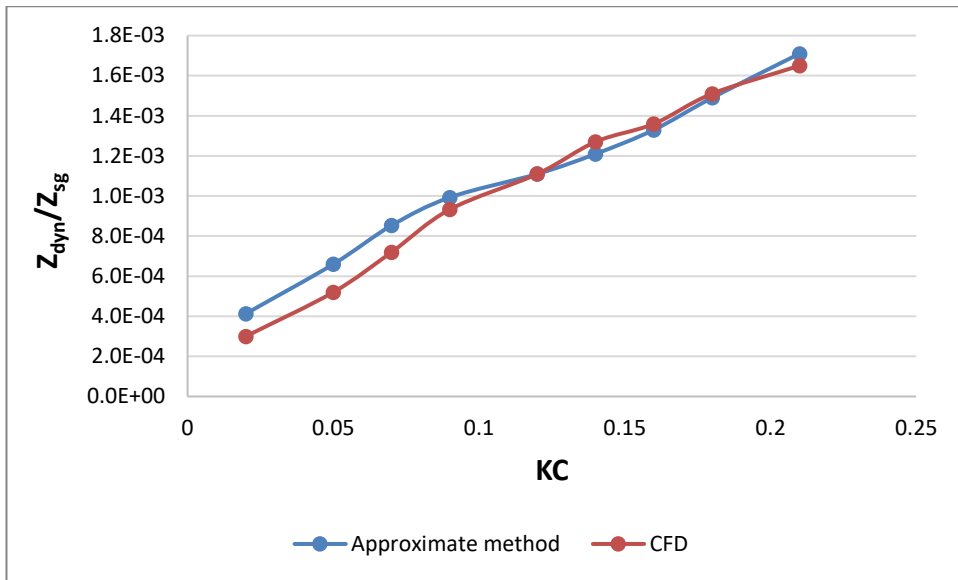


Figure 6.12-1 Response ratio of subsea protective structure far from boundaries

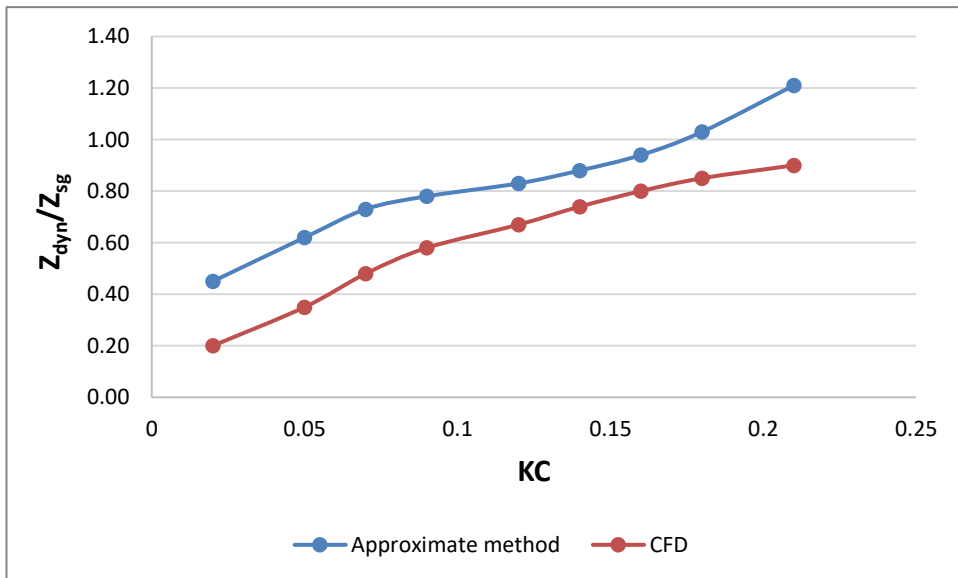


Figure 6.12-2 Response ratio of subsea protective structure at $h/D = 0.2$

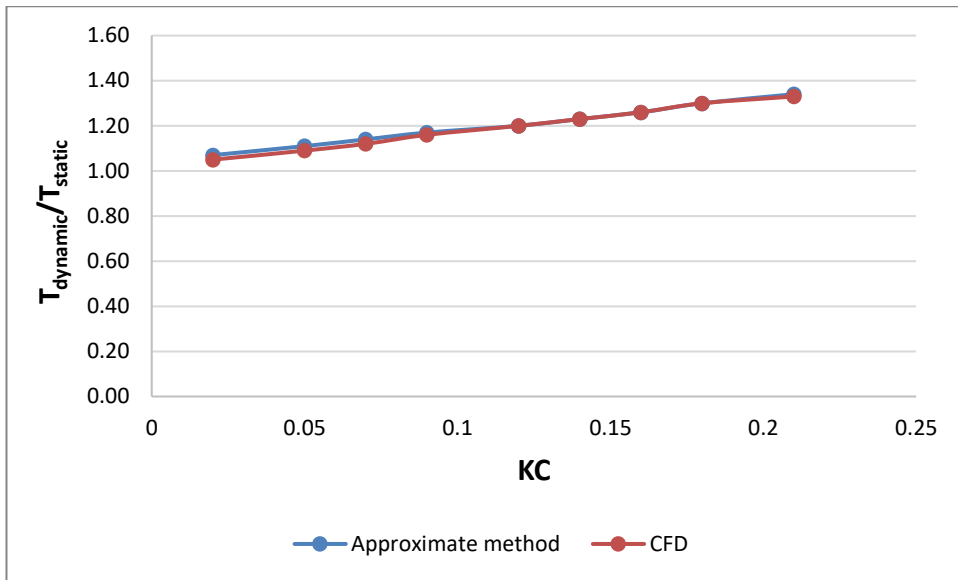


Figure 6.12-3 Non-dimensional line tension far from boundaries

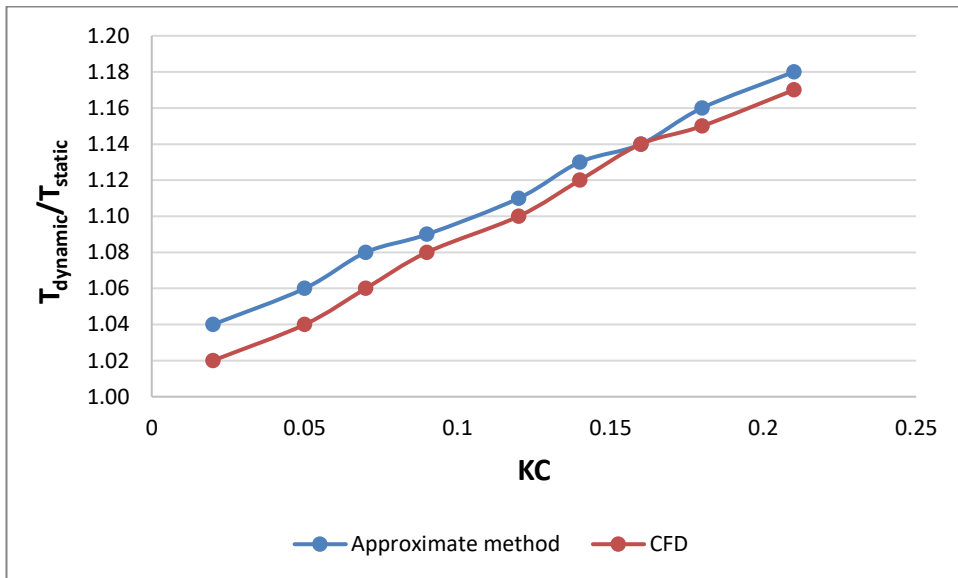


Figure 6.12-4 Non-dimensional line tension at h/D = 0.2

There is a noticeable trend of increasing response as KC increases for both methods. The calculated response of the subsea protective structure far from boundaries using hydrodynamic data of the approximate method agreed with results obtained using CFD (Figure 6.12-1). In Figure 6.12-2, there is a noticeable difference between both methods. The response derived using hydrodynamic data of the approximate method was higher than the response derived using data of the CFD analysis, because added

mass and damping derived using CFD were higher. It is observed that an increase in the hydrodynamic coefficients of a subsea protective structure would reduce its response as it approached the seabed, due to increased interaction of particles of flow within the structure and the seabed.

Figure 6.12-3 shows the tension in the line derived using hydrodynamic coefficients of both methods. The tension in the line increased as KC increased and there was no noticeable difference in the line tension results, while there was a noticeable difference in the results of Figure 6.12-4 as the structure was close to the seabed. The line tension determined using hydrodynamic coefficients of the CFD analysis was lower than the line tension derived using data of the approximate method because the response of the subsea protective structure was lower as a result of the estimated added mass and damping using CFD were higher than the estimated added mass and damping of the approximate method.

The line tension DAF (Figures 6.12-5 and 6.12-6) derived using the hydrodynamic coefficients of the approximate and Fluent simulation methods showed that at all heights above seabed for the range of KC (0.02 -0.21) considered, snap loading did not occur since the dynamic tension was lower than the static tension in all cases.

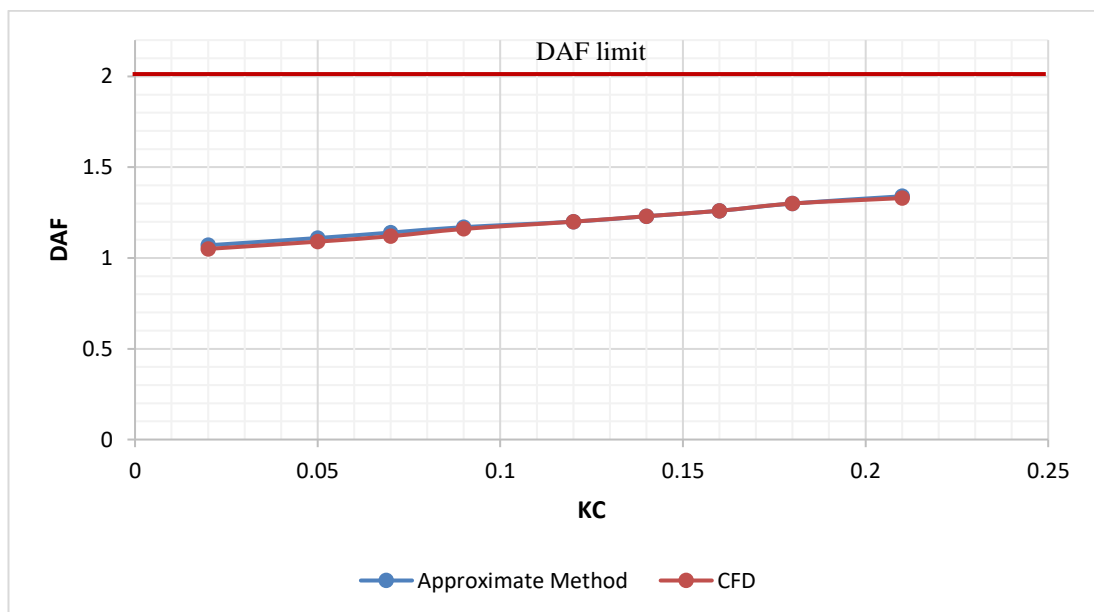


Figure 6.12-5 Line tension DAF of subsea protective structure far from boundaries

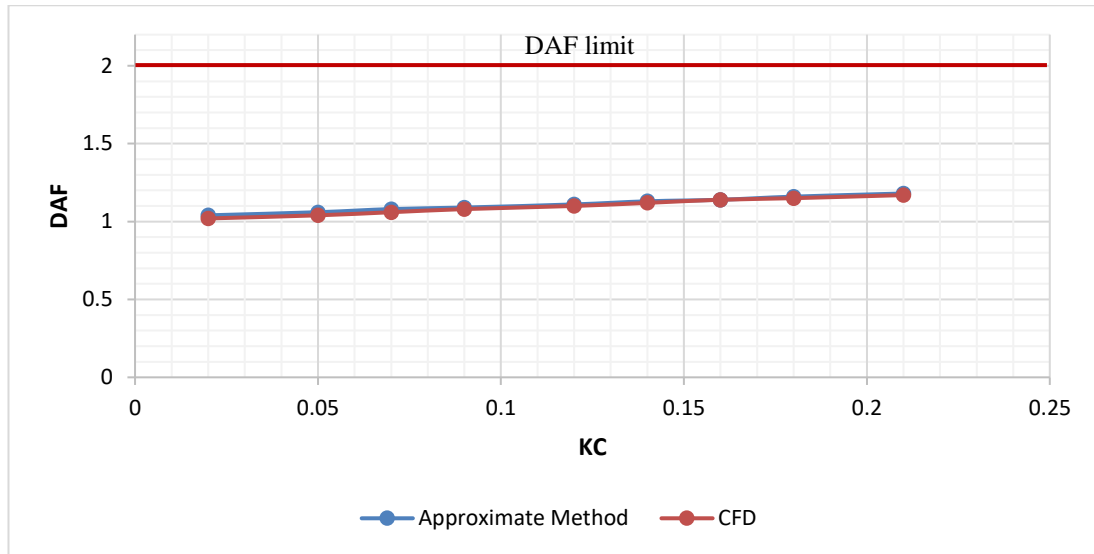


Figure 6.12-6 Line tension DAF of subsea protective structure at $h/D = 0.2$

Another factor to consider during installation is seabed impact. In this case, impact will occur if the heave amplitude of motion of the subsea structure is greater than the gap between the seabed and the lowest part of the structure. At $h/D = 0.2$, Table D.1-2 shows that impact at the different KC numbers considered will only occur at KC 0.18 and 0.21 using the hydrodynamic coefficients of the approximate method.

6.13 Chapter Summary

This chapter discussed the installation analysis of the subsea protective structure using the hydrodynamic coefficients derived from the approximate method and Fluent simulation method. The comparison between hydrodynamic coefficients of the approximate method and Fluent simulation method was presented. This was done for different KC numbers and heights above the seabed. It was reported that the trend in the results of both methods showed increasing values of the hydrodynamic coefficients as KC increases, and the hydrodynamic coefficients of the Fluent simulation method were higher than the coefficients obtained from the approximate method.

Installation analysis using Orcaflex was discussed based on the requirements to carry out analysis of the subsea protective structure, where static and dynamic analyses were

presented. The response of the subsea protective structure and line tension were lower when using the hydrodynamic coefficients of the Fluent simulation method. The results also showed that the response of a subsea protective structure can be lowered by increasing its added mass and damping.

7 Research Contribution

7.1 Introduction

The research focused on the hydrodynamic properties of subsea structures and their effect on installation analysis. Due to the difficulty experienced in estimating these parameters, the main focus was on the heave added mass and damping. The objective was to determine, using simple methods, existing data and CFD, the added mass and damping of a complicated subsea structure at various water depths and study the effect of these results on installation analysis.

7.2 Research Contribution

The present study produced the following outcomes which are beneficial to both academics and the offshore industry:

1. This research has provided a better understanding of the flow field around vertically oscillating suction-cans and subsea protective structures well away from surface and seabed and close to seabed using Computational Fluid Dynamics. Numerical flow visualization was presented in this case for the suction-can and subsea protective structure which showed fluid interaction with these structures and vortex shedding regimes.
2. This research has proffered to the industry an analytical method to estimate the added mass and damping of subsea structures such as suction-cans and subsea protective structures far from boundaries and in close proximity to the seabed.
3. This research has demonstrated the usefulness of the analytical method in terms of saving cost and time in running CFD simulations, particularly in the early stages of design, when comparative results are needed quickly and some approximations are acceptable.

4. The research presented a Fluent simulation method that was used in deriving the added mass and damping of a suction-can and subsea protective structure at various heights above seabed.
5. This research has shown the effect of using simplified analysis rather than CFD on the calculated response of a subsea protective structure.
6. This research has provided a method used in estimating the equivalent linearized damping, derived from the sinusoidal varying force over a time record by fitting a line that touches the peak of these forces. This line is formed by calculating the force magnitude expressed as $magF = F_{33}e^{-B_e\omega t} + A$.
7. The installation analysis performed, showed increasing response of the subsea protective structure at different KC as it progresses to the seabed, which is useful in understanding the influence of submergence on the added mass and damping of subsea structures oscillating in heave direction at various Keulegan Carpenter number.

8 Conclusion and Recommendations for Further Study

In this thesis, methods employed to calculate and use hydrodynamic coefficients for simple and complicated subsea structures such as the suction-can and subsea protective structure respectively, far from boundaries and in close proximity to the seabed were investigated and discussed, thereby leading to the following conclusions and some recommendations for further research highlighted in the following sections.

8.1 Conclusion

The objective of this thesis was the estimation of the hydrodynamic properties of subsea structures and its influence on the dynamic response of the structures well away from the surface and seabed and in close proximity to the seabed. Literature review demonstrated a lack of data for performing installation analysis. CFD and simplified analysis techniques were developed for these two main phases in the installation process. The main conclusions for this research are summarized below:

1. A simplified analysis model was developed to provide an understanding of the important phenomena when a flat-bottomed structure (circular disc) is oscillating near the seabed. Although circular discs are common in offshore engineering practice, the analytical analysis can be applied to other flat-bottomed shapes to estimate their added mass and damping well away from surface and seabed and close to seabed.
2. A method for simplified analysis was proposed for a subsea protective structure. The proposed method was used in estimating the added mass and damping of the protective structure at various heights above seabed. The method considered the flow in and out of the suction-can, a component member

of the protective structure, and can be applied to other subsea structures similar to those used in this thesis.

3. CFD analysis of the suction-can was performed and it was observed from flow visualisation that the downstroke and upstroke do not produce the same effects on the flow because of the closed top of the suction-can. This causes different flow circulation values to be produced in both downstroke and upstroke. A net lift force is thus obtained over each cycle as a result of this.
4. Flow visualisation shows that the flow and vortex shedding pattern are dependent on structure's geometry and KC.
5. The mass of the entrapped water within the suction-can has an influence on the added mass of the suction-can.
6. The response of the subsea structure can be altered to suit installation by changing the added mass and damping values. It was shown that increasing the added and damping would lower the response.
7. CFD requires care if satisfactory results for installation analysis are to be obtained.

8.2 Recommendations for Further Work

A few areas were identified that needed further investigation. These would be beneficial to the industry because of their relevance in installation analysis. This research has contributed to the development of analysis techniques for calculating the hydrodynamic coefficients of subsea structures and studied the impact of these parameters on the calculated response of the structure, but due to time constraint, other important areas and topics relating to subsea installation could not be looked into. Some of these areas/topics are:

1. More work is needed to be done in the estimation of the hydrodynamic coefficients to cover a wide range of subsea structures.
2. The influence of the Keulegan Carpenter number on the hydrodynamic coefficients should be extended beyond 1.0 for the case of the suction-can and 0.21 for the case of the subsea protective structure.

3. The Fluent simulation and analytical methods should be extended to calculate the magnitude of the added mass and damping in other directions of motion of the subsea structure and the cross terms (e.g. between sway and roll) should be identified. Results of analyses including sway and roll would give the overall motion of the structure which is important during the final set down of the structure.
4. The effect of $v \frac{dm}{dt}$ term and non-linear damping are important and should be investigated because they can significantly change the calculated response of the subsea protective structure.

References

ABS Record, 2009. *Thialf*. s.l.:American Bureau of Shipping.

AIAA, 1998. *AIAA Guide for the verification and validation of Computational Fluid Dynamics simulations*. Reston, VA: American Institute of Aeronautics and Astronautics.

American Geoscience Institute, 2017. *American Geoscience Institute*. [Online] Available at: <https://www.americangeosciences.org/critical-issues/faq/what-are-advantages-and-disadvantages-offshore-wind-farms>

Anon., 2017. *SCRIBD*. [Online] Available at: <https://www.scribd.com/doc/52057007/Lessons-from-Structural-Failures-in-Offshore-Structures-and-Pipelines>

An, S. & Faltinsen, O. M., 2013. An experimental and numerical study of heave added mass and damping of horizontally submerged and perforated rectangular plates. *Journal of Fluids and Structures*, Volume 39, pp. 87-101.

ANSI 30.9, 2014. *Codes of practice for fabrication, attachment, use, inspection, testing and maintenance of slings*. New York: American Society of Mechanical Engineers (ASME).

ANSI, 1984. *IEEE Standard Dictionary of Electrical and Electronics Terms I.E.E.E. Standard Dictionary of Electrical and Electronics Terms*. New York: Institute of Electrical and Electronics Engineers.

ANSYS 17.0, 2016. *SHARCNET*. [Online] Available at: https://www.sharcnet.ca/Software/Ansys/17.0/en-us/help/tgd_usr/tgd_user_report_qualitymeasure.html#tgd_user_Tb_skew_quality

ANSYS, 2006. *FLUENT 6.3 Documentation*. s.l.:ANSYS Inc..

ANSYS, 2009. *ANSYS FLUENT 12.0 User's Guide*. s.l.:ANSYS, Inc..

ANSYS, 2011. *FLUENT 14.0 Documentation*. s.l.:ANSYS Inc.

Avlesen, H., Berntsen, J. & Furnes, G., 2002. *On the current conditions along the Ormen Lange pipeline path during an extreme, idealized storm*, Bergen: Technical Report, Department of Applied Mathematics, University of Bergen.

- Bai, Y. & Bai, Q., 2010. *Subsea engineering handbook*. Houston, Texas: Gulf Professional Publishing.
- Bai, Y. & Bai, Q., 2012. *Subsea engineering handbook*. Waltham: Elsevier.
- Barltrop, N. & Adams, J. A., 1991. *Dynamics of fixed marine structures*. Oxford: Butterworth Heinemann.
- Bergem, O., 2015. *Modeling Cranemaster in Orcaflex: Engineering Guide*. Stathelle: Cranemaster.
- Biinform, 2016. *Vietnam Ship Building Industry Factsheet*, Vietnam: StoxPlus.
- Birkhoff, G., 1960. *Hydrodynamics: A study in logic, fact and similitude*. Princeton, New Jersey: Princeton University Press.
- Borgman, L. E., 1967. *Ocean wave simulation for engineering design*, Berkeley, California: University of California.
- Bottega, W. J., 2006. *Engineering vibrations*. London New York: Taylor and Francis Group, LLC.
- Braun, T., 2013. *Template installation*. [Online]
Available at: https://www.youtube.com/watch?v=Ti95Ot_Bw2w
[Accessed April 2021].
- Bunnik, T. & Buchner, B., 2004. *Numerical prediction of wave loads on subsea structures in the splash zone*. Toulon, The International Society of Offshore and Polar Engineers.
- Caley, 2019. *Rope: Steel Wire vs Synthetic Fibre*. [Online]
Available at: <https://caley.co.uk/rope-steel-wire-synthetic-fibre/>
[Accessed 14 June 2019].
- Carnevale, P., 2017. *TetraSpar: Industrialized floating foundation*. s.l.:s.n.
- CERTEX, 2012. *Fiber Rope*. [Online]
Available at: <https://www.certex.com/product-catalog/fiber-rope/>
[Accessed 20 January 2013].
- Chen, Z., Zhao, T., Jiao, J. & Mao, D., 2017. Simulation and motion analysis of deepwater manifold lifting. *Journal of Marine Science and Technology*, 25(6), pp. 696-704.
- Chung, J. & Hulbert, G. M., 1993. A Time Integration Algorithm for Structural Dynamics With Improved Numerical Dissipation: The Generalized- α Method. *ASME Journal of Applied Mechanics*, 60(2), pp. 371-375.

CM Labs, 2011. *Vortex - Offshore knuckle boom crane performing a subsea lift of a template from vessel to seabed*. [Online]

Available at: <https://www.youtube.com/watch?v=KBGr74TMTrU>

[Accessed April 2021].

Courant, R., Friedrichs, K. & Lewy, H., 1928. Über die partiellen Differenzgleichungen der mathematischen Physik. *Mathematische Annalen*, December, Volume 100, pp. 32-74.

Day, S., 2009. *Theory and Practice of Marine CFD*. Glasgow: Department of Naval Architecture and Marine Engineering, University of Strathclyde.

Det Norske Veritas, 2007. *DNV-RP-C205 Environmental conditions and environmental loads. Recommended Practice*. Oslo: Det Norske Veritas.

Det Norske Veritas, 2011. *DNV-RP-H103 Modelling and analysis of marine operations. Recommended Practice*. Oslo: Det Norske Veritas.

Det Norske Veritas, 2014. *Lifting operations (VMO Standard - Part 2-5)*. Oslo: Det Norske Veritas AS.

Det Norske Veritas, 2015. *Introduction to subsea production systems*. Oslo: Det Norske Veritas.

Dixon, M. A. & David, E., 2008. *Installation-driven field developments for deepwater subsea projects*. Houston, Texas, Offshore Technology Conference, p. 6.

DLB Micoperi 30 brochure, 2018. *Micoperi Organisation*. [Online]

Available at: <https://www.micoperi.com/en/fleet/dlb-micoperi-30>

DSM Dyneema Press Releases, 2010. *Launch of Dyneema® XBO Fibre at OTC 2010 Takes Synthetic Ropes to a New Level*. [Online]

Available at: [https://www.offshore-](https://www.offshore-technology.com/contractors/installation/dyneema/pressreleases/press1-218/)

[technology.com/contractors/installation/dyneema/pressreleases/press1-218/](https://www.offshore-technology.com/contractors/installation/dyneema/pressreleases/press1-218/)

[Accessed 14 June 2019].

Du Buat, C., 1779. *Principles d'hydraulique*. Paris: Monsieur le Chevalier Du Buat.

Dvorak, P., 2017. *Foundations that float*. s.l.: Windpower Engineering & Development Publisher.

European Commission, 2006. *Ocean energy conversion in Europe: Recent advancement and prospects*. Greece: Centre for Renewable Energy Sources.

European Defence Agency, 2016. *Study on industrial and technological competences in the naval sector - Executive summary*, s.l.: European Defence Agency.

- Fackrell, S. A., 2011. *Study of added mass of cylinders and spheres*. Windsor, Ontario: University of Windsor.
- Faizal, M., Ahmed, R. M. & Lee, Y.-H., 2014. *A design outline for floating point absorber wave energy converters*. s.l.:Hindawi Publishing Corporation.
- Faltinsen, M. O., 1990. *Sea loads on ships and offshore structures*. Cambridge: The Press Syndicate of the University of Cambridge.
- Frank, W., 2007. *Oscillation of cylinders in or below the free surface of deep fluids*. Washington, D.C: Naval Ship Research and Development Center.
- Garrido-Mendoza, C. A., 2015. *Hydrodynamic forces on heave plates for offshore systems oscillating close to seabed or the free surface*. Madrid: Technical University Madrid.
- Garrido-Mendoza, C. A. et al., 2015. Computation of flow features and hydrodynamic coefficients around heave plates oscillating near a seabed. *Journal of Fluids and Structures*, Volume 59, pp. 406-431.
- Gilmore, J., Stenvers, D. & Chou, R., 2008. *Some recent developments of rope technologies – Further enhancements of high performance ropes*. Quebec City, QC, Institute of Electrical and Electronics Engineers, p. 7.
- Graham, J. M. R., 1980. The forces on sharp-edged cylinders in oscillatory flow at low Keulegan-Carpenter numbers. *Journal of Fluid Mechanics*, 97(1), pp. 331-346.
- Grim, O., 1953. *Berechnung der durch schwingungen sines schlffskoorpors erseugton hydrodynamnisohen kraefte*. s.l.:Jahrbuch der Schifftsbautechnischen Geaellschaft.
- Gu, H., Stansby, P., Stallard, T. & Moreno, E. C., 2018. Drag, added mass and radiation damping of oscillating vertical cylindrical bodies in heave and surge in still water. *Journal of Fluids and Structures* 82, pp. 343-356.
- Gupta, A. & Singh, R. P., 1986. *Fatigue behaviour of offshore structures*. New Delhi: Springer-Verlag Publishers.
- Haskind, M. D. & Newman, J. N., 1962. *The exciting forces and wetting of ships in waves*, Washington, D.C.: Defence Technical Information Center.
- Havelock, T. H., 1929. *Forced surface-waves on water*. s.l.:Philosophical Magazine.
- Hearle, J. W., Burgoyne, C. J. & Hobbs, R. E., 1992. *Fatigue and length effects in fibre ropes*, Madrid: IABSE workshop, Length effect on fatigue of wires and strands.

- Heerema Marine Contractors, 2017. *Well-deserved retirement of Hermod*, Leiden: Heerema Marine Contractors.
- Heerema, P. S. & Michelsen, F. C., 1978. *The Semi-Submersible Crane Vessel "Balder"*. London, Society of Petroleum Engineers, p. 8.
- Hendrik Veder, 2013. *Fibre rope product catalogue*. Rotterdam: Hendrik Veder Group.
- Hidetsugu, K., Fumiaki, A., Kensuke, B. & Yutaka, I., 2000. *Principles and characteristics of viscous damping devices (gyro-damper), the damping forces which are highly amplified by converting the axial movement to rotary one*. Auckland, New Zealand Society for Earthquake Engineering.
- Housseine, C. O., Monroy, C. & de Hauteclocque, G., 2015. *Proceedings of 34th International Conference on Ocean, Offshore and Arctic Engineering*. St.John's, NL, Canada, OMAE 2015.
- Huang, S., 2010. *Subsea systems and installation*. Glasgow: University of Strathclyde.
- IEEE, 1990. *IEEE Standard Glossary of Software Engineering Terminology*. New York: Institute of Electrical and Electronics Engineers.
- IMCA, 2007. *Guidelines for Lifting Operations*, London: The International Marine Contractors Association.
- International Energy Agency, 2013. *World Energy Outlook 2013*, Paris: Corlet.
- Ireland, J., Macfarlane, G. & Drobyshevski, Y., 2007. *Investigation into the sensitivity of the dynamic hook load during subsea deployment of a suction can*. San Diego, California, The International Conference on Offshore Mechanics and Arctic Engineering.
- Issa, R. I., 1985. Solution of the implicitly discretised fluid flow equations by operator-splitting. *Journal of computational physics*, Volume 62, pp. 40 - 65.
- ITTC, 2002. *Procedures for Resistance, Propulsion and Propeller Open Water Tests*. Venice, International Towing Tank Conference.
- Iverson, W. H. & Balent, R., 1951. A correlating modulus for fluid resistance in accelerated motion. *Journal of Applied Physics*, pp. pp. 324-328.
- Jakobsen, S. M. E., 2008. *Passive heave compensation of heavy modules*. Stavanger: University of Stavanger.

- Joesen, A. & Paul, D., 2011. *A low tech, low risk system for the installation of large structures in deep water*. Aberdeen, Society of Petroleum Engineers, p. 8.
- Johansen, E. B., 2018. *Cranemaster Product Datasheet*. Stathelle: Cranemaster.
- Journée, J. & Massie, W., 2001. *Offshore Hydromechanics*. First Edition ed. Delft: Delft University of Technology.
- Kaneko, S. et al., 2014. *Flow-Induced Vibrations: Classifications and Lessons from Practical Experiences*. Tokyo: Elsevier Ltd.
- Koo, W. & Kim, J.-D., 2015. Simplified formulas of heave added mass coefficients at high frequency for various two-dimensional bodies in a finite water depth. *International Journal of Naval Architecture and Ocean Engineering*, pp. Pages 115-127.
- Kopsov, I. E. & Sandvik, P. C., 1995. *Analysis of subsea structure installation*. The Hague, The Netherlands, International Society of Offshore and Polar Engineers, p. 7.
- kwaśniewski, L., 2013. *Application of grid convergence index in FE computation*. Warszawa, Warsaw University of Technology.
- Lamb, H., 1945. *Hydrodynamics*. New York: Dover Publications.
- Idel'chik, I. E., 1966. *Handbook of Hydraulic Resistance: Coefficients of Local Resistance and of Friction*. Jerusalem: Israel Program for Scientific Translations Ltd..
- Luneau, J., 1949. *Sur l'effet d'inertie des sillages de disques circulaires se déplaçant dans l'eau d'un mouvement uniformément accéléré*. Paris: Comptes Rendus de l'Académie des Sciences.
- Marintek, 2003. *Review: Norwegian marine technology research institute*. Trondheim: Norwegian Marine Technology Research Institute.
- McKenna, H. A., 2005. *Evaluation of new and used fiber ropes*. Washington, DC, Institute of Electrical and Electronics Engineers.
- McKenna, H. A., Hearle, J. W. & O'Hear, N., 2004. *Handbook of fibre rope technology*. Cambridge: Woodhead Publishing.
- Menter, F. R., 1994. Two-Equation Eddy-Viscosity Turbulence Models for Engineering Applications. *American Institute of Aeronautics and Astronautics*, Volume 32, pp. 1598-1605.
- Moan, T., 2004. *Safety of offshore structures*, Singapore: Centre for Offshore Research & Engineering, National University of Singapore.

- Moon, T., 2014. *Offshore Magazine*. [Online]
Available at: <https://www.offshore-mag.com/content/dam/offshore/print-articles/volume-74/11/1114HeavyLift-Poster102414-Ads.pdf>
- Morison, J. R., O'Brien, M. P., Johnson, J. W. & Schaaf, S. A., 1950. The forces exerted by surface waves on piles. *Journal of Petroleum Technology*, May, pp. 149 - 154.
- Morrison, D. & Cermelli, C., 2003. *Deployment of subsea equipment in ultradeep water*. Cancun, 22nd International Conference on Offshore Mechanics and Arctic Engineering.
- Munson, B. R., Young, D. F., Okiishi, T. H. & Huebsch, W. W., 2009. *Fundamentals of Fluid Mechanics*. Sixth ed. Iowa: John Wiley & Sons, Inc..
- Nam, B., Kim, N. & Hong, S., 2017. Experimental and numerical study on coupled motion responses of a floating crane vessel and a lifted subsea manifold in deep water. *International Journal of Naval Architecture and Ocean Engineering*, 9(5), pp. 552-567.
- NASA, 2021. *Turbulence Modeling Resource*, Hampton, Virginia: s.n.
- National Institute of Standards and Technology, 2003. *NIST/SEMATECH e-Handbook of Statistical Methods*. Gaithersburg, Maryland: National Institute of Standards and Technology.
- Niedzwecki, J. M. & Thampi, S. K., 1991. Snap loading of marine cable systems. *Applied Ocean Research*, Volume Vol. 13, pp. pp. 2-11.
- Oberkampf, W. F. & Trucano, T. G., 2002. *Verification and validation in Computational Fluid Dynamics*, Albuquerque, New Mexico: Sandia National Laboratories.
- OPRED, 2018. *Guidance notes: Decommissioning of offshore oil and gas installations and pipelines*. s.l.:Offshore Decommissioning Unit, Offshore Petroleum Regulator for Environment and Decommissioning and Department of Business, Energy and Industrial Strategy.
- Orcina, 2018. *Orcina*. [Online]
Available at:
<https://www.orcina.com/SoftwareProducts/OrcaFlex/Documentation/Help/>
- Orcina, 2019. *OrcaFlex documentation (version 10.3d)*. Cumbria: Orcina Ltd.

- Porter, W. R., 1960. *Pressure distributions, added mass, and damping coefficients for cylinders oscillating in a free surface*, Berkeley, California : University of California, Institute of Engineering.
- Rachain, J. & Coleman, S., 2016. *Drilling Formulas*. [Online]
Available at: <http://www.drillingformulas.com>
- Ridge, I. M. et al., 2007. *High strength fibre cored steel wire rope for deep hoisting applications*. Johannesburg, OIPEEC Conference.
- Roache, P. J., 1998. *Verification and validation in computational science and engineering*. Albuquerque, New Mexico: Hermosa Publishers.
- Roe, T., Macfarlane, G. & Drobyszeski, Y., 2008. *Heave added mass and damping of a suction can in proximity to the sea floor*. Estoril, American Society of Mechanical Engineers.
- Rosenblueth, E., ASCE, M. & Herrera, I., 1964. On a kind of hysteretic damping. *Journal of the Engineering and Mechanics Division: Proceedings of the American Society of Civil Engineers*.
- Rowe, S. J., Mackenzie, B. & Snell, R., 2001. *Deepwater installation of subsea hardware*. Houston, Texas, Society of Naval Architects and Marine Engineers.
- Sarpkaya, T. & Isaacson, M., 1981. *Mechanics of wave forces on offshore structures*. New York: Van Nostrand Reinhold Co. .
- SAS Winches, 2017. *Offshore Technology*. [Online]
Available at: <https://www.offshore-technology.com/contractors/lifting/saswinches/attachment/saswinches2/>
- Schlichting, H., 1979. *Boundary-layer theory*. 7th edition ed. New York: McGraw-Hill.
- Shabana, A. A., 1991. *Theory of Vibration*. 1 ed. Chicago: Springer-Verlag New York.
- Sharcnet, 2009. *Sharcnet*. [Online]
Available at:
https://www.sharcnet.ca/Software/Gambit/html/users_guide/ug0304.htm#metric_equiangle_skew
- Slater, J. W., 2008. *National Aeronautics and Space Administration*. [Online]
Available at: <https://www.grc.nasa.gov/WWW/wind/valid/tutorial/tutorial.html>

- Sloan, F., Bull, S. & Longerich, R., 2005. *Design modifications to increase fatigue life of fiber ropes*. Washington, DC, The Institute of Electrical and Electronics Engineers.
- Sloan, F., Nye, R. & Liggett, T., 2003. *Improving bend-over-sheave fatigue in fiber ropes*. San Diego, CA, Institute of Electrical and Electronics Engineers, pp. 1054-1057.
- Smith, J. R., 2000. *Alternating taut-slack dynamics of a vertically tethered subsea unit*. Glasgow: University of Strathclyde.
- STA, 2010. *Control and summary sheet*. Houston, TX : Stewart Technology Associates.
- Subsea Deployment Systems Ltd., 2013. *Subsea installation without a heavy lift vessel: A step change in subsea installation*, Westhill: s.n.
- Subsea Deployment Systems Ltd, 2013. *A low risk, low cost method for the installation of subsea structures: A step change in subsea installation*, Aberdeen: s.n.
- Sumer, M. B. & Fredsoe, J., 1999. *Hydrodynamics around cylindrical structures*. Lyngby: World Scientific Publishing Co. Pte. Ltd.
- Takács, G. & Rohaľ-Ilkiv, B., 2012. *Model predictive vibration control: Efficient constrained MPC vibration control for lightly damped mechanical structures*. London: Springer-Verlag London.
- Tao, L. & Thiagarajan, K., 2003. Low KC flow regimes of oscillating sharp edges I. Vortex shedding observation. *Applied Ocean Research*, February, 25(1), pp. 21-35.
- Tasai, F., 1959. On the damping force and added mass of ships heaving and pitching. *Journal of Zosen Kiokai*, p. 105.
- Teigen, P., 2002. *Investigation of deep water installation operations in random waves and current*. Kitakyushu, Japan, International Society of Offshore and Polar Engineers.
- Thorgersen, S., 2014. *Comparison study of deepwater installation methods*. Stavanger: University of Stavanger.
- Timoshenko, S., 1937. *Vibration problems in engineering*. New York: D. Van Nostrand Company, Inc..
- Torben, S. R. et al., 2007. *Fibre rope deployment system for ultradeepwater installations*. Houston, Texas, Offshore Technology Conference, p. 11.

- Treves, T., 1980. Military Installations, Structures, and Devices on the Seabed. *The American Journal of International Law*, October, 74(4), pp. 808-857.
- Tsuneishi Shipbuilding Co., Ltd., 2014. *Tsuneishi Heavy Industries (Cebu), Inc.*. [Online]
Available at: <https://www.tsuneishi.co.jp/english/news/topics/2014/07/444/>
- TTA Group, 2008. *TTA7: Technology strategy for deepwater and subsea production systems*. Stavanger: TTA group of companies and organisations.
- Umaine, J., 2016. *Wikimedia Commons*. [Online]
Available at: https://en.wikipedia.org/wiki/File:Foundations_NREL.jpg
- Ursell, F., 1949. *On the heaving motion of a circular cylinder on the surface of a fluid*. s.l.:Quarterly Journal of Mechanics and Applied Mathematics.
- Usha Martin, 2014. *Wire rope handbook*. Kolkata: Usha Martin Limited.
- Vassalos, D. & Kourouklis, A., 1998. *An experimental, theoretical and full-scale investigation on the snap loading of marine cables*, Sudbury, Suffolk: Health and Safety Executive.
- Versteeg, H. K. & Malalasekera, W., 1995. *An introduction to Computational Fluid Dynamics, The Finite Volume Method*. Essex, England: Longman Group.
- Wadhwa, H., Krishnamoorthy, B. & Thiagarajan, K. P., 2010. *Variation of heave added mass and damping near seabed*. Shanghai, ASME 29th International Conference on Ocean, Offshore and Arctic Engineering.
- Wang, A. et al., 2012. *Latest progress in deepwater installation technologies*. Rhodes, Greece, International Society of Offshore and Polar Engineers, p. 12.
- Webber, N. B., 1965. *Fluid mechanics for civil engineers*. California: E. & F. N. Spon.
- White, D. J. & Cheuk, C. Y., 2011. Modelling the dynamic embedment of seabed pipelines. *Canadian Geotechnical Journal*.
- Whitehill, S. A. & Whitehill, E. C., 1995. *Tension-tension fatigue test results for aramid and wire ropes*. Chester, Pa: Whitehill Mfg. Corp..
- Wille, P., 2005. *Sounds and images of the ocean*. Berlin: Springer-Verlag Berlin Heidelberg.
- Williams, S. C. P., 2016. *News Feature: Skimming the surface of underwater landslides*. s.l.:National Academy of Sciences.

Woody, T., 2017. *Seabed Mining: The 30 People Who Could Decide the Fate of the Deep Ocean*, New York: Oceans Deeply.

Yih, S. C., 1969. *Fluid Mechanics: A concise introduction to the theory*. New York: McGraw-Hill.

Yunxia, W., Jianhui, L. & Chunlei, Z., 2016. Study on dynamic characteristics of coupled model for deep-water lifting system. *Journal of Ocean University of China (Oceanic and Coastal Sea Research)*, 15(5), pp. 809-814.

Zhou, L., Duan, M.-L. & Guo, Z.-Y., 2015. *Risk analysis of subsea jumper in installation period based on fuzzy FMEA*. Incheon, Korea, Advances in Structural Engineering and Mechanics (ASEM 15), pp. 25-29.

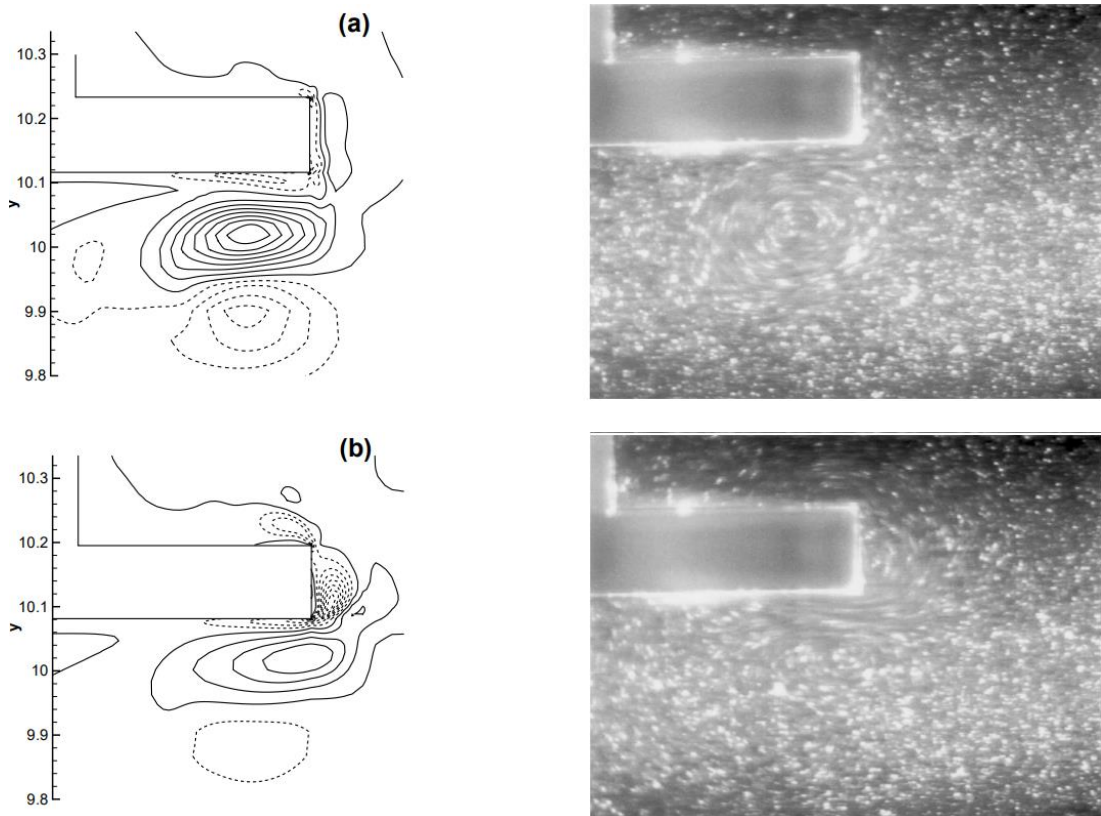
Zielinski, T. P. & Duda, K., 2011. Frequency and damping estimation methods - an overview. *Metrological and Measurement Systems*, January, pp. pp. 505-528.

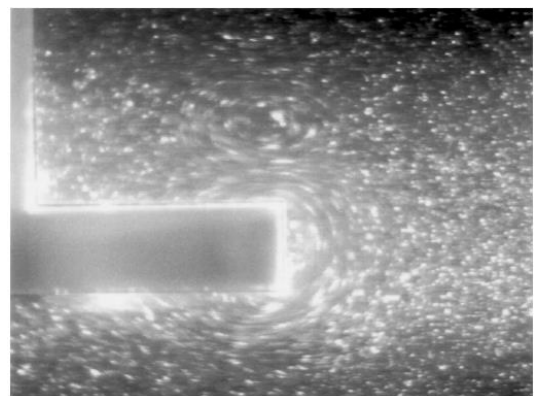
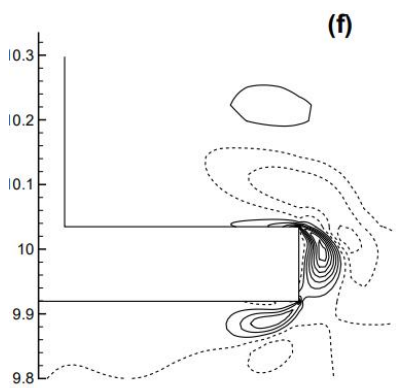
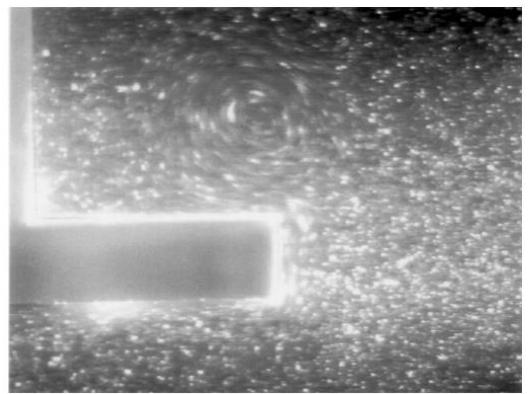
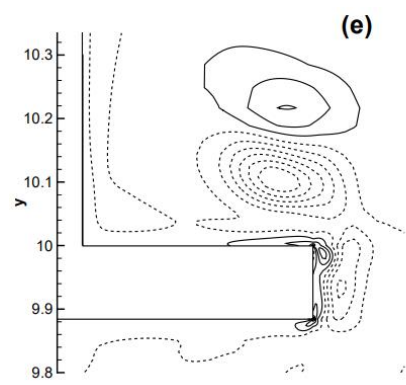
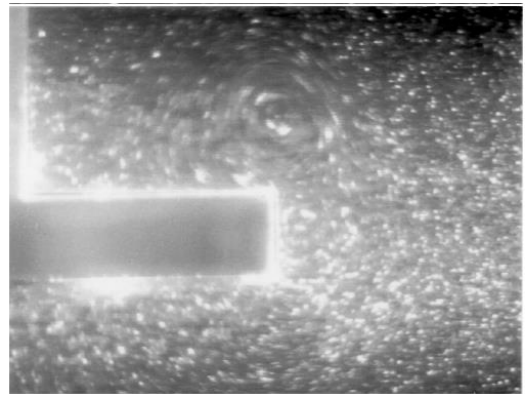
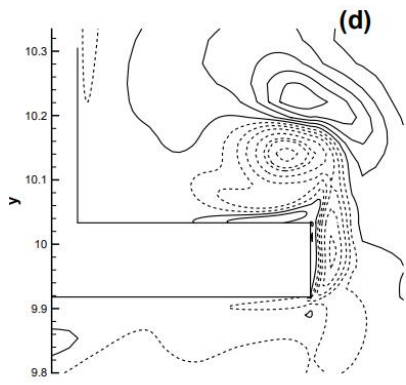
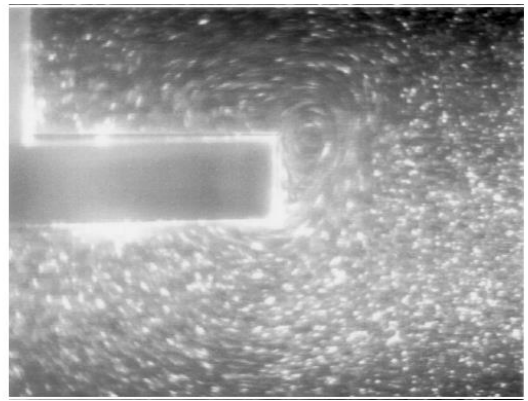
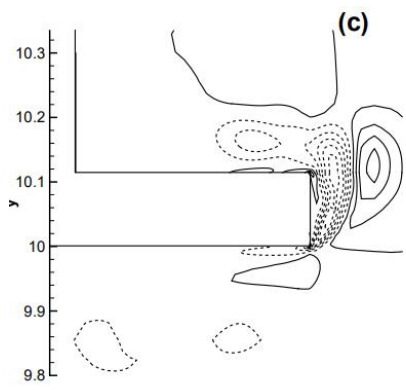
Zoontjes, R., Siegersma, H. & Ottens, H., 2009. *Using CFD to determine heave added mass and damping of a suction pile*. Honolulu, Hawaii, American Society of Mechanical Engineers.

Appendix A

A.1 Vortex shedding from edge of disc

The flow around a disc of 0.609 m diameter and 0.0254 m thick attached to the bottom of a surface-piercing cylinder is presented in Figure A.1-1. The disc was forced to oscillate vertically at $KC = 0.197$. The dashed lines according to Tao et al. (2003) indicate negative vorticity, and the photographs to the right show the flow from the experiment performed by Thiagarajan (1993).





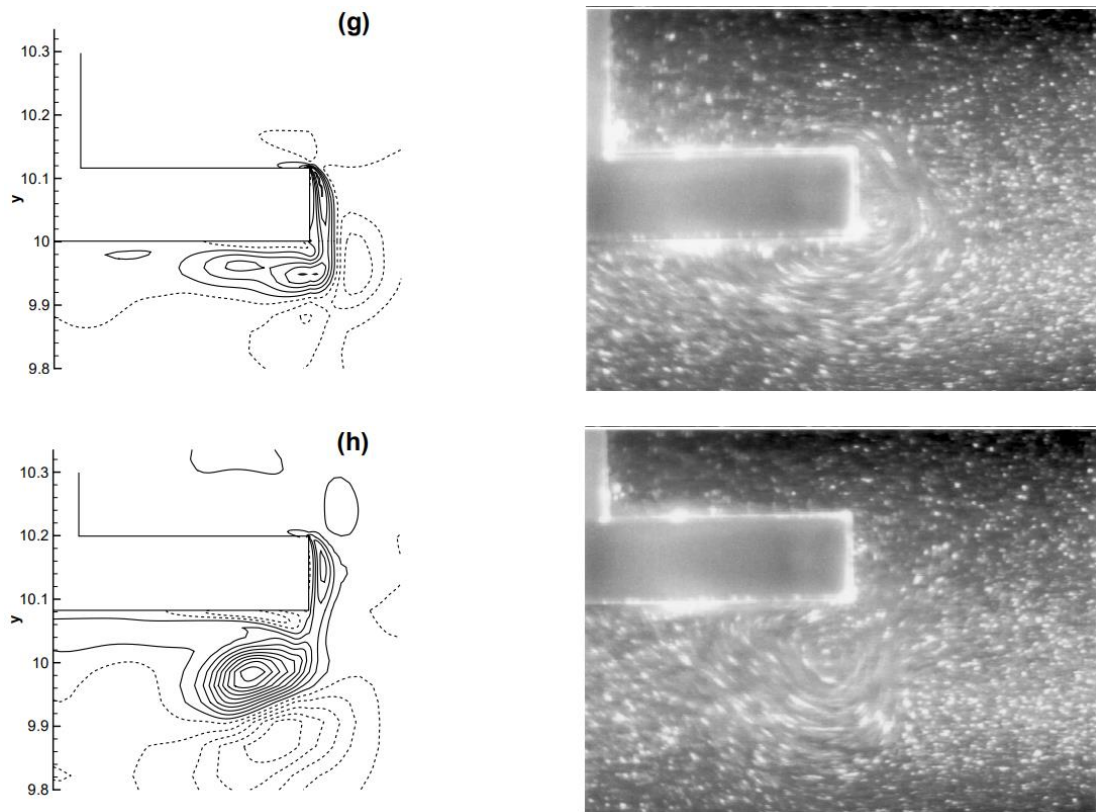


Figure A.1- 1 Vortex shedding from edges of disc for one cycle of oscillation (Tao et al. 2003)

A.2 Vortex Generation around Disc for different Critical KC Values

Figures A.2-1(a), (b) and (c) from Garrido-Mendoza et al. (2015) show the vortex generated around the disc for three cases – KC numbers just under ($KC/KC_{cri} = 0.96$), equal to ($KC/KC_{cri} = 1.00$), and just over the critical KC ($KC/KC_{cri} = 1.04$) respectively. The blue lines represent negative vorticity and initial condition in this case is the Top Dead Center. The results show the disc oscillation for one cycle. From observation of Figures A.2-1(a) and (b), entrapment of vortices by the seabed from previous cycles does not occur compared to Figure A.2-1(c).

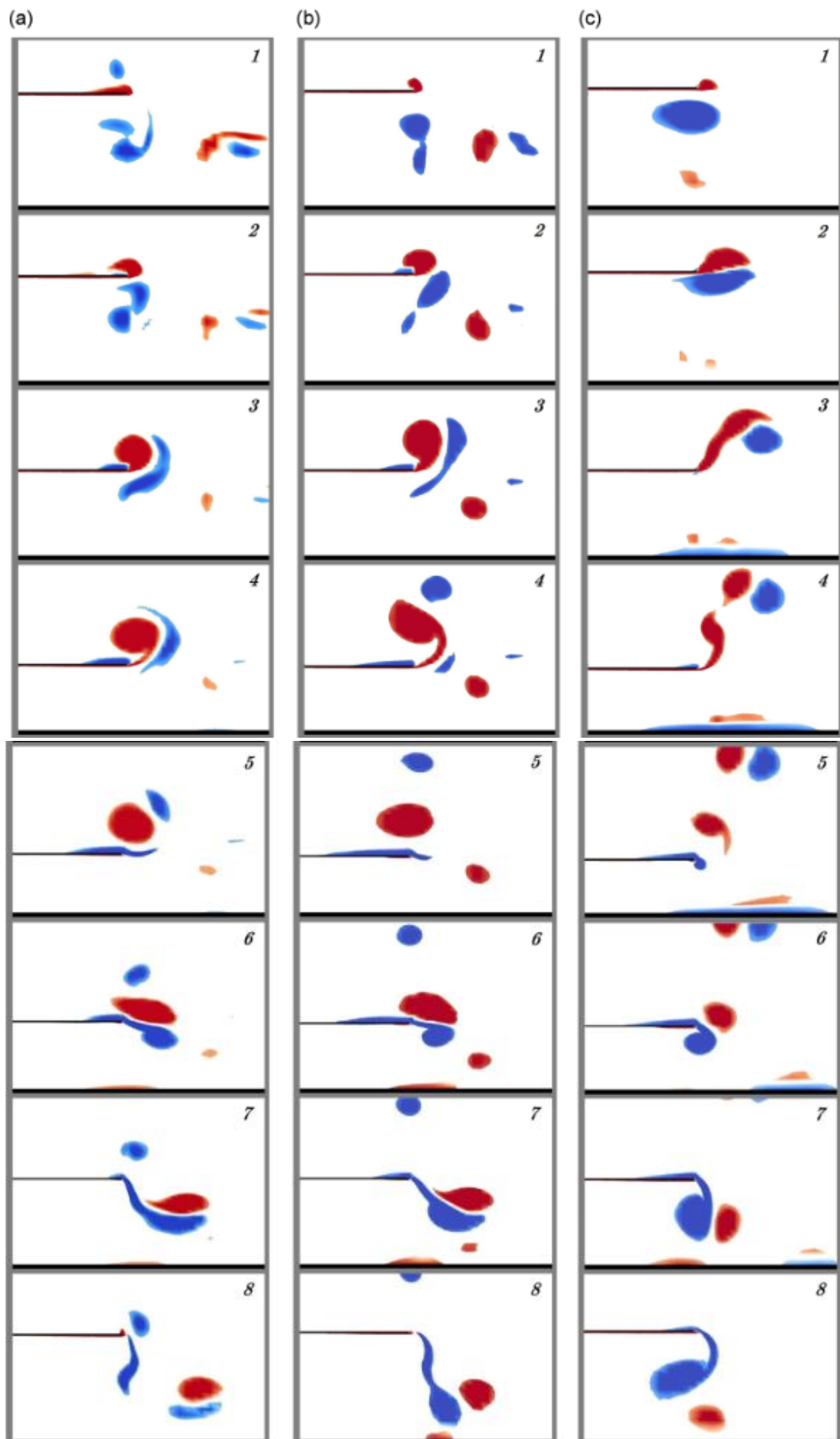


Figure A.2- 1 Vortex generation around disc at different KC to critical KC ratios Garrido-Mendoza et al. (2015)

A.3 Added Mass Coefficients for Three-Dimensional Bodies

Figure A.3-1 was extracted from Det Norske Veritas, DNV-RP-H103 – Modelling and analysis of marine operations. A recommended Practice that shows the hydrodynamic added mass coefficients for various flat plates in infinite fluid.

Table A-2 Analytical added mass coefficient for three-dimensional bodies in infinite fluid (far from boundaries). Added mass is $A_{ij} = \rho C_A V_R$ [kg] where V_R [m³] is reference volume


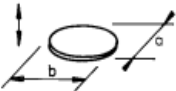
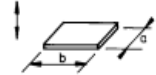

Body shape		Direction of motion	C_A				V_R
Flat plates	Circular disc 	Vertical	$2/\pi$				$\frac{4}{3} \pi a^3$
	Elliptical disc 	Vertical	b/a	C_A	b/a	C_A	$\frac{\pi}{6} a^2 b$
			∞	1.000	5.0	0.952	
			14.3	0.991	4.0	0.933	
			12.8	0.989	3.0	0.900	
10.0			0.984	2.0	0.826		
7.0			0.972	1.5	0.758		
6.0	0.964	1.0	0.637				
Rectangular plates 	Vertical	b/a	C_A	b/a	C_A	$\frac{\pi}{4} a^2 b$	
		1.00	0.579	3.17	0.840		
		1.25	0.642	4.00	0.872		
		1.50	0.690	5.00	0.897		
		1.59	0.704	6.25	0.917		
		2.00	0.757	8.00	0.934		
		2.50	0.801	10.00	0.947		
		3.00	0.830	∞	1.000		
Triangular plates 	Vertical	$\frac{1}{\pi} (\tan \theta)^{3/2}$				$\frac{a^3}{3}$	

Figure A.3- 1 Analytical added mass coefficient for three-dimensional bodies far from boundaries

A.4 Subsea Structure Installation Phases

In-Air Lift from Deck

This is the initial stage where the structure is lifted off the deck of either an offshore construction vessel or a supply boat. A crane with sufficient capacity is used in lifting the structure with bumper frames and tugger lines attached to it to control its pendulum motion due to movement at the crane tip during over boarding. The dynamic forces quantified at this stage exerted on the structure are due to wind loading directly exerted

on the structure and wave loads exerted on the vessel and causing motion that is transmitted to the structure.

Load deployment with an offshore crane vessel at this phase can either be carried out on the same side as the crane which is suitable for very wide offshore structures and line structures or on opposite side as the crane, usually suitable for piles and spools. Deploying from same side as crane is most common as it saves time but extra care must be taken whilst rotating the structure with the crane and its tuggers.

The flexibility of slings may have an important effect on dynamic impact forces at this stage.

Passage through the Splash Zone

Also known as the air-sea interface, there is a great threat of damage to the structure and the installation vessel. During lowering, waves with high wave heights and high winds can create a lurch pendulum motion of the structure allowing it to swing uncontrollably with the potential of hitting the vessel. This operation is monitored by on board computers which display the loads at the main hook, auxiliary hook, sling hook and the outreach distance of the lifting crane. As explained by Kopsov and Sandvik (1995) as the structure is exposed to extreme direct wave loading, its hydrodynamic properties are sensitive to oscillation frequency and are immersion dependent due to the change in the displaced volume and parts of the structure. This zone has an associated hydrodynamic force known as slamming force that acts abruptly when the structure hits the water surface. The slamming force is a short-term force applied in the lifting analysis, which must be accounted for in order to determine the limiting sea states. The recommended practice according to DNV-RP-H103 (2011) expresses this force as:

$$F_{slam} = 0.5\rho C_s A_s v_s^2 \quad \text{Equation A.4- 1}$$

where, ρ is the density of sea water, C_s is the slamming coefficient which is dependent of the shape of the structure and usually determined empirically or theoretically, A_s is the slamming area and v_s is the slamming impact velocity expressed in DNV's recommended practice (DNV-RP-H103) by:

$$v_s = v_c + \sqrt{v_{ct}^2 + v_w^2} \quad \text{Equation A.4- 2}$$

where, v_c is the lowering velocity of the hook; v_{ct} is the amplitude of velocity at the crane tip in the heave direction and v_w , the vertical water particle velocity.

This assumes that the v_{ct} and v_w are separate maximum values that are unlikely to occur together. Otherwise, a vector addition should be used.

The lowering velocity varies for each installation phase. Caution is applied during lowering through the splash zone with lowering speeds less than the deepwater phase where the structure is no longer susceptible to surface waves. The slamming impact velocity expressed in Equation A.4-2 is different for a suction-can due to excitations of the entrapped water enclosed in the can which in turn leads to an increased velocity calculated by:

$$v_s = v_c + \sqrt{v_{ct}^2 + v_w^2 \cdot k^2} \quad \text{Equation A.4- 3}$$

where, k represents the amplification factor (Det Norske Veritas, 2011).

According to DNV-RP-H103 (2011), the characteristics hydrodynamic force on a structure passing through the wave zone is a time dependent function of the hydrodynamic force expressed in the simplified method by the equation:

$$F_{hydro} = \sqrt{(F_D + F_{slam})^2 + (F_M + F_\rho)^2} \quad \text{Equation A.4- 4}$$

Where, F_D is the hydrodynamic drag force; F_{slam} is the slamming force; F_M is the hydrodynamic mass force and, F_ρ the varying buoyancy force.

The characteristic hydrodynamic force on the structure when lowered through the wave zone also depends on its geometry and determines the number of load cases. A spool piece which differs from a protection structure will have a lesser number of load cases compared to the protection structure which may be divided into four load cases to account for its roof, suction buckets, either perforated or closed and structural beams which have little significance on the final result. The following figure below illustrates load cases for a subsea protective structure when lowered through the water surface with associated hydrodynamic force.

Deepwater Lowering

The deepwater lowering stage of subsea modules constitutes most of the lowering time. This time is dependent on water depth and winch speed. The hydrodynamic properties of the subsea module are constant due to the absence of free surface effects. Although as a result of the crane tip motion, the structure experiences a dynamic loading when it oscillates through the water column. Immediately after the air-sea interface, when fully submerged, lowering is stopped to allow flooding and disconnection of tugger wires by a remotely operated vehicle. Depending on the installation technique the lowering could be stopped to alter the system properties in order to avoid resonance.

Resonance may occur when the frequency of the surface waves generates crane tip motions which correspond to the frequency of the lowering system. The lowering system in this case is the wire and the structure: the vertical motion may then create resonance movements in the subsea load and wire. Large dynamic forces caused by resonance in the lowering system in deepwater may not be able to be avoided as the structure is lowered to the seabed due to the change in axial stiffness of the lowering line and the (usually fixed) payload properties. The elastic modulus is a material property also responsible for change in line stiffness. This elastic modulus varies for various materials such as steel and fibre ropes. Fibre ropes are the preferred choice for deepwater applications not only for their wholly or partly buoyant characteristic but their very low stiffness compared to steel wire ropes. After a safe passage of the structure through this zone with one or several stops it gets to the next stage where lowering comes to a halt for final set down. Once a large length of lifting wire is payed out the sling flexibility becomes unimportant, due to their short lengths thereby not having any significant impact on the system.

Near Seabed Location: 3 – 10 m Above

Lowering is stopped at this stage to prepare the structure for final set down while remotely operated vehicles carry out final surveys of the landing area. In order to minimize the dynamic response of the structure due to excitations from the surface vessel, either a constant tension is activated or a heave compensator is applied which could be active or passive.

In the case of constant tension, the offshore operator sets the required constant force. And this is approximately maintained, often by a system of hydraulic rams and an accumulator

Alternatively, the tension can be controlled by an active heave compensator: the procedure involves a rapid adjustment of the line tension using the measured force from a load cell that is observed by the control system to ensure the actual value does not differ significantly from the initial set value. If this value differs, the winch then pays in or out wire rope depending on the response of the structure to maintain the initial set value. For an active heave compensator system there is a lot of paying in and paying out of the cable carried out by the winch system to keep the structure held at a constant tension. This tension adjustment assists with safely landing of the structure on the seabed by reducing to a great extent the influence of the surface vessel motions on the subsea structure and preventing the cable from slacking.

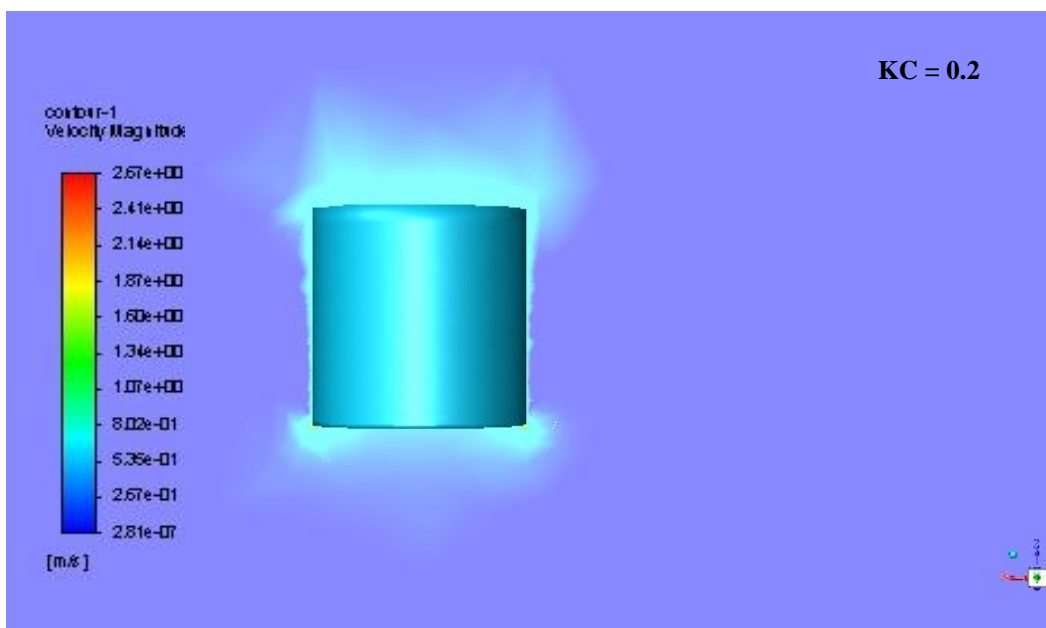
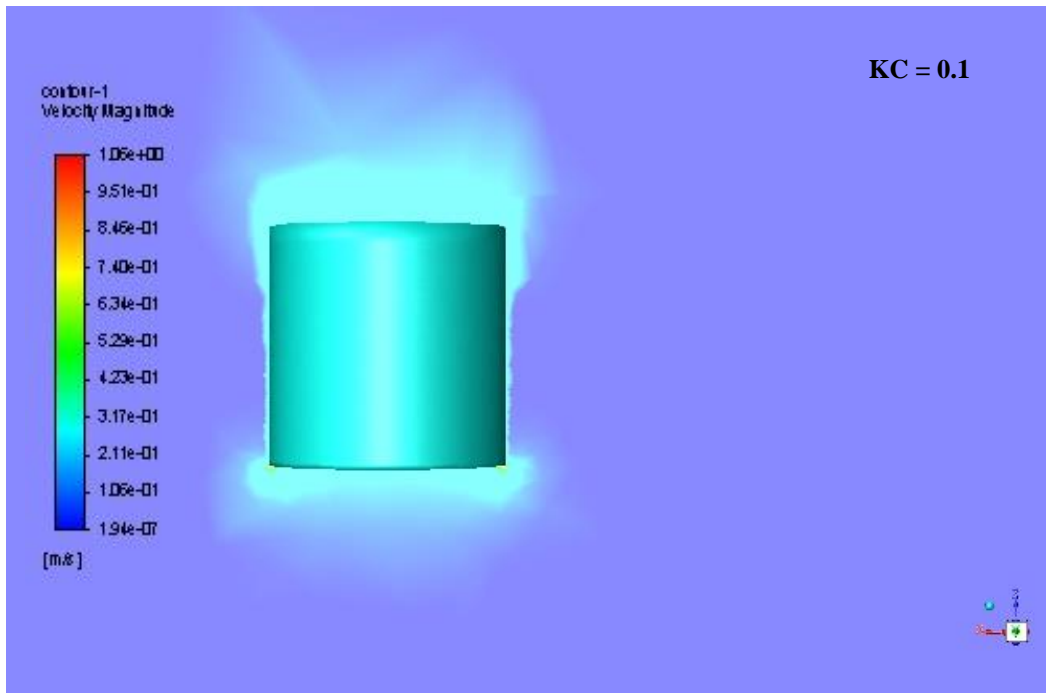
Instead of the preset tension for the constant tension method, heave compensators can be applied to the lowered structures position making the structure less sensitive to the vessel motions. The Active Heave Compensation system is used in controlling the relative position of the structure to the seabed and this is made possible by a control system in conjunction with sensors that determine the position of the structure.

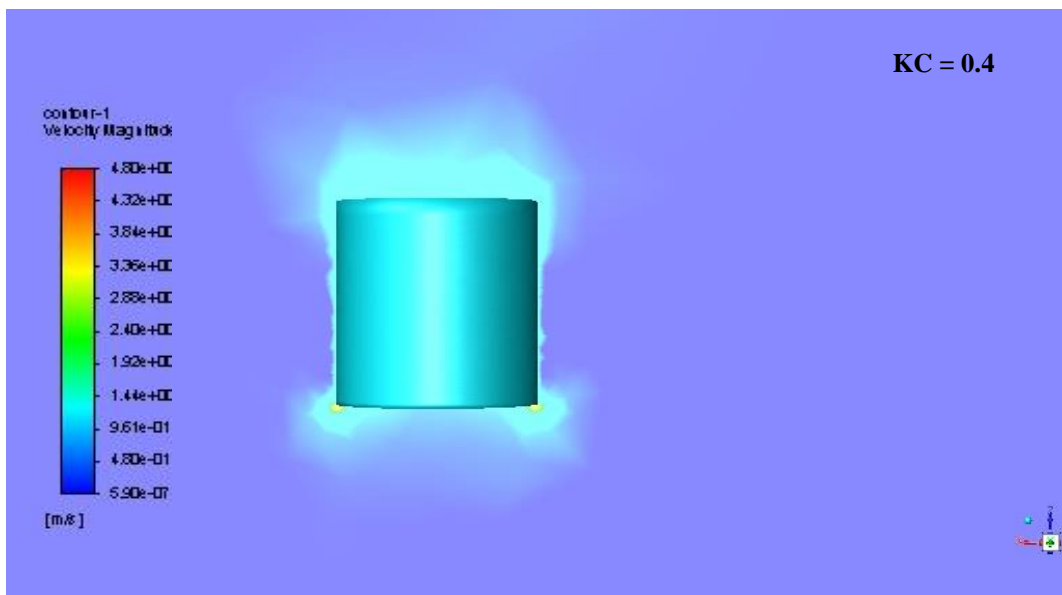
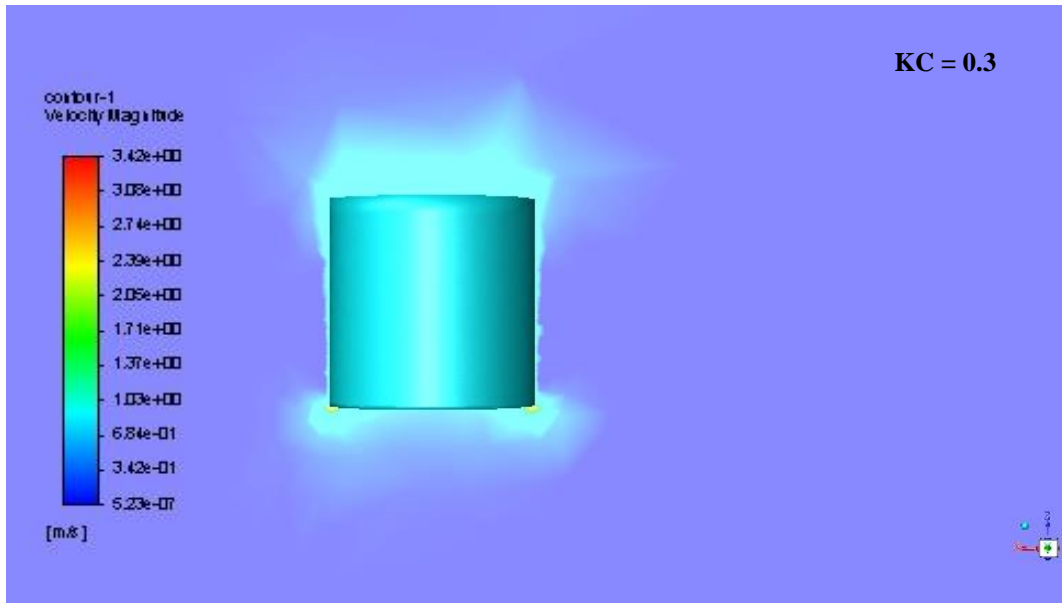
Seabed Landing

This is a critical phase in the installation process as the motions of subsea structure influenced by the surface waves could be amplified if proper mitigation measures to reduce its response are not applied because the hydrodynamic properties of the structure are influenced by its proximity to the seabed. Care must be taken in choosing the right lowering speed at this stage as high speeds may erode the seabed surface as a result of water escaping from underneath the heaving structure causing an uneven seabed and also damage to the structure if it impacts the seabed too hard.

Appendix B

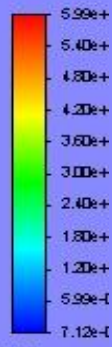
B.1 Contour of Velocity Magnitude of Suction-Can Well Away from Surface and Seabed





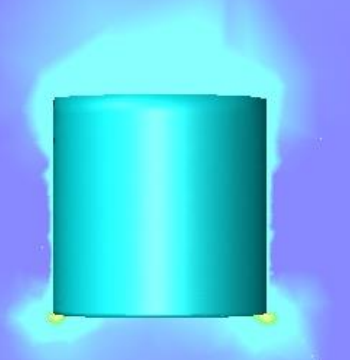
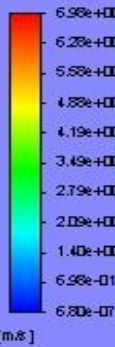
KC = 0.5

contour-1
Velocity Magnitude

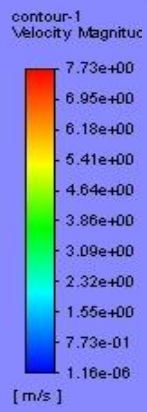


KC = 0.6

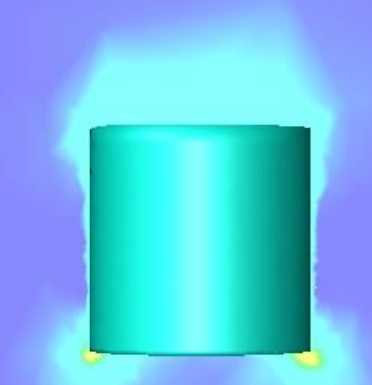
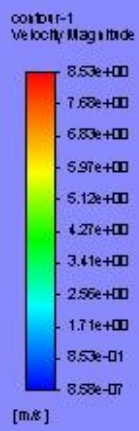
contour-1
Velocity Magnitude



KC = 0.7



KC = 0.8



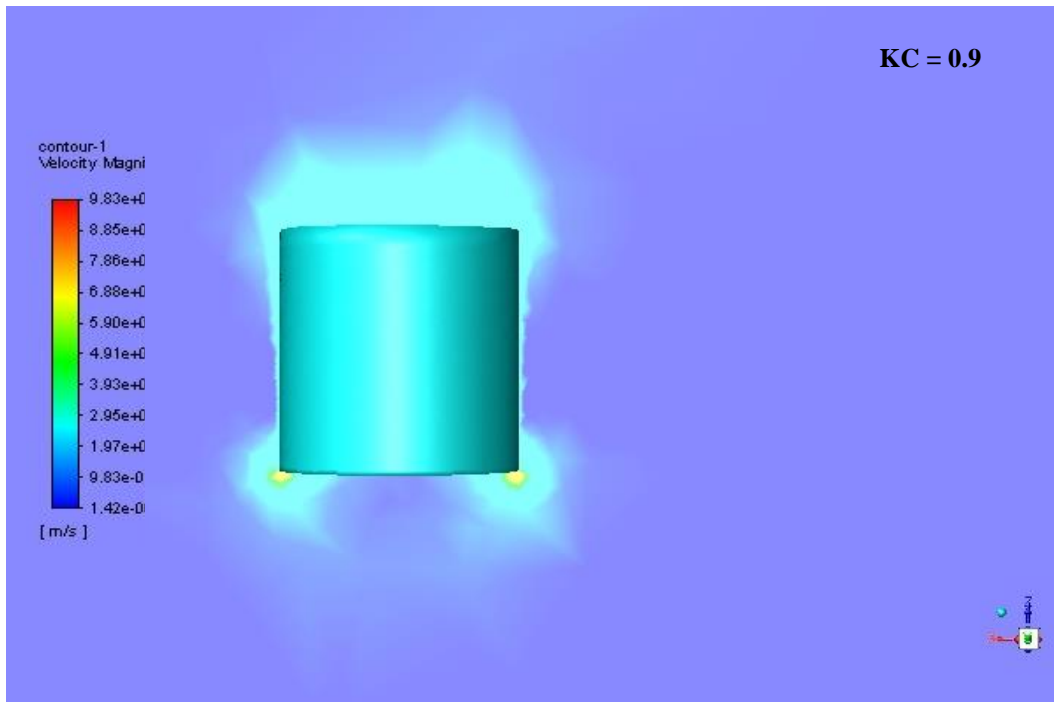
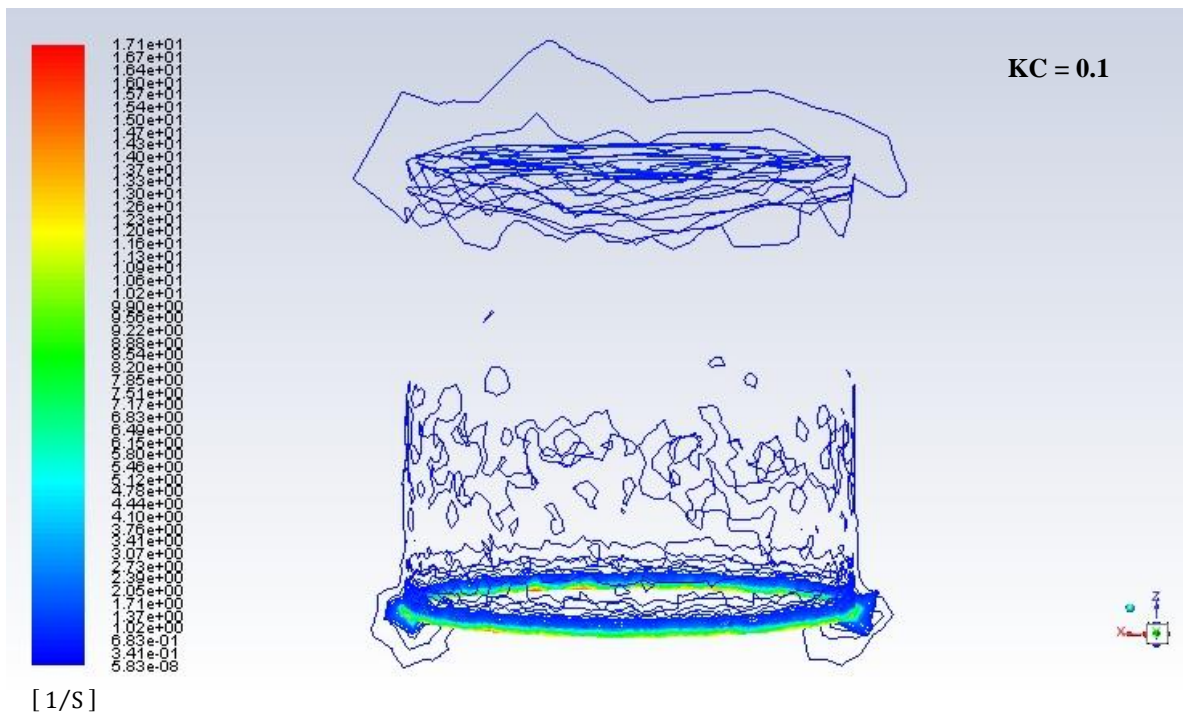
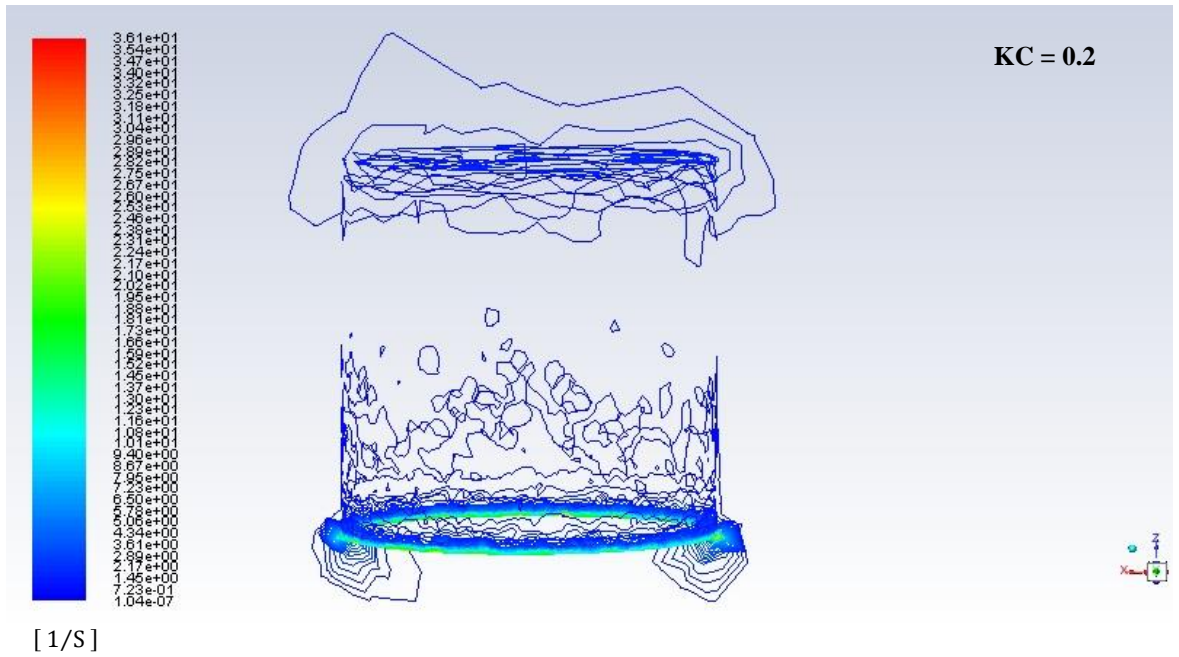


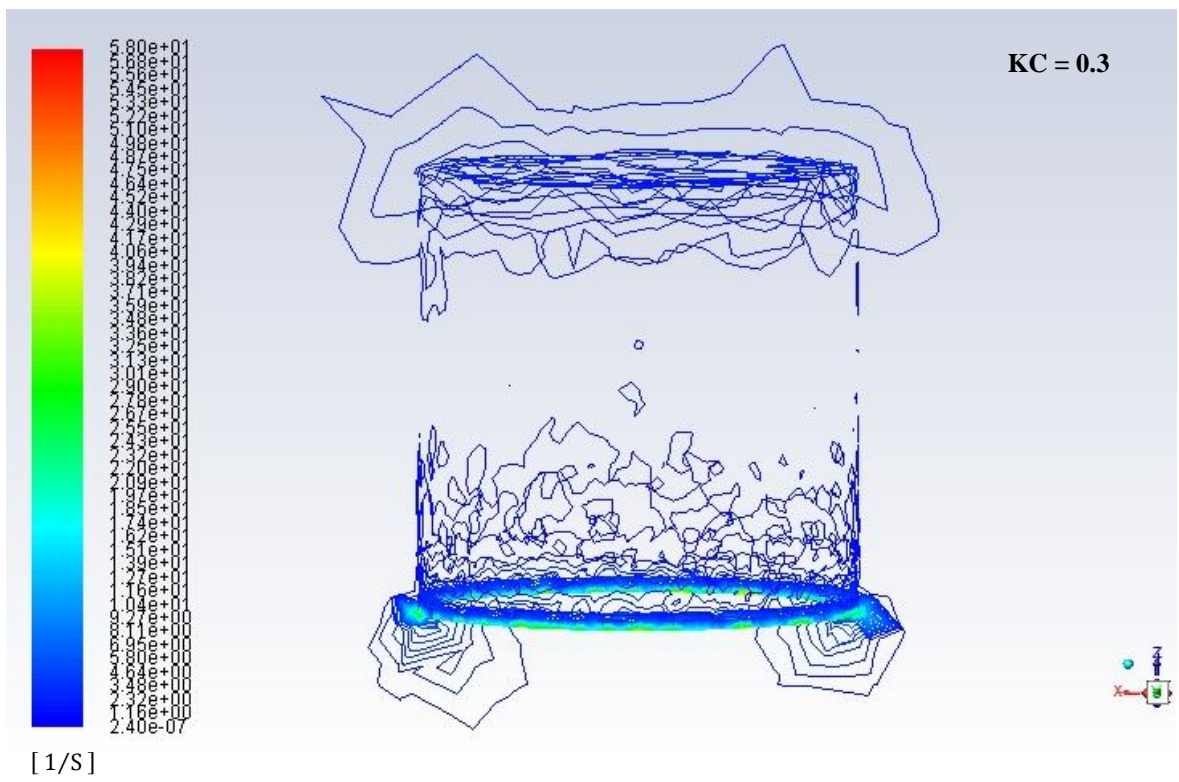
Figure B.1- 1 Contours of velocity magnitude of suction-can well away from surface and seabed for KC 0.1 - 0.9

B.2 Contours of Vorticity Magnitude of Suction-Can Well Away from Surface and Seabed

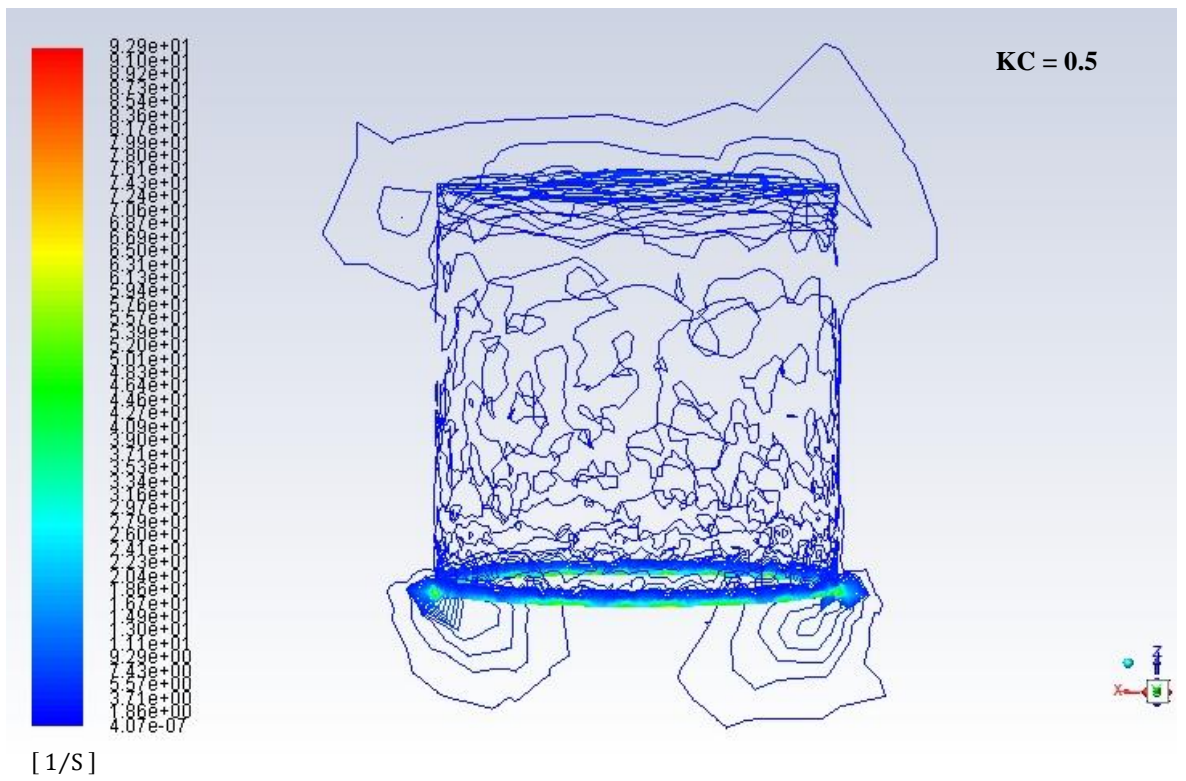
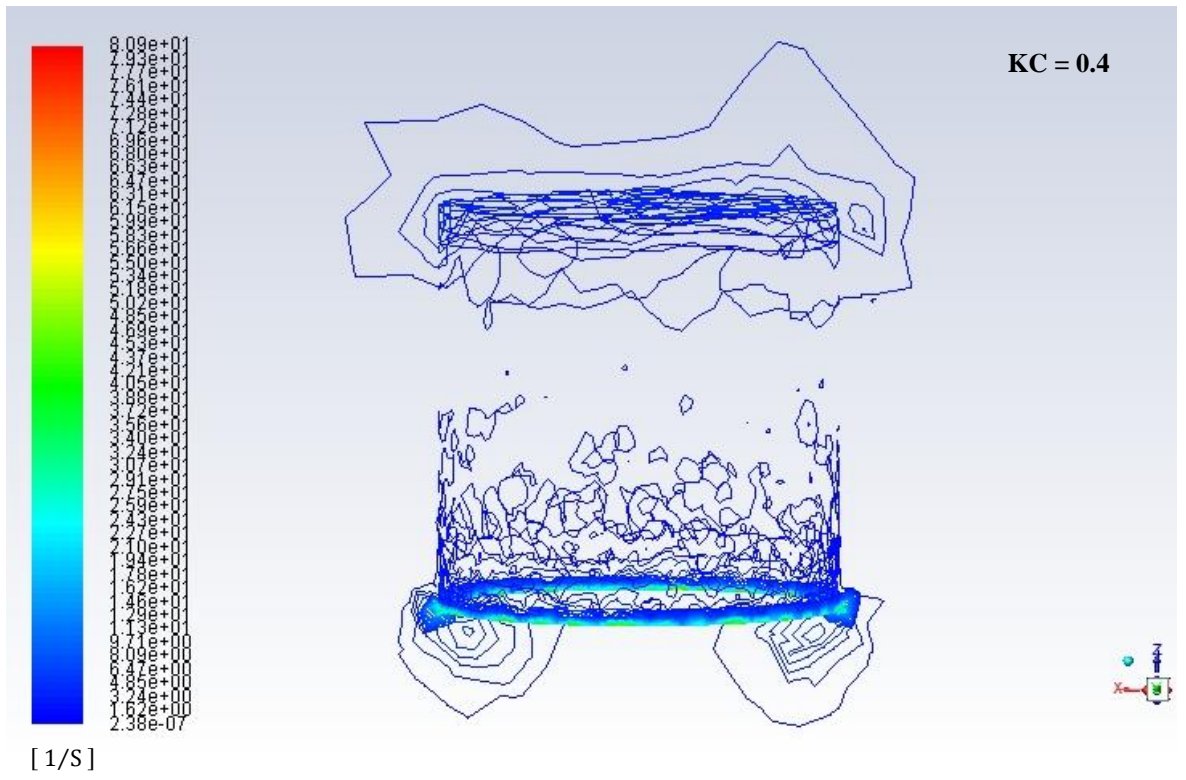


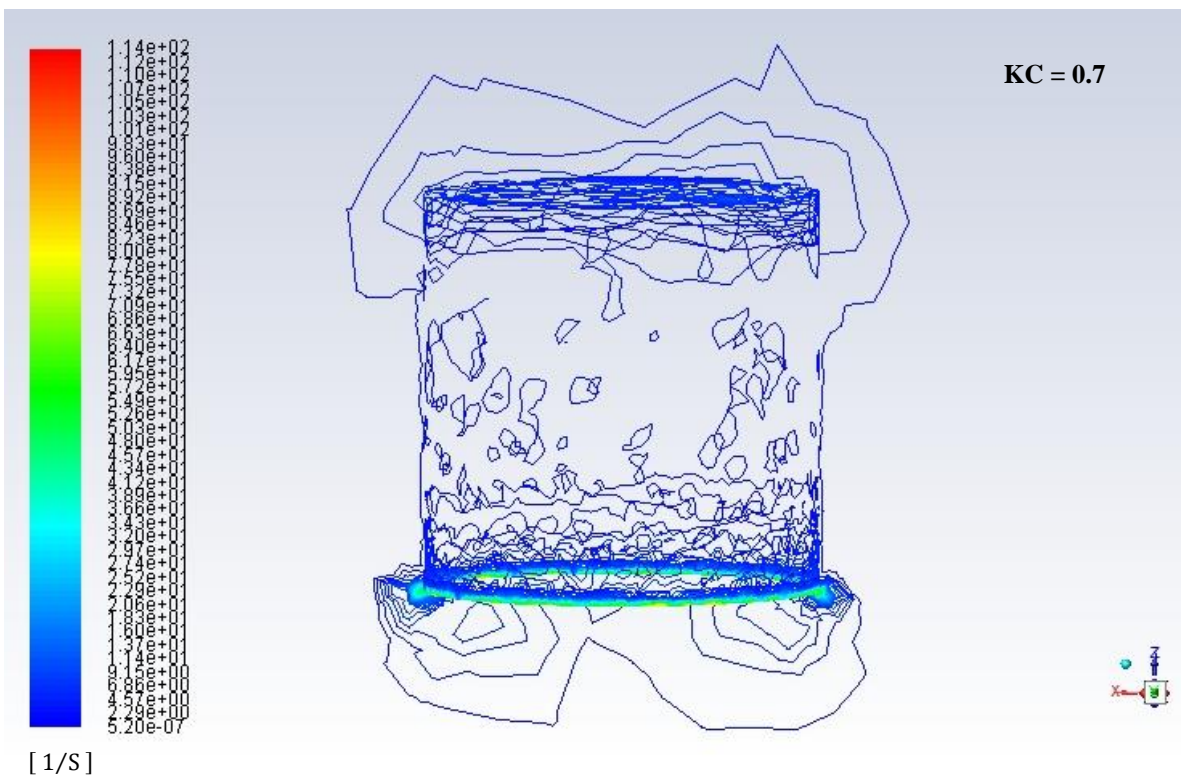
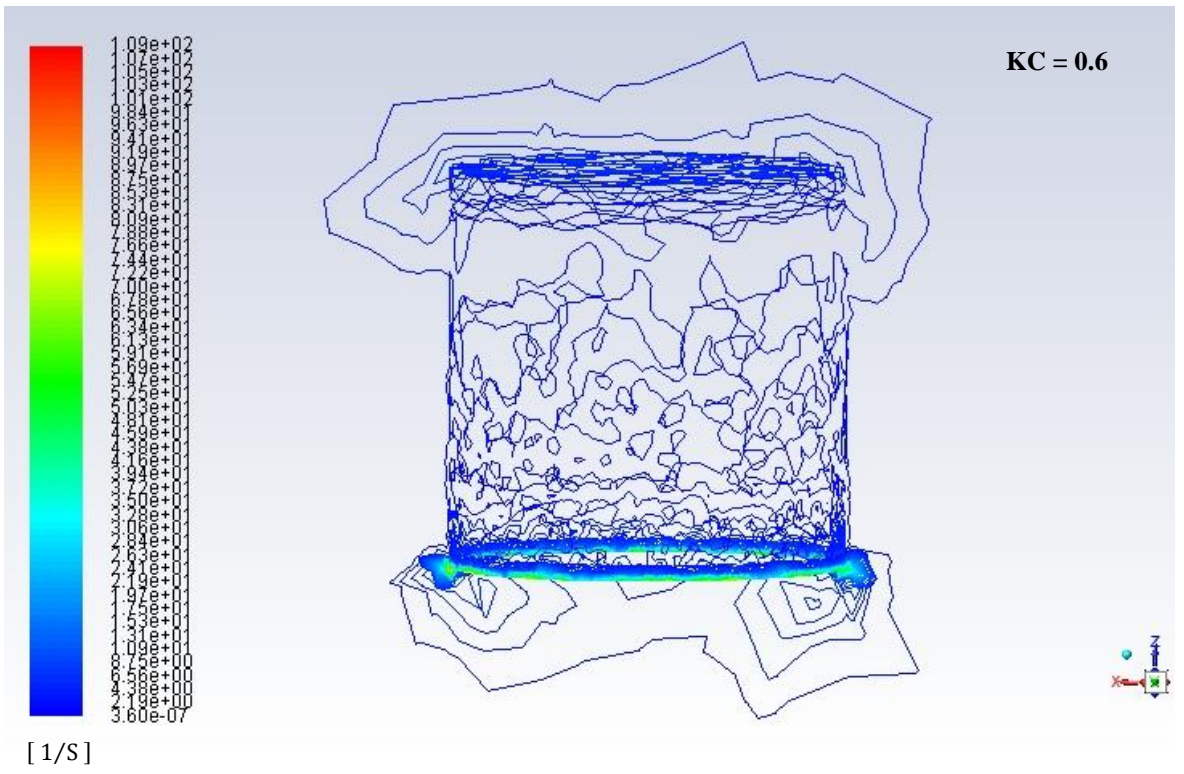


[1/S]



[1/S]





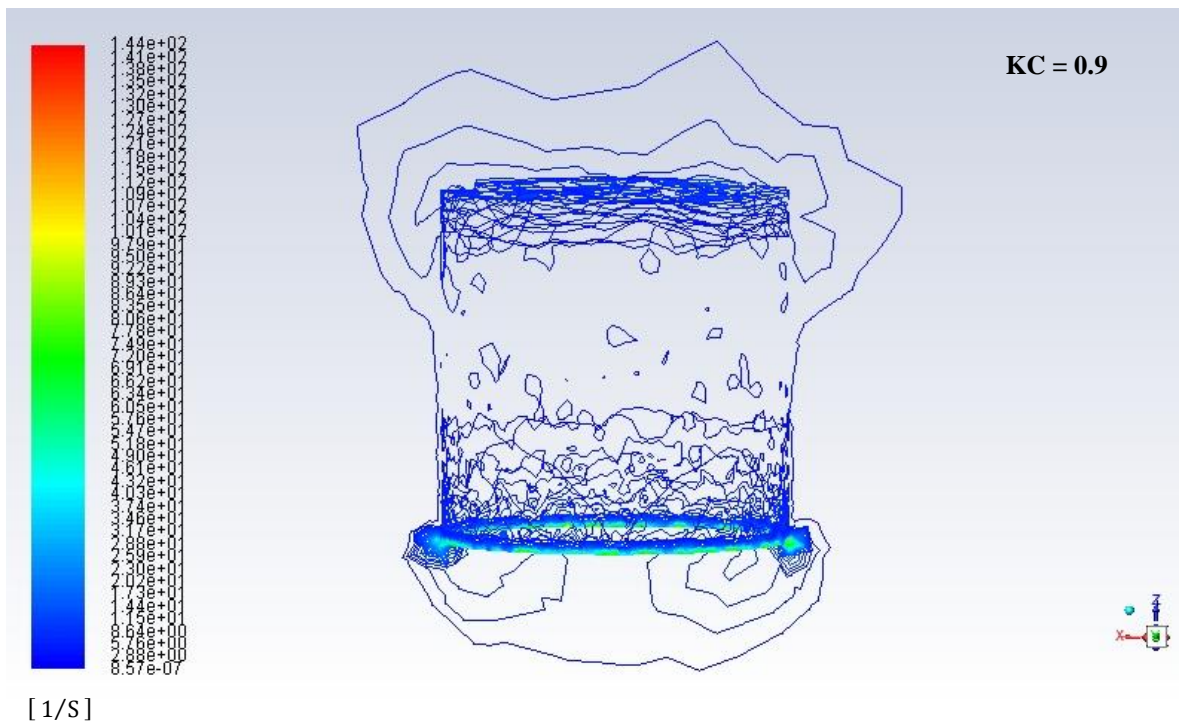
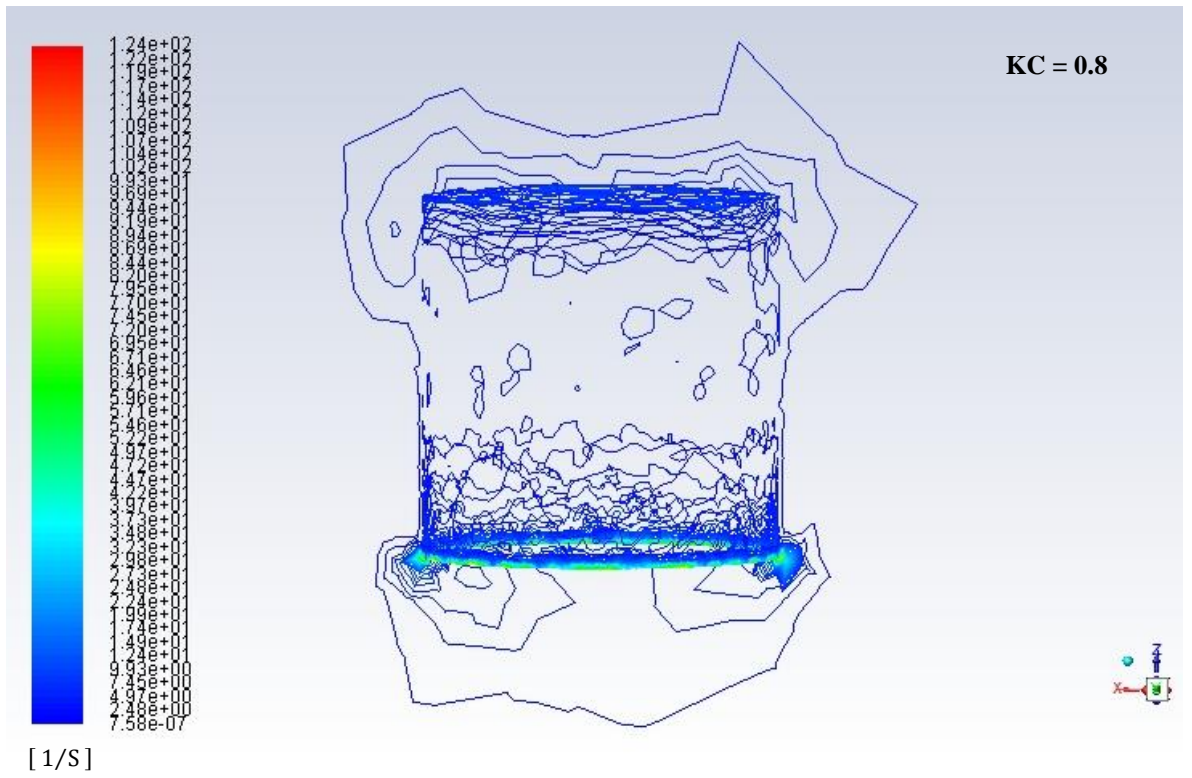
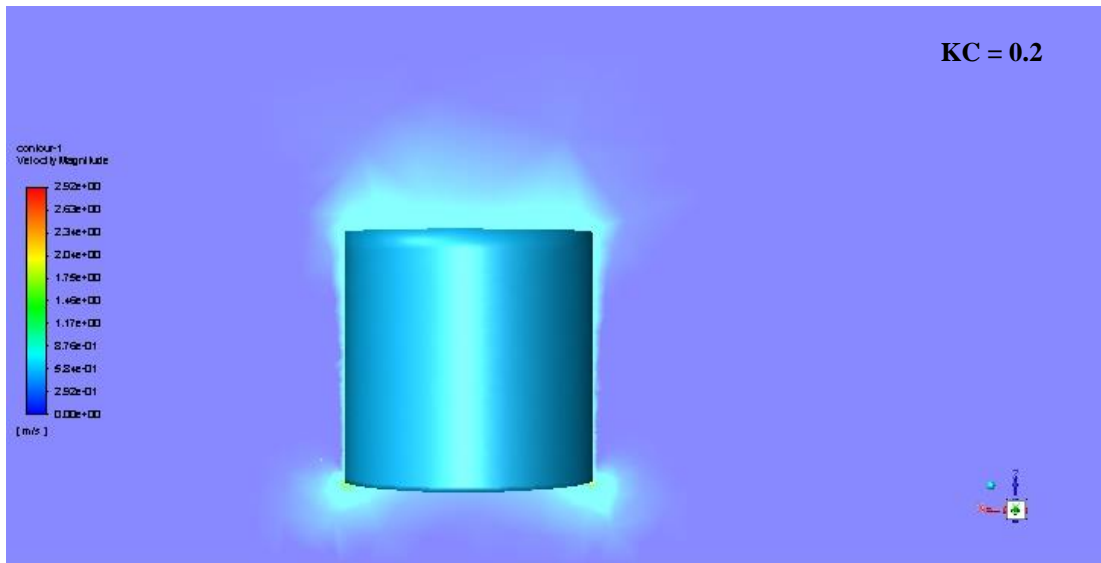
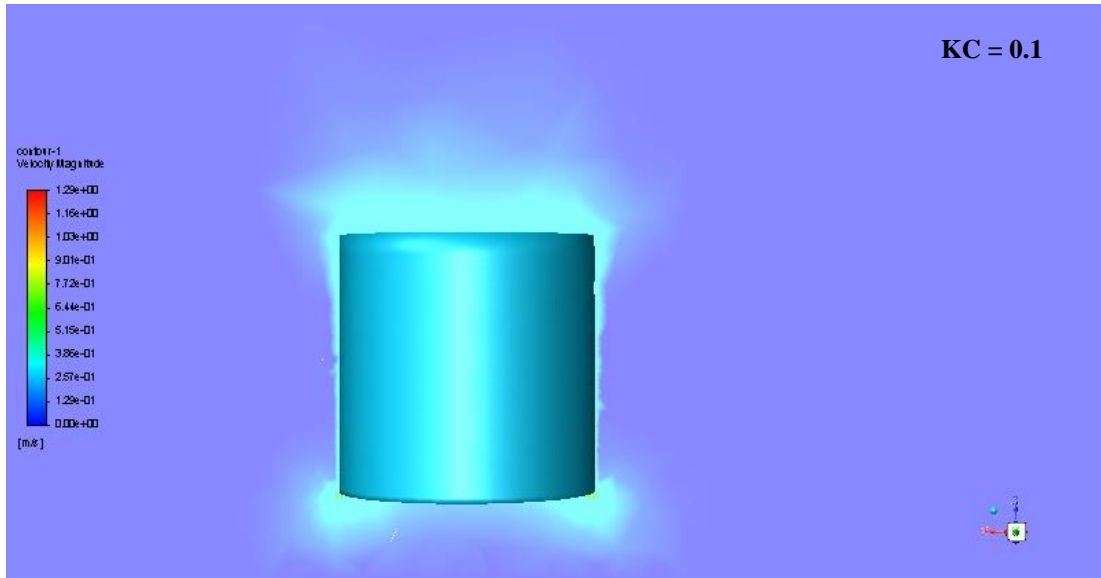
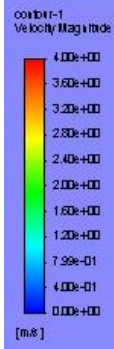


Figure B.2- 1 Contours of vorticity magnitude of suction-can well away from surface and seabed for KC 0.1 - 0.9

B.3 Contours of Velocity Magnitude of Suction-Can at $h/D = 0.4$



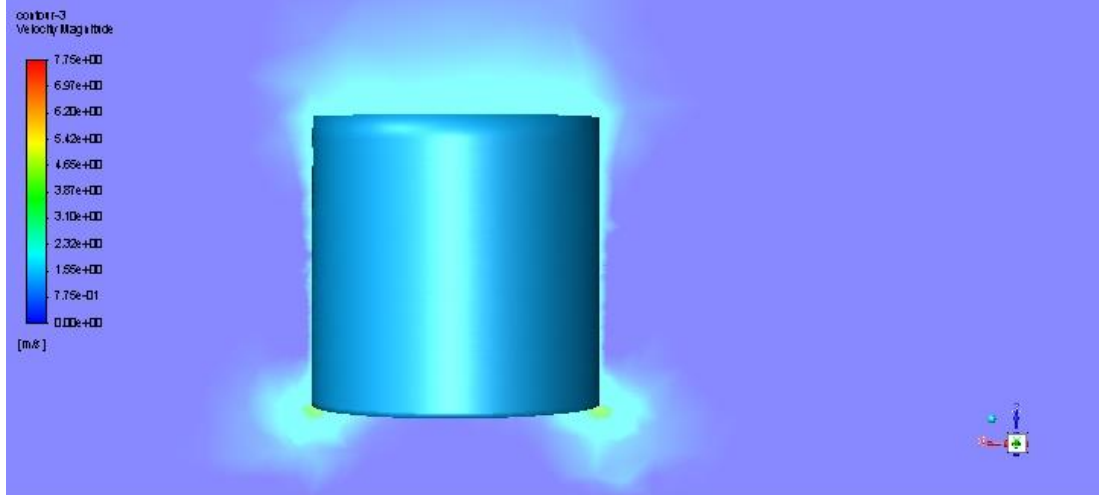
KC = 0.3



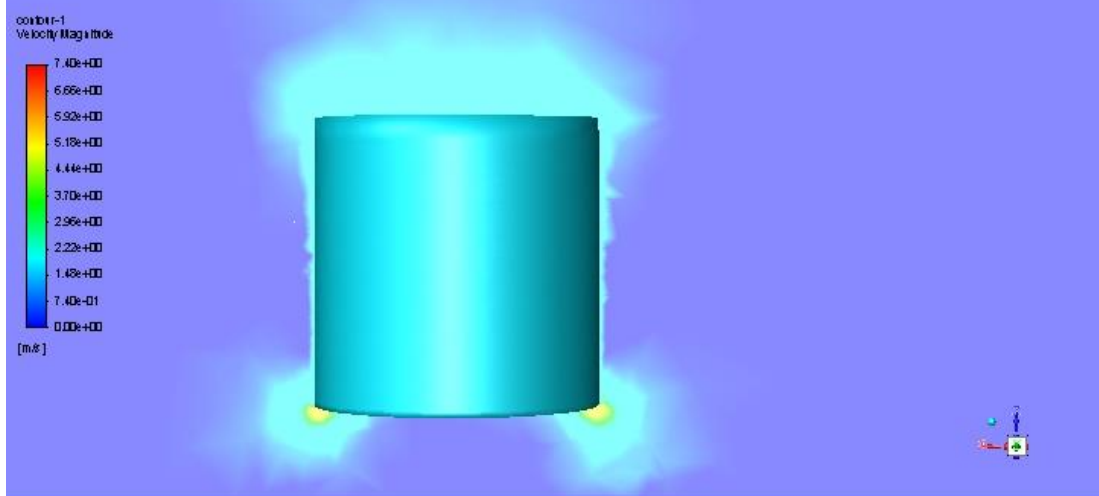
KC = 0.4



KC = 0.5



KC = 0.6



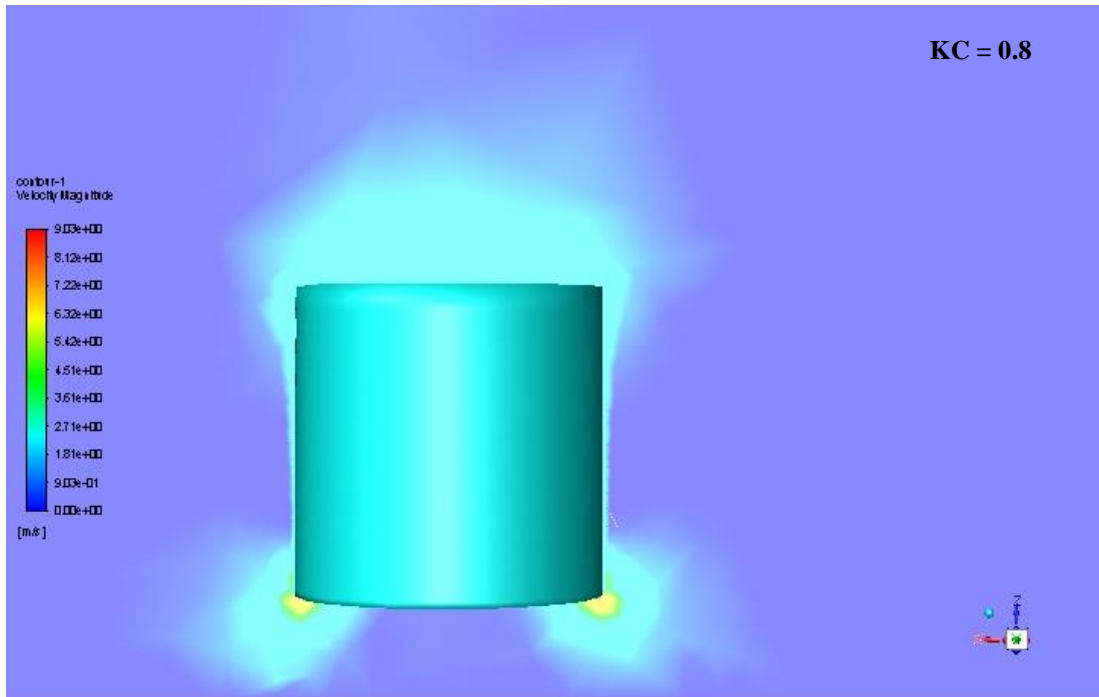
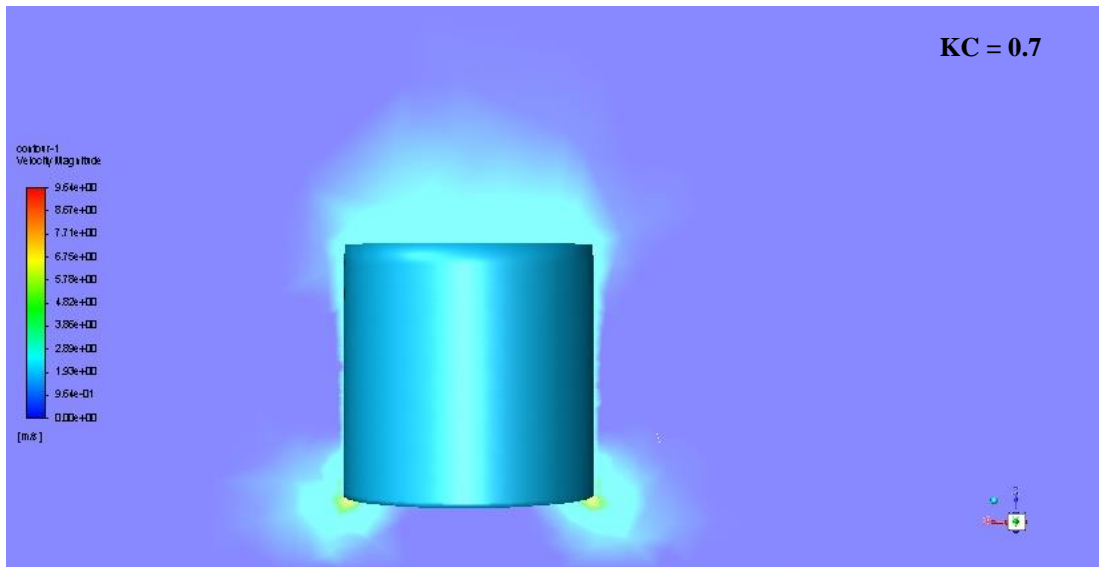


Figure B.3- 1 Contours of velocity magnitude of suction-can for $KC = 0.1 - 0.8$ at $h/D = 0.4$

APPENDIX C

C.1 Calculation of Added Mass and Damping of Subsea Protective Structure

The analytical calculation of the hydrodynamic coefficient of the subsea protective structure is presented in this section. The same procedure could be applied to other subsea structures of similar geometries. The dimensions of the subsea protective structure are presented in Table 5.3-1.

Outer Bucket: The added mass and damping of the outer bucket are presented in Table C.1-1. There is a gradual increase in the coefficients as KC increases. KC estimated with an equivalent diameter of 4.0 m.

Table C.1- 1 Added mass and damping of outer bucket

Parameter	Seabed clearance	KC								
		0.08	0.15	0.23	0.30	0.38	0.45	0.53	0.60	0.67
Added mass (kg)	Far from boundaries	119598	122359	124567	127327	130087	132847	135055	137816	140576
	h/D = 0.4	120798	124759	127927	131887	135847	139808	142976	146936	147800
	h/D = 0.2	126619	132380	136988	142748	134119	137720	140600	144200	147800
Added mass Coefficient	Far from boundaries	1.428	1.461	1.488	1.521	1.554	1.587	1.613	1.646	1.679
	h/D = 0.4	1.443	1.49	1.528	1.575	1.623	1.67	1.708	1.755	1.765
	h/D = 0.2	1.512	1.581	1.636	1.705	1.602	1.645	1.679	1.722	1.765
Damping (Ns/m)	Far from boundaries	4519	7176	8983	11014	12872	14606	15921	17494	18999
	h/D = 0.4	4519	7176	8983	11014	12872	14606	15922	17494	18999
	h/D = 0.2	6454	10248	12828	15727	18380	14606	15921	17494	18999
Damping ratio	Far from boundaries	0.362	0.575	0.719	0.882	1.031	1.17	1.275	1.401	1.522
	h/D = 0.4	0.362	0.575	0.719	0.882	1.031	1.17	1.275	1.401	1.522
	h/D = 0.2	0.517	0.821	1.027	1.26	1.472	1.17	1.275	1.401	1.522

Central Bucket:

KC estimated with an equivalent diameter of 1.0 m.

Table C.1- 2 Added mass and damping of central bucket

Parameter	Seabed clearance	KC								
		0.30	0.60	0.90	1.20	1.50	1.80	2.10	2.40	2.70
Added mass (kg)	Far from boundaries	2873	3014	3155	3297	3445	3586	3728	3869	4010
	h/D = 0.4	2891	3051	3210	3370	3538	3697	3857	4016	4724
	h/D = 0.2	2919	3106	3293	3480	3844	4064	4284	4504	4724
Added mass Coefficient	Far from boundaries	1.19	1.248	1.307	1.365	1.427	1.485	1.544	1.602	1.661
	h/D = 0.4	1.197	1.263	1.33	1.396	1.465	1.531	1.597	1.663	1.956
	h/D = 0.2	1.209	1.286	1.364	1.441	1.592	1.683	1.774	1.865	1.956
Damping (Ns/m)	Far from boundaries	172	274	360	436	510	576	638	697	754
	h/D = 0.4	172	274	360	436	510	576	638	697	754
	h/D = 0.2	172	274	360	436	510	576	638	697	754
Damping ratio	Far from boundaries	0.885	1.407	1.846	2.238	2.617	2.953	3.272	3.576	3.868
	h/D = 0.4	0.885	1.407	1.846	2.238	2.617	2.953	3.272	3.576	3.868
	h/D = 0.2	0.885	1.407	1.846	2.238	2.617	2.953	3.272	3.576	3.868

H-Beam:

Since the position of the H-Beam is not affected by the seabed, the calculation will be based on the structure well away from the surface and the seabed.

The added mass of the H-beam far from boundaries = $0.5\rho\pi r^2L = 724.85$.

The estimated drag, $C_d = 2.27$. Derived from the drag force of two-dimensional profiles in DNV RP H103, and based on the expressions:

$$C_d = C_{d1} \cos \alpha + C_{d2} \sin \alpha$$

$$C_d = -C_{d1} \sin \alpha + C_{d2} \cos \alpha$$

Therefore, damping at various KC numbers, estimated with an equivalent diameter of 24 m:

Table C.1- 3 Damping of H-Beam at various KC numbers

KC	0.01	0.03	0.04	0.05	0.06	0.08	0.09	0.10	0.11
Damping (Ns/m)	1926	3852	5778	7704	9630	11556	13482	15408	17334
Damping Ratio	0.005	0.010	0.016	0.021	0.026	0.031	0.037	0.042	0.047

Horizontal Beam:

The added mass of the Horizontal Beam far from boundaries = $\rho\pi r^2L = 8771.01$

The drag coefficient in this case varies with Reynolds number. The drag coefficients for the various KC numbers used in deriving the Reynolds number together with the diameter of the cylinder was obtained (Munson, et al., 2009) and presented in Table C.1-4. Table C.1-4 also contains the damping at various KC numbers, estimated with an equivalent diameter of 13.04 m.

Table C.1- 4 Drag coefficient and damping of Horizontal beam at various KC numbers

KC	0.02	0.05	0.07	0.09	0.12	0.14	0.16	0.18	0.21
C_d	1.2	0.59	0.29	0.35	0.38	0.40	0.42	0.47	0.50
Damping (Ns/m)	2129	2094	1543	2484	3371	4258	5217	6672	7985

The added mass and damping for seabed clearance $h/D = 0.4$ and $h/D = 0.2$ would be equal to the values obtained for the far-from-boundaries case since there is no seabed influence.

Hatch Beam:

The added mass of the Hatch Beam when well away from the surface and seabed

$$= \rho \pi r^2 L = 253.59$$

The added mass and damping for seabed clearance $h/D = 0.4$ and $h/D = 0.2$ would be equal to the values obtained for the far-from-boundaries case since there is no seabed influence.

The drag coefficient and damping are presented in Table C.1-5 at different KC numbers, estimated with an equivalent diameter of 10.9 m.

Table C.1- 5 Drag coefficient and damping of Hatch beam at various KC numbers

KC	0.03	0.06	0.08	0.11	0.14	0.17	0.19	0.22	0.25
C_d	1.2	1.2	1.2	1.2	1.2	1.2	1.13	1.00	0.80
Damping (Ns/m)	2129	4258	6388	8517	10646	12776	14035	14195	12775

Inclined Beam:

The added mass of the Inclined Beam far from boundaries $= \rho \pi r^2 L = 3766.61$

The drag coefficient in this case varies with Reynolds number. The drag coefficients for the various KC numbers used in deriving the Reynolds number together with the

diameter of the cylinder was obtained (Munson, et al., 2009) and presented in Table C.1-6. Table C.1-6 also contains the damping at various KC numbers, estimated with an equivalent diameter of 5.6 m.

Table C.1- 6 Drag coefficient and damping of inclined beam at various KC numbers

KC	0.05	0.11	0.16	0.21	0.27	0.32	0.37	0.43	0.48
C_d	1.2	0.59	0.29	0.35	0.38	0.40	0.42	0.47	0.50
Damping (Ns/m)	1008	986	728	1169	1589	2005	2458	3141	3757

The added mass and damping for seabed clearance $h/D = 0.4$ and $h/D = 0.2$ would be equal to the values obtained for the far-from-boundaries case since there is no seabed influence.

Total added mass and damping of structure well away from surface and seabed and close to seabed:

$$Ma =$$

$$\frac{2 \cdot Ma_{hbeam} + Ma_{centralbucket} + 4 \cdot Ma_{horizontalbeam} + 4 \cdot Ma_{outerbucket} + 35 \cdot Ma_{hatchbeam} + 4 \cdot Ma_{inclinedbeam}}{4}$$

$$Ca = \frac{Ma}{\rho \cdot V}$$

$$C =$$

$$\frac{2 \cdot C_{hbeam} + C_{centralbucket} + 4 \cdot C_{horizontalbeam} + 4 \cdot C_{outerbucket} + 35 \cdot C_{hatchbeam} + 4 \cdot C_{inclinedbeam}}{4}$$

$$\xi_{dw} = \frac{C}{2M\omega}$$

Presented in Table C.1-6:

Table C.1- 7 Added mass and damping of subsea protective structure

Parameter	Seabed clearance	KC								
		0.02	0.05	0.07	0.09	0.12	0.14	0.16	0.18	0.21
Added mass (kg)	Far from boundaries	541740	537859	546832	558014	569202	580383	589357	600542	611723
	h/D = 0.4	546558	562562	575393	591393	607401	623404	636236	652235	656399
	h/D = 0.2	569870	593101	611720	634947	600795	615419	627159	641779	656399
Added mass Coefficient	Far from boundaries	1.372	1.400	1.423	1.451	1.479	1.508	1.530	1.559	1.587
	h/D = 0.4	1.384	1.424	1.457	1.497	1.538	1.578	1.611	1.651	1.662
	h/D = 0.2	1.443	1.502	1.549	1.608	1.521	1.558	1.588	1.625	1.662
Damping (Ns/m)	Far from boundaries	109172	198049	280508	372613	463721	554312	613225	637569	605531
	h/D = 0.4	109172	198049	280508	372613	463721	554312	613229	637569	605531
	h/D = 0.2	116912	210337	295888	391465	485753	554312	613225	637569	605531
Damping ratio	Far from boundaries	0.013	0.024	0.033	0.043	0.054	0.063	0.070	0.072	0.068
	h/D = 0.4	0.013	0.023	0.032	0.042	0.052	0.061	0.067	0.069	0.065
	h/D = 0.2	0.014	0.024	0.033	0.043	0.055	0.062	0.068	0.070	0.065

Table C.1- 8 Added mass and damping contribution from each member of the subsea protective structure, initial KC for each member

Subsea Protective Structure Member		Outer Bucket	Central Bucket	H-Beam	Horizontal Beam	Hatch Beam	Inclined Beam
Far From Boundaries	Ma (kg)	119598	2873	724.85	8771.01	253.59	3766.61
	c_{a33}	1.428	1.19	0.50	1.0	1.0	1.0
	C (Ns/m)	4519	172	1926.02	2129.27	2129.27	1008
	ξ	0.362	0.885	0.005	1.2	1.2	1.2
h/D = 0.4	Ma (kg)	120798	2891	724.85	8771.01	253.59	3766.61
	c_{a33}	1.443	1.197	0.50	1.0	1.0	1.0
	C (Ns/m)	4519	172	1926.02	2129.27	2129.27	1008
	ξ	0.362	0.885	0.005	1.2	1.2	1.2
h/D = 0.2	Ma (kg)	126619	2919	724.85	8771.01	253.59	3766.61
	c_{a33}	1.512	1.209	0.50	1.0	1.0	1.0
	C (Ns/m)	6454	172	1926.02	2129.27	2129.27	1008
	ξ	0.517	0.885	0.005	1.2	1.2	1.2

Table C.1- 9 Comparison between added mass and damping coefficient of approximate method and CFD analysis of the subsea protective structure

KC	Far From Boundaries			
	Added mass coefficient, C_a		Damping ratio, ξ	
	Approximate method	CFD	Approximate method	CFD
0.02	1.372	1.591	0.013	0.030
0.05	1.400	1.595	0.024	0.040
0.07	1.423	1.601	0.033	0.045
0.09	1.451	1.609	0.043	0.047
0.12	1.479	1.618	0.054	0.050
0.14	1.508	1.629	0.063	0.055

0.16	1.530	1.642	0.070	0.064
0.18	1.559	1.657	0.072	0.067
0.21	1.587	1.673	0.068	0.070
KC	h/D = 0.4			
	Added mass coefficient, Ca		Damping ratio, ξ	
	Approximate method	CFD	Approximate method	CFD
0.02	1.384	1.660	0.013	0.036
0.05	1.424	1.667	0.023	0.039
0.07	1.457	1.678	0.032	0.045
0.09	1.497	1.696	0.042	0.050
0.12	1.538	1.715	0.052	0.052
0.14	1.578	1.736	0.061	0.055
0.16	1.611	1.761	0.067	0.060
0.18	1.651	1.784	0.069	0.065
0.21	1.662	1.810	0.065	0.077
KC	h/D = 0.2			
	Added mass coefficient, Ca		Damping ratio, ξ	
	Approximate method	CFD	Approximate method	CFD
0.02	1.443	1.757	0.033	0.043
0.05	1.502	1.772	0.043	0.050
0.07	1.549	1.794	0.055	0.055
0.09	1.608	1.823	0.062	0.060
0.12	1.521	1.856	0.068	0.065
0.14	1.558	1.891	0.070	0.070
0.16	1.588	1.928	0.065	0.075
0.18	1.625	1.965	0.069	0.081
0.21	1.662	2.003	0.065	0.085

APPENDIX D

D.1 Response of Subsea Protective Structure

The response of the subsea protective structure using the derived added mass and damping from the approximate method and CFD analysis is presented in this section. Orcaflex is used in calculating the response of the subsea protective structure at different amplitudes of motion at the crane tip of the installation vessel.

Table D.1- 1 Response of subsea protective structure far from boundaries

KC	Response Ratio (Z_{dyn}/Z_{sg})	
	Approximate Method	CFD
0.02	4.13E-04	3.00E-04
0.05	6.60E-04	5.20E-04
0.07	8.53E-04	7.20E-04
0.09	9.93E-04	9.33E-04
0.12	1.11E-03	1.11E-03
0.14	1.21E-03	1.27E-03
0.16	1.33E-03	1.36E-03
0.18	1.49E-03	1.51E-03
0.21	1.71E-03	1.65E-03
Z_{sg} : Distance between bottom of structure and seabed = 1500 m		

Table D.1- 2 Response of subsea protective structure at $h/D = 0.2$

KC	Response Ratio (Z_{dyn}/Z_{sg})	
	Approximate Method	CFD
0.02	0.45	0.20
0.05	0.62	0.35
0.07	0.73	0.48
0.09	0.78	0.58

0.12	0.83	0.67
0.14	0.88	0.74
0.16	0.94	0.80
0.18	1.03	0.85
0.21	1.21	0.90
Z_sg: Distance between bottom of structure and seabed = 1.2 m		

Table D.1- 3 Line tension far from boundaries

KC	Effective Tension ($T_{dynamic}/T_{static}$)	
	Approximate Method	CFD
0.02	1.07	1.05
0.05	1.11	1.09
0.07	1.14	1.12
0.09	1.17	1.16
0.12	1.20	1.20
0.14	1.23	1.23
0.16	1.26	1.26
0.18	1.30	1.30
0.21	1.34	1.33
$T_{static} = 5366$ KN		

Table D.1- 4 Line tension at $h/D = 0.2$

KC	Effective Tension ($T_{dynamic}/T_{static}$)	
	Approximate Method	CFD
0.02	1.04	1.02
0.05	1.06	1.04
0.07	1.08	1.06
0.09	1.09	1.08
0.12	1.11	1.10
0.14	1.13	1.12
0.16	1.14	1.14
0.18	1.16	1.15
0.21	1.18	1.17
$T_{static} = 5366$ KN		

D.2 Theory related to the ORCAFLEX analyses

Line Theory

The numerical analysis uses a finite element model (see Figure D.2-1) for the line which is made up of a series of line segments. The line segments are modelled as massless segments with a node at each end of the segment. This makes possible modelling deepwater multicomponent lines such as multicomponent mooring lines with segments comprising of chain and wire/rope.

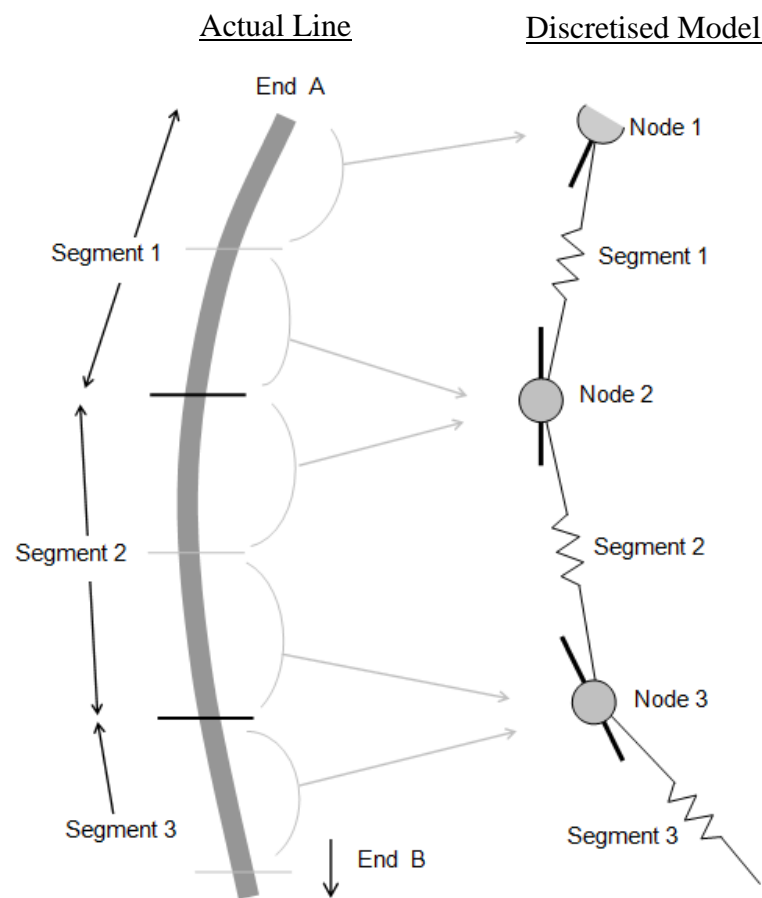


Figure D.2- 1 Numerical line model (Source: Orcina)

The model segments are considered massless since their properties such as mass, weight and buoyancy are lumped to the nodes. Figure D.2-1 shows each node as a rode

short in length and has the combined properties of half on one segment to the left of the node and the properties of half of the other segment the right of the node except for end nodes which have only the properties of only one half of the segment next to them.

The model segments are straight massless element that models just the axial and torsional properties of the line (Orcina, 2018). Figure D.2-2 shows in detail the line model.

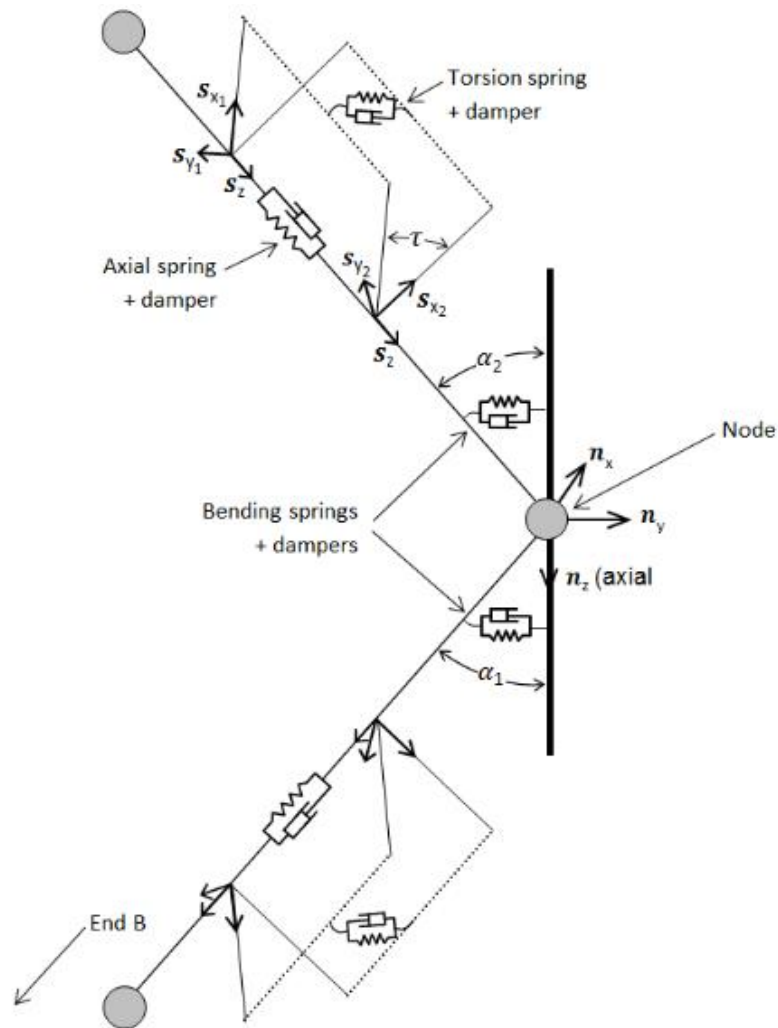


Figure D.2- 1 Showing a single mid-line node and the segments either side of it, and various spring-dampers

Winch Theory

Installation analysis would require specifying either the length or tension in the winch control mode while conducting a static analysis. The tension in the wire, T_w can be equated to the winch drive force, F_w and expressed in terms of the wire stiffness, K and the strain. Mathematically expressed as

$$T_w = F_w = K\epsilon \quad \text{Equation D.2- 1}$$

where, ϵ is the wire strain given as $(l - l_0)/l_0$, l is the total length of the wire and l_0 is the unstretched length of the paid out wire which is set to the specified length for the static analysis. In this case the tension and the winch drive force are derived from the specified length.

If the control mode is set to the specified tension, that is the tension, T_w and the winch drive force, F_w set to the specified tension for the static analysis, then the unstretched length paid out would be derived from these known parameters by applying the equation above.

For the dynamic analysis, the winch control described in the OrcaFlex documentation by Orcina may take a number of different forms (Orcina, 2018): “it may be given for the whole simulation or individually for each stage; it can define constant values, change in value or rate of change; and it may be constant, time-varying or defined by external function”. The documentation also pointed out that “In all cases, however, at any one time the winch is either length-controlled or tension-controlled, and its properties can be calculated accordingly”. See OrcaFlex documentation (Orcina, 2018) for more on winch theory.

Wave Theory

Ocean waves are best described by their height, length, speed and direction of propagation, and by their occurrence (irregular) and mode of occurrence (randomness). The random and irregular shape of ocean waves best describes a real sea state, categorised into two wave models which are a linear random wave model and a non-linear wave model (DNV-RP-C205).

Table D.2-1 presents the characteristics of waves and the following figure shows a graphical representation of the wave parameters.

Table D.2- 1 Definition of wave parameters with formulas

Parameter	Definition and formula	Units
Wave length	Denoted by λ , is the distance between successive crests.	m
Wave period	Denoted by T , is the time interval between successive crests as they pass a fixed point	sec
Phase velocity	The phase velocity, c also known as the wave speed or celerity is the propagation velocity of the wave where, $c = \lambda/T$.	m/s
Wave frequency	The wave frequency is simply the inverse of the wave period denoted by	Hz
Wave number	The wave number, $k = 2\pi/\lambda$.	m^{-1}
Wave angular frequency	The wave angular frequency, $\omega = 2\pi/T$.	rads/sec
Surface elevation	Distance measured from the still water level to the wave surface given by $z = \eta(x, y, t)$.	m
Wave crest height	Distance from the still water level to the crest, denoted by A_c	m
Wave trough depth	Distance from the still water level to the trough, denoted by A_T	m
Wave height	This is the vertical distance from the trough to the crest and is given by $H = A_c + A_T$	m

Various wave theories for regular linear and nonlinear waves: Airy, Dean, Stokes' 5th or Sinusoidal wave theories. The regular wave theory is the simplest type of theory where the wave crest height is equal in magnitude to the wave trough depth. DNV-RP-C205 gives full details of these wave theories with the recommended Dean's nonlinear wave theory suitable for all regular waves. The Airy wave theory is a simple form of

the linear wave theory but only suitable for small waves where the wave height is much smaller than the wave length and water depth unlike the sinusoidal wave theory which is only suitable for long waves in a shallow water environment, and the Stoke's 5th wave theory suitable for short waves in deepwater environments.

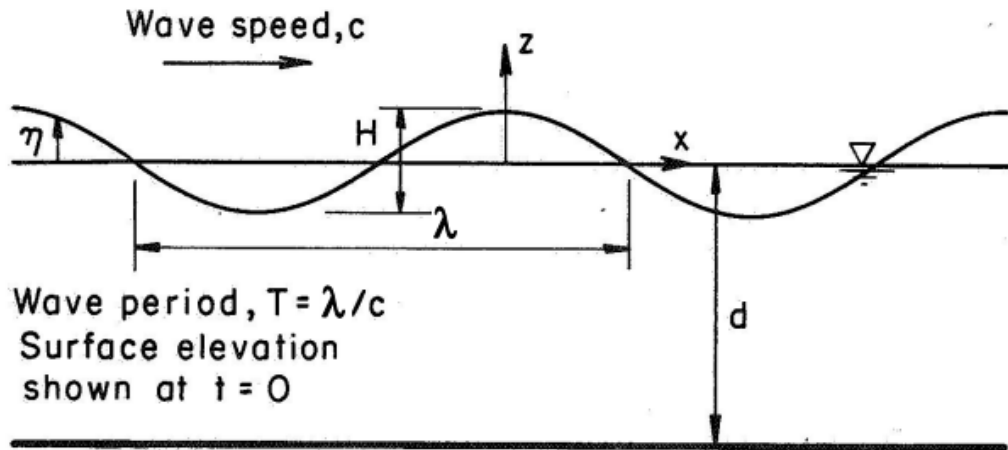


Figure D.2- 2 Regular travelling wave properties (Source: DNV-RP-H103)

In the case of a more realistic sea state representation, irregular waves known as random waves may be applied which is the summation of several sinusoidal or regular wave components. DN-RP-H103 stated that the simplest of form of this wave model is the linear long-crested wave model given by:

$$\eta_1(t) = \sum_{k=1}^N \eta_k \cos(\omega_k t + \varphi_k) \quad \text{Equation D.2- 2}$$

where, the random phases distributed uniformly between 0 and 2π are denoted by φ_k and according to the recommended practice, DN-RP-H103, “mutually independent of each other and of the random amplitudes which are taken to be Rayleigh distributed with mean square value”

$$E[\eta_k^2] = 2S(\omega_k)\Delta\omega_k \quad \text{Equation D.2- 3}$$

where, $S(\omega_k)$ is the wave spectrum which describes short term stationary random sea states and $\Delta\omega_k = (\omega_{k+1} - \omega_{k-1})/2$.

There are several wave spectra such as the Pierson-Moskowitz and JONSWAP spectra, which is mostly applied for wind seas and as explained in DN-RP-H103, the Pierson-Moskowitz spectrum was originally for fully developed seas while the JONSWAP spectrum is an extension of the Pierson-Moskowitz spectrum to include fetch seas. The JONSWAP (Joint North Sea Wave Project) spectrum is suitable for numerical analysis of deepwater installation processes since it describes conditions such as wind sea conditions that frequently occur for the most severe sea-state